UNIVERSITÀ DI SIENA 1240

Department of Physical Sciences, Earth and Environment

PhD in Experimental Physics

XXXVI Cycle

Coordinator: Prof. Riccardo Paoletti

Measurement of cosmic-ray Helium flux in extended acceptance with the CALET experiment

Disciplinary Scientific Sector: FIS/01

A thesis submitted in partial fulfillment of the requirements
for the degree of Doctor of Philosophy

PhD Student
Marco Mattiazzi
University of Siena
Via Roma 56

MARCO MATTIAZZI
01/07/2024 13:35:01

Signature

Supervisor
Prof. Gianmaria Collazuol
University of Padova

Tutor
Dott. Paolo Brogi
University of Siena

2023/2024

Contents

Introduction

State-of-the-art detectors operating in space have paved the way for high-precision direct measurements of galactic cosmic-ray (CR) spectra. Recent results for proton and helium nuclei have shown unexpected spectral features that deviate from the single power law predicted by the standard CR model. From a few hundred GeV to a few TeV, a hardening of the spectral index, *i.e.* an enhancement of the flux, has been measured by several experiments (*e.g.* AMS-02, PAMELA, DAMPE, and CALET) using different experimental techniques (magnetic spectrometers, calorimeters). At tens of TeV, both the DAMPE and CALET calorimeters have recently observed a flux softening. These results have pushed the boundaries of direct measurements of CR spectra, helping to shed light on the acceleration and propagation mechanisms of CRs in the Galaxy. Nevertheless, the high-energy region of the spectra, from tens to hundreds of TeV, still suffers from significant uncertainties, mainly due to the very limited statistics.

In this context, the main objective of this Thesis is to improve the statistical precision of the CR helium flux measurement with CALET data, focusing on the high-energy region. This is achieved by extending the fiducial geometrical acceptance of the present analysis [8].

The CALorimetric Electron Telescope (CALET) is a multi-purpose space-based experiment that has been acquiring data onboard the International Space Station (ISS) since mid-October 2015. The mission is sponsored by JAXA (Japan Aerospace eXploration Agency) with the collaboration of ASI (Italian Space Agency) and NASA (National Aeronautics and Space Administration). The CALET instrument consists of three sub-systems. The Total AbSorption Calorimeter (TASC), a deep homogeneous calorimeter with an equivalent thickness of 27 radiation lengths (X_0), measures the particle energy. The IMaging Calorimeter (IMC) is a sampling calorimeter with an equivalent thickness of 3 X_0, primarily designed to visualize the particle trajectory and its early shower profile. The CHarge Detector (CHD) is a two-layer hodoscope for identification of nuclear species over a wide dynamic range, from $Z = 1$ to $Z = 40$.

In Chapter 1, an overview of cosmic ray physics is given, from its earliest stages to the current developments.

In Chapter 2, the CALET telescope is extensively described in terms of components and performance. A selection of CALET results, obtained during the first ~ 7.5 years of operation, is also reported.

In Chapter 3, the event reconstruction procedure that is common with *in-flight* and simulated data is described. For each event, such procedure provides all the information needed for the helium analysis, such as the track, the energy deposited in the calorimeter, and the charge estimators for the identification of the impinging particle identification. The selection criteria (pre-selection), that ensures a well-reconstructed sample of events, is also explained in detail.

Chapter 4 is mainly focused on a newly developed selection, based on a machine-learning technique, that improves the helium analysis, especially at high energies. In particular, the main novelty is the introduction of multivariate analysis based on Boosted Decision Trees (BDTs) to enhance the rejection of background events whereby the trajectory of the primary particle is misidentified. The charge identification and the unfolding procedure to infer the primary energy from the fraction of energy deposited in the calorimeter, are also discussed. The former is performed as a function of deposited energy, in order to ensure an almost constant efficiency over the entire range, while limiting proton contamination. For the second, two different approaches have been studied: the Bayesian iterative approach and the SVD-based approach. In both cases, the stability of the unfolding procedure has been validated and the related statistical uncertainty has been evaluated by using the *bootstrap* method. Finally, a preliminary measurement of helium flux in fiducial acceptance is provided.

Chapter 5 describes the steps taken to extend the analysis to enlarged acceptances `K1` and `K3`, *i.e.* including events with larger tilt angle that do not cross the CHD sub-detector. Theoretically, such extensions could allow a statistical gain of up to 60 percent, with respect to the fiducial acceptance. In particular, BDT-based selections and energy-dependent charge selections are defined for these two separate extended acceptances, the former more conservative (`K1`) than the latter (`K3`), differing in the number of IMC layers traversed. After verifying the stability of the iterative unfolding procedure, the corresponding flux measurements for both configurations are reported with their statistical uncertainties.

In Chapter 6, a preliminary evaluation of the systematic errors is reported for both the analysis in the fiducial acceptance `A1` and in the extended acceptances `K1` and `K3` . Finally, the flux measurements with their total errors, are presented and discussed.

Chapter 1

Galactic Cosmic-Ray Physics

Although more than a century has passed since the discovery of cosmic rays, the full picture of their origin, as well as the nature of their acceleration and propagation mechanisms, has yet to be completely assessed. This chapter provides an overview of cosmic ray research from its earliest stages to current developments.

1.1 Historical overview

The history of cosmic rays can be traced back to the beginning of the 20^{th} century, when systematic investigations into the enigma of the spontaneous discharge of an isolated electroscope[1] began. The prevailing view at the time was that this unknown *penetrating radiation* would come from the Earth's crust[2]. However, a series of courageous experimental measurements led to a paradigm shift. In 1912, Victor Hess carried out a series of high-altitude balloon flights (up to 5200 m) to measure the ionisation level of the atmosphere, leading to the discovery of what would later be called cosmic rays. As shown in the left panel of the Fig. 1.1, the results proved that, apart from a small initial decrease in the ionisation rate, the amount of radiation increased with altitude. These results were later confirmed by Kolhöster, who made measurements up to an altitude of 9200 m (right panel of the Fig. 1.1) between 1913 and 1914, confirming the extraterrestrial origin[3] of this penetrating radiation.

The name "cosmic rays" was later coined by Robert Millikan in 1926, who became convinced of their non-terrestrial origin after making measurements at various depths in high-altitude lakes. However, CRs were initially thought to be high-energy photons (the "*ultra γ-ray*" hypothesis) resulting from the

---

[1] This phenomenon was first reported by the French scientist Charles Augustin de Coulomb at the end of the 18^{th} century in his third work (1785) of his "*Mémoires sur l'électricité et le magnétisme*".

[2] This hypothesis was motivated by the existence of radioactive elements discovered at the time by Henri Becquerel and Marie and Pierre Curie. In fact, the first experiments with these radioactive sources showed that a charged electroscope discharges when a radioactive rod is approached.

[3] It is worth noting that the hypothesis that cosmic rays would come exclusively from the Sun was also ruled out, as Hess did not observe any significant day-night asymmetry in his measurements.

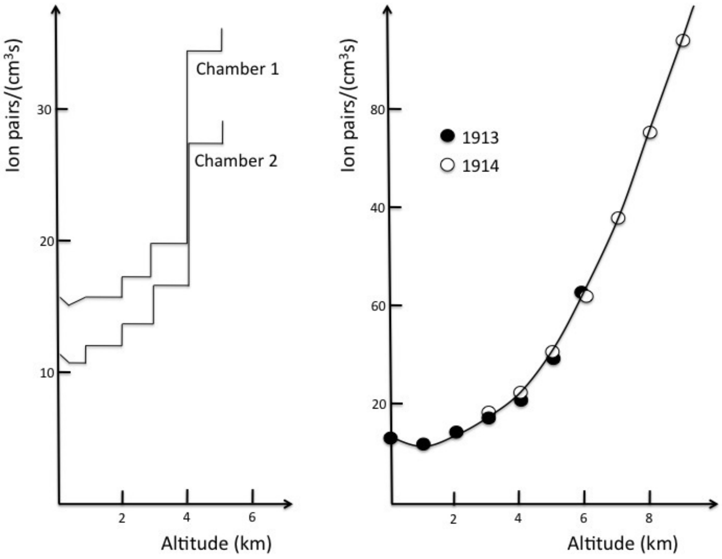

FIGURE 1.1: Levels of ionizing radiation as a function of altitude measured by Hess [88] in 1912 (right panel) and by Kolhöster in 1913-14 (left panel). The ionisation rate found by Kolhöster was about 10 times higher than the rate measured at sea level, confirming its extraterrestrial origin. Figure taken from [65].

synthesis of light elements, such as helium, in the interstellar medium (*"birth cries of atoms"* according to the Millikan's famous expression).

In 1927, Clay [55] discovered instead that this radiation is made by charged particles, observing that the intensity of the CR varied with latitude[4] as a consequence of the Earth's magnetic field. Since then, the geomagnetic effect of the CRs has been confirmed in several experimental campaigns. The world-wide Compton and Alvarez [30] campaign was the first to observe the East-West effect[5], demonstrating that CR are predominantly positively charged particles.

In 1938, Pierre Auger and Ronald Maze [34], while performing measurements at high altitude discovered[6] *extensive air showers* (EAS), *i.e.* a cascade of secondary particles produced by the interaction of a primary CR with particles in the air. By observing signals in coincidence between detectors placed up to 300 meters apart, they estimated that the energy of the primary CRs reached up to $\sim 10^{15}$ eV, a surprising result, given that the maximum energies achievable in the laboratory at the time were several orders of magnitude

---

[4] Clay observed that the intensity of the CR decreased by more than 10% as he approached the equator.

[5] *i.e.* , the intensity of low-energy cosmic rays coming from the East is lower than those coming from the West.

[6] It is worth mentioning the contribution of Bruno Rossi. In 1934, during an expedition to Eritrea, aiming to measure the East-West effect, he observed signals in coincidence larger than the expected background for uncorrelated events. However, these results were published (in Italian) in an Italian journal [64], where he stated that unfortunately he had not had time to carry out more detailed measurements to investigate the nature of these particle cascades.

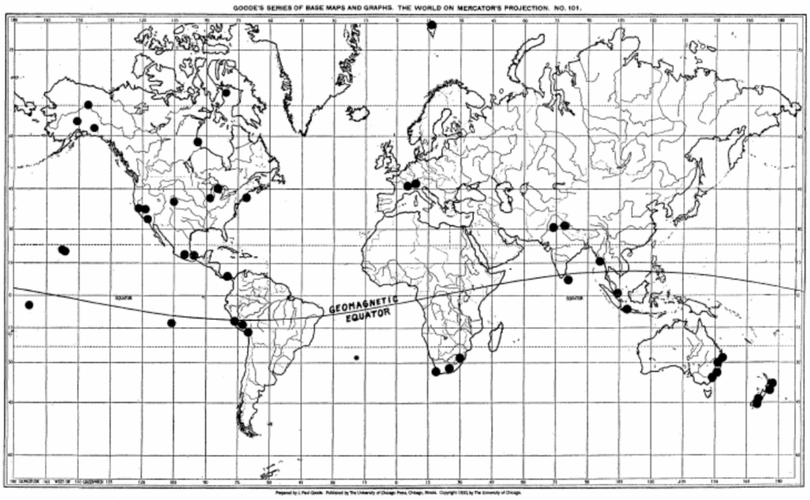

FIGURE 1.2: Map showing location of Compton's major stations for observing cosmic rays. Figure taken from [58].

lower.

In the same years, the use of CRs as "high-energy beams" for the emerging field of particle physics became possible thanks to rapid improvements in experimental techniques. An important contribution was the invention of coincidence circuits[7] by Boethe and Kolhöster, which provided the first triggers for the CR detection. The first breakthrough came in 1932, when Carl Anderson discovered the positron by studying the tracks left by CRs in a Wilson cloud chamber immersed in a magnetic field. The original image of the positron track photographed by Anderson is shown in Fig. 1.3. The following year, the discovery of antimatter was confirmed by the experiment of Blackett and Occhialini (1933). They also demonstrated the conversion of a photon into an electron-positron pair, as predicted by Dirac's relativistic electron theory, improving the experimental technique by means of a coincidence circuit invented by Rossi. These pioneering findings paved the way for the discovery of new particles. The muon was discovered in 1936 by Anderson himself and Neddermeyer, the pion in 1947 by Powell, Lattes, Occhialini, and Muirhead, and many other particles were discovered up to the 1950s. Later, the development of particle accelerators became the main focus of subatomic physics research, splitting the two scientific communities.

Nevertheless, CR research has continued to achieve significant results. In 1962, John Linsley first observed a particle of energy $\sim 10^{20}$ eV using the detector array of the Volcano Ranch experiment in New Mexico [97]. This energy is about several orders of magnitude greater than the maximum energy reached by the LHC, the most powerful man-made accelerator. In addition, the discovery of this particle set the stage for the subsequent development of large-scale EAS detectors for the study of ultra-high-energy cosmic ray (UHECR).

---

[7] For a detailed historical account of the development of coincidence techniques in cosmic ray physics, see the work [45] of L. Bonolis.

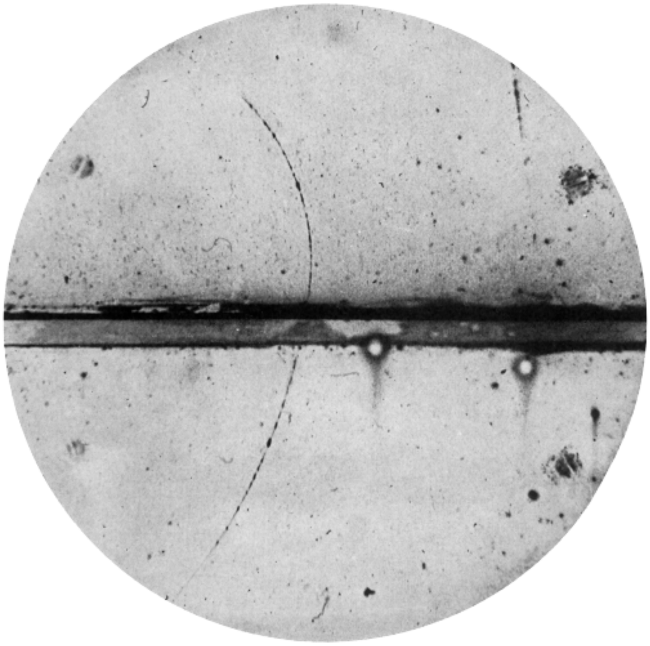

FIGURE 1.3: Photograph from Anderson's cloud chamber showing for the first time a positron track. The curvature of the trajectory indicates that the particle, entering from the bottom, is positively charged. Figure taken from [31]

Currently, frontier research on CRs is performed with space-based and ground-based experiments[8]. Satellite and balloon experiments enable a direct measurement of galactic CRs by identifying the charge and the energy of the primary particle. Operating with magnetic spectrometers (*e.g.* AMS-02, PAMELA, . . .) and calorimetric instruments (*e.g.* CALET, DAMPE, . . .), they cover a wide range of energies up to hundreds of TeV. In contrast, ground-based experiments can only perform indirect measurement of cosmic rays, mainly through the lateral, longitudinal and temporal development of the air particle showers. In this case, the energy range spans from about 100 TeV up to the highest measured energies $\sim 10^{20}$ eV. Finally, an intriguing hypothesis is that the CR anti-matter spectra may contain signatures of dark matter (DM) particles[9], shedding light on their enigmatic nature.

The properties of the observed CR energy spectrum and its composition will be discussed in the next section.

---

[8] In addition, underground-based experiments enable the measurement of astrophysical neutrinos and the muon component of CRs, which is the most penetrating component.

[9] This technique belongs to the class of indirect dark matter search. It is based on the detection of anomalous components in CR spectra that emerge from annihilation of DM pairs in the galactic halo [68]. For example, the positron and electron+positron CR spectra may contain this kind of signatures, therefore limits on DM annihilation and decay parameters can be achieved with a suitable modeling of the astrophysical background (*e.g.* see [106]).

1.2 Energy spectrum and abundances

The energy spectrum, together with its composition, is the main experimental source of information on the acceleration and propagation mechanisms of cosmic rays. The term CR energy spectrum is commonly used to indicate the *differential intensity*[10] or *flux* of cosmic rays. The spectrum can be measured as function of the particle kinetic energy (or the kinetic energy per nucleon) or in rigidity $R = \frac{pc}{Ze}$. The former is mainly used by experiments measuring the particle energy only via calorimetric instruments, whereas the rigidity is usually adopted in experiments that are equipped with magnetic spectrometers. The CR spectrum covers a wide range, from relatively low energies (tens of MeV) to extremely high-energies (above 10^{20} eV). The all-particle flux can be modeled at the first order, with a single power law

$$\Phi(E) \propto E^{-\gamma}$$

that emerges from the stochastic nature of the acceleration mechanism. However, the spectral index γ depends also on the transport of CRs in the interstellar medium, as we will see in section 1.4. A general overview of the available data from a large variety of experiments is given in Fig. 1.4 where the differential flux is multiplied[11] by E^2. From this spectrum, it is possible to identify several regions marked by different spectral features.

For energies below a few tens of GeV, the cosmic ray flux is strongly influenced by the solar activity. Thus, the intensity of the low-energy cosmic rays is affected by solar modulation deviating from the power law trend of the higher energy region.

For energies between $\sim$ 10 GeV and $\sim$1 PeV, cosmic rays are assumed to be of galactic origin and accelerated, according to the standard paradigm, by diffusive shocks from supernova (SN) explosions. The spectrum follows a power law with an approximately constant spectral index $\gamma \approx 2.7$. However, recent measurements from a variety of space-based experiments (*e.g.* [8, 19, 29, 57]) have shown that there are deviations from the single power-law trend, with spectral "*breaks*" at different energies depending on the element involved. These unexpected features could provide crucial information on how galactic CRs are accelerated and on their propagation.

From "*knee*" ($\sim$ PeV) to "*ankle*" (few EeV) energies, the spectrum becomes steeper and the spectral index increases from 2.7 to 3.1. Although alternative theories have not been definitively ruled out, the leading hypothesis is that a transition from the galactic to the extra-galactic component of CRs is taking place in this energy interval.

The energy region above the "*ankle*" is the domain of UHECRs and the spectral index becomes harder again $\gamma \sim 2.5$. Since at these energy scale, the protons begin to have a *Larmor radius* larger than the radius of the galaxy, the flux is assumed to come only from extra-galactic component(s).

---

[10] The differential CR intensity (flux) Φ is defined as $dN = \Phi\, dE\, dA\, d\Omega\, dt$, where dN/dE are the number of particles in the infinitesimal energy interval $[E, E + dE]$ crossing the area dA, from solid angle $d\Omega$ during the time dt.

[11] This is a common practice to highlight the spectral features of the steep CR flux.

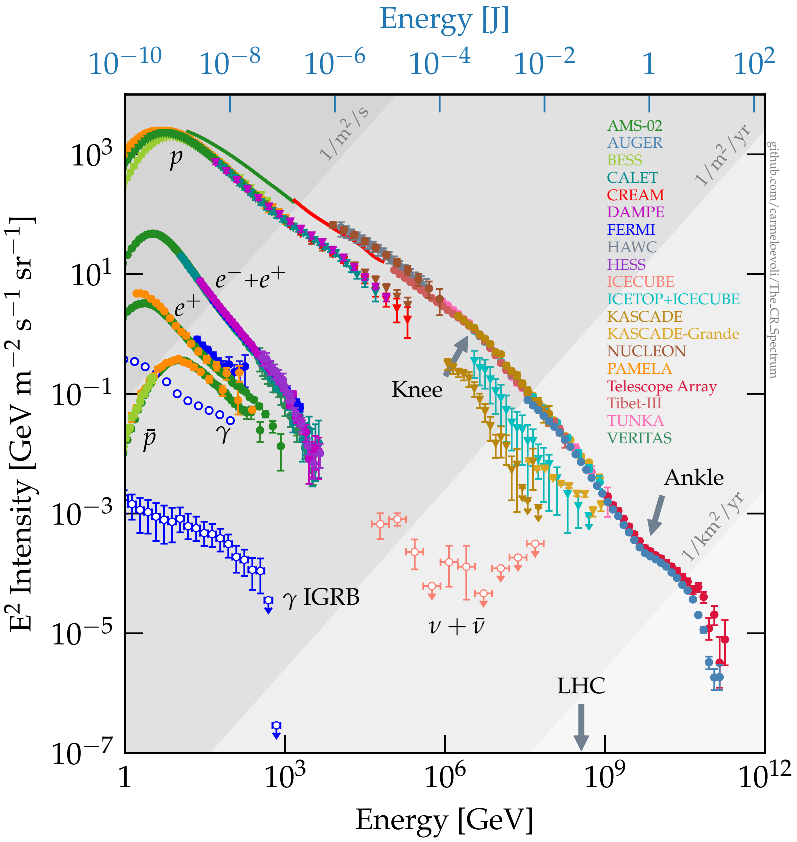

FIGURE 1.4: An overview of the *all-particle* CR energy spectrum from several experiments. Some individual components, such as proton, antiproton, electron+positron, *etc.* are also shown. The intensity $\Phi(E)$ is multiplied by E^2 to highlight the spectral features, as the “*knee*" ($\sim$ PeV) and the “*ankle*" (few EeV). Figure taken from [71].

A further suppression of the flux occurs at $\sim 5 \times 10^{19}$ eV. This threshold is known as the GZK cutoff because above this energy protons begin to lose significant amount of energy on their path due to interaction with the cosmic microwave background (CMB) radiation[12].

In terms of chemical composition, CR are mainly protons (about 88%) and helium nuclei (about 10%). Electrons (and positron) account for about

---

[12] One of the first questions posed by the scientific community concerned the “*natural*" end of the CR spectrum. In 1966 Greisen [84] and, independently, Zatsepin and Kuzmin [140] pointed out that UHECRs would lose energy through interaction with (at that time, newly discovered) CMB photons. In particular, the following photodisintegration processes through the Δ^+ resonance

$$p + \gamma \to \Delta^+ \to \pi^+ + p$$
$$p + \gamma \to \Delta^+ \to \pi^0 + n$$

can occur with the subsequent emission of high-energy neutrinos and photons. In the case of the interaction with CMB photons, this channel becomes significant if the energy of a UHECR proton is greater than $\sim 5 \times 10^{19}$ eV, making unlikely its arrival from an acceleration site more distant than about 30 Mpc, as reported in Ref. [118].

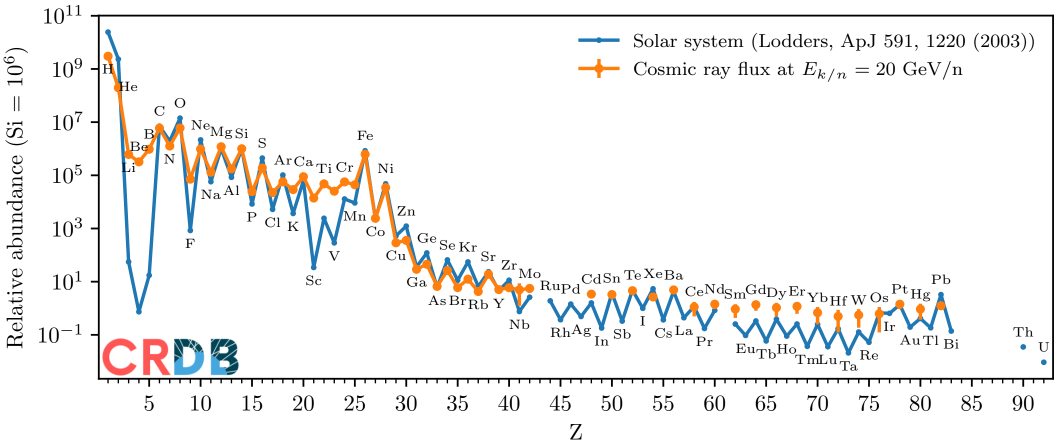

FIGURE 1.5: Relative elemental abundance in cosmic ray (orange) and in the Solar System (blue) one. Figure taken from CR review of the Particle Data Group [134] where the relative Solar system abundances are from Ref. [98], while cosmic data are extracted from the database [103].

1%, while the remaining heavier nuclei (the "*metals*") complete the CR composition. The study of the relative abundances of CRs is crucial because it provides key information on the propagation of CRs and on their origin. A comparison of the relative abundances (normalised to silicon) of CRs with those of our Solar System[13] is shown in Fig. 1.5 from hydrogen to uranium. Since direct CR measurements allow the identification of individual species or, in some cases, even single isotopes, data are mainly taken from satellite-based or balloon-borne experiments.

At first glance, the fairly good similarity over the whole range of elements suggests a common origin. Namely, CRs are supposed to be produced by stellar nucleosynthesis and accelerated to the highest energies by cosmic accelerators (such as shocks from SN explosions, pulsars, ...). The "*odd-even*" effect[14] is present in both cases.

However, on closer inspection, some significant discrepancies emerge. On the one hand, there is the under-abundance of hydrogen and helium in the cosmic rays. The origin of this feature is still unknown, but one of the hypothesis that have been proposed, would point in the direction of a different composition of the CR sources.

On the other hand, there is the remarkable overabundance in CRs of the Li-Be-B group of elements and of the sub-iron elements (such as Sc, Ti and V). These differences in abundances can be explained by considering the *spallation* (also referred to as fragmentation) process undergone by primaries elements (*i.e.* carbon and oxygen in the former case and iron in the second case) when they interact with the nuclei of the interstellar medium (ISM) during

---

[13] The elemental abundances of our Solar System are inferred in a variety of ways, such as the analysis of the chemical composition of meteorites and photospheric measurements of the Sun.

[14] The "*odd-even*" means that nuclei with an even number of protons and neutrons are more stable and therefore more abundant than those with an odd number.

their propagation and produce the so-called secondary elements. Therefore, the primary-to-secondary ratio provides an estimate of the average amount of material traversed by the CR particles from the acceleration site to Earth. This in turn allows an estimation of the average confinement time, as we will see in the section 1.4. In particular, a key information for CR propagation models is provided by the B/C ratio, since carbon nuclei are expected to be produced and accelerated close to the sources, while boron is assumed to be a pure secondary, *i.e.* produced entirely by the fragmentation of heavier nuclei. Therefore, the B/C ratio allows a direct estimation of the average amount of material traversed by CRs, as well as it constraints the spatial diffusion coefficient and its energy dependence.

Finally, it is worth mentioning an independent technique for estimating the average confinement time of CRs in the Galaxy, based on the ratio of long-lived radioactive isotopes (such as ^{10}Be, ^{26}Al, . . .) to their stable secondary.

1.3 Acceleration mechanisms

Understanding the mechanisms of CR acceleration is crucial both for the physical interpretation of the experimental data and for the identification of candidate sites for their production. In particular, a reliable model explaining the acceleration processes must take into account the following properties derived from observations:

- The energy spectrum of CRs, whether nuclei or electrons, follows a power law where the γ coefficient is approximately between 2 and 3. Thus, this trend suggests a non-thermal[15] acceleration mechanism.
- The elemental abundance of primary CRs below the *knee* energy region is similar to the chemical composition of the Solar System.
- The maximum energy of a detected CR is $\sim 10^{20}$ eV. However, the bulk of CR is below the *knee* energy where the spectral index is almost constant.

In the next paragraphs, some of the proposed acceleration mechanisms will be explained.

1.3.1 Fermi acceleration mechanism

Historically, one of the first model to explain the CR acceleration was the one proposed by Enrico Fermi in his renowned paper [76]. This model is now known as the "*second-order* Fermi acceleration mechanism".

---

[15] Under extreme conditions, the thermal radiation found in the cosmos can reach energies of keV and above. However, the power-law spectrum of the cosmic rays does not show any sign of a characteristic temperature scale, and therefore it cannot be the result of thermal processes. Stochastic processes such as the Fermi acceleration mechanism, magnetic reconnection, etc. are some examples of non-thermal acceleration mechanisms.

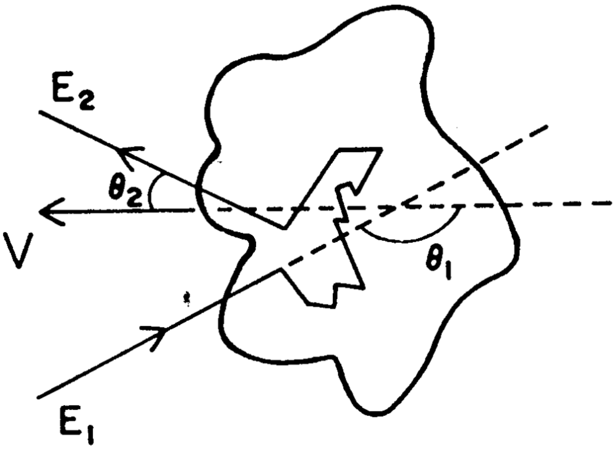

FIGURE 1.6: Schematic of the *second-order* Fermi acceleration mechanism in a moving ionized gas cloud. Figure taken from [79]

Second-order acceleration mechanism The main idea behind it is that charged CR particles are stochastically accelerated in the reflections with the *magnetic mirrors*[16]. In the astrophysical context, the magnetic mirrors are slowly moving interstellar gas clouds, that act as massive scatterer for the charged CR particle entering in it. Let us repeat the calculations, starting from the injection of a charged particle with energy E_1 into an ionised cloud moving with velocity V at an angle θ_1. After diffusion[17] inside the cloud, the particle exits with an angle θ_2 as shown in Fig. 1.6. In the cloud rest frame, the total particle energy is

$$E_1^* = \gamma E_1(1 - \beta \cos\theta_1)$$

in which $\beta = \frac{V}{c}$ and $\gamma = 1/\sqrt{1-\beta^2}$ is the Lorentz factor. Since the mass of the gaseous cloud (M) is much larger than that of the incoming particle (m), the process can be modelled as a collision against a wall where $E_2^* = E_1^*$ in the cloud frame of reference. Hence, transforming back in the laboratory frame, the energy after the collision is

$$E_2 = \gamma E_2^*(1 + \beta \cos\theta_2^*)$$

and therefore, the relative energy gain is

$$\xi = \frac{\Delta E}{E} = \frac{1 - \beta\cos\theta_1 + \beta\cos\theta_2^* - \beta^2\cos\theta_1\cos\theta_2^*}{1-\beta^2} - 1 \tag{1.1}$$

Thereafter, the average of the quantities $\cos\theta_1 \cos\theta_2^*$ is required to derive the mean energy gain per collision $\langle\xi\rangle$. Since a large number of scatterings occurs

---

[16] Magnetic mirrors refer to regions where particles can be reflected without collision, but due to the strong non-uniformity of the magnetic field. An example in the Earth's magnetosphere is *van Allen radiation belts* where charged particles, *e.g.* electrons and protons, are trapped between two magnetic mirrors.

[17] The multiple collisionless scatterings within the cloud can be modelled as a *random walk* because the inhomogeneities of the magnetic field are random as well.

within the moving cloud , the exit angle θ_2^* is actually random and thus, the $\langle\cos\theta_2^*\rangle = 0$. On the other hand, for the entry angle θ_1 there is a higher probability of a head-on collision than a tail-on collision. In the former case, there is a net energy gain, in the latter a net energy loss. Specifically, the probability $P(\theta_1)$ is proportional to the relative velocity between the particle and the cloud, $v + V\cos\theta_1$, where v is the velocity of the charged particle. In the ultra-relativistic limit ($v \approx c$), one gets $P(\theta_1) \propto (1 - \beta\cos\theta_1)$ and

$$\langle\cos\theta_1\rangle = \frac{\int_{-1}^{1}\cos\theta_1(1-\beta\cos\theta_1)d\cos\theta_1}{\int_{-1}^{1}(1-\beta\cos\theta_1)d\cos\theta_1} \simeq -\frac{\beta}{3}$$

The insertion of this term into the equation 1.1 yields an average energy gain per single collision of

$$\langle\xi\rangle = \frac{\langle\Delta E\rangle}{E} = \frac{1+\beta^2/3}{1-\beta^2} - 1 \approx \frac{4}{3}\beta^2 \tag{1.2}$$

where a non-relativistic cloud was considered ($\beta \ll 1$). Since $\langle\Delta E\rangle/E \propto \beta^2$, it is called *second-order* Fermi acceleration. Furthermore, a power-law distribution of particle energies can be obtained from this model. This will be described in the next section, while addressing the "*first-order*" Fermi acceleration mechanism.

However, this model has a number of issues that do not fit with the picture provided by Galactic CR observations. One of the main problem is the very slow acceleration process[18]. In fact, the average collision rate would be only a few per year, since the typical velocity of interstellar clouds is much lower than the speed of light $\beta = \frac{V}{c} \sim 10^{-4}$, and the typical scale of magnetic field irregularities in the interstellar medium is $l_0 \sim 0.1$ pc. In addition, the power law exponent is a free parameter in this model and therefore it cannot provide a theoretical explanation for the observed spectral index.

First-order acceleration mechanism In order to overcome the problem of the very slow acceleration time, Fermi proposed an update of his mechanism in Ref. [75]. The main idea behind this revision is to consider an acceleration process in which the particle gains energy only through head-on collisions. In particular, it can be shown (see *e.g.* Ref. [65]) that in this way the average energy gain for each collision is proportional to β,

$$\langle\xi\rangle \approx \frac{4}{3}\beta.$$

---

[18] An estimate of the characteristic acceleration time

$$\tau_F^{2nd} = \frac{\langle\Delta t\rangle}{\langle\Delta E\rangle/E} = \frac{3}{2}\frac{l_0 c}{V^2} \sim 10^7\,\mathrm{yr}$$

where l_0 is the typical scale of magnetic field irregularities in the interstellar medium and $\langle\Delta t\rangle = 2l_0/c$ is the average time between two collisions.

and so it is called *first-order* Fermi acceleration. In addition, this mechanism enables the enhancement of the acceleration time by a β factor[19], albeit it is still a fairly slow process. It is also worth noting that the Fermi acceleration mechanism leads to a power law, as required experimentally. A derivation, based on Ref. [79], is as follows. Let ξ be the average energy gain for a single collision, such that $\Delta E = \xi E$. Thus, after k collision, one gets

$$E_k = E_0(1+\xi)^k$$

where E_0 is the injection energy into the acceleration site. Then, the probability that a particle can still be accelerated after k interactions is $(1-P_{esc})^k$, where P_{esc} represent the probability that the particle leaves the acceleration region in a single collision. Since the number of iterations n to reach the energy E is $n = \frac{\ln(E/E_0)}{\ln(1+\xi)}$, the number of particles that are accelerated to an energy $\geq E$ is

$$N(>E) \propto \sum_{m=n}^{\infty}(1-P_{esc})^m = \frac{(1-P_{esc})^n}{P_{esc}}$$

and therefore (see Ref. [79]) the power law spectrum is obtained as

$$N(>E) \propto \frac{1}{P_{esc}}\left(\frac{E}{E_0}\right)^{\lambda} \tag{1.3}$$

where the exponent $\lambda \approx \frac{P_{esc}}{\xi}$.

1.3.2 Diffuse shockwave acceleration

The diffuse shockwave acceleration (DSA) mechanism is the standard paradigm for explaining the acceleration of GCRs. It belongs to the class of *first-order* Fermi mechanisms because the net energy gain is linearly proportional to the shock velocity U. Since the pioneering works of Axford et al.(1977) [35], Krymskii(1977) [96], Bell(1978) [38], Blandford et Ostriker [44] and Drury(1983) [69], the DSA mechanism has been developed using several approaches and it has been studied in a variety of astrophysical environments.

The main idea behind this mechanism is based on a strong shockwave[20] propagating through a medium (*e.g.* the interstellar medium in front of supersonic SN remnants) with a velocity U higher than the local speed of sound c_s. According to the Bell's treatment [38] also presented in Longair's book [99], it is assumed that there is a stream of high-energy particles that diffuse in front of and behind the shockwave front. Since these particles are relativistic and the shock is not, their directions of propagation becomes isotropic in the moving fluid's frame of reference, as a result of collisionless scatterings driven by magnetic turbulences. A schematic representation of this process as viewed in different frames of reference, is shown in the Fig. 1.7. Let us start

---

[19] As mentioned in Ref. [118]

[20] A shock wave is characterized by a sudden and intense increase in pressure, temperature, and density as it travels through the medium.

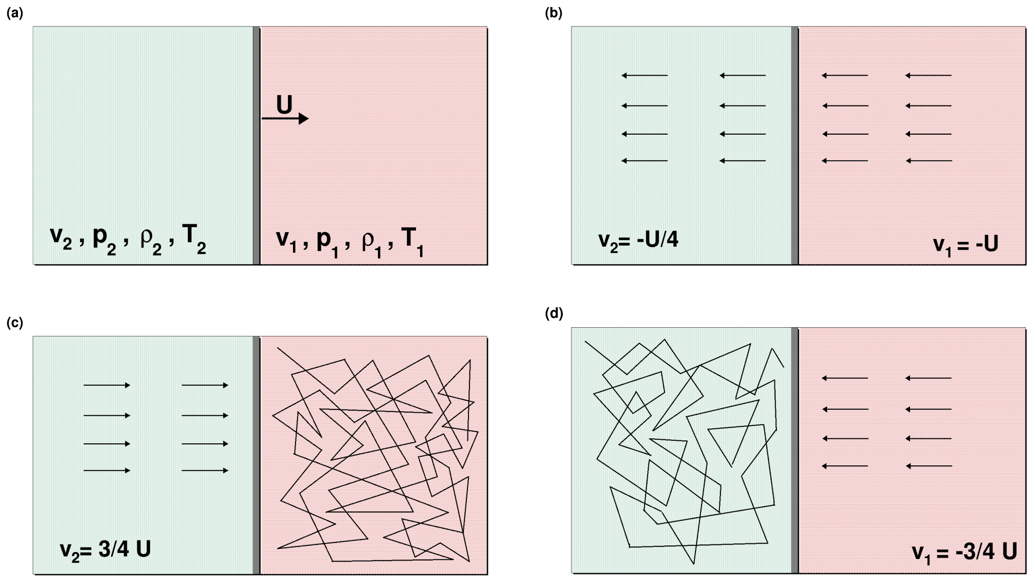

FIGURE 1.7: Schematic of the diffusive shock acceleration mechanism in different frames of reference. *(a)* The shock front travel with supersonic velocity U through the interstellar gas that is characterized by density ρ_1, temperature T_1 and pressure p_1. *(b)* The shock front is at rest and the gas velocities *upstream* (*downstream*) of the shock front is $v_1 = -U$ ($v_2 = -U/R$), where R is the *compression* factor. *(c)* Upstream gas is stationary. *(d)* Downstream gas is stationary.

by taking the frame of reference where the shock front is at rest (Fig. 1.7b), we have that the gas velocities *upstream* (the region in front that has not been shocked yet) and *downstream* (the region which has already been shocked) of the wave front are respectively $v_1 = -U$ and $v_2 = -U/R$, where R is the *compression* factor. In the case of a non-relativistic strong[21] shock, R is equal to $\frac{\rho_1}{\rho_2} = \frac{\gamma+1}{\gamma-1}$,where γ is the adiabatic index. For a monoatomic gas the index is $\gamma = 5/3$ and therefore the compression factor is $R = 4$. On the other hand, if we consider the reference system where the upstream gas is stationary (Fig. 1.7c), the *downstream* gas moves with speed $3/4U$ relative to the *upstream* gas. Hence, when the relativistic particle crosses the shock front, it gains in energy $\xi \sim U/c$. Likewise, when particles diffuse in the downstream region (Fig. 1.7d), they receive the same net gain in energy because they collide with a gas moving towards the surface of the shock with a velocity of $3/4U$. Therefore, the average energy gain that can be achieved by completing the cycle upstream-to-downstream-to-upstream, is

$$\langle \xi \rangle \approx \beta_{sh}$$

where $\beta_{sh} = U/c \sim 10^{-2}$ from the hypothesis of SN explosion ejecting mass with a typical speed of $U \sim 10^4$ km s^{-1}.

---

[21] *i.e.* the *Mach* number $U/c_s \gg 1$

In order to derive the energy spectral index, the escape probability P_{esc} is needed. Following Bell's argument [38] based on classical kinetic theory, the probability of a particle leaving the acceleration region after an encounter is given by

$$P_{esc} = \frac{\phi_{esc}}{\phi} = \beta_{sh} = \frac{U}{c} \tag{1.4}$$

where $\phi = \frac{n}{4}c$ is the particle flux crossing the shock front from upstream to downstream region, whereas $\phi_{esc} = nv_2 = n\frac{U}{4}$ is the average particle flux escaping the acceleration site because the particles are isotropic in the downstream region due to the local magnetic fields. Since we are dealing with non-relativistic shock, only a small sample of particles leaves the acceleration region per cycle. Thus, the lambda exponent from the formula 1.3, is

$$\lambda_{DSA} \approx \frac{P_{esc}}{\xi} \sim 1$$

and therefore, the differential energy spectrum is expected to follow the power law

$$N(E)dE \propto E^{-2}dE$$

that is what we were looking for based on experimental results. It is worth noting that this power-law index depends only on the compression ratio, but it is independent on the accelerated particles providing an universal mechanism for a multitude of astrophysical environments [67].

Maximum CR energy An order of magnitude estimate of the maximum energy achievable by CR particles via DSA mechanism can be estimated with the following simplified argument from Ref. [118]. Let the energy gain rate be expressed as

$$\frac{\Delta E}{\Delta t} = \xi \frac{\mathrm{E}}{\mathrm{T_{cycle}}}$$

where $\mathrm{T_{cycle}}$ is the characteristic time needed to complete a back-and-forth encounter. This can be evaluated for a shock travelling with velocity U, as

$$T_{cycle} = \frac{\lambda_{cycle}}{U} \approx \frac{E}{Ze\,B\,U}$$

where the Larmor radius r_L is considered as the typical confinement length λ_{cycle}. Since the energy rate is thus independent on initial particle energy E, the maximum energy can be derived by using the overall shock acceleration time $\mathrm{T_{shock}}$, as

$$E_{max} = \frac{\Delta E}{\Delta t}\mathrm{T_{shock}} \sim (100\,\mathrm{Z})\,\mathrm{TeV}$$

where the typical parameters $\mathrm{T_{shock}} \sim \mathcal{O}(1000)$ yr for SNR acceleration, and $B \sim \mathcal{O}(\mu G)$ are assumed. More sophisticated calculations can be found *e.g.* in Refs. [39, 67] where the estimate can be up to an order of magnitude higher for certain types of astrophysical shock blasts. It is also worth noting that the maximum energy achievable depends on the charge of the CR particle.

Therefore, the energy spectrum is expected to steepen in the *knee* region, first for light nuclei and at progressively higher energies for heavier elements.

In conclusion, although the DSA mechanism can reasonably approximate the power law of the observed CR spectrum with its spectral index for energies below about 10^{15} eV, it cannot explain observations at higher energies. Specifically, the Larmor radius r_L of the CR particle in the Galactic magnetic field becomes comparable to the size of the Galactic disk itself, above 10^{18} eV. Thus, a transition between the galactic and extragalactic components is expected, since our Galaxy seems to lack sufficiently large sources, with magnetic fields strong enough, to accelerate the UHECRs. A commonly used method for defining the necessary conditions for a candidate CR source to accelerate particles up to a certain energy is the *Hillas* criterion, which will be discussed in the next section.

1.3.3 Candidate production sites

Identifying sources that can accelerate cosmic rays up to the observed energies is an open problem. Although the exact sources are still unknown, the standard paradigm predicts that the acceleration mechanism for energies below the *knee* is related to SN explosions and occurs in the vicinity of the corresponding strong shock. The main idea[22] is based on the balance between the energy loss due to the escape of CRs from the galactic disk and the rate of cosmic rays produced by galactic SNRs. On the one hand, an order-of-magnitude of the rate of CR energy loss by escape from the Galactic disk is given by (from Ref. [118])

$$P_{CR} = \frac{dE_{CR}}{dt} \approx \frac{\rho_{CR}\mathcal{V}_G}{\tau_{esc}} \sim 3 \times 10^{40}\,\mathrm{erg}\,s^{-1}$$

where we assume a galactic volume[23] equal to $\mathcal{V}_G = 5 \times 10^{66}$ cm^3, an average CR density[24] equal to $\rho_{CR} \approx 1$ eV cm^{-3}, and a characteristic CR confinement time of about $\tau_{esc} \approx 10^7$ yr, as it will be discussed in the section 1.4. On the other hand, the amount of kinetic energy released by a typical core-collapse SN[25] of $10M_\odot$ is of the order of $K \sim 10^{51}$ erg. Assuming a galactic SN rate of about three per century $f_{SN} \sim 10^{-9}$ s^{-1} and η the efficiency of energy conversion from shock to CRs, we obtain the power

$$P_{SN} \approx \eta \times f_{SN} \times 10^{51} = \eta \times 10^{42}\mathrm{erg}\,s^{-1}$$

---

[22] As first proposed by Baade and Zwicky (1934) in Ref. [36].

[23] Our Galaxy has a spiral structure with the Sun on one of its arms, about 8 kpc from the Galactic centre. It is usually approximated as a flat disk with radius of $\sim$ 15 kpc and thickness of $\sim$ 300pc.

[24] The CR density ρ_{CR} is assumed to be constant on a time scale much larger than the confinement time τ_{esc}

[25] In CCSNe about 99% of the the gravitational energy is carried away by neutrinos and only 1% is converted into kinetic energy of the shock wave.

By equating $P_{CR} = P_{SN}$ an acceleration mechanism with an efficiency of $\eta = 0.01 - 0.1$ is required to ensure a steady CR flux, as suggested by Ginzburg and Syrovatskii (1963) in Ref. [81]. As we have seen in the previous section, the DSA mechanism provides an energy transfer compatible with this range. However, this mechanism is not suitable for UHECR.

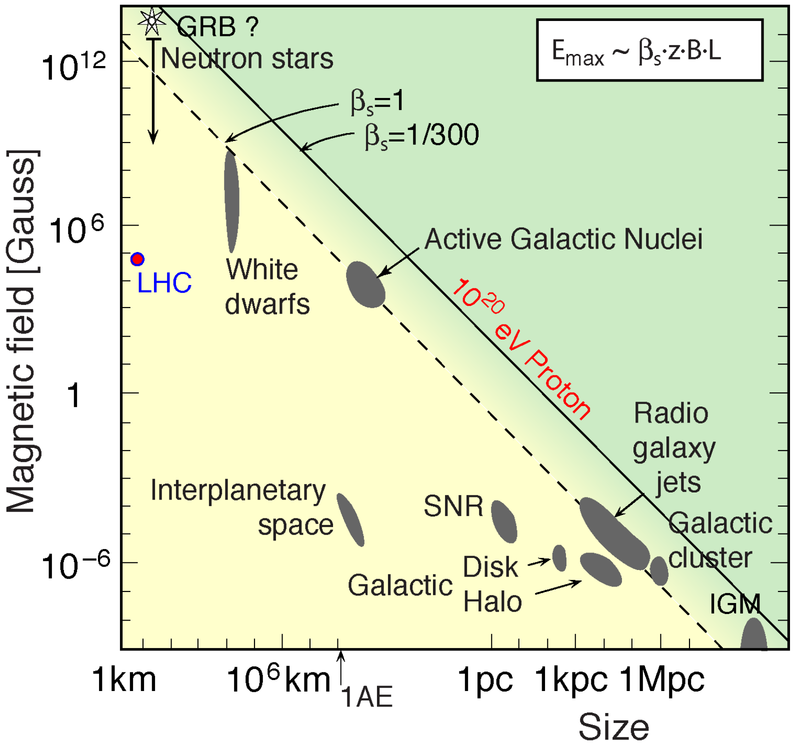

FIGURE 1.8: Hillas diagram showing potential cosmic-ray sources depending on their magnetic field strength and size. The candidate sources above the solid and dashes lines can accelerate CR protons up to 10^{20} eV in the case of classical and relativistic shocks, respectively. Figure adapted from Ref. [89]

A simple geometric criterion is that proposed by Hillas (1984) in Ref. [89] which gives an upper limit on the maximum energy that can be obtained from a candidate source, based on its size and the surrounding magnetic field. This is valid for both *one-shot* and gradual acceleration mechanisms, and it requires the particle to be confined within the dimensions of the astrophysical object, *i.e.* within its Larmor radius. In formula, it can be expressed as[26]

$$E_{max} \lesssim (10^{18}\text{eV})\, Ze\, \beta_{sh} \left(\frac{\text{L}}{\text{kpc}}\right) \left(\frac{\text{B}}{\mu\text{G}}\right) \tag{1.5}$$

where β_{sh} is the velocity of the shock wave in units of c and L is the size of the acceleration region in kpc. An effective way of visualising potential

---

[26] In the case of *one-shot* acceleration, a similar form is obtained where L can be, for example the diameter of the astrophysical object providing the energy to the particles.

sources at a fixed energy for a given ion is via the Hillas diagram, as shown in Fig. 1.8. As can be seen from this figure, only a few large sources or sources with high magnetic fields are capable of accelerating CRs to energies of 10^{20} eV. Active galactic nuclei (AGN), magnetars, radio galaxies and gamma-ray bursts (GRBs) are some potential candidates.

1.4 Propagation through the Galaxy

After being accelerated near the source, GCRs propagate through the ISM of our Galaxy. Since they are charged particles, they scatter in the inhomogeneities of the galactic magnetic field, losing information about the position of their production site. This explains their highly isotropic distributions and confinement times in the Galaxy.

However, in addition to spatial diffusion, CRs are subject to additional physical processes that determine their propagation properties. In fact, they can interact with matter of the ISM[27], leading to fragmentation processes, losing or gaining energy, or, if they are unstable nuclei, they can decay. Moreover, the possible existence of a galactic wind can give rise to convective phenomena resulting in adiabatic energy losses.

Therefore, the standard approach to modelling the propagation of CRs through the galaxy is via the cosmic ray transport equation. This takes into account the main processes affecting the cosmic ray dynamics from production site to detection point. The master equation for CR propagation is explained in the section 1.4.2, following the treatment described in Ref. [123]. Instead, from an experimental point of view, the *secondary-to-primary ratios* are key diagnostic tools for probing CR propagation through the Galaxy. This topic will be discussed in the next section.

1.4.1 Secondary-to-primary ratio

Comparing the chemical composition of the CRs reaching the Earth with the solar system elemental abundance, it reveals strong similarities, albeit with some important discrepancies. These mainly concern the light elements Li, Be, B and the elements lighter than Fe, from Z=21 to Z=25, *i.e.* the so-called sub-irons. Specifically, considering the ratio $\mathfrak{R}$ between *secondary* elements Li, Be and B (hereafter also called *light* elements and denoted by the letter $\mathcal{L}$) and the primaries C, N and O (hereafter called *medium* elements and denoted by the letter $\mathcal{M}$) for the CRs $\mathfrak{R}_{CR}$ and the Solar System $\mathfrak{R}_{SS}$,

$$\mathfrak{R}_{CR} \approx 0.25 \qquad \mathfrak{R}_{SS} \approx 10^{-5}$$

---

[27] The interstellar medium is mainly made by atomic and molecular Hydrogen ($\approx$ 90%), followed by Helium ($\approx$ 9%) and by a small fraction of other elements (metals). It accounts for $10 - 15\%$ of the total Galaxy mass. The density of the interstellar medium is $\rho_{ISM} \sim 1$ proton per cm^3, whereas in the halo it is lower. The energy desity is $\rho_B^{ISM} = \frac{B^2}{8\pi} \approx 1$ eV cm^{-3}. The interstellar magnetic field is $\sim 4\mu$G, while that of the halo is unknown. However, the local turbulence properties are more relevant than the absolute magnitude for CR diffusion below 10^{15} eV, as stated in Ref. [123].

Such an increase in the abundances of the light elements [28] in CRs can be explained by the processes of spallation that occur when a primary nucleus interacts with the matter of interstellar medium, producing secondary particles. The secondary-to-primary ratios can therefore provide valuable insights into the mechanism of cosmic ray propagation, such as an estimate of the confinement time and the escape length. In fact, by defining the *grammage* or *path length* as[29]

$$\Lambda = d\,\rho_{ISM} = (v_{CR}t)\,\rho_{ISM} \tag{1.6}$$

where v_{CR} is the CR velocity and ρ_{ISM} is density of the interstellar medium, one can set the following couple of differential equations[30]

$$\begin{aligned} \frac{dN_{\mathcal{M}}}{d\Lambda} &= -\frac{N_{\mathcal{M}}}{\lambda_{\mathcal{M}}} \\ \frac{dN_{\mathcal{L}}}{d\Lambda} &= -\frac{N_{\mathcal{L}}}{\lambda_{\mathcal{L}}} + \mathcal{P}_{\mathcal{ML}}\frac{N_{\mathcal{M}}}{\lambda_{\mathcal{M}}} \end{aligned}$$

where N is the number density of the primary ($\mathcal{M}$) or secondary ($\mathcal{L}$) nuclear species, $\lambda_{\mathcal{L}}$ and $\lambda_{\mathcal{M}}$, are the average mean free path for light and medium elements, respectively. The average spallation probability is represented by $\mathcal{P}_{\mathcal{ML}}$. Now, setting the initial conditions $N^0_{\mathcal{M}} = N_{\mathcal{M}}(\Lambda = 0)$ and $N_{\mathcal{L}}(\Lambda = 0) = 0$, these lead to

$$\begin{aligned} N_{\mathcal{M}}(\Lambda) &= N^0_{\mathcal{M}}\,e^{-\frac{\Lambda}{\lambda_{\mathcal{M}}}} \\ N_{\mathcal{L}}(\Lambda) &= N^0_{\mathcal{M}}\,\frac{\mathcal{P}_{\mathcal{ML}}}{\lambda_{\mathcal{M}}}\,\frac{\lambda_{\mathcal{M}}\lambda_{\mathcal{L}}}{\lambda_{\mathcal{L}} - \lambda_{\mathcal{M}}}\,(e^{-\frac{\Lambda}{\lambda_{\mathcal{L}}}} - e^{-\frac{\Lambda}{\lambda_{\mathcal{M}}}}) \end{aligned}$$

where the ratio is

$$\mathfrak{R}(\Lambda) = \frac{N_{\mathcal{L}}(\Lambda)}{N_{\mathcal{M}}(\Lambda)} = \frac{\mathcal{P}_{\mathcal{ML}}}{\lambda_{\mathcal{M}}}\,\frac{\lambda_{\mathcal{M}}\lambda_{\mathcal{L}}}{\lambda_{\mathcal{L}} - \lambda_{\mathcal{M}}}\,(e^{-\Lambda(\lambda_{\mathcal{L}}{}^{-1} - \lambda_{\mathcal{M}}{}^{-1})} - 1).$$

Using the mean values (taken from Ref. [118]) $\lambda_M \approx 6\ \mathrm{g\,cm^{-2}}$, $\lambda_L \approx 8.4\ \mathrm{g\,cm^{-2}}$ and $\mathcal{P}_{\mathcal{ML}} = 0.28$, the average *grammage* that a *medium* element $\mathcal{M}$ should cross in order to match the observed light-to-medium element ratios is

$$\Lambda_{esc} = d_{esc}\,\rho_{ISM} \approx 5\,\mathrm{gcm^{-2}}$$

and, by assuming $\rho_{ISM} \approx 1.6 \times 10^{-24}\,\mathrm{gcm^{-3}}$, the average galactic *escape length* is

$$d_{esc} \approx 1\,\mathrm{Mpc}$$

---

[28] The low value for the solar system abundance of Li, Be and B, is due to the fact that these elements act as *catalysts* for the thermonuclear reactions taking place in stars.

[29] It represents the (average) amount of material that CRs must pass through before interacting with an atom in the ISM.

[30] As reported in Ref. [99], these simplified set of equations are obtained from an approximation of the diffusion-loss equation where diffusion-energy losses are neglected and the injection term is set to zero as well.

This value, when compared with the average radius and thickness of our Galaxy, can be explained in terms of the *random walk* experienced by CRs due to the scattering processes with the inhomogeneities of the interstellar magnetic field. Specifically, it indicates that the propagation of the CRs in the Galaxy can be modelled as a diffusive motion[31] and, given the high value Λ_{esc}, its treatment can be decoupled from the primary CR acceleration mechanism.

From the *escape length* d_{esc}, one can also derive the average *residence time* of CR in the Galaxy, as[32]

$$\tau_{res} \approx \frac{d_{esc}}{c} \sim 10^7 \text{ y} \tag{1.7}$$

However, since the Larmor radius r_L increases linearly with energy, the residence time should decrease with increasing energy. This dependence is actually observed in the experimental data. Specifically, it is usually parametrized through power law that depends on the rigidity $R = r_L B$, as

$$\Lambda_{esc}(R) = c\, R^{-\delta} \tag{1.8}$$

where the free parameters δ and c can be derived both by theoretical considerations or by fitting the available experimental results. A typical value for δ is in the range 0.3-0.6. Thus, the *confinement* time can be expressed with respect to energy as

$$\tau_{esc}(E) = \tau_0\, E^{-\delta} \tag{1.9}$$

1.4.2 Transport equation for CR

Nowadays, one of the most accepted description of the cosmic ray transport equation at energies below $\lesssim 10^{17}$ eV is the diffusion model with the inclusion of a convection term. According to the derivation provided by Strong and Moskalenko in Ref. [122], the CR transport equation can be expressed in momentum and space coordinates, as

$$\begin{aligned}\frac{\partial n(\vec{r},p,t)}{\partial t} &= Q(\vec{r},p,t) + \vec{\nabla}\cdot(D_{xx}\vec{\nabla}n - \vec{V}_c n) + \frac{d}{dp}p^2\, D_{pp}\frac{d}{dp}\frac{1}{p^2}n + \\ &- \frac{\partial}{\partial p}[\dot{p}n - \frac{1}{3}p(\vec{\nabla}\cdot\vec{V}_c)n] - n\frac{1}{\tau_f} - \frac{1}{\tau_r}\end{aligned} \tag{1.10}$$

where

- $n(\vec{r},p,t)$ is the CR density per unit of total particle momentum p at position $\vec{r}$.

---

[31] This can be parametrized with spatial diffusion coefficient $D(\Lambda)$ as function of the *grammage* that, in turn, can be dependent on the energy of CR particle.

[32] An independent technique for assessing the galactic *escape* time τ_{esc} is based on radioactive nuclei, as *e.g.* ^{10}Be, ^{26}Al, etc. The main advantage of this method (similar to *radiocarbon* dating technique) is that it does not require any prior knowledge of ρ_{ISM}. More detail can be found on Refs. [99, 118].

- $Q(\vec{r}, p, t)$ is the source term .
- D_{xx} is the spatial diffusion coefficient.
- $\vec{V}_c$ is the convection velocity.
- D_{pp} is diffusion coefficient in momentum space.
- $\dot{p} = \frac{dp}{dt}$ is the gain or loss rate of momentum.
- τ_f and τ_r are the timescales for loss by fragmentation of by radioactive decay, respectively.

A detailed analysis of the different components of the Equation 1.10 can be found in Ref. [123], while the physical content of the main terms are summarized hereafter.

The source term $Q(\vec{r}, p)$ can be regarded as the sum of the injection term and the spallation-decay term. In the standard scenario, the ion injection spectrum follows a power law $\frac{dQ(p)}{dp} \propto p^{-\gamma}$, where the γ index depends on the nuclear species. The spallation-decay term can be accounted as $\sum_j \frac{P_{ij}}{\tau_j(p)}$ where P_{ij} is the probability that the nuclear species j gives origin to nucleus i via decay or inelastic scattering with a target particle of the ISM. The τ_j can be derived by $1/\tau_j = 1/\tau_{decay} + \beta c/\lambda_j$, where λ_j is the interaction length and τ_{decay} is the decay time of the parent nucleus.

The spatial diffusion coefficient D_{xx} arises from particle scattering on random magneto-hydrodynamic (MHD) waves and discontinuities. A typical value found in literature, is $D_{xx} \sim 3 - 5 \times 10^{28}\,\mathrm{cm^2\,s^{-1}}$ at energy $\sim 1\,\mathrm{GeV/n}$. This is derived from the joint fit of different CR measurements. It also depends on the particle rigidity as $\mathrm{R}^{0.3} - \mathrm{R}^{0.6}$ according to the empirical diffusion model taken into account.

The diffusion coefficient in momentum space D_{pp} is used to model the stochastic re-acceleration provoked by the scattering of CR particles against a randomly moving MHD turbulent wave. An estimate is provided by the formula $D_{pp} = \frac{p^2 V_A^2}{9 D_{xx}}$ where V_A is the Alfvén velocity that represents the characteristic velocity of weak disturbances propagating in a magnetic field. A more rigorous treatment can be found on Refs.[40, 116]. Beyond diffusion, convection[33] mode driven by galactic winds can also play a role in CR transport and induce further adiabatic energy losses.

Regarding the way of solving the CR transport equation to make a comparison between ground-based and satellite-based experiments, some assumptions are needed. Following the treatment of Ref. [86], the main ones are summarized below.

---

[33] The canonical convection models are the *one-zone* model and the *two-zone* model. As reported in Ref. [86], the *one-zone* model assumes convection and diffusion everywhere. In contrast the *two-zone* model has diffusion alone up to some distance from the plane, and diffusion plus convection beyond.

1. Steady-state solution. It can be achieved analytically by setting $\frac{\partial n}{\partial t} = 0$ or numerically by making the computation until the steady-state is reached.
2. Boundary conditions. The common choice is $n = 0$ in the the *halo* boundary *i.e.* where the particles can escape into the intergalactic region. Since the intergalactic flux cannot be negligible, this condition can be modified with a more physics-based approximation.

In addition, the solution of the complete system of equation including secondary (tertiary, *etc.*) particles is usually accomplished in an iterative way. Specifically, the results achieved by the evolution of heavy primaries are regarded as the source terms for the secondaries, and so on. Moreover, the solar modulation can be integrated in the calculations, if needed.

In the case of cosmic electron and positron, the CR transport is still described by the equation 1.10 but with additional energy loss terms as bremsstrahlung, inverse Compton scattering and synchrotron radiation.

An advanced numerical tool for simulating CR propagation is the public available GALPROP[34] code [121]. The ambitious objective of GALPROP project is to provide a common framework that fits in a single model all the available experimental data about the CR spectra (nuclei, electrons/positrons,γ-rays, *etc.*), CR source distributions and the Galaxy structure. Other tools[35] from the CR scientific community are DRAGON [72, 73] and USINE [102].

Conversely, the Leaky Box Model (LBM) is an analytical method that it will be discussed in the next paragraph. Despite it is a simplified model of the real propagation mechanisms, this approximation is still largely adopted for providing a first-order interpretation of CR experimental data, especially the secondary-to-primary ratios.

Leaky-box model

Before the epoch of the largely available high-speed computing, the LBM has been commonly used for interpreting CR experimental data. The main idea behind the LBM is to treat the Galaxy as a box from which cosmic rays can diffuse freely but, when they reach the boundaries, they can escape into the intergalactic medium with a certain probability. Specifically, starting with the following approximation of the master equation for CR propagation,

$$\frac{dN_i}{dt} = D\nabla^2 N_i + \frac{d}{dE}[b(E)\,N_i] + Q(E) - \lambda_i\,N_i + \sum_{j>i} P_{ji}\,\lambda_j\,N_j \tag{1.11}$$

the LBM is derived according to a set of assumptions, summarized as follows.

---

[34] The Galactic Propagation (GALPROP) was originally developed by Strong and Moskalenko [122]. Specifically, the CR transport equation 1.10 is numerically solved on a spatial grid. In addition, the user can opt to perform the calculations in 2D, assuming cylindrical symmetry, or in full 3D configuration.

[35] These are mainly used considering 2D model with cylindrical symmetry, as a consequence of the their limited spatial resolution.

- The confinement volume of the Galaxy is fixed[36] and the distribution of matter and radiation is assumed to be *uniform*.
- The particle injection is provided by Q sources *uniformly* distributed over the galactic volume and it is constant.
- The diffusion term in 1.11 is replaced by

  $$D\nabla^2 N \rightarrow -\frac{N}{\tau_{esc}(E)}$$

  where τ_{esc} is an average escape time that depends on energy and particle type but it is independent on the particle's position.
- As the CR particle reach the boundaries, they have a certain probability to leak out into the intergalactic medium. This results in an *exponential* distribution of *path length* as

  $$N(\Lambda) \propto \exp(-\Lambda/\Lambda_{esc})$$

  where Λ_{esc} represents the average escape length.

The LBM allows first-order estimate of the spectrum at the *source*, *i.e.* near the production site where the CRs are accelerated. One assumption is that the flux at the Earth's position follows a power law $\Phi(E) \propto E^{-\alpha}$, which is supported by many experimental observations. Another assumption is that the escape time follows the power law described in the equation 1.9. This estimate is then based on the transport equation, expressed as

$$-\frac{N_i}{\tau_{esc}} + Q_i - \frac{N_i\, c}{\lambda} = 0$$

in which a steady-state solution is assumed $\frac{dN_i}{dE} = 0$ and the terms for energy losses $b(E)\, N_i$ and spallation processes P_{ji} are neglected. The solution is

$$N_i(E) = \frac{Q_i(E)\, \tau_{esc}(E)}{1 + \frac{c\tau_{esc}}{\lambda_I}} \tag{1.12}$$

Furthermore, with the additional assumption $c\tau_{esc}\, \lambda^{-1} = \frac{\Lambda_{esc}}{\lambda'} < 0.1$, one gets

$$\Phi_i(E) \sim Q_i\, E^{-\delta}$$

Assuming $\alpha = 2.7$, *i.e.* the typical value below the knee ($\sim 10^{15} eV$), one obtains

$$Q_i \sim E^{-\alpha+\delta} = E^{-2.1}$$

which is a fairly good approximation to the source coefficient, that should be around -2 according to the acceleration models.

---

[36] Usually, it is assumed as cylinder with thickness of about 300-500 pc and a radius 10-15 kpc.

1.5 Current measurements of the Helium and Proton spectra

The state-of-the-art detectors in space, has marked the beginning of the era of high-precision measurements of galactic cosmic ray spectra. A compilation of recent results for proton and helium nuclei are shown in Fig. 1.9 from direct measurements ATIC [110], CREAM [138], AMS02 [23, 24], NUCLEON [83], DAMPE [29, 57] and CALET [8, 19]. These exhibit unexpected spectral features that deviate from the single power law predicted by the standard cosmic-ray model (described in the previous sections). At energies around a few hundred GeV per nucleon, the existence of a hardening (*i.e.*, flux enhancement) of the spectral index ($\Delta\gamma \sim 0.2$) has been confirmed by several experiments, while at a few tens of TeV another change in the spectral index has recently been observed by DAMPE and CALET, the softening. Such features are of paramount importance because they can provide valuable insights into the origin and propagation mechanism of cosmic rays. In particular, they may signal the superposition of multiple sources with different cutoff energies, the presence of a nearby source on top of the background component [139], or, in the case of hardening, the existence of a re-acceleration mechanism occurring during propagation [113, 135]. However, only further experimental data will allow us to understand their origin and validate the proposed theories.

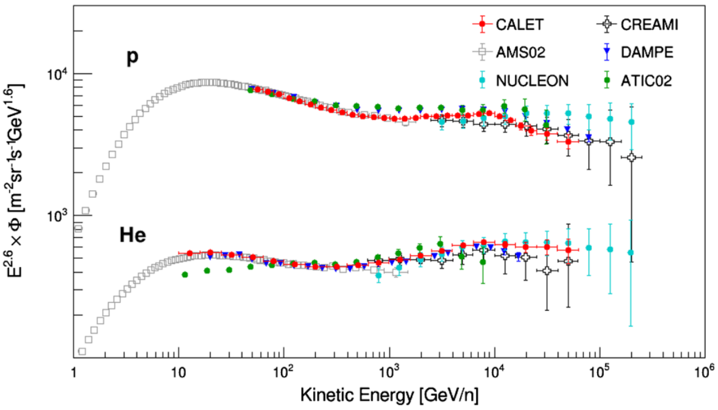

FIGURE 1.9: Compilation of the proton and helium fluxes multiplied by $E^{2.6}$ as a function of kinetic energy per nucleon. The CALET experimental points are taken from [8, 19] and encoded in red. The other results are from [23, 24, 29, 57, 83, 110, 138]. Figure taken from [8]

In this context, the range from tens to hundreds of TeV needs to be further investigated, since the recent direct measurements are affected by significant systematic and statistical errors due to the limited geometrical acceptances of detectors operating in space. As far as direct measurements are concerned, the energy range from hundreds of TeV to PeV is still unexplored. The investigation of this interval could thus pave the way for the discovery of new spectral features, as hinted by recent results from indirect measurements [2].

These open questions have motivated the new analysis of the helium flux, presented in this work using CALET data.

Chapter 2

The CALET experiment

CALET (CALorimetric Electron Telescope) is a space-based experiment led by the JAXA (Japan Aerospace eXploration Agency) in collaboration with the Italian Space Agency (ASI) and with National Aeronautics and Space Administration (NASA).

On August 19, 2015, the CALET payload was successfully launched in orbit on the H2 rocket from the Tanegashima Space Center (Japan). On August 24, 2015, the CALET instrument reached the International Space Station (ISS) by the HTV-5 Transfer Vehicle, where it was robotically attached to port #9 of the Japanese Experiment Module-Exposed Facility (JEM-EF). An image of CALET on the ISS is shown in Fig. 2.1

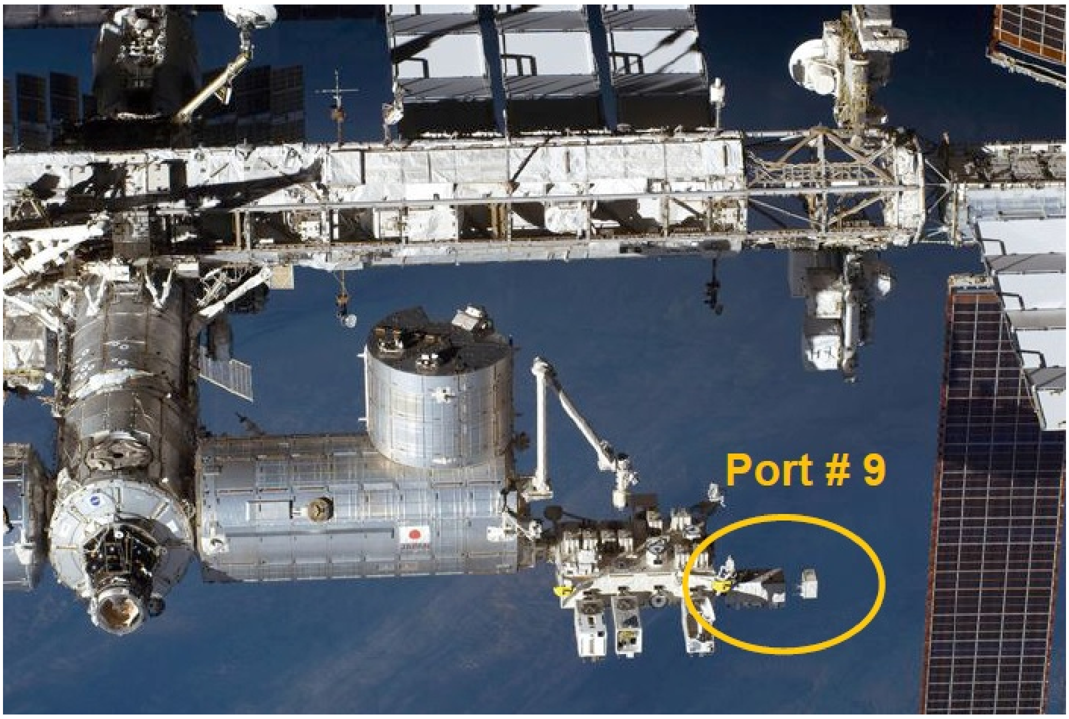

FIGURE 2.1: The CALET instrument installed on port #9 of the JEM-EF. Credit:JAXA

Following the on-board commissioning phase, it has been acquiring data smoothly since October, 2015. Orbiting at an altitude of about 400 km, CALET experiment permits thus long-term observations of high-energy charged particles (cosmic rays) and photons (gamma rays) without the interference of the

Earth's atmosphere. These data provide valuable insight into the origin, acceleration and propagation mechanisms of cosmic rays, and also contribute to a better understanding of high-energy gamma-ray astronomy as well as to the hypothetical dark matter candidates. Selected CALET results, obtained during the first ~ 7.5 years of operation, are discussed in the section 2.5.

2.1 Overview of the CALorimetric Electron Telescope

The CALET payload has a total weight of 612.8 kg, the dimensions are $1.9 \times 0.8 \times 1.0\,\mathrm{m}^3$ and the nominal power consumption is 507 W. Data is transmitted to Earth via two channels: the high-speed channel that operates at an average speed of 600 kilobits per second (kbps), and the low-speed channel operating at 50 kbps. As schematically shown in Fig. 2.2, the payload consists of the main calorimeter telescope (CAL), the CALET Gamma-ray Burst Monitor (CGBM), the Mission Data Controller (MDC) [85], and additional equipment such as the Advanced Stellar Compass (ASC) and Global Position Sensor Receiver (GPSR).

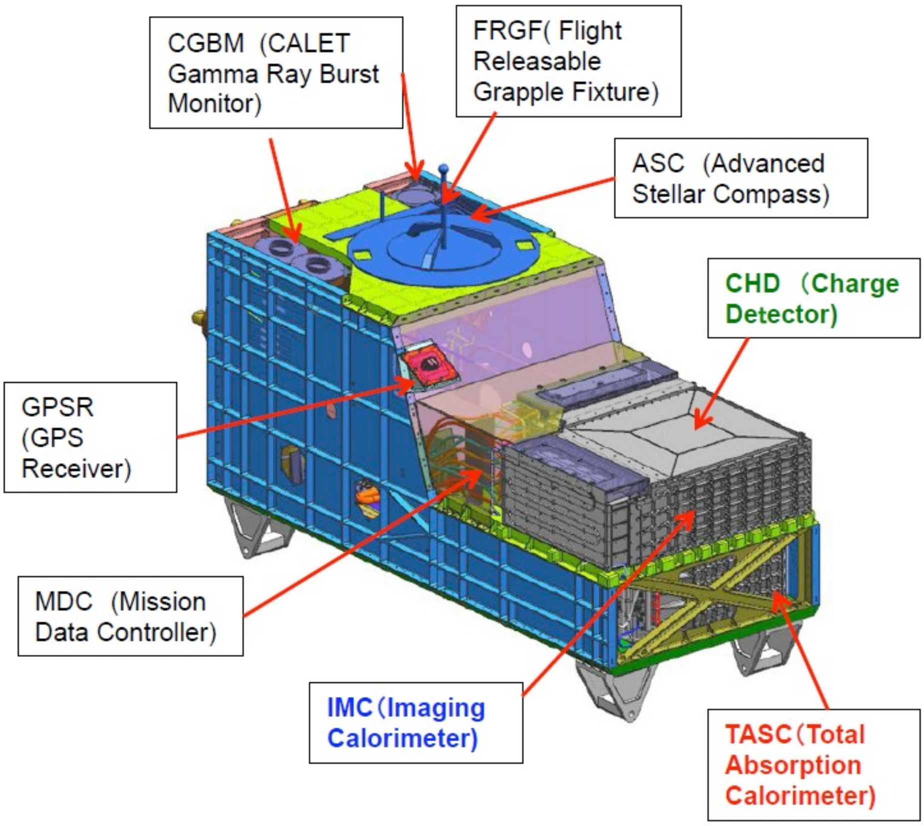

FIGURE 2.2: Schematic of the CALET payload with its components.

The CGBM is an auxiliary instrument designed primarily to detect gamma ray transients. It enables the gamma-ray burst (GRB) observations covering

FIGURE 2.3: The HXM and the SGM sensors of the CGBM.

a wide energy range, from low energy X-ray (∼ 7 keV) to gamma rays (∼ 20 MeV). A Soft Gamma-rays Monitor (SGM) and two Hard X-rays Monitors (HXM) are the sensors making the CGBM, as shown in Fig. 2.3. Each HXM unit is composed by two layers of cylindrical-shaped $LaBr_3(Ce)$ scintillator crystals readout by a PMT (Hamamatsu R6232-05). The HXM field of view is about 58° from the vertical axis and it is determined by the 410 mm beryllium collimator placed at the entrance window. The SGM unit is made of cylindrical-shaped BGO scintillator coupled with a PMT (Hamamatsu R6233-20). Since GRBs are beyond the scope of this Thesis, the performance of the CGBM will not be discussed here. Detailed information can be found elsewhere, *e.g.* in Refs. [94, 136].

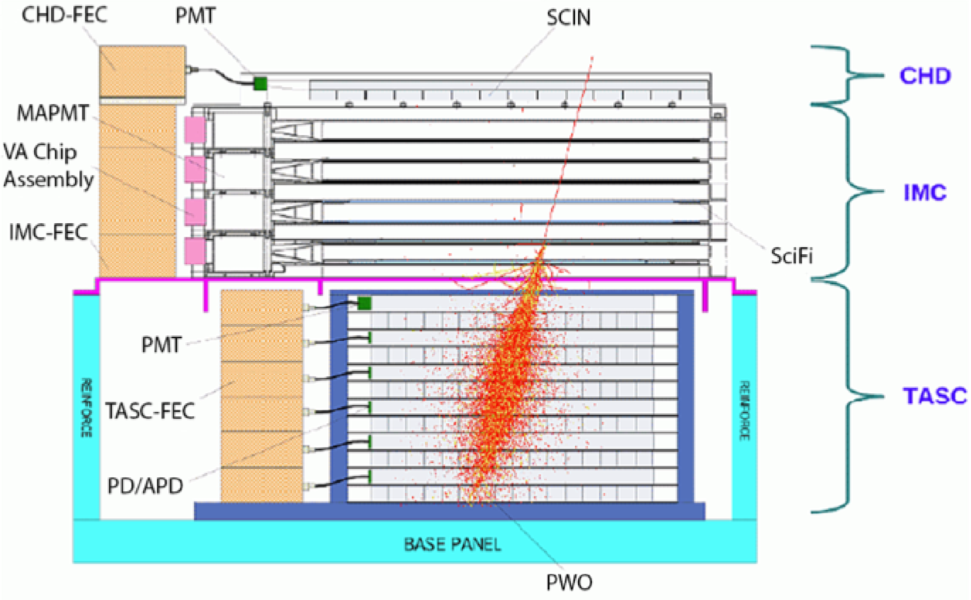

FIGURE 2.4: Schematic side-view of the main CALET instrument composed by the CHD, IMC and TASC sub-systems. A simulated electron at 1 TeV is superimposed to highlight the shower containment capabilities of the calorimeter.

The CAL is the main detector of the CALET mission. It is all-calorimetric instrument, primarily designed to measure with high-precision the inclusive electron (electron+positron) spectrum, covering the energy range from 1 GeV to 20 TeV. The total thickness is equivalent to 30 X_0 radiation length and

$\sim 1.3\ \lambda_p^I$ proton interaction length. The field of view is about 45° from the zenith, and the maximum effective geometrical factor for electron and light nuclei is $\sim 1200\ \text{cm}^2\,\text{sr}$. It consists of three sub-systems: the total absorption calorimeter (TASC), the imaging calorimeter (IMC) and the charge detector (CHD). A schematic side-view is illustrated in Fig. 2.4.

The TASC is a homogeneous calorimeter with equivalent thickness of $27\,X_0$ radiation length. It is primarily designed to fully contain CR electron and to measure their energy up to the multi-TeV region. Hence, the energy resolution for electromagnetic shower is very good ($< 2\%$). On the other hand, the equivalent thickness is only $\sim 1.3\lambda_p^I$ interaction length for hadrons and therefore an important fraction of hadronic cascades leaks out from the calorimeter. An example of the shower containment capabilities of the TASC is shown in Fig. 2.5 for simulated 10 GeV γ-ray, 1 TeV electron and 10 TeV proton.

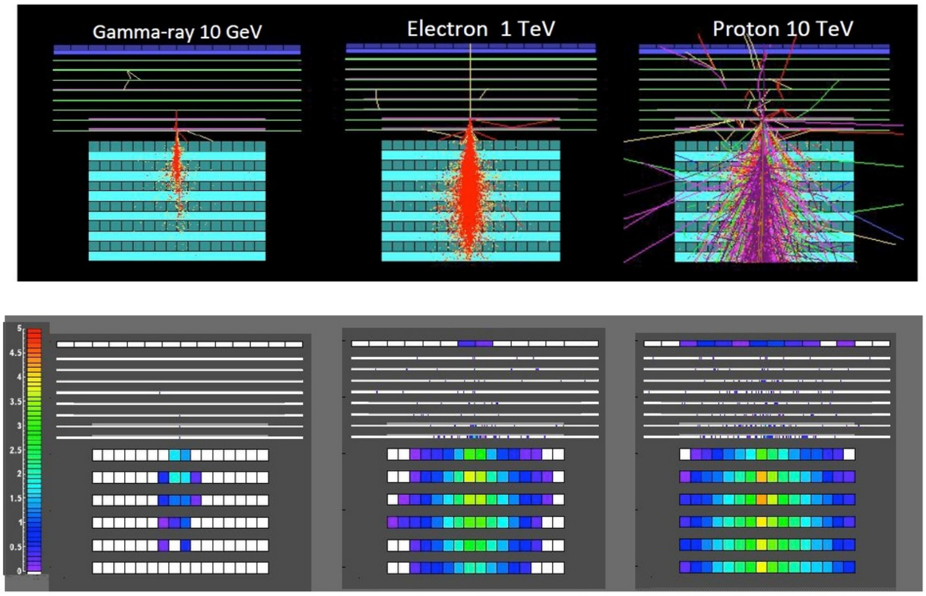

FIGURE 2.5: Event display for a simulated 10 GeV γ-ray, 1 TeV electron and 10 TeV proton.

Above the TASC, there is the IMC, a finely segmented sampling calorimeter. It allows an high-resolution track reconstruction, providing an image of the early shower profile.

At the top of the instrument, there is the CHD that permits the charge identification of the incoming CR particle, over a wide dynamic range from $Z = 1$ to $Z \sim 40$.

These three sub-systems are described extensively in the next sections.

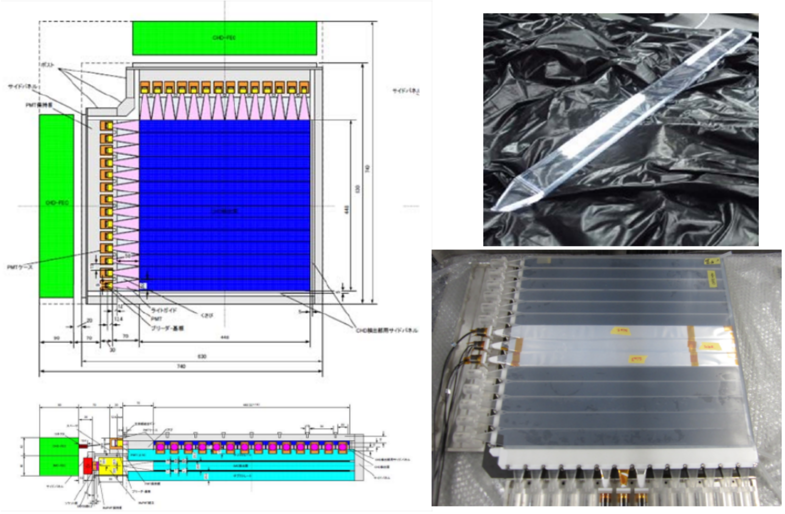

FIGURE 2.6: (Left) Structural design of the CHD detector. (Right) Example of CHD paddle consisting of the plastic scintillator EJ204 and the acrylic light guide. Figure taken from [117].

2.2 CALET sub-systems

2.2.1 Charge detector

The charge detector is a two-layer hodoscope placed at the top of the instrument. It is designed to measure the charge of the incoming CR particles by exploiting the Z^2 dependence of the energy loss by ionization $\frac{dE}{dx}$ by a Minimum Ionizing Particle (MIP). The structural design of the CHD detector is displayed in the left-hand panel of Fig. 2.6, taken from Ref. [117]. Each layer is segmented into 14 plastic scintillator paddles, with dimensions $32\,\mathrm{mm}\,(\mathrm{W}) \times 10\,\mathrm{mm}\,(\mathrm{H}) \times 450\,\mathrm{mm}\,(\mathrm{L})$. The paddles are arranged along the x and y directions in the top and bottom layers, respectively. A single paddle is made by EJ204 plastic scintillating material coupled to a PMT[1] (Hamamatsu R11823) through an acrylic light guide, as illustrated in the right-hand panel of Fig. 2.6.

Scintillating paddle performance The light output of a plastic scintillator depends on the nature of the penetrating particle. For ions heavier than helium, the light yield per unit distance $\frac{d\mathcal{L}}{dx}$ is *non-linear* but has a tendency to decrease as the charge increases. This saturation of the light output is driven by quenching effects and, on a first order approximation, it can be modelled by the Birks' semi-empirical formula

$$\frac{d\mathcal{L}}{dx} = \frac{A\,\frac{dE}{dx}}{1 + B\,\frac{dE}{dx}}$$

---

[1] The amplification, shaping and digitization of PMT signals is performed via Front-End Custom (FEC) electronics similar to the one implemented for TASC sub-system but with a single channel mono-range readout.

where B is a parameter that depends on both the scintillating material and the quenching probability, while A represents the scintillation efficiency without quenching. As already pointed out, for a MIP, the $\frac{dE}{dx}$ can be simplified as $\alpha\, Z^2$.

An extension of this parametrization, provided in Ref. [129], is the Tarlé model in which the $\frac{d\mathcal{L}}{dx}$ is regarded as the sum of two components: the saturated *core* component and the unsaturated *halo* component where there is no quenching. It can be expressed as

$$\frac{d\mathcal{L}}{dx} = \frac{A(1-f_h)\,\frac{dE}{dx}}{1+B(1-f_h)\,\frac{dE}{dx}} + A\, f_h \frac{dE}{dx}$$

where f_h represents the fraction of energy loss for the production of secondary electrons (δ-rays).

Another model is the one provided by Voltz in Ref. [133] where it splits the $\frac{d\mathcal{L}}{dx}$ into a *prompt* and *delayed* components. As reported in Ref. [54], the contribution from *delayed* term can be neglected for CHD scintillators. In contrast, the *prompt* component can be expressed as

$$\frac{d\mathcal{L}}{dx} = A\left[(1-f_h)\,\exp\left(-B\,(1-f_h)\,\frac{dE}{dx}\right)\right]\frac{dE}{dx}$$

The 2$^{\text{nd}}$ order expansion of this parametrization (Voltz-II) was adopted for calibrating CHD paddles in X and Y layers using CALET *in-flight* data. The mean pulse heights for nuclei from hydrogen to iron are shown in Fig. 2.7 with the related fit functions. The same data were also fitted with the Tarlé

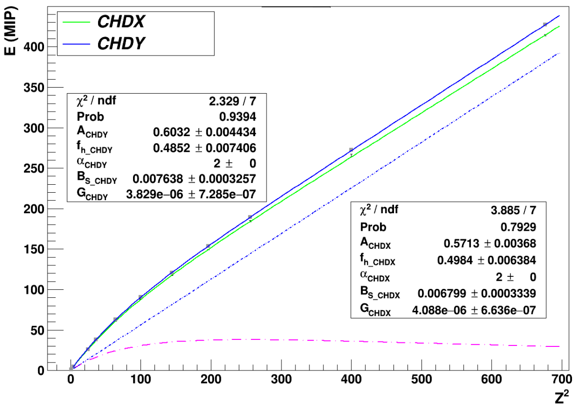

FIGURE 2.7: Mean pulse height for nuclei from hydrogen to iron, as a function of Z^2 using CALET *in-flight* data. The fit with Voltz-II parametrization is shown with green (blue) line for CHD-X (CHD-Y). The *core* and *halo* contributions for CHD-Y, are represented with the magenta and blue dashed lines, respectively. Figure taken from [119].

model, showing a good agreement. However, the Voltz-II parametrization was selected because it shows a better agreement with data. The particle charge (Z) is then achieved from the measured deposited energy in the hit CHD paddle, by inverting the Voltz-II function. Further details of this procedure can be found in Ref. [119].

Another significant issue, that degrades the charge resolution, is the back-scattering of shower-originated secondary particles produced within the calorimeter. The number of such particles, grows as function of the primary energy of the incoming ion. This decreases the CHD resolution by broadening the charge distributions of the relatively large CHD paddles that integrate the energy of the back-scattered particles.

2.2.2 Imaging calorimeter

The imaging calorimeter is positioned just below the CHD. It is a fine-grained sampling calorimeter that has been designed primarily to reconstruct the trajectory of the incoming particle and its early shower profile. The IMC consists of 16 layers of scintillating polystyrene fibers (SciFi) for the particle tracking and 7 tungsten (W) planes that acts as absorbers. An aluminum honeycomb structure, which supports the IMC detector, is located below each absorber, while a pair of SciFi layers, disposed along orthogonal directions, are glued above each tungsten plate. A schematic view of the IMC sub-system is depicted in Fig. 2.8, where the different components are highlighted.

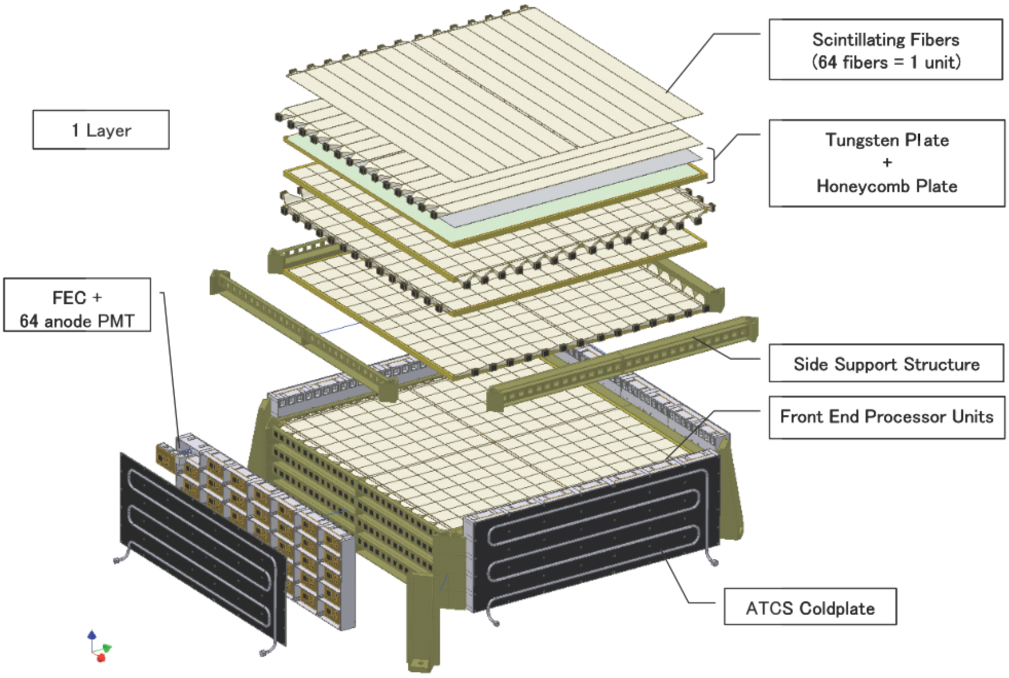

FIGURE 2.8: Exploded view of the IMC sub-sytem.

Each active layer comprises 448 SciFis with cross section of 1 mm^2 and length of 448 mm. The scintillating fibers are grouped in "belts" of 32 elements. The belts are readout two by two through a multi-anode PMT (Hamamatsu R7600-M64), with 8 dynodes stages[2] and 64 anodes, as shown in the right panel of Fig. 2.9. The front-end chip is the Viking VA32-HDR14.3, a dedicated 32 channel ASIC characterized by high dynamic range, low noise and low power consumption [37, 131].

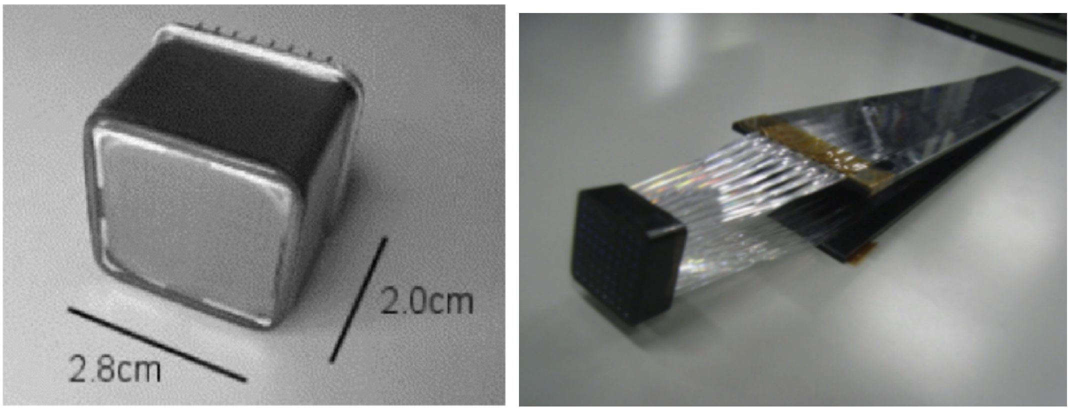

FIGURE 2.9: (Left) The MA-PMT Hamamatsu R7600-M64 used for the IMC SciFi readout. (Right) Two 8 fiber belts coupled with the MA-PMT. Figure taken from [49].

The thickness of the 7 tungsten absorbers increases progressively towards the bottom of the IMC. Conversely, the area decreases until the last set of absorbers reaches the size of the first TASC layer (X1). Specifically, the dimensions of the upper three plates are 44.8 cm × 44.8 cm × 0.07 cm, the intermediate two layers are 38.4 cm × 38.4 cm × 0.07 cm and the bottom ones are 32.0 cm × 32.0 cm × 0.35 cm. The total equivalent thickness in terms of radiation length is 3 X_0, where each of the first five plates is 0.2 X_0 thick, while the last two thickest layers is 1.0 X_0. Thus, the IMC has been designed to be a pre-shower calorimeter. In fact, electrons and γ rays have a high probability of interacting in one of the tungsten planes. Conversely, for hadrons this probability is low because the total equivalent thickness is only about one tenth of the proton interaction length (λ_p^I).

On the other hand, the high level of segmentation of the IMC detector enables it to

- Reconstruct the trajectory of the incoming particle, separating it from secondary back-scattered particles.
- Establish the interaction point where the shower starts.
- Improve the particle identification by providing an independent charge measurement.

---

[2] This custom design enhances the response linearity with respect to the standard 12 dynodes version, as stated in Ref. [137]

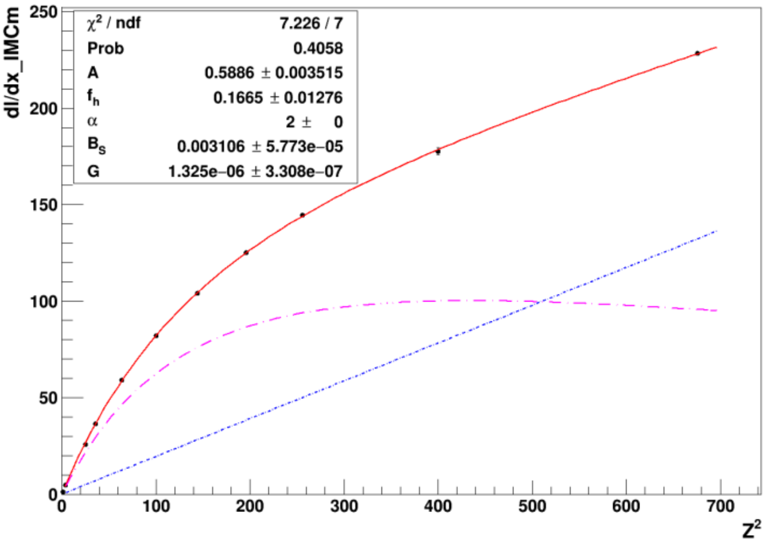

FIGURE 2.10: Mean pulse height for nuclei from hydrogen to iron, as a function of Z^2 using CALET *in-flight* data. The fit with Voltz-II parametrization is shown with red line for IMC. The *core* (*halo*) contribution based on CHD-Y, is represented with the magenta (blue) dashed line. Figure taken from [119].

The details of charge measurement with IMC is provided in section 3.2.2. As far as light saturation is concerned, it has been corrected with Voltz-II parametrization in the same way as for the CHD subsytem. The results are shown in Fig. 2.10 taken from Ref. [119] where more information on this procedure can be found.

As a side note on the nomenclature, the IMC layers are identified as `X1`-`Y8`, where `X1` is the upper layer near the CHD and `Y8` is the lower layer near the first layer of the TASC.

2.2.3 Total absorption calorimeter

The TASC is positioned below the IMC. It is a deep homogeneous calorimeter, structured in 12 layers which are arranged in orthogonal pairs, as shown in the Figure 2.11. Each layer comprises an array of 16 lead-tungstate (PWO) logs. The dimensions of a single log are 19 mm (width), 20 mm (height) and 450 mm (length). The 192 PWO logs enable thus the 3D reconstruction of the shower profile, albeit with coarser segmentation compared to IMC subsystem. The comprehensive equivalent thickness is about 27 X_0 or $\sim 1.3\ \lambda_p^I$ for impinging particle at normal incidence.

The TASC readout is performed in two different ways. The PWO logs of the first TASC layer (`X1`) are readout by PMTs with the aim of providing a quick trigger signal. Conversely, the logs of all the other layers are readout by hybrid package made by a photo-diode (PD) together with an avalanche photo-diode (APD), as shown in the left-hand panel of Figure 2.12. Specifically, the Hamamatsu S8664-1010 is the APD sensor with an active area of

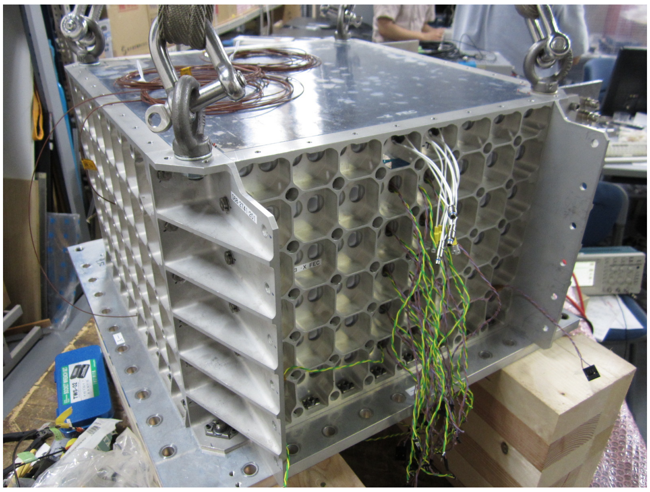

FIGURE 2.11: Total Absorption Calorimeter. Credits: JAXA.

$10 \times 10\,\text{mm}^2$, whereas the S1227-33BR is the PD sensor with an active area of $2.4 \times 2.4\,\text{mm}^2$. The front-end circuit (FEC) for each log, is designed to provide an high-dynamic range covering 6 order of magnitude, *i.e.* from 0.5 MIP up to 10^6 MIP. This is achieved using a dual charge sensitive amplifiers (CSA) followed by a pulse shaping amplifiers with two gains (high and low) for each APD and PD. Figure 2.13 shows a block diagram of the FEC, taken from Ref. [92] where more information can be found.

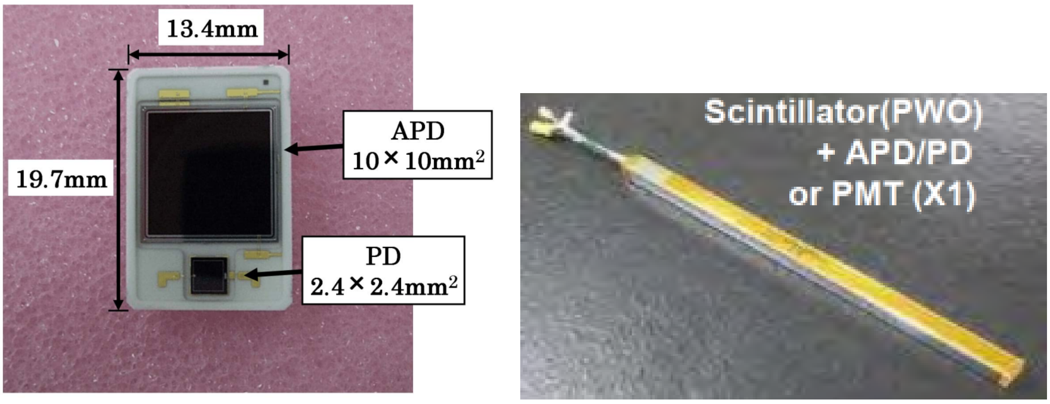

FIGURE 2.12: (Left) Example of TASC log readout, made by the APD sensor with an active area of $10 \times 10\,\text{mm}^2$, and the PD sensor with an active area of $2.4 \times 2.4\,\text{mm}^2$. (Right) PWO log.

The energy calibration process is basically divided into three steps. MIP calibration, which consists of establishing the linear conversion factor from ADC unit to energy deposit using non-interacting MIP particles. Linearity verification[3] of each gain range. Cross-calibration of the adjacent gain range. More details on the full calibration procedure can be found in Ref. [32]. In summary, the absolute energy calibration was achieved with a resolution accuracy of 2% above 100 GeV. The systematic error in the energy scale was

---

[3] Before the launch, the linearity was check by ground-based calibrations using UV pulse laser, as reported in Ref. [104].

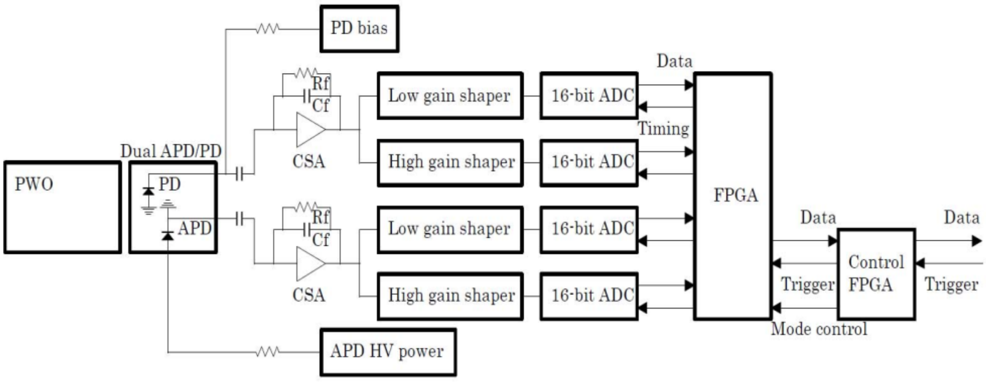

FIGURE 2.13: Block diagram of Front-End-Circuit for the TASC read-out. Figure taken from [92]

found to be $\leq 2\%$. This enables the measurement of the all-electron spectrum in the TeV energy region with a high degree of accuracy. Furthermore, taking advantage of the very wide dynamic range of TASC channels, it is possible to derive the primary energy of protons and other nuclei from 1 GeV up to $\sim$ 1 PeV. However, the energy resolution for hadrons is worse ($\sim$ 30%).

2.3 Trigger system

Since the CALET latency for event acquisition is about 5 ms, specific triggers are needed to efficiently select only high-energy particles. The trigger logic is based on the coincidence of low-level discriminators (LD) from the following detector components: CHD X-Y, IMC X1-X4, Y1- Y4, and TASC X1. In detail the analog signals provided as an input of the threshold discriminator (TD), consist of the following signals :

- $T_{\mathrm{CHD-X}}$ ($T_{\mathrm{CHD-XY}}$) the sum of the signals of all the paddles belonging to CHD-X (CHD-Y) layer.
- $T_{\mathrm{IMC-Xi,i+1}}$ ($T_{\mathrm{IMC-Yi,i+1}}$) the total energy deposit in a pair of consecutive IMC X (Y) layers, starting from X1 (Y1) to X8 (Y8).
- $T_{\mathrm{TASC-X1}}$ the energy deposit of all the PWO logs of the first TASC layer.

The operating LD thresholds are summarized in the table below and three trigger modes are implemented to effectively collect data, as follows.

- The **High-Energy Shower Trigger (HET)** targets high-energy electrons from 10 GeV to $\sim$ 20 TeV, high-energy gamma-rays from 10 GeV to about 10 TeV and protons and nuclei from 10 GeV to $\sim$ 1 PeV. This is the main trigger mode for the CALET mission. In particular, it requires a large energy deposit in the middle of the detector, *i.e.* $T_{\mathrm{TASC-X1}}$ and $T_{\mathrm{IMC-X7,8}}$, $T_{\mathrm{IMC-Y7,8}}$. In this way, it enables the suppression of low-energy events, while providing a large solid angle acceptance. Since the thresholds are high, the SAA (South Atlantic Anomaly) does not

Comprehensive view of the required thresholds for the on-board CALET trigger system. All values are reported in MIP unit.

Trigger Mode	T_{CHDX} T_{CHDY} [MIP]	T_{IMCX12} T_{IMCY12} [MIP]	T_{IMCX34} T_{IMCY34} [MIP]	T_{IMCX56} T_{IMCY56} [MIP]	T_{IMCX78} T_{IMCY78} [MIP]	T_{TASCX1} [MIP]
HET	–	–	–	–	7.5	55
	–	–	–	–	7.5	
LET	0.7	0.7	0.7	0.7	2.5	7
	0.7	0.7	0.7	0.7	2.5	
ST	0.7	0.7	0.7	0.7	0.7	0.7
	0.7	0.7	0.7	0.7	0.7	
Heavy-HET	50.0	–	–	–	7.5	55
	50.0	–	–	–	7.5	
Heavy-LET	50.0	0.7	0.7	0.7	2.5	7
	50.0	0.7	0.7	0.7	2.5	
Heavy-ST	50.0	0.7	0.7	0.7	0.7	0.7
	50.0	0.7	0.7	0.7	0.7	

affect significantly the trigger rate, and thus this trigger mode is always in operation.

- The **Low Energy Shower Trigger (LET)** is designed for selecting low-energy particles that make showers within the detector, such as high-latitude[4] electrons in the energy range between 1-10 GeV, and GRBs gamma rays at energy ≥ 1 GeV. In addition, the signals from the CHD and the upper layers of the IMC are required to exceed the LD thresholds in order to reduce the incident angle range of the low-energy particles. Instead, the energy deposition that is required at the center of the detector is much lower than for a high-energy trigger, but sufficiently high to reject MIPs.

- The **Single Trigger (ST)** aims to acquire non-interacting proton and helium particles for calibration purposes. All the sum signals T are required to pass a threshold equal to 0.7 MIP unit. This trigger mode is active only in a fixed time window (11:30 - 14:30 UT) each day [126].

Additionally, the **Heavy Ion Trigger (Heavy-)** mode mainly targets CR nuclei with charge > 26. It is defined for each configurations (HET, LET and ST) with further conditions on the energy deposit in the CHD layers. An updated version of the trigger modes for low energy and calibration events is available in Ref. [33], which does not change the definition of HET.

The logic diagram describing how CALET trigger is interfaced with the data acquisition system (DAQ) is shown in Fig. 2.14 for the sake of completeness.

---

[4] If the geomagnetic rigidity cut-off is lower than 2 GV.

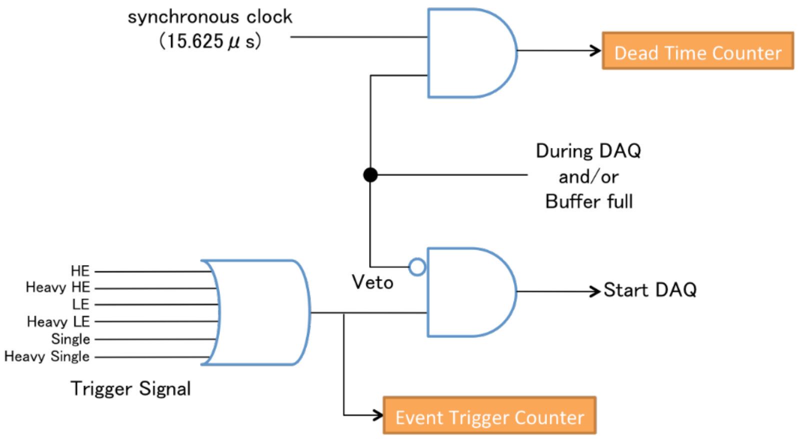

FIGURE 2.14: The logic diagram describing the interface between the CALET trigger and the data acquisition system (DAQ). Figure taken from [33].

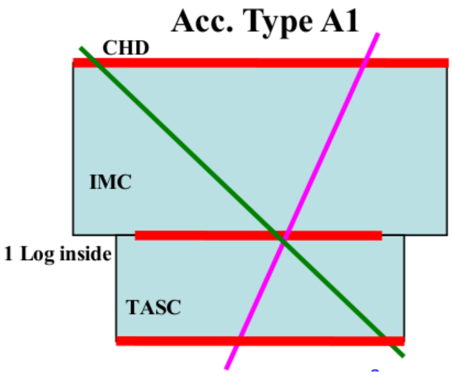

FIGURE 2.15: Fiducial volume definition for `A1` acceptance.

2.4 Geometric factor and acceptance categories

Since the HET requires only a large energy deposit in the central part of the instrument, the acquired events cover a wide range of impact angles. Therefore, different categories of acceptances can be defined, depending on the trajectory of the event. The acceptances used in helium analysis are schematically depicted in Figs. 2.15, 2.16 and 2.17. Specifically, the geometrical requirements are as follows.

- `A1` the impinging particle must cross the entire detector, from the top of the CHD to the bottom of the TASC, with a 2 cm clearance from the edge of the TASC first layer.

- $\mathtt{C}_i$ the particle must cross the entire TASC and the IMC starting from the i^{th} layer in X view.

- $\mathtt{D}_i$ the event must cross the IMC detector from the i^{th} layer in X view, and at least 26.4 cm (equivalent to about 30 X_0) of the TASC, to ensure a reliable energy determination. For category `D0`, the incoming particle must also cross the top CHD layer.

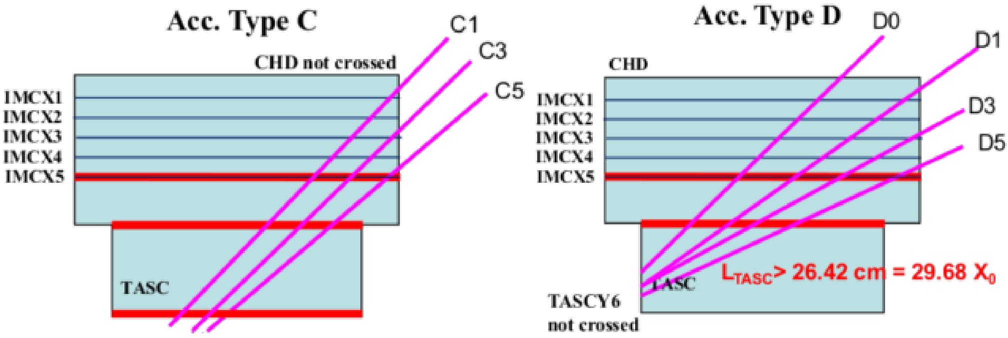

FIGURE 2.16: Fiducial volume definition for acceptance categories $\mathtt{C}_i$ and $\mathtt{D}_i$.

- `B1` is similar to `A1`, but it must transverse one of the two external log of the first TASC layer.
- `A` is as `A1` but with the additional constraint of 2 cm clearance from the edge of the TASC last layer.

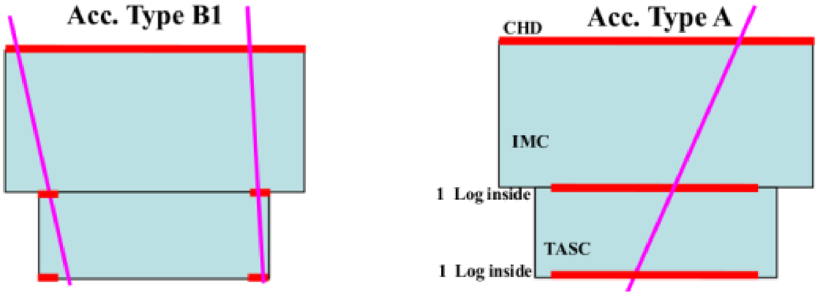

FIGURE 2.17: Fiducial volume definition for acceptance categories `B1` and `A`.

The relative geometric factor (GF) for each category, is numerically calculated using MC simulations, in which a detailed CAD model of the CALET instrument has been integrated. The GF, also indicated as $S\Omega$, is thus obtained as

$$GF_{Acc} = \frac{N_{Acc}}{N_0} S_0\Omega_0 \tag{2.1}$$

where N_{Acc}, N_0 are the number of MC events generated within the considered acceptance and in total, respectively; $S_0\Omega_0$ is the geometric factor of the MC-generating surface, with S_0 the area of the surface and Ω_0 the solid angle. The geometric factors for all the aforementioned acceptance categories are summarized in Table 2.1. In addition, their relative ratios with respect to the total geometric factor are shown in Fig. 2.18.

TABLE 2.1: Geometric factors for all the acceptance categories. In the third column, the GF ratio with respect to `A1` is shown.

Acceptance Category	Geometric Factor [cm^2 sr]	Ratio (w.r.t. `A1`)
`A1`	510	1.000
`B1`	60	0.118
`C1`	66.8	0.131
`C2`	40.8	0.080
`C3`	41.3	0.081
`C4`	42.3	0.083
`C5`	41.3	0.081
`D0`	80.6	0.158
`D1`	30.6	0.060
`D2`	21.9	0.043
`D3`	27.5	0.054
`D4`	36.2	0.071
`D5`	45.9	0.090
`A`	419.0	0.822

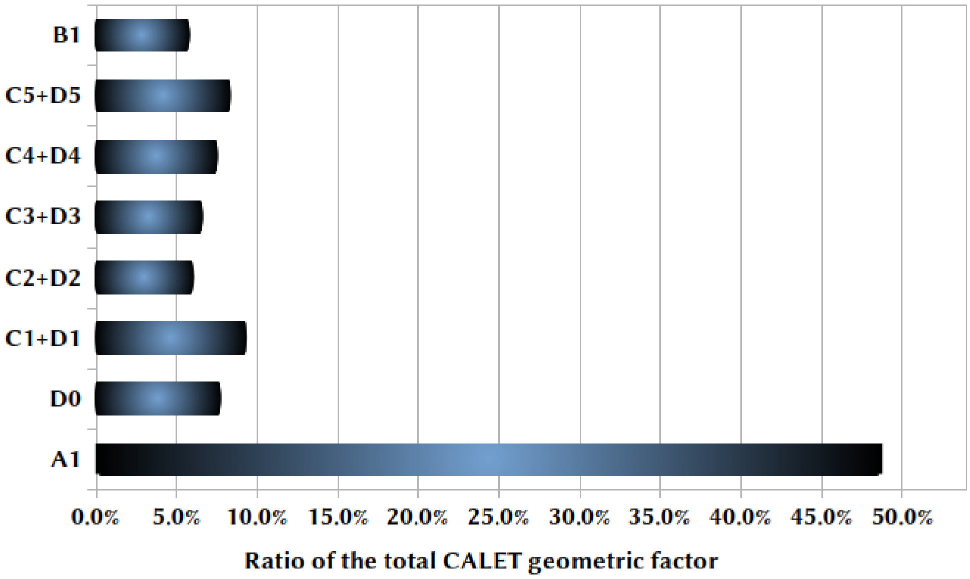

FIGURE 2.18: Fraction of the total geometric factor for the acceptance categories `A1`, `D0`, `B1` and C_i+D_i.

2.5 Selected CALET results

During its 7.5 years of observations on the ISS, CALET has already achieved many significant scientific results of its broad science program. These include the high-resolution measurement of the inclusive electron spectrum up to 7.5 TeV [11], the fluxes and flux ratios of nuclei from proton [19] to nickel [6–8, 10, 12, 17], the solar modulation of cosmic rays depending on the charge sign [5], observations of GRBs [53] and the search for their GW counterparts [3]. Some of these observations are reviewed in the following paragraphs.

2.5.1 All-Electron spectrum

The primary scientific objective of the CALET mission was to perform a high-precision measurement of the *electrons+positrons* spectrum. The flux of CR electrons is about an order of magnitude lower with respect to that of protons, because electrons experience additional energy loss through synchrotron and inverse Compton radiation emission during propagation in the Galaxy compared to nuclei. As radiative losses become increasingly important at high energies, the distance to the sources that could contribute significantly to the total flux decreases with energy. In the TeV region, the number of potential sources is limited to a few, and the all-electron flux can thus provide a detectable spectral signature of nearby astrophysical sources.

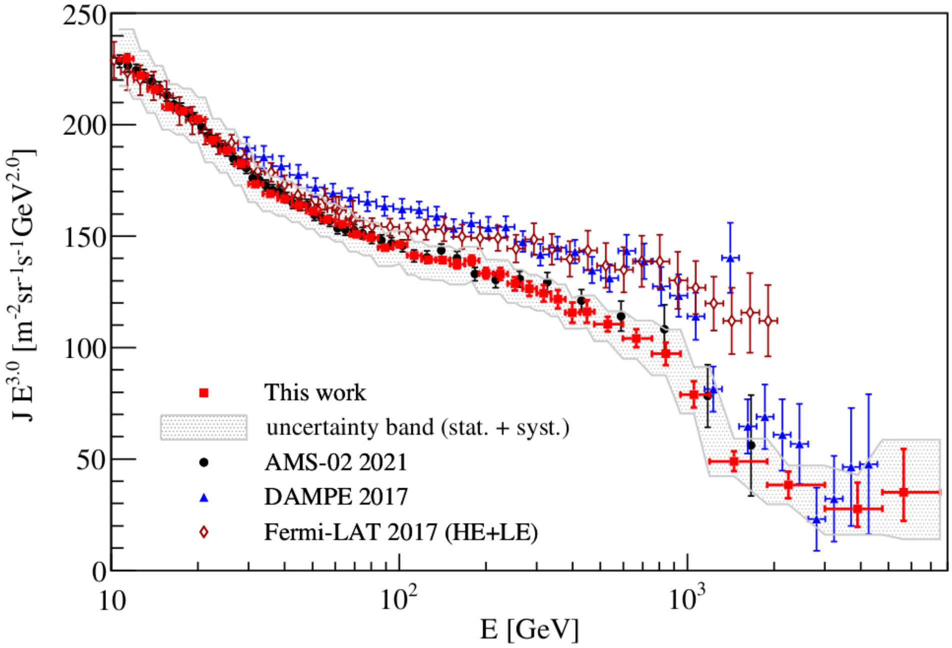

FIGURE 2.19: All-electron spectrum measured by CALET based on 2637 days of flight data. The spectra observed by AMS-02, DAMPE and FERMI-LAT are shown for comparison. Figure taken from [11]

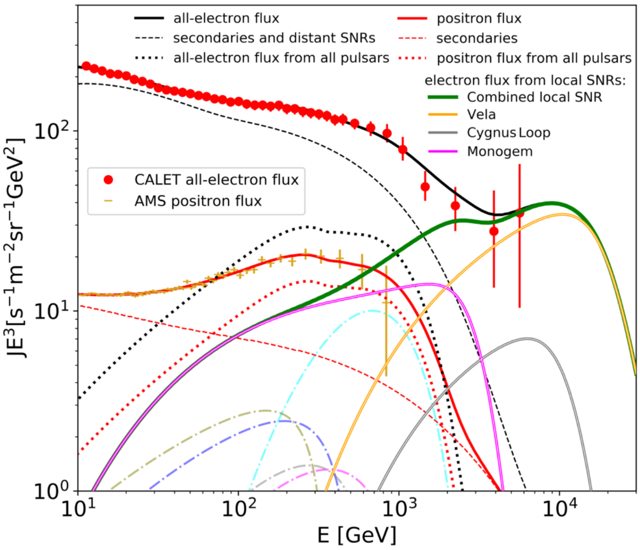

FIGURE 2.20: Possible spectral fit of CALET all-electron observations. This model includes pulsars and nearby SNR sources as individual sources, with the Vela SNR dominating in the TeV region. Figure taken from [11] where more detail can be found.

Figure 2.19 shows the latest results of CALET all-electron spectrum, compared with those of the Fermi-LAT, AMS-02 and DAMPE experiments. The CALET all-electron flux is consistent with the AMS-02 spectrum (which uses a different experimental technique) in the whole range, but is in tension with those of FERMI-LAT and DAMPE from $\sim$ 60 GeV up to $\sim$1 TeV. The spectrum shows a clear deviation from a single power law with a statistical significance greater than 6.5σ, as reported in Ref. [11].

A clear suppression of the flux, with the spectral index going from -3.15 to -3.91, is observed around 1 TeV, confirming previously published results by H.E.S.S [26], DAMPE [63], and Fermi-LAT [1]. This is consistent with the expected effects of radiation loss during propagation from distant sources, except for the highest energy bin, where the observed 9 electron candidates above 4.8 TeV could be an indicator for local sources as suggested by the early theoretical work of Nishimura [109] and quoted in the review [105]. An interpretation of the flux taking into account potential contributions from pulsars and nearby SNR sources, is proposed in the same CALET paper [11]. The adopted model[5] combines both the positron flux measured by AMS-02, and individual sources, including pulsars and SNRs, with Vela, Cygnus Loop and Monogem providing, respectively, the leading terms above 1 TeV. The model, shown in Fig. 2.20, is then used to estimate the expected number of events above 4.8 TeV, and it turns out to be consistent with the existence of nearby SNRs. However, since the number of events is small, further observations will be needed in order to reach a final conclusion.

---

[5] More detail can be found in Ref. [107].

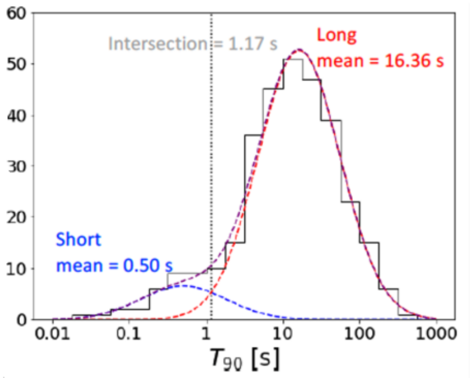

FIGURE 2.21: Time duration of the 327 GRBs detected by CALET monitor from October, 2015 to June, 2023. Figure taken from [132]

2.5.2 Gamma-ray observations

The CALET instrument can also detect high-energy gamma rays and transients. The CAL enables the observations of gamma rays in the energy range from 1 GeV to 10 TeV with an energy resolution of 3% and an angular resolution of 0.4°, with the highest efficiency at 10 GeV. A special low-energy trigger, operating only at low geomagnetic latitudes, is used to obtain measurements from 1 GeV to 10 GeV. Overall, these observations provide insights into the properties of galactic diffuse gamma rays and galactic and extraterrestrial point sources. Fig. 2.22 shows the skymap of gamma-ray intensities for LE-γ (top panel) and HE-γ (bottom panel) events , where the contours represent the CAL exposures. As reported in Refs. [4, 132], 23 sources can be visually identified, albeit the level of statistical significance is still under evaluation. In addition, this sky-map shows good agreement with the Fermi-LAT one, considering that CAL exposures are not uniform.

Gamma-ray bursts are monitored in the energy range from 7 keV to 20 MeV by the CGBM, briefly introduced in the section 2.1, and in the energy range from 1 GeV to 10 TeV by the combined CAL+CGBM system, using the trigger signals provided by the CGBM. Figure 2.21 shows the time distribution of the 327 GRBs observed by the CGBM from October, 2015 to June, 2023.

In addition, CALET is contributing to the search for the X-ray and gamma-ray counterparts of gravitational wave events. The results of this search using events from the third observation run (O3) of LIGO/Virgo, are reported in Ref. [4] . No candidates events have been found that satisfy the selection criteria, but upper limits to the time-averaged fluxes are provided.

2.5.3 Cosmic nuclei

Although CALET is primarily designed to measure the leptonic component of CRs, its calorimetric depth is enough to measure the steep energy spectrum of nuclei in the range from tens of GeV to about one PeV. These spectra

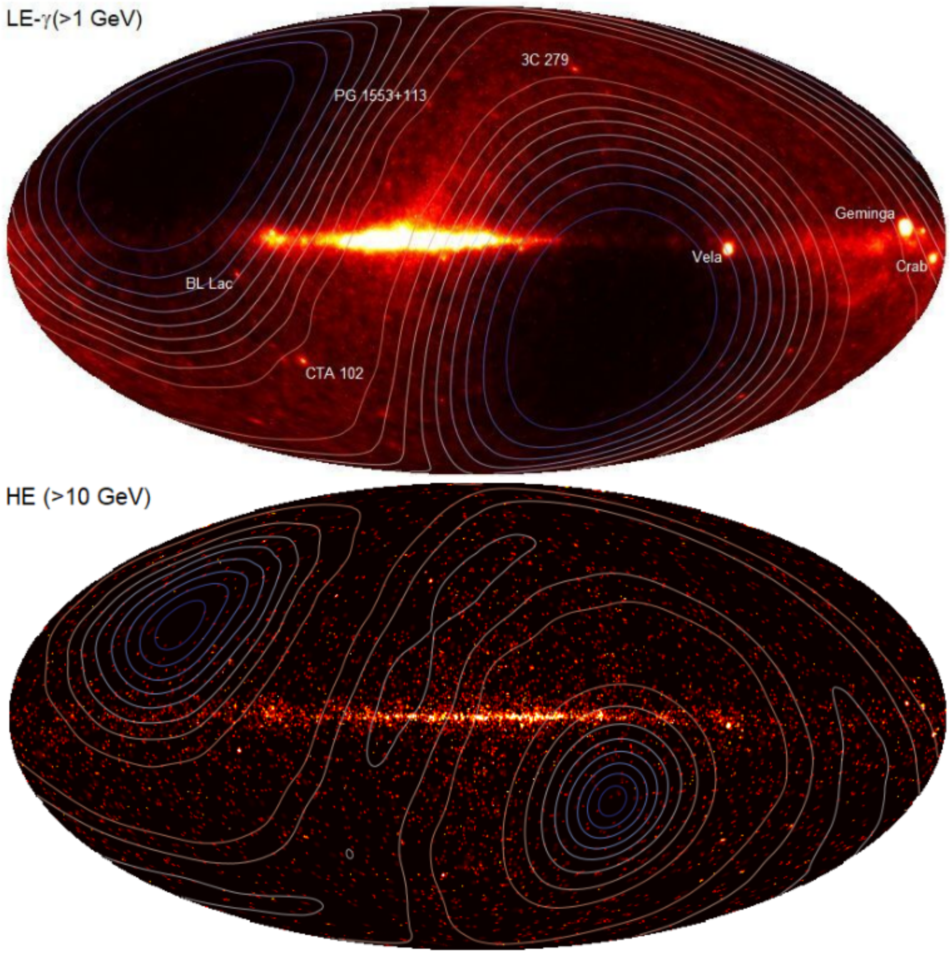

FIGURE 2.22: Sky map for LE-γ (top) and HE-γ (bottom) events in galactic coordinates. The relative exposures are represented with contours superimposed to the gamma-ray intensities. Figure taken from [21].

can indeed provide crucial information about the sources and possible acceleration mechanisms, but also about their propagation through the galaxy. In particular, recent results published by CALET collaboration show unexpected spectral features.

In this section we will recall some of the most important results, namely secondary and primary abundance ratios and proton and helium fluxes, since the improvement of the measurement of the helium flux is the goal of this Thesis.

Boron-to-Carbon ratio The secondary-to-primary abundance ratios[6] are key probes of cosmic-ray propagation in the Galaxy, as discussed in section 1.4. In this regard, the boron-to-carbon ratio is the most important one to discriminate between different propagation models, because boron is mainly of secondary origin.

Fig. 2.23 shows the B/C flux ratio as measured by CALET, and published in Ref. [20]. It covers an energy range from 8.4 GeV/n to 3.8 TeV/n, and is based on $\sim$ 7.2 years of CALET data.

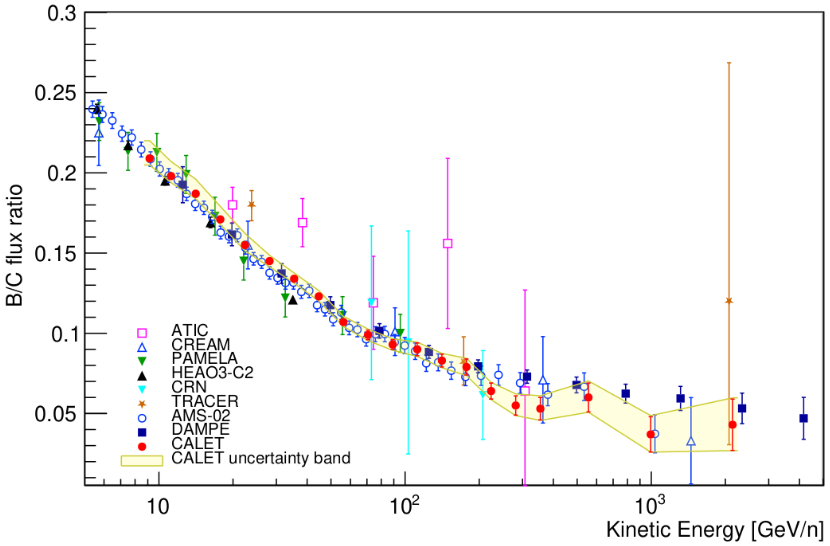

FIGURE 2.23: Recent CALET measurements of B-to-C ratio, as a function of kinetic energy per nucleon. The CALET data is represented in red, whereas the other direct experiments are shown for comparison and encoded in the legenda. Figure taken from [20].

The B/C ratio from CALET is consistent with the PAMELA [16] and AMS-02 [25] measurements, whereas the normalizations of the single boron and carbon fluxes are consistent with PAMELA results but in tension (see *e.g.* Ref. [6]) with the ones provided by AMS-02.

---

[6] From an experimental point of view, the flux ratios have also the advantage to be less affected by systematic errors.

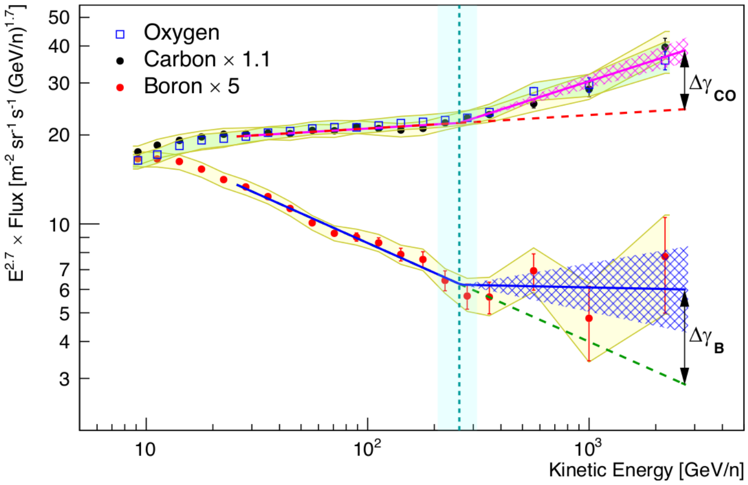

FIGURE 2.24: Boron, Carbon and Oxygen energy spectra from CALET data are encoded with red dots, black dots and blue open squares, respectively. The fluxes are fitted with DPL functions (solid lines), whereas the dashed lines represent the extrapolation of a SPL function derived by fitting the data in the energy range [25, 200] GeV/n. The vertical cyan dashed line represents the expected value of the transition energy E_0 with its $\pm 1\sigma$ error interval. Figure taken from [20]

Fitting the observed ratio with a leaky-box model[7], the flattening in TeV/n region is compatible with a non-zero value of the residual path length[8] Λ_0. This corroborates the hypothesis that some of the secondary B nuclei may be produced near the CR source. However, other trends cannot be ruled out (for example, a single power law) because the statistical accuracy at high-energies is not sufficiently high.

Furthermore, the boron, carbon and oxygen spectra exhibit a spectral hardening at around 200 GeV/n, albeit with different strength for boron with respect to carbon and oxygen. Fig.2.24 shows the CALET fluxes fitted with double power-law (DPL) functions[9] where the results support a stronger hardening $\Delta\gamma_B = 0.32 \pm 0.14$ for Boron (secondary) with respect to Carbon and Oxygen (primaries) $\Delta\gamma_{C-O} = 0.19 \pm 0.04$, even if with low statistical significance.

---

[7] The shape of the fitting function is parametrized as

$$\Lambda(E) = kE^{-\delta} + \Lambda_0$$

[8] The residual path length can be viewed as the source grammage, *i.e.* the average amount of matter traversed within the acceleration site.

[9] The DPL parametrisation is

$$\Phi(E) := c \begin{cases} E^{\gamma} & \mathrm{E} \leq \mathrm{E}_0 \\ E^{\gamma+\Delta\gamma} E_0^{-\Delta\gamma} & \mathrm{E} > \mathrm{E}_0 \end{cases}$$

Proton flux The recent measurements of CALET proton flux spans over three order of magnitude, *i.e.* from 50 GeV to 60 TeV. Fig. 2.25 shows the last published CALET proton spectrum as function of the kinetic energy of the primary particle in fiducial acceptance `A` [19]. The measured flux exhibits a significant deviation from a the single power law spectrum predicted by the standard CR model. The first feature is the progressive spectral hardening, starting from few hundreds of GeV, that corroborates the previous measurements made by magnetic spectrometers (AMS-02, PAMELA) and ballon experiments (CREAM). The second unexpected spectral feature is the steep softening around 10 TeV. This observation confirms the results obtained by the DAMPE experiment within the errors. Overall, the CALET proton spectrum is well fitted with a double smoothly broken power law (DBPL) function

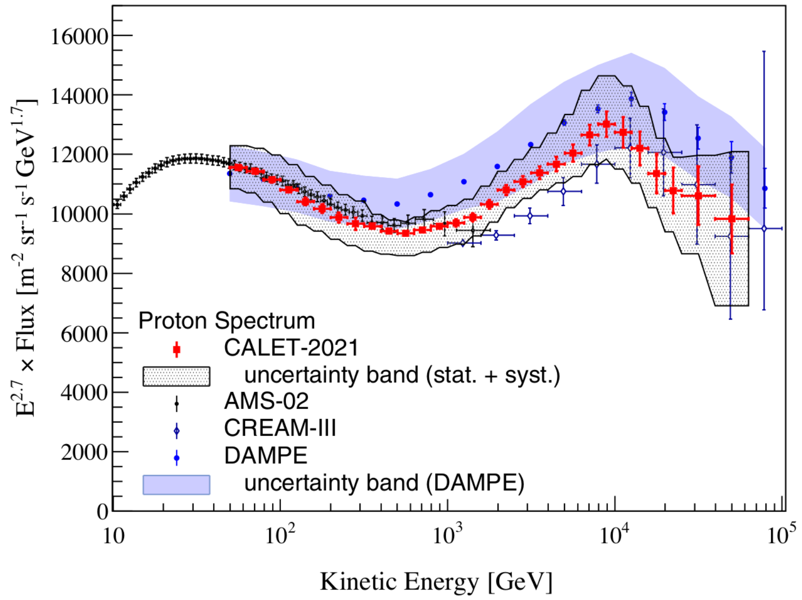

FIGURE 2.25: CALET proton flux (multiplied by $E^{2.7}$) as function of the kinetic energy. The results of direct measurements from other experiments (AMS-02, DAMPE, CREAM) are shown for comparison. Figure taken from [19]

$$\Phi(E) = C\,\varphi(E)\left(\frac{E}{1\,\mathrm{GeV}}\right)^{\gamma}$$

where

$$\varphi(E) = \left[1+\left(\frac{E}{E_0}\right)^{s}\right]^{\Delta\gamma/s}\left[1+\left(\frac{E}{E_0}\right)^{s_1}\right]^{\Delta\gamma_1/s_1}$$

The DBPL fit parameters are the power law index $\gamma = -2.83^{+0.01}_{-0.02}$, the first spectral break $\Delta\gamma = 0.28^{+0.04}_{-0.02}$ at energy $\mathrm{E}_0 = 584^{+61}_{-58}$ GeV and the second spectral break $\Delta\gamma_1 = 0.34^{+0.06}_{-0.06}$ at energy $\mathrm{E}_1 = 9.3^{+1.4}_{-1.1}$ TeV.

Helium flux CALET has also measured the helium flux covering the broad energy range from about 40 GeV to $\sim$ 250 TeV. Fig. 2.26 shows the published

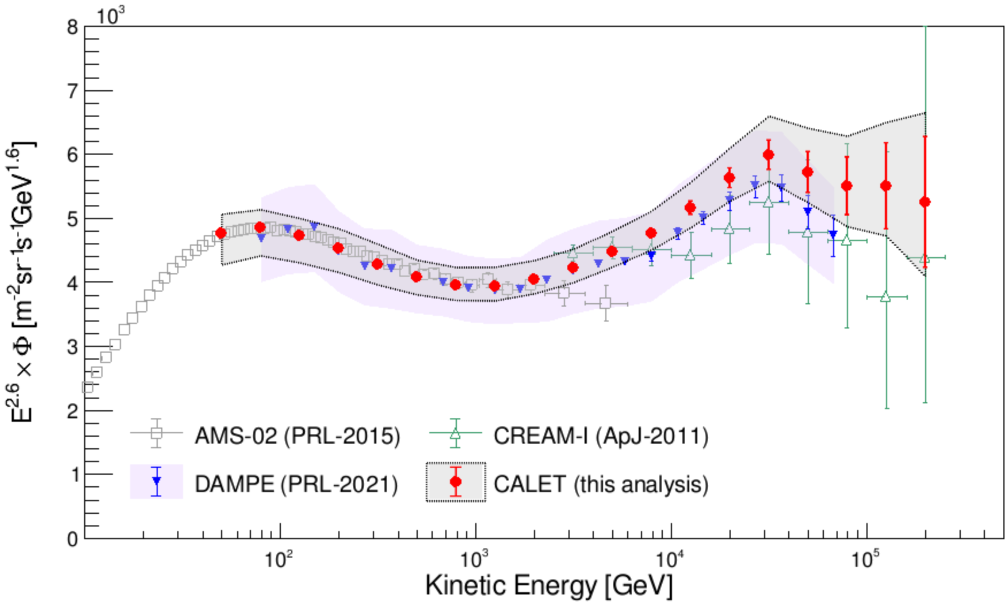

FIGURE 2.26: CALET helium flux (multiplied by $E^{2.6}$) as function of the kinetic energy. The results of direct measurements from other experiments (AMS-02, DAMPE, CREAM) are shown for comparison. Figure taken from [8]

helium spectrum as function of the kinetic energy. This is derived selecting events in fiducial acceptance `A1`.

Again, a significant deviation from the single power law spectrum is clearly visible, with a statistical significance greater than 8σ, as stated in Ref. [8]. In particular, the presence of hardening around a few hundred GeV is observed as well as the onset of a softening around 30 TeV. This result is in agreement (within errors) with the measurements of the DAMPE experiment [29]. Overall, both the hardening and the softening features are found to be well-fitted with DBPL with fit parameters $\gamma = -2.703\ ^{+0.005}_{-0.006}\ (stat)\ ^{+0.032}_{-0.009}\ (syst)$, $\Delta\gamma = 0.25\ ^{+0.02}_{-0.01}\ (stat)\ ^{+0.02}_{-0.03}\ (syst)$, $E_0 = 1319\ ^{+113}_{-93}\ (stat)\ ^{+267}_{-124}\ (syst)$ GeV, $\Delta\gamma_1 = -0.22\ ^{+0.07}_{-0.10}\ (stat)\ ^{+0.12}_{-0.09}\ (syst)$, $E_1 = 33.2\ ^{+9.8}_{-6.2}\ (stat)\ ^{+5.8}_{-5.3}\ (syst)$ TeV. However, the high-energy region of the spectra, from tens to hundreds of TeV, still suffers from significant uncertainties, mainly due to the very limited statistics. Therefore, an independent helium analysis using machine-learning (ML) techniques, has been investigated by the author of this work, with the aim of improving the present helium measurement. This analysis, developed first in the fiducial acceptance `A1` and then in the extended acceptances `K1` and `K3`, will be the subject of this thesis.

Chapter 3

Event Analysis

This chapter outlines the event reconstruction procedure for both *in-flight* and simulated data. For each event, such procedure provides the track, the energy deposited in the calorimeter, and the charge estimators for particle identification. The first step of the analysis, the pre-selection, is also explained. In particular, this set of selection criteria ensures a well-reconstructed sample of events for use in the following stages of the analysis.

3.1 Dataset and Live Time

The scientific analysis of CALET data is performed by using the same workflow (event reconstruction, selection, *etc.*) both for *in-flight* data and simulated data.

Flight Data (FD)

In the analysis of this work, the total observation time of CALET experiment is 2637 days, from October 13^{th}, 2015 to December 31^{th}, 2022. The *live time*, fraction to the total observation time is about 85%, confirming the smooth operation of the instrument and the quick recoveries of any issues which have been experienced while collecting data. It corresponds to 1.74×10^8 seconds, as shown in Fig. 3.1.

Simulated Data (MC)

Monte-Carlo simulations are crucial for analysing cosmic-rays CALET data, as they are involved in key steps, such as the evaluation of efficiencies, the unfolding matrix for primary energy recovery, different background contributions, *etc.*

In the analysis of this work, MC simulations were performed with the `EPICS` [93] package for both helium and proton particles. A detailed CAD-based modeling of the CALET instrument was developed and integrated into the simulation package. The helium and proton samples were isotropically generated from the surface of a sphere with radius 78 cm and centered at $z = 25$ cm with `EPICS` and `COSMOS` [114]. DPMJET-III [112] was adopted as the hadron interaction model. Both types of particles were simulated in decades of energy according to a single power law E^{δ}, where the power-law

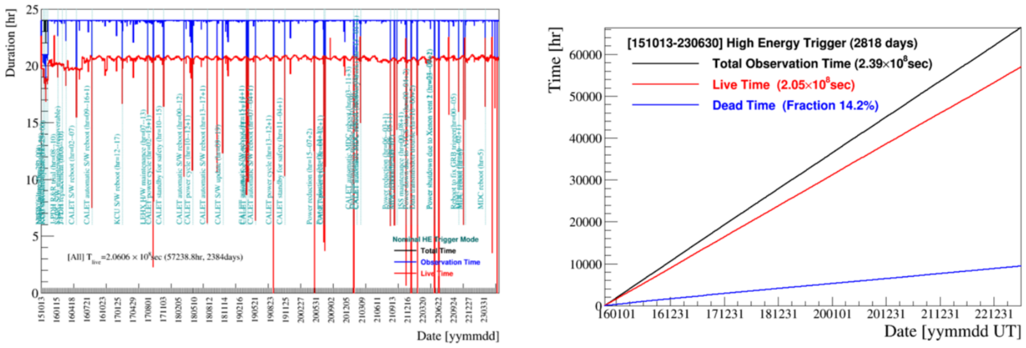

FIGURE 3.1: (Left) Daily and (Right) accumulated observation time of CALET experiment on ISS from October 13^{th}, 2015 to December 31^{th}, 2022. The total, observation and live times are represented in black, blue and red, respectively. Figures taken from [126].

index is $\delta = -1$ from 2 GeV to 20 TeV, and $\delta = -2.5$ from 20 TeV to 1 PeV. In the former case, the total number of events generated per decade are 3×10^8 (proton) and 2.5×10^8 (helium). In the latter case 8.7×10^7 (proton) and 4.3×10^7 (helium) events. A summary of the MC samples that were used in this analysis is given in Table 3.1.

Particle	Kin.Energy [GeV]	Spectrum	Events
p	[2, 20]	E^{-1}	3×10^8
p	[20, 200]	E^{-1}	3×10^8
p	[200, 2 $\times 10^3$]	E^{-1}	3×10^8
p	[2 $\times 10^3$, 20 $\times 10^3$]	E^{-1}	3×10^8
p	[20 $\times 10^3$, 1 $\times 10^6$]	$E^{-2.5}$	8.7×10^7
^{4}He	[2, 20]	E^{-1}	2.5×10^8
^{4}He	[20, 200]	E^{-1}	2.5×10^8
^{4}He	[200, 2 $\times 10^3$]	E^{-1}	2.5×10^8
^{4}He	[2 $\times 10^3$, 20 $\times 10^3$]	E^{-1}	2.5×10^8
^{4}He	[20 $\times 10^3$, 1 $\times 10^6$]	$E^{-2.5}$	4.3×10^7

TABLE 3.1: Summary of the EPICS-based simulated data used in the analysis of this work.

Re-weighting Since the proton and helium spectra are generated according to a single power law of kinetic energy, the MC data have been re-weighted to follow a profile based on the results of previous experiments. The reference re-weighting reproduces the behaviour of a combined fit with a special broken power law to the AMS-02 [23, 24] and CREAM-I [138] data. The fit

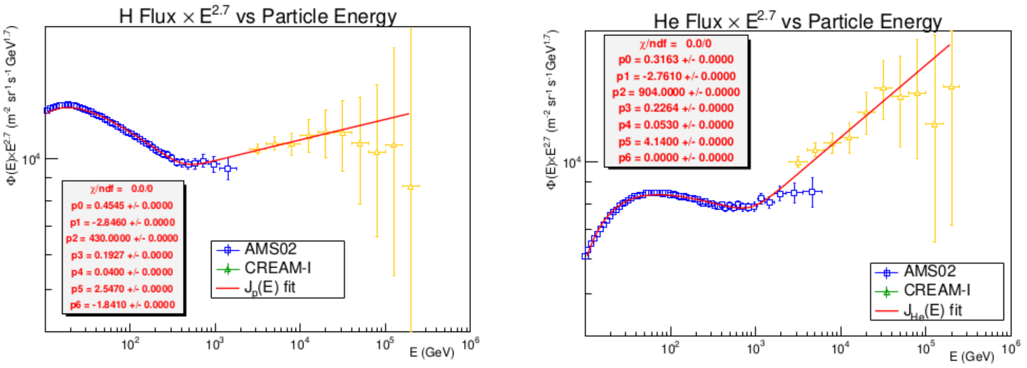

FIGURE 3.2: (Left) Proton $J_p(E)$ and (Right) Helium $J_{He}(E)$ profiles obtained via the fit of the AMS-02 [23, 24] and CREAM-I [138] data.

function is

$$J_k(E) = p_0 \left(\frac{E}{45\,\text{GeV}}\right)^{p_1} \left[1 + \left(\frac{E}{p_2}\right)^{\frac{p_3}{p_4}}\right]^{p_4} \left(1 - \frac{p_5}{E} - \frac{p_6}{E^2}\right) \qquad \text{with} \quad k = p, He$$

The fit results are shown in the Fig. 3.2 and summarized in table 3.2. The weight w is computed for each MC event as follows

$$w = \frac{J_k(E)}{E^{-1}} \frac{E_0^{-1}}{J_k(E_0)} \qquad \text{with} \quad k = p, He$$

in which E_0 is the lower bound of the energy range of MC event generation.

Parameter	Proton $J_p(E)$	Helium $J_{He}(E)$
p_0	0.454	0.316
p_1	-2.846	-2.761
p_2 [GeV]	430.0	904.0
p_3	0.193	0.226
p_4	0.040	0.053
p_5 [GeV]	2.547	4.140
p_6 [GeV^2]	-1.841	0

TABLE 3.2: Fit parameters for the re-weighting functions $J_p(E)$, $J_{He}(E)$.

Furthermore, alternative re-weighting following a single power laws with different spectral indices were also considered to evaluate the systematics of the re-weighting procedure, as discussed in section 6.3.2.

Absolute normalization In order to make a comparison between simulated and FD distributions, an overall scaling factor $\mathcal{N}$ is required to adjust MC event normalization. These factors (for proton and helium) are estimated as follows

$$\mathcal{N}_k = \frac{S\Omega_0 \times T}{N_{MC}} \int_{\mathrm{E}_0}^{\mathrm{E}_{\mathrm{max}}} J_k(E)\, dE \qquad \text{with} \quad k = \mathrm{p, He}$$

where:

- $S\Omega_0$ is the fiducial geometrical acceptance.
- T represents the live-time of FD sample under analysis.
- N_{MC} are the number of events simulated in the energy range $[\mathrm{E}_0, \mathrm{E}_{\mathrm{max}}]$.

It is worth pointing out that this scaling factor is used only for visualization purpose, when comparing MC and FD samples. In fact, the analysis for helium flux measurement is completely independent on the N_{MC} factor.

3.2 Helium Event Reconstruction

3.2.1 Tracking

A reliable and efficient track (and vertex) reconstruction algorithm is essential to maximize the performance of CALET experiment, ensuring high-quality data. In fact, tracking is leveraged to establish the acceptance category (*i.e.* the topology of the event), but also to identify CHD paddles and IMC fibers crossed[1] by the incoming CR particle. In addition, it enables the evaluation of the TASC-based topological variables, such as the lateral width of the shower. Thus, an original[2] reconstruction technique has been implemented based on combinatorial Kalman filter algorithm [78, 120]. This method takes advantage of the high IMC segmentation to address the challenging task of finding the primary track among the plethora of shower-originated secondaries. A detailed discussion of the current implementation can be found in Refs. [49, 51, 100] and summarized briefly in the next paragraphs, following the treatment described in Ref. [100].

Algorithm

The track search problem in CALET can be simplified by reducing it into two independent two-dimensional problems in XZ and YZ views, respectively. The top IMC layer is the starting point for track search. Initially, the neighbouring fired[3] fibers (“hits") in each IMC layer are clustered. Their positions[4] with their related uncertainties, are regarded as possible candidate track points in the combinatorial Kalman filter algorithm.

---

[1] This information is employed for the construction of charge estimators, as discussed in the subsection 3.2.2, as well as for the identification of the first interaction point.

[2] As reported in Ref. [100], the combinatorial Kalman filter algorithm for track and vertex reconstruction is “widely used in high- energy experiments at the accelerators, but not applied so far in a calorimetric CR experiment".

[3] A threshold sufficiently higher than electronic noise is set.

[4] These are obtained by calculating the center of gravity of the fibers belonging to the cluster.

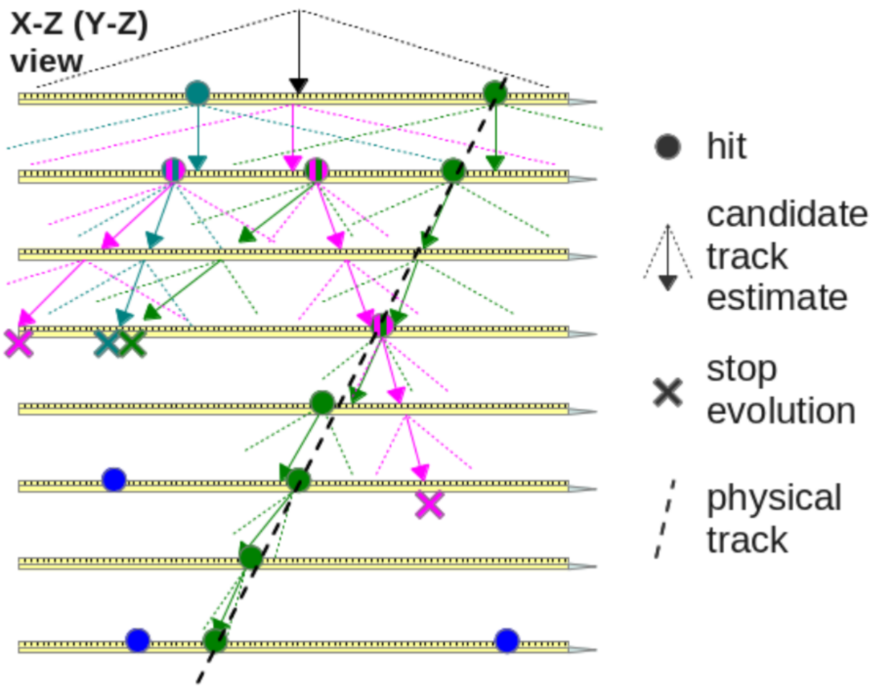

FIGURE 3.3: Simplified schematic of the track reconstruction based on combinatorial KF algorithm. Figure taken from Ref. [49].

Afterwards, the first set of candidate tracks is estimated from each possible combination of clusters in the first two layers by fitting with a straight line. Each candidate track is then developed in its own way such that at the next layer, the direction and position are uniquely determined by the previous state. Namely, its incident angle and its impact point on the next layer $k+1$ are estimated using only the information from the previous layer k. Now, in the combinatorial Kalman filter, a new candidate track is generated and propagated independently for each cluster on the k+1 layer that is, within error, close to the predicted state. As a result, this procedure can be computationally time-consuming since exponential growth in the number of candidate tracks can occur in each new iteration. Therefore, some stopping criteria are needed to terminate the evolution of unlikely candidate tracks on a layer-by-layer basis. Specifically, the current implementation requires that the χ^2/NDF, resulting from the residuals of the KF estimate with respect to the true cluster position, must be less than an user-defined threshold (usually < 10) and the number of missing consecutive hits is smaller or equal to 2. In the case of high-energy events, the strategy to reduce the number of candidate tracks is based on the definition of a region of interest (ROI) in the IMC where only clusters belonging to it are selected. This ROI is constructed using the TASC-based shower axis, with further optimization depending on the topology of the event in the IMC, as described in Ref. [100].

Then, for candidate tracks reaching the last point, the estimation of the angle of incidence and the point of impact on the first layer is performed by the so-called *smoothing* procedure, *i.e.* back-propagating the information obtained from the complete set of measurements. In the ensemble of tracks that reach the last layer, two complementary categories can be recognized: *equivalent* and *non-equivalent* tracks. Two tracks are *equivalent* if they are associated to the same hit for each IMC layer, except in the ones where the track has missing hit. From the set of *equivalent* tracks, the one with the lowest χ^2 is considered. Lastly, the *non-equivalent* track that have the best match with the TASC shower core is selected as the track of the primary particle.

A simplified schematic of this reconstruction procedure is shown in Fig. 3.3.

Performance

Tha KF track fitting has been in-depth investigated and tuned based on different MC samples as discussed in Refs. [51, 100]. An evaluation of the tracking performance has been carried out by selecting high-energy triggered (HET) events reconstructed in acceptance `A` from EPICS-based simulated helium sample. The angular resolution is estimated as the difference between the incident angle $\theta_{x,y}^{reco}$ reconstructed by the KF algorithm and the the true MC angle $\theta_{x,y}^{reco}$ in which the simulated event was generated. Angular resolution of 0.13° is achieved for both views, as shown in Fig. 3.4 for X view.

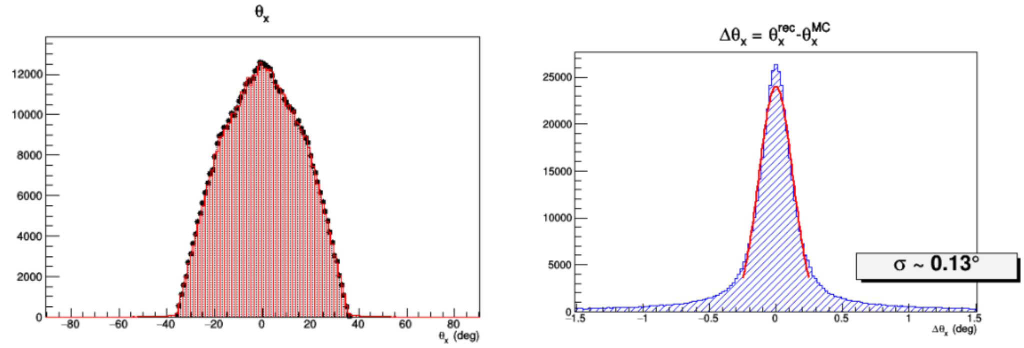

FIGURE 3.4: (*Left*) Reconstructed incident angle in XZ view (red) superimposed to the related true distribution (black dots) of MC generated angles.(*Right*) Residuals between the MC generated and the reconstructed angle in XZ view. The angular resolution is taken from the width of the peak fitted with a Gaussian function.

Similarly, the spatial resolution is derived from the distribution of the residuals for y (and x) coordinate of the impact point on the top of the CHD. Specifically, the difference between the reconstructed position y_0^{reco} (and x_0^{reco}) and the actually generated MC position y_0^{MC} (and x_0^{MC}). The resolution, obtained from the width of the Gaussian fit, is 414 (and 404) μm for the Y (and X) view, as shown in Fig 3.5.

Although the KF algorithm provides good performance, failure to reconstruct the primary track projection in a view can occasionally occur. In this case, the incorrect reconstruction of the event topology is due, in most cases,

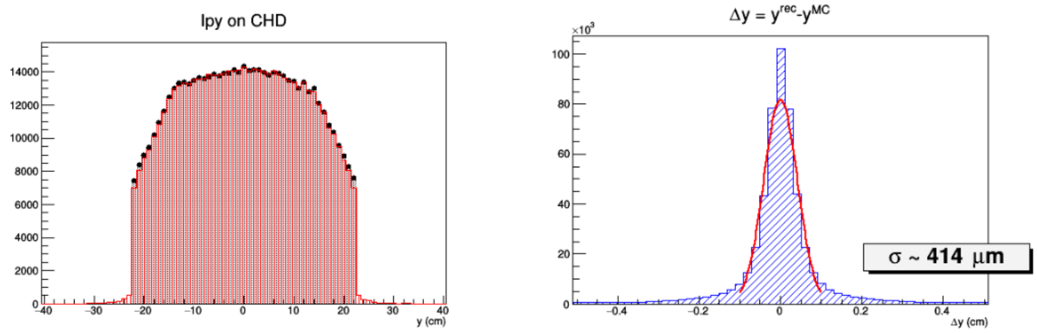

FIGURE 3.5: (*Left*) Reconstructed impact point on top of CHD in y coordinate (red) superimposed to the true distribution (black dots) of the same MC generated position.(*Right*) Residuals between the MC generated and the reconstructed y coordinate. The spatial resolution is taken from the width of the peak fitted with a Gaussian function.

to the track of a secondary particle being misidentified as a primary trajectory. As a result, this can lead to the incorrect classification of the primary particle charge, and the acceptance category.

Figure 3.6 shows an example taken from FD. This event is categorized as acceptance `A1`, due to misidentification of the near horizontal shower in the YZ view. In addition, the erroneous reconstruction of the primary track leads to the misassociation of the hits belonging to it in the IMC and the CHD, and consequently to a wrong reconstruction of the charge.

This kind of events contribute to the so-called *off-acceptance* background that depends on the energy of the incoming particle. It is greater in the low-energy region, *i.e.* below 100 GeV, because the weak development of the shower in the TASC makes difficult to identify correctly the primary particle and the ROI for KF tracking. Then, it decreases with increasing energy up to few TeV of particle energy, and finally, increases again due to the proliferation of back-scattered particles in the IMC, which progressively enhances the complexity of track finding problem. In this work, a strategy based on a machine-learning approach was studied to improve the rejection of such background after the KF tracking, as discussed extensively in the first part of the next Chapter 4.

3.2.2 Charge estimators

Measurement of the charge (Z) of the incident CR particle is based on the ionization energy losses in both the CHD layers, and multiple independent $\frac{dE}{dx}$ samplings in the different scintillating fiber layers of the IMC. The energy deposits are corrected according to the path length travelled by the incoming particle through the scintillating material, either paddles (CHD) or fibers (IMC). The correction factor is proportional to $\cos(\theta)$, where θ is the angle between the instrument axis (z axis) and the reconstructed trajectory of the particle.

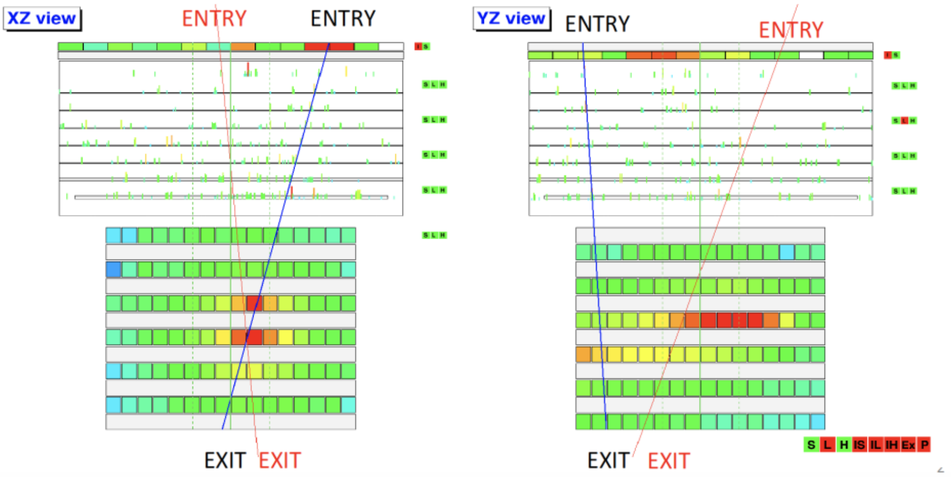

FIGURE 3.6: Event from *in-flight* data that is categorized as `A1` acceptance by the KF reconstruction algorithm, but actually belongs to the *off-acceptance* background since it is generated by a nearly horizontal shower. This is clearly visible in the YZ view on the right-hand figure. In addition, the reconstructed KF track (blue line) and shower axis (red line) differ in both entry and exit points.

CHD-based estimator

A CHD-based charge estimator is obtained combining the two independent $\frac{dE}{dx}$ measurements: one from the top layer (CHD-X) and one from the bottom layer (CHD-Y). The crossed paddles are determined from the reconstructed trajectory. Then the MIP charge is converted into the raw charge Z_{CHD}^{RAW} via the fitted Tarlé functions which are described in section 2.2.1. It is worth mentioning that the number of photoelectrons produced by a MIP in a single paddle is generally large ($>$ 100) and therefore fluctuations are negligible. Lastly, the single estimator Z_{CHD}^{RAW} is constructed as the average of the two estimators in view X and Y.

IMC-based estimator

In contrast to the CHD-based charge measurement, the building of IMC charge estimator Z_{IMC} can rely on several $\frac{dE}{dx}$ samples collected from the 16 layers of scintillating fibers. Nevertheless, there are two additional challenging issues: the limited photo-electron statistics of the individual IMC fibers and the identification of the interaction point (IP) at which the incoming particle starts showering. The former is $\sim 7-8$ photo-electron per MIP, *i.e.* about one order of magnitude lower than the case of 1 cm thick CHD paddle. The latter is due to the probability of IP occurring within the IMC. This is enhanced by the tungsten absorbers interposed between alternating scintillating fibers layer, especially the last two thick plates. Therefore, only the first 12 scintillating fibers layers above the thick absorbers are used. Listed below are summarized the steps to construct the Z_{IMC} estimator:

- The interaction point is localized by an application-specific IP reconstruction algorithm, as discussed extensively in Refs. [49, 51]. The main idea is to look for an abrupt increase of the energy deposits along the track. This point, beyond which the particle can no longer be considered a MIP, is defined as the IP.
- The average $\frac{dE}{dx}$ is calculated for each layer upstream the reconstructed IP.
- The *raw* charge Z_{IMC}^{RAW} is estimated by means of a *trimmed-mean*, with 30% truncation level. A minimum sample of 4 points is required.
- The MIP average energy deposit is converted via the Voltz-II parametrisation (see section 2.2.2) into the Z_{IMC}^{RAW} .

Back-scattering corrections

The raw charge estimators Z_{CHD}^{RAW} and Z_{IMC}^{RAW} are found to be energy dependent, due to the amount of back-scattered particle that affects the charge measurement and increases with energy. A correction is applied to restore the proton and helium peaks to the nominal value $Z = 1$ and $Z = 2$ regardless of primary particle energy. The following energy-dependent correction functions are used.

$$Z_{\mathrm{CHD}} = a(E) \times [Z_{CHD}^{RAW}]^{b(E)} \tag{3.1}$$

$$Z_{\mathrm{IMC}} = c(E) \times [Z_{IMC}^{RAW}]^{d(E)} \tag{3.2}$$

Specifically, the energy range is divided into five bin per decade, and the relative peak positions of Z_{CHD}^{RAW} and Z_{IMC}^{RAW} , are extracted from each distribution. Then, the value of a, b, c, d parameters[5] is calculated (simultaneously for proton and helium) for each energy bin and are fitted with specific poly-logarithmic functions to obtain the correction on an event-by-event basis. Specifically, the energy range is divided into five bin per decade, and the relative peak positions are extracted from each distribution. In Fig. 3.7, the proton and helium IMC-based and CHD-based charge peaks with respect to the total energy deposited in TASC are shown for FD (left panel) and EPICS (right panel), before and after this correction.

Since this procedure only corrects the positions of the proton and helium peaks, residual discrepancies are observed after this calibration between the widths of the FD charge distributions and the MC distributions. Therefore, an additional *fine-tuning* of the shape of the MC distributions is needed, to correctly reproduce the FD, this procedure is described in the section 4.2.

---

[5] Since the values of a, b, c, d are expected to be ~ 1 in the ideal case, the deviation from this reference value can be regarded as the contribution of back-scattered particles.

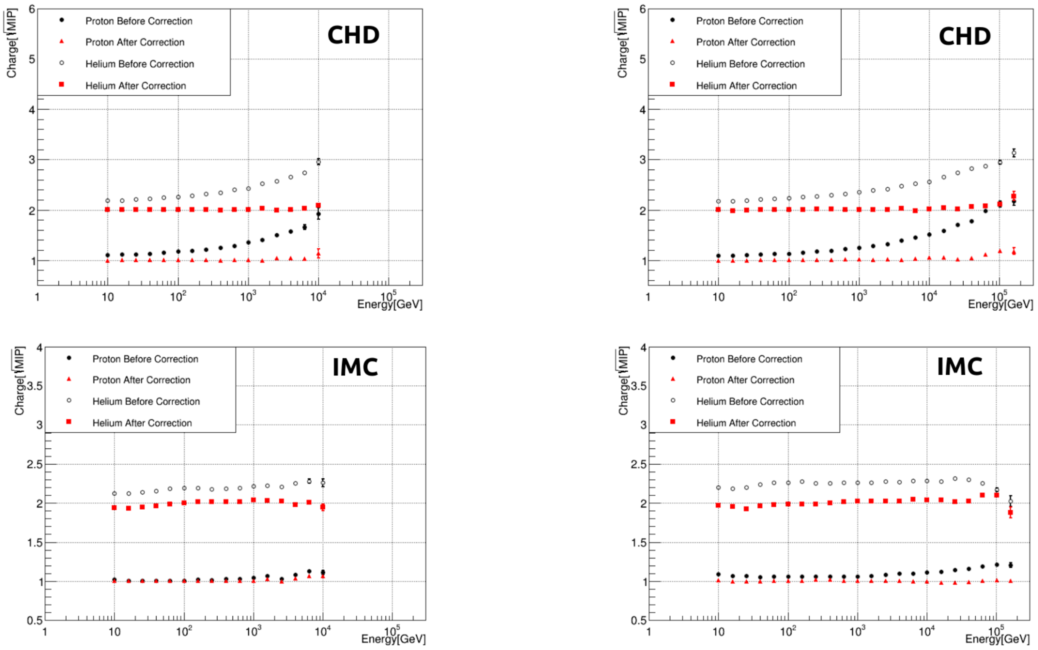

FIGURE 3.7: Energy dependence of CHD-based and IMC-based raw charges. The panel on the left-hand (right-hand) side represents FD (EPICS) results. Black filled (open) circle are protons (helium) before correction. Instead, red filled triangle (square) encodes proton (helium) after correction.

3.2.3 Deposited energy reconstruction

The TASC allows the measurement of the electromagnetic shower core initiated by CR hadrons interacting in its first layers or upstream (in the IMC). The deposited energy in the calorimeter is almost linearly proportional to the primary energy of the incoming particle. This permits its recovery (on average), although there are large fluctuations from event-to-event. As a result, the performance in terms of energy resolution is inferior compared with that of hadron calorimeters designed for accelerator experiments[6] due to the limited thickness of space-based calorimeters. Nevertheless, it is sufficient for reconstructing the steep energy spectrum of CR nuclei with a resolution that is almost independent on the primary energy.

In this analysis, the total energy deposited in the TASC is defined as the sum of all log signals above a 0.2 MIP[7] threshold. The logs #11,#12 and #13 of the TASC layer #9 are excluded from the sum, since their response is not fully stable over the entire observation time. Moreover, the TASC logs signals are extensively calibrated and corrected, as discussed in Refs. [32, 104].

Test-beam additional calibrations Since the data analysis of CERN-SPS test-beam campaign [27, 108, 127] using the CALET structural thermal model [28, 128] has shown some discrepancies between observed energy deposits and

---

[6] A review can be found in Ref. [74].

[7] In TASC the unitary MIP corresponds to 20.47 MeV.

MC simulated ones, a shower energy correction (SEC) factor is introduced to finely tune the energy response. The SEC is evaluated by making use of the results from beam tests performed during the 2015 campaign with ion beams of the 13, 19, and 150 GeV/n. Table 3.3 summarizes the results achieved with a dedicated data analysis.

Beam Energy (GeV/c)	Shower Energy Correction
52	0.896 ± 0.034
76	0.920 ± 0.025
600	0.968 ± 0.020

TABLE 3.3: Shower energy (SEC) corrections for helium derived from the data analysis of CERN-SPS 2015 beam test results.

The MC shower energy is fine-tuned scaling the total energy with an energy-dependent correction factor (CF) on event-by-event basis. Specifically, CF is set to 0.896 below 52 GeV, and to 0.968 above 600 GeV. In the middle, an energy-dependent CF is used instead. This is obtained by interpolating each pairs of CFs with a first-order logarithmic polynomial. In addition, SEC is also required for the proton sample since it is used to estimate the contaminations. The CFs for protons are taken from the Ref. [9], estimated from the analysis of the 2012 test beam campaign at CERN [28, 43].

The beam-test results were fitted with different interpolation functions, also called *models*, to evaluate the systematic errors of this energy scale correction. The structure of these models and how they contribute to the flux estimate are discussed in detail in section 6.3.1.

Using the same data-set from test beams, the consistency of trigger efficiencies with MC results is also tested. The trigger efficiencies are found to be in agreement (within the uncertainties) with the ones from MC simulations, thus no corrections are applied in MC data.

3.3 Pre-selection

As a first step, helium analysis begins with what is known as pre-selection, a set of criteria used to obtain a well-reconstructed sample of events [8, 101]. The main objective is to discard the vast majority of background events belonging to FD that are not simulated or that are not in the interest of this analysis. In this way, two equivalent event samples are obtained for real and simulated data. These are used in the next steps of the analysis, namely the rejection of the residual off-acceptance events and the charge identification. Briefly, the pre-selection is realized by applying, in sequence: the *off-line trigger* validation, *track quality* cut, *geometric conditions* (acceptance classification) and *electron rejection* cut. A detailed discussion follows in the next subsections.

3.3.1 Off-line Trigger Validation

The CALET hardware trigger for high-energy (HE) particles requires large energy deposits in the first TASC layer and in the last four IMC layers. The on-board HE trigger is affected by the variations of detector gain with respect to temperature, position and time. Hence, an off-line trigger has been implemented to address this issue. This trigger validation requires tighter thresholds than the on-board trigger. Specifically, it requires that the energy deposit sums of IMC layers X7,Y7 and X8,Y8 are greater than 50 MIP[8]. Then, it demands that the energy deposit on the first layer(X1) of TASC is higher than 100 MIP.

For helium nuclei, these conditions reject non interacting events, and ensures that the selected ones interact in the first part of the instrument. A more detailed discussion regarding this efficiency and the evaluation of systematic errors made by imposing these thresholds can be found in the sections 4.5 and 6.2.

3.3.2 Track quality criteria

In order to ensure the selection of high-quality sample of candidates, the events must be successfully traced by the combinatorial Kalman filter in both X and Y views of the IMC detector. The so-called `FitFlag` f_{KF} encodes the information on how the track is reconstructed in both views. Table 3.4 summarizes the associated condition for each possible f_{KF} values. The tightest condition is $f_{\mathrm{KF}} = 3$ that ensures the cleanest sample. For helium analysis, the KF tracking performs with high-efficiency and, therefore, this stringent condition is not critical, in most of the energy range. Hence, the condition $f_{\mathrm{KF}} = 3$ is used in the analysis presented in this work, whereas the looser criterion $f_{\mathrm{KF}} = 3||6||9||12$ is studied for the assessment of the related systematics uncertainties, as discussed in subsection 6.2. However, it is worth pointing out that the `FitFlag` criteria do not completely suppress the *off-acceptance*

`Fit Flag` (IMC)	X-Z view	Y-Z view
3	KF	KF
6	*Shower* fit	KF
9	KF	*Shower fit*
12	*Shower fit*	*Shower fit*

TABLE 3.4: Summary of the track quality criteria labelled as `FitFlag` . In a given detector view, the acronym KF stands for performing the fit using IMC hits selected by the combinatorial Kalman filter, whereas *Shower fit* means only a fit of the shower axis in the TASC detector if the KF algorithm fails the reconstruction.

---

[8] One MIP corresponds to energy deposit of minimum ionizing vertical muons at 2 GeV, *i.e.* 1.66 MeV for CHD paddle, 0.145 MeV for IMC fiber and 20.47 MeV for TASC log.

background, *i.e* the occasional misidentification of a secondary track as the trajectory of the primary particle. Therefore, the rejection of this background component is still a critical task, and the strategy designed to mitigate it, is explained in chapter 4.

3.3.3 Geometric Requirements

Each events is classified into one of the so-called *acceptances*, which differ in their geometric requirements. All possible acceptances are described in the section 2.4, together with the descriptions of their corresponding fiducial volumes. In the case of `A1` acceptance, the reconstructed track must cross the entire detector, from the top of the CHD to the bottom of the TASC, with a 2 cm margin from the edge of the TASC first layer. A schematic of the `A1` fiducial volume is illustrated in Fig. 2.15. This configuration provides a *geometric factor* $S\Omega_{\mathrm{A1}}$ equal to 510 cm^2 sr which is about 49% of the total geometric factor $S\Omega_{\mathrm{TOT}}$ of the CALET instrument. Acceptance `A1` is the acceptance configuration considered in the Chapter 4 and currently used in the standard helium analysis.

3.3.4 Electron Rejection

Electron are much less abundant that helium nuclei in the CRs, nevertheless at low energies they can contribute to the helium flux contamination. Aiming at rejecting the contamination from CR electron, an empirical Moliere-like concentration ρ_M is defined as follows. For each IMC layer crossed by the track, the sum of all energy deposits within a Moliere radius, defined as ± 9 scintillating fibers, of each fiber matching the track is calculated. This sum is then divided by the total sum of energy deposits in the IMC. At the same time, by requiring this concentration to be less than 0.75 and the fraction of energy deposited in the last TASC layer to be larger than 1%, more than 90% of electrons are discarded while maintaining a very high efficiency for helium nuclei ($>$ 99.9% above 60 GeV of kinetic particle energy) as shown in subsection 4.5.

Chapter 4

Improving the measurement of helium flux with a machine-learning technique

The main objective of this work is to improve the accuracy of helium flux measurements at high-energies, which is crucial for understanding the mechanisms of CR acceleration and propagation. This chapter is therefore dedicated to the newly improved analysis using a machine-learning (ML) technique, that I have developed for this purpose.

The first part of this chapter is a detailed description of the new ML selections based on Boosted Decision Trees (BDT) to enhance the quality of the helium sample candidates. This approach has been studied with the aim of broadening the fiducial acceptance, and thus the statistics, that is the most relevant limiting factor to further extend the helium flux measurement to higher energies. In fact, selections that depend on the topology of the event are essential to avoid the inflation of the *off-acceptance* background when using extended acceptances.

Next, the charge identification and unfolding procedure to infer the primary energy, from the fraction of energy deposited in the calorimeter, are explained. For the latter, two different approaches have been investigated: the Bayesian iterative approach and the SVD-based approach. In both cases, the stability of the unfolding procedure and its bias-variance trade-off have been then validated both with simulated and *in-flight* data. In addition, the statistical uncertainty of this procedure has been evaluated via the *bootstrap* method. Finally, a preliminary measurement of helium flux in the fiducial acceptance is provided.

4.1 ML-based selections

During the reconstruction of an event, the tracking algorithm may occasionally fail to identify the primary track, leading to an incorrect classification of the acceptance. This class of events belongs to the so-called *off-acceptance background*, which is particularly critical at low and very high energies. Thus, additional selections are required to reduce this background.

A strategy to reject it with high efficiency, especially at low energies, is described in Ref. [8]. In order to go beyond that result, a ML approach has been adopted in this work. The choice of ML algorithm fell on Boosted Decision Trees (BDT) as[1] in the CALET electron analysis [13, 15, 41]. This approach has also been studied with the aim of extending the fiducial acceptance since selections that depend on the topology of the event, are crucial to avoid the inflation of the *off-acceptance* background when using extended acceptances.

As a first step, the size and composition of the *off-acceptance* background has been characterized for `A1` acceptance, as shown in Fig. 4.1. These events can be divided into two groups. The first consists of events whose original trajectory belongs to one of the acceptance categories described in the section 2.4. The second category is made by events that are not comprised in any of the already defined acceptances, and it can be further split into two classes. One is $\mathtt{J}_i$ type events, *i.e.* those in which the true track has the same shape as $\mathtt{D}_i$ but traverses less than ~ 27 cm in the TASC. The other is type `0` events, *i.e.* all those that do not fit into the previous categories. These consist mainly of events that cross the TASC laterally.

The main source is from acceptance `0` events, followed by the `J0` and `D0` events, which collectively account for 85% of this background, as can be seen from the table 4.1. Then, the input variables were selected, as described in the following section 4.1.1.

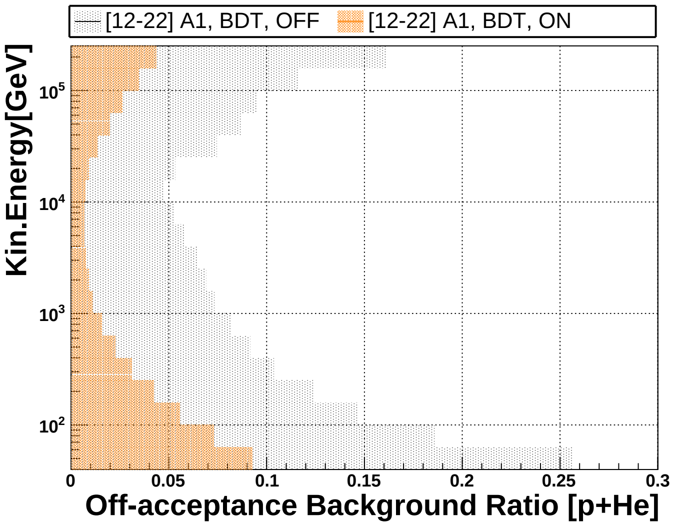

FIGURE 4.1: Comparison between off-acceptance background ratio from EPICS simulated data (proton and helium samples), with and without BDT-based selections.

4.1.1 Feature selection

The selection of the input variables, also referred to as[2] *feature selection*, is crucial, for the reliability and performance optimization of the ML algorithm.

---

[1] In the study of Ref. [52] for CALET electron analysis, the BDT technique has been demonstrated to perform best against a variety of ML algorithms based on artificial neural networks.

[2] This is the terminology mostly used in machine-learning context.

Off-Acceptance Type	0	D_0	J_0	others
sum [%]	51	8	26	15
proton [%]	27	1	5	6
helium [%]	24	7	21	9

TABLE 4.1: Off-acceptance background breakdown for acceptance `A1`.

After an extensive test campaign, 13 variables were selected for the analysis of this work. As reported in Ref. [101], these can be grouped into two categories, as follows.

- Energy deposition profile, based on the fraction of energy deposited on each TASC layer. All layers, except the 2nd, 3rd and 4th, have been used.
- Topological variables built from the difference between the track reconstructed with combinatorial Kalman filter and with the method of moments [82]. The former mainly exploits the information provided by the IMC sub-system, whereas the latter leverages on TASC segmentation. In detail, Δ^X_{TK} and Δ^Y_{TK} defined as the difference between position in X and Y coordinates of the impact point on the first TASC layer, and Θ^X_{TK} and Θ^Y_{TK}, defined as the difference between the reconstructed angle of the tracks in X and Y views respectively, have been selected.

Topological variables

The first step consists of scrutinizing the signal-to-background separation capability of the the topological variables (Θ^X_{TK} , Θ^Y_{TK} , Δ^X_{TK} , Δ^Y_{TK}). The type `0` events are considered as background. In the Fig. 4.2 the results for Θ^X_{TK}, Θ^Y_{TK} (top half) and Δ^X_{TK} , Δ^Y_{TK} (bottom half) for several TASC deposited energy bins, ranging from 7.5 GeV up to 300 TeV, is shown. The MC distributions are based on EPICS simulated data both for helium and for proton samples.

Next, the consistency between the simulated distributions and those from the data has been checked.This was done by requiring the existence of all charge estimators (*i.e.* charge greater than zero) and by using the preselection described in the previous section. In the Figs. 4.3 and 4.4 the comparisons of Θ^X_{TK} , Θ^Y_{TK} and Δ^X_{TK} , Δ^Y_{TK} distributions from *in-flight* data and EPICS simulations are shown for several TASC deposited energy bins ranging from 7.5 GeV up to 300 TeV. The agreement between data and simulations is good over the entire energy range, as shown by the almost perfect overlap of the two corresponding cumulative curves.

Energy deposition profile

Similarly, for the energy deposition profile, the most significant layers were first examined for their signal-to-background separation capability. Again, the background consists of type `0` off-acceptance events.

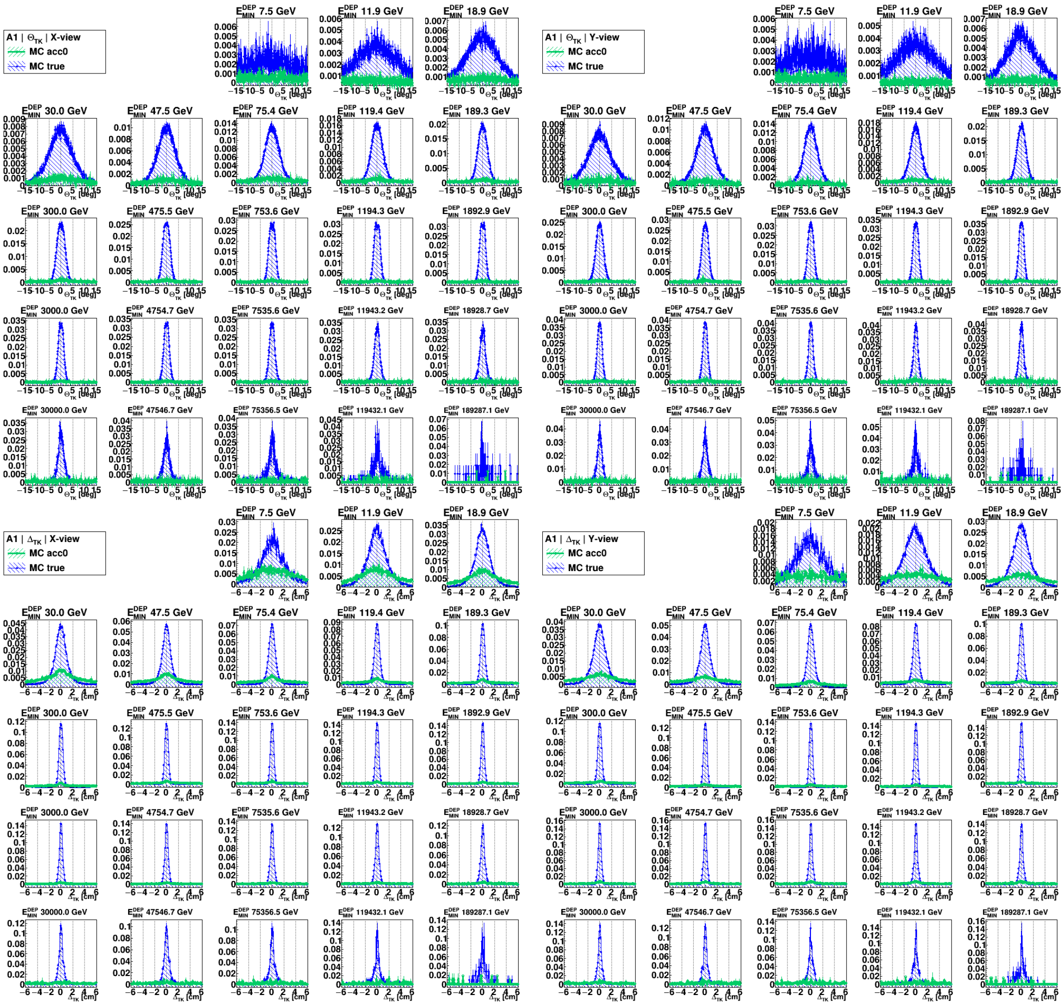

FIGURE 4.2: Signal-to-background separation for Θ^{X}_{TK} , Θ^{Y}_{TK} (top half) and Δ^{X}_{TK} , Δ^{Y}_{TK} (bottom half) based on EPICS simulated data for several TASC deposited energy bins ranging from 7.5 GeV up to 300 TeV.

In the Fig. 4.5, the signal-to-background separations for the fraction of energy deposited in the *first* (X1), the *last* (Y6) and two adjacent intermediate (X4 and Y4) layers, are shown. The simulated distributions are derived from EPICS including both helium and proton samples. The distributions are presented for several energy bins, ranging from 7.5 GeV up to 300 TeV of deposited energy.

It is worth pointing out that the fraction of energy deposited in the:

- First layer (X1), allows good signal-to-background separation in the low energy region, while its contribution is negligible at high-energy.
- Intermediate layers (X4 and Y4), allow fairly good rejection of the background in high-energy range.
- Last layer(Y6), permits discrimination of signal events from background events over the entire energy range.

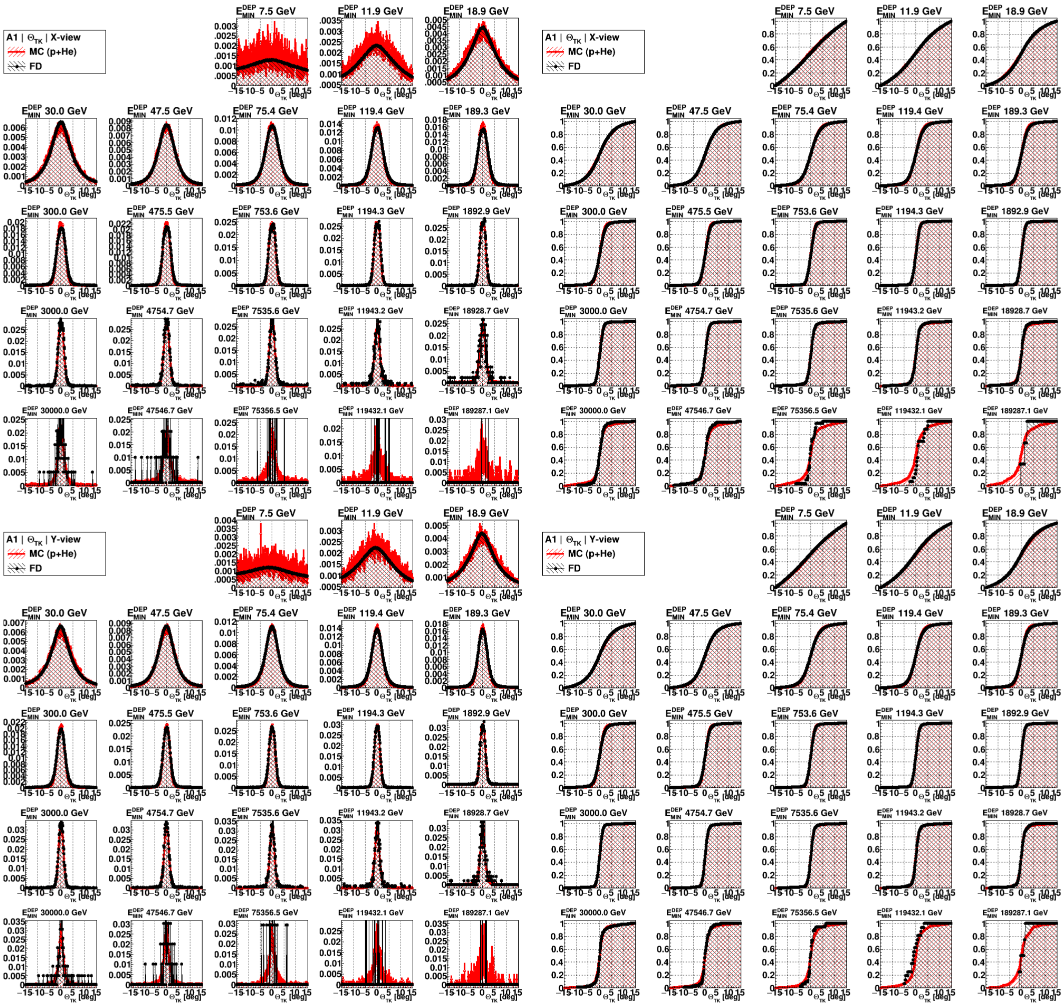

FIGURE 4.3: (Left) Comparison of Θ^{X}_{TK} (top half) and Θ^{Y}_{TK} (bottom half) distributions from *in-flight* data and EPICS simulated data for several TASC deposited energy bins ranging from 7.5 GeV up to 300 TeV. (Right) The cumulative of the distributions are illustrated in the left column.

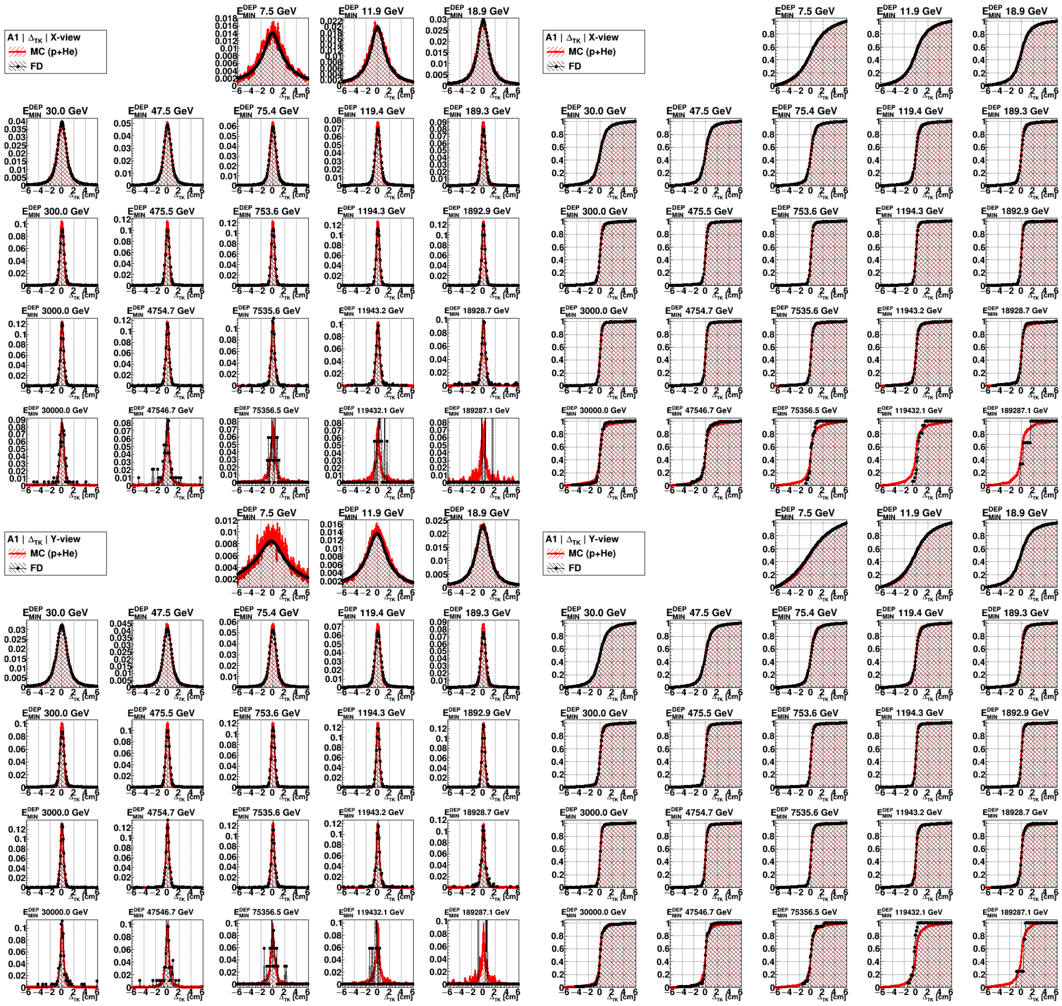

FIGURE 4.4: (Left) Comparison of Δ^X_{TK} (top half) and Δ^Y_{TK} (bottom half) distributions from *in-flight* data and EPICS simulated data for several TASC deposited energy bins ranging from 7.5 GeV up to 300 TeV. (Right) The cumulative of the distributions are illustrated in the left column.

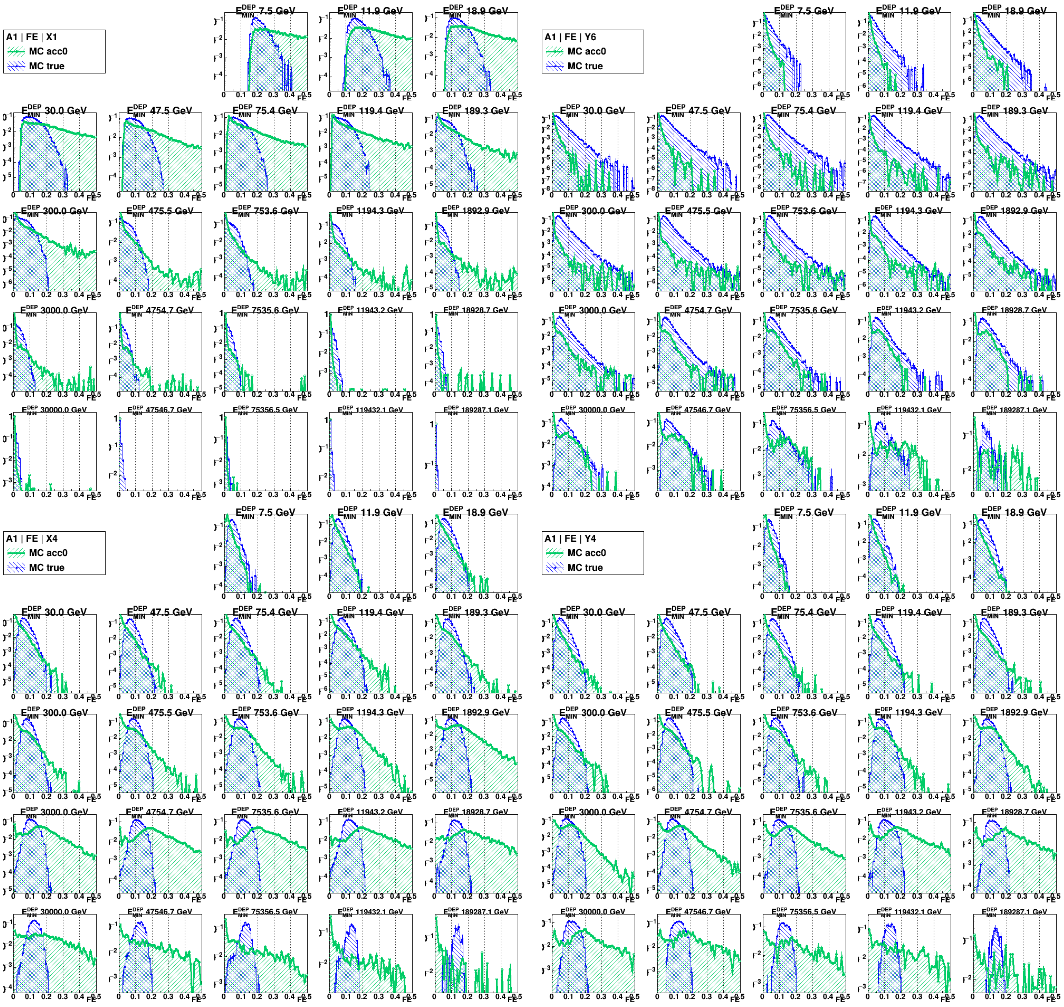

FIGURE 4.5: Signal-to-background separation for the fraction of energy deposited in the *first* (X1) and last (Y6) layers (top half) and in the intermediate X4-Y4 layers (bottom half) of the TASC, based on EPICS simulated data. The energy bins ranges from 7.5 GeV up to 300 TeV.

4.1.2 Introduction to Boosted Decision Trees (BDT)

Boosted decision trees belongs to the class of supervised machine-learning algorithms. The main idea of boosting is to take a set of simple models and then combine them sequentially to build a robust and reliable classifier. The simple models that are only slightly better than a random guess are called[3] *weak learners*, while the final classifier is called *strong learner*. As the name suggests, decision trees with low-depth are the weak learners in the BDT context.

Decision Trees

Decision Trees(DT) are rooted binary trees, in classification problem where only two categories of events are involved. As first conceived by Ref. [46] and further developed by Refs. [47, 48, 115], the *growing* of a DT starts from a root node that is recursively partitioned until one of the specified stopping criteria is met. A crucial aspect affecting the DT's performance and structure is the choice of splitting index (SI) that establish how a node is partitioned into child nodes during the building of the DT. In general, a SI metric is:

- Symmetrical in the purity[4] of signal and background, since a cut that mainly selects the background is just as good as one that filters out the background to the same amount.
- Maximal when there is no separation between signal and background, *i.e.* the purity is equal to 0.5.
- Minimal as perfect separation is reached, *i.e.* only background (or signal) node.

As reported in Ref. [56], the common SIs are[5] the *Gini index* [80], the *misclassification error* and the *cross entropy* and the most widely used in BDT analysis, including the one of this work, is the *Gini index*.

In order to prevent a significant over-training[6], stopping criteria for terminal nodes (also called leaves) need to be included in the DT growing. The main conditions are as follows:

- *Maximum Tree Depth* to limit the allowed complexity of the model.
- *Minimum Leaf Size*, such that a minimum number of events (or effective events) are required in each node. This condition prevents further partitioning of the tree and it ensures the statistical significance of every node.

---

[3] In the context of statistical learning. For more detail see *e.g.* the book [87].

[4] In this context, the purity is defined as $\frac{\sum_s w_s}{\sum_s w_s + \sum_b w_b}$ where $\sum_s w_s$ and $\sum_b w_b$ are, respectively, the weighted sums over signal and background events of the training sample.

[5] Defined as $p(1-p)$; $-p\log(p) - (1-p)\log(1-p)$ and $1 - max(p, 1-p)$, respectively.

[6] Over-training phenomenon occurs when the machine-learning (or in general the statistical) model learns too much from the training sample but performs poorly on the test sample, derived from simulations or real data. It is also referred to as over-fitting in machine-learning context.

- *Minimum Signal Purity* requires a minimum level of purity to categorize an event as signal.

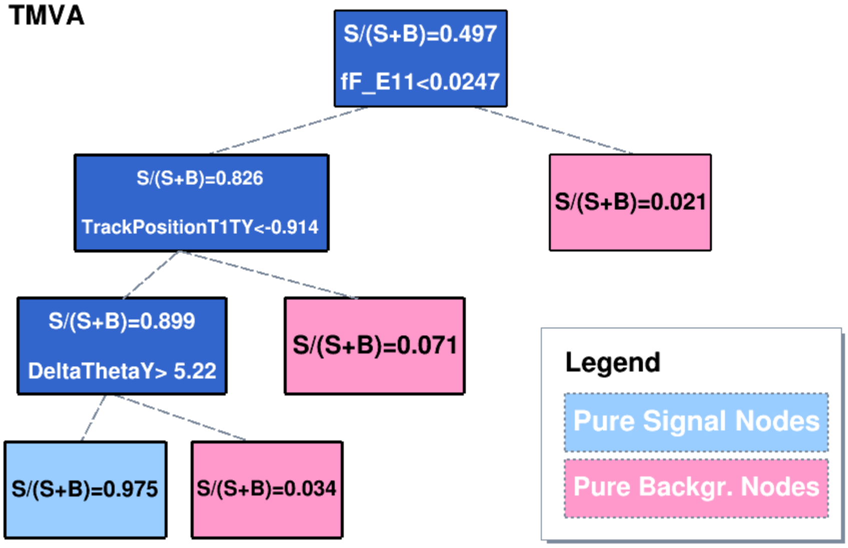

FIGURE 4.6: Example of decision tree with depth level equal to 3, built from the 13 features described in the paragraph 4.1.1 of this work.

An example of decision tree based on the analysis presented in this work, is shown in Fig. 4.6. Nevertheless, in most real-world cases, a single DT is highly prone to over-training when they are constructed as strong learner and, instead, it is a weak classifier, when the allowed maximum tree depth is low. Hence, one possible option to overcome this issue, is to move from one to an ensemble of DTs (*forest*) where the final classifier is obtained making a weighted average of the predictions of each DT.

Boosting

Boosting is a general technique, independent on the nature of ML-algorithm, that enhances the performance of *weak* learners by combine them into a *strong* learner in an additive manner. This final classifier is built iteratively as

$$t(\vec{x}) = \sum_{k=1}^{M} \alpha_k t_k(\vec{x})$$

The starting point is a weak learner model $t_0(\vec{x})$ derived from the trained data $D_0(x,y) = \{(\vec{x}_1, y_1), \ldots, (\vec{x}_n, y_n)\}$ where $\{y_i\}_{i=1,\ldots,n}$ are binary variables in which the possible outcomes are ± 1. For the k iteration, a weight α_k is associated to the learner $t_k(\vec{x})$ depending of the boosting algorithm and each point of the trained data $D_{k-1}(x,y)$ are re-weighted accordingly. Then, the learner t_{k+1} is trained by the dataset $D_k(x,y)$. This procedure is repeated until the M iteration is reached.

In the AdaBoost [77] implementation, the re-weighting factor is calculated at each step as follows

$$\alpha_k = \beta \times \ln \frac{1-\epsilon_k}{\epsilon_k}$$

in which:

- ϵ_k is the *misclassification rate* defined as the ratio of misidentified events $\sum_{i\,|\,t_k(\vec{x}_i)y_i=-1}^{M} w_i$ over the total number of events $\sum_i^M w_i$.
- β is the *learning rate*. The optimal value[7] is 0.5.

And the weight of each point in $D_k(x,y)$, become

$$w_i \leftarrow w_i \frac{e^{\alpha_k \Theta_k(\vec{x}_i, y_i)}}{2\sqrt{\epsilon_k(1-\epsilon_k)}}.$$

where $\Theta_k(\vec{x}_i, y_i)$ is the misclassification function that is equal to 1 if $t_k(\vec{x}_i)y_i = -1$ and 0 otherwise; and $2\sqrt{\epsilon_k(1-\epsilon_k)}$ is the normalisation factor. It is worth noting that at each iteration, the training of k-learner is focused on the mistakes of its predecessor.

Main properties The main features of the BDT method compared to other ML-techniques (*e.g.* Artificial Neural Network, Deep Neural Network, etc.) are:

- Small number of hyper-parameters. In addition, the set of parameters that significantly affect the performance are usually a few.
- Less prone to the so-called “curse of dimensionality" for increasing number of features.
- No need of *normalization*, *standardization* or *regularisation* of the input features.
- Robust against weakly discriminating input variables. Furthermore, these variables can be recognized through the feature ranking described in the paragraph 4.1.6.
- Good level of interpretability, although this decreases when an aggressive boosting is applied.

4.1.3 Classifier distributions

In this analysis, BDT classifier distributions have been evaluated using the `TMVA` package [91] (integrated in `ROOT` framework) by dividing the deposited energy range into six intervals as follows: < 30 GeV, $30-120$ GeV, $120-300$ GeV, 300 GeV -6.5 TeV, $6.5-20$ TeV, > 20 TeV.

---

[7] A proof of this statement is available in Ref. [95].

As a first step, the simulated data for `A1` acceptance are randomly split into training and test samples. The BDT response for signal and background is evaluated using the training sample. The performance are thus preliminary assessed by visually inspecting the degree of overlap between the two distributions. Afterwards, the same procedure is repeated for the test sample.

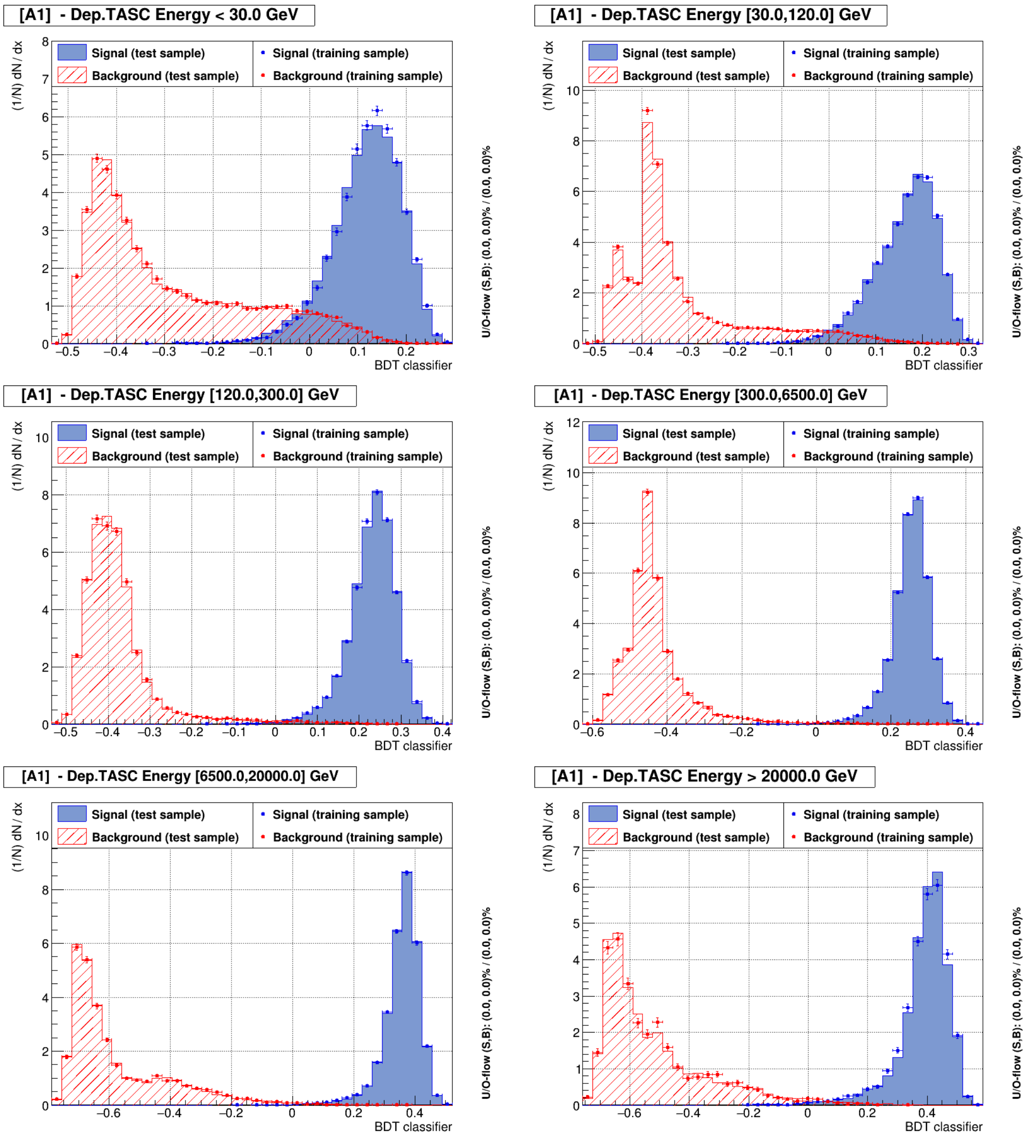

FIGURE 4.7: BDT model performance, for each energy intervals, evaluated splitting randomly the MC data into test and training samples and selecting events in `A1` acceptance. The BDT classifier distributions of the test samples are represented by histograms filled in blue (signal) and red (background) respectively. The same distributions from the training samples are superimposed with markers.

The reliability of the BDT model is then examined with the so-called overtraining test, in which the distributions obtained from the two sub-samples mentioned above are superimposed on each other and their consistency is checked. The results, shown in the Fig. 4.7, exhibit good agreement for each energy interval. It is worth mentioning that only simulated data are used at this level. In addition, it is required that the IMC-based and the CHD-based charge estimators are greater than zero.

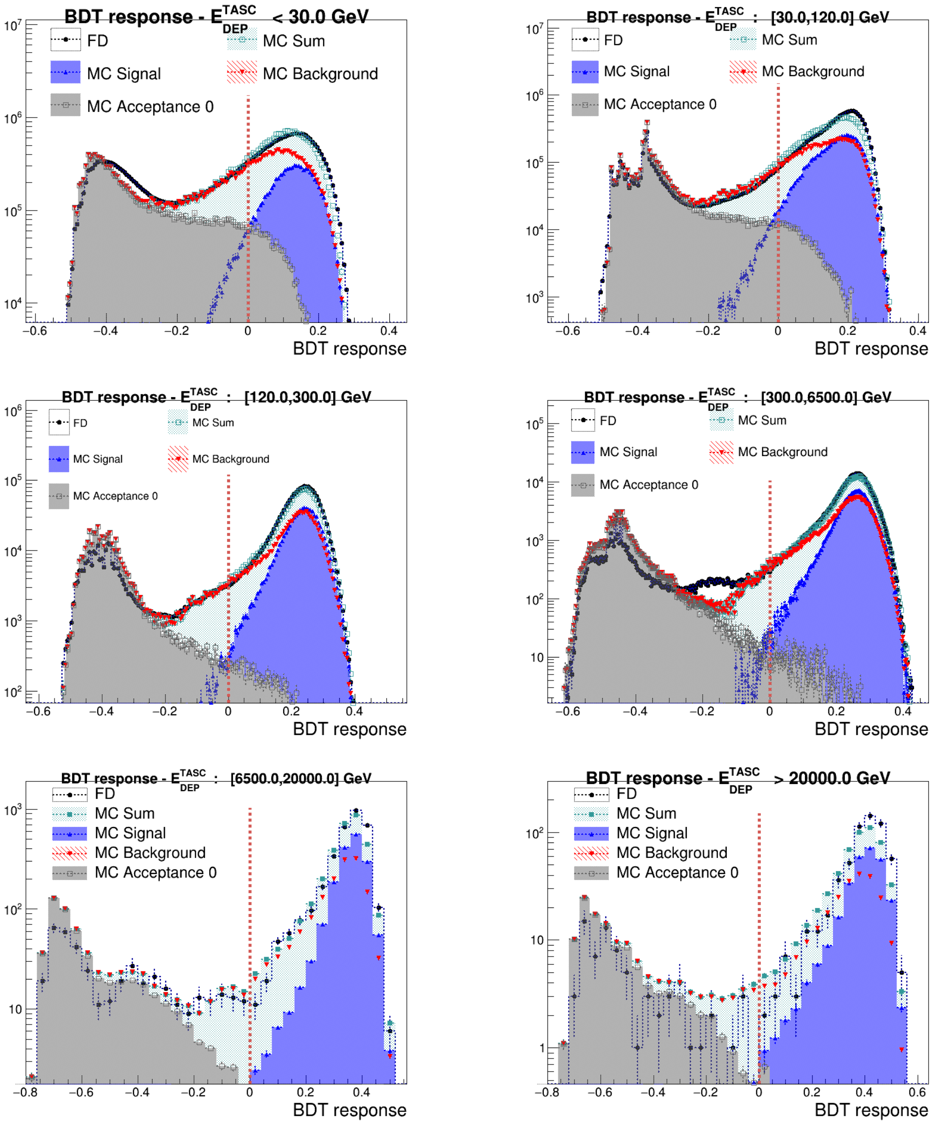

FIGURE 4.8: BDT model performance for FD compared with simulated data for each energy intervals. The individual contributions due to signal (blue), background (red), off-acceptance (grey open square) events of type 0 are shown. The red dashed line is placed at 0, which is approximately the selected threshold set to distinguish the signal from the background.

Thereafter, the BDT classifiers are calculated taking into account *in-flight* data. Hence, BDT distributions from FD are compared with the response derived from simulations, by summing accordingly the re-weighted contributions from the helium and proton MC samples. The results illustrated in Fig. 4.8, show the overall distributions for FD and MC in black filled dots and in green square markers, respectively. In addition, the individual contributions derived from EPICS simulations are also reported. The distribution of helium events from true `A1` acceptance (MC signal) is shown with blue filled upward triangles, whereas the complementary distribution (MC background) and the contribution from off-acceptance events of type `0` (MC Acceptance 0) are represented with red filled downward triangles and grey open squares, respectively.

Overall, they exhibit a fairly good agreement for each energy interval.

4.1.4 Optimization of BDT working point

Aiming to establish the optimal BDT *working point*, for the signal-to-background discrimination, several figures of merit have been studied for each energy intervals. Using a modified `TMVA` package routine, the *signal* ε_S and *background* efficiencies ε_B, the *signal purity* $\pi_S = \frac{S}{S+B}$, the signal efficiency multiplied by purity $\eta_S = \varepsilon_S \times \pi_S$ and the *significance* $\Sigma_S = \frac{S}{\sqrt{S+B}}$ have been estimated as shown in Fig. 4.9.

The numerical maximum of *significance* has been selected as the best threshold for each energy intervals and the values are summarized in table 4.2.

Deposited Energy Range	BDT Working Point
$10 - 30$ GeV	-0.004
$30 - 120$ GeV	-0.023
$120 - 300$ GeV	-0.015
$0.3 - 6.5$ TeV	-0.028
$6.5 - 20$ TeV	-0.026
> 20 TeV	-0.009

TABLE 4.2: BDT working points based on the numerical maximization of the figure of merit *significance* for `A1` acceptance.

4.1.5 Hyper-parameters tuning

As previously mentioned, one of the main advantages of the BDT method is the relatively small number of model parameters. In fact, one of the most time-consuming and cumbersome step in implementing a real-world case machine learning model, is the tuning of hyper-parameters.

In accordance with the nomenclature of the `TMVA` package [91], the scanned parameters are *number of trees* (`Ntrees`) in the forest, and *maximum depth* (`MaxDepth`) of the single DT allowed. The other options and parameters have not been changed with respect to the default ones[8], except for the variable `nCuts`, which represents the granularity of variable range in which the scanning for optimal splitting condition is performed, that was increased from 20 to 50.

---

[8] More details can be found in the `TMVA` manual [91].

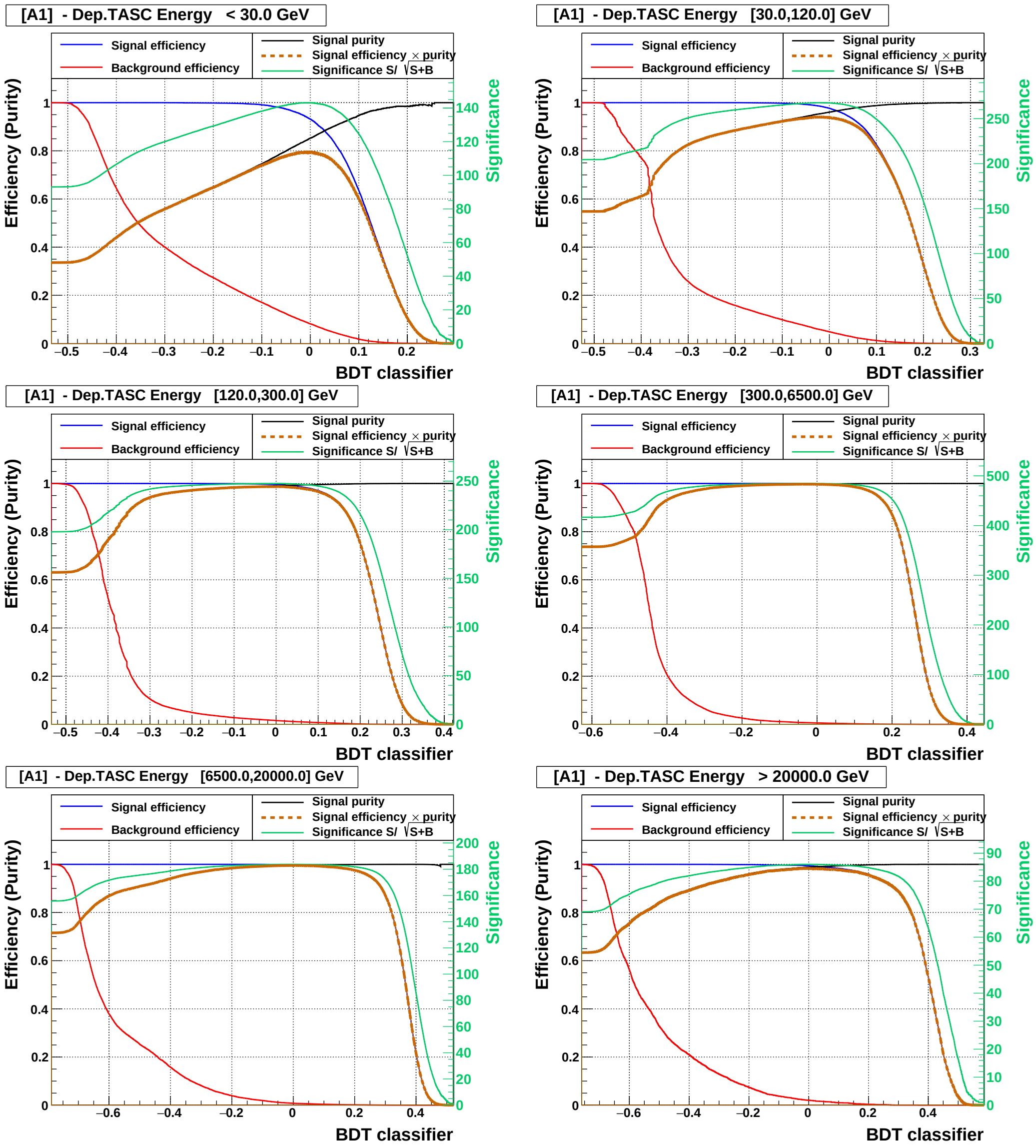

FIGURE 4.9: Figures of merit as function of the BDT score in `A1` acceptance for each energy intervals.

In the analysis of this work, at first, the performance has been evaluated setting the *number of trees* equal to 500, 850 and 1000, while fixing the maximum depth to 3. Subsequently, the *maximum depth* of the tree was scanned from 3 to 6, by letting the the number of trees equal to 1000. In order to establish the optimal values for these hyper-parameters, the Receiver Operating Characteristic (ROC) curves were calculated for each model and for each wide energy bins. These curves provide a comprehensive quantification of the binary classifier's behaviour as the threshold set to separate signal from background, changes. The results are shown in figure 4.10 where all models have almost the same Area Under the Curve (AUC) and therefore, they are basically independent on the choice of hyper-parameters investigated. Hence, the default `TMVA` values, `Ntrees` equal to 850 and `MaxDepth` equal to 3, have been selected for this analysis. Additional validation tests, based on the stability of the measured helium flux for different hyper-parameters values, are explained in the paragraph 4.7.1.

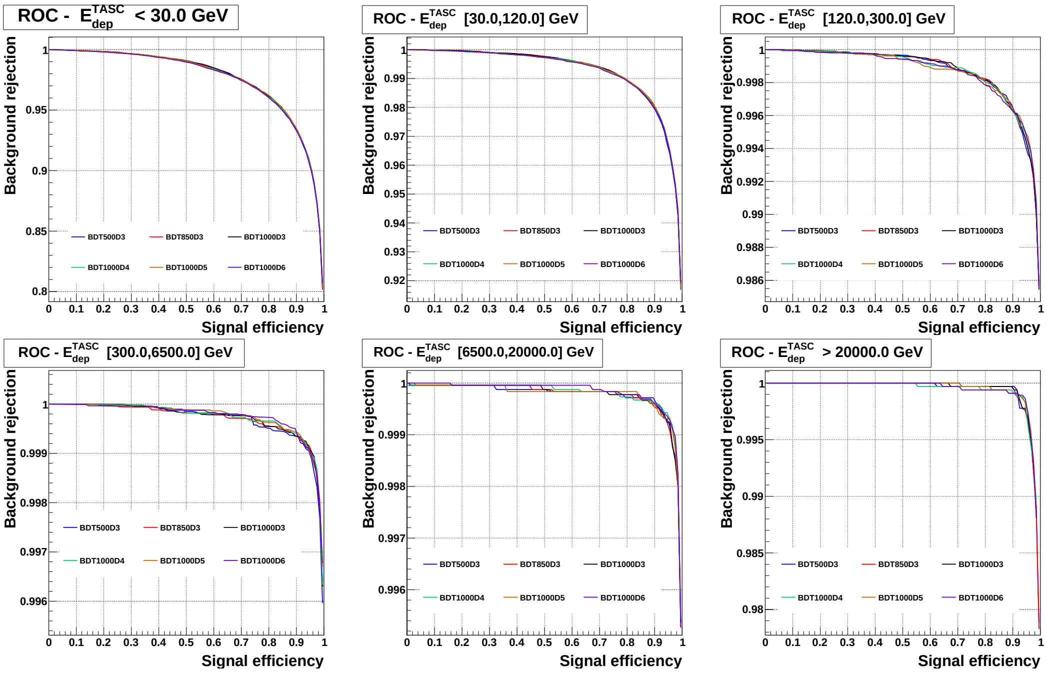

FIGURE 4.10: ROC curve for each energy interval in which the BDT training has been carried out. The performance has been evaluated varying the hyper-parameters: *number of trees*, *maximum depth* of the tree. Fixing the maximum depth as default value (3), the *number of trees* were changed in the set 500, 850, and 1000. The *maximum depth* of the tree instead was scanned from 3 to 6, by letting the number of trees equal to 1000.

4.1.6 Feature ranking

An additional test, that is useful for monitoring the accuracy of the designed model, is the feature ranking. In fact, an high number of input variables increases the model complexity, making it more vulnerable to over-training. Thus, the feature importance has been estimated "by counting how often the variables are used to split decision tree nodes, and by weighting each split occurrence by the separation gain-squared it has achieved and by the number of events in the node" as quoted in `TMVA` user's guide [91] (where the algorithm is taken from Ref. [46]) in order to verify whether or not there are poorly discriminating input variables that can be discarded. Results, normalized to 1, are illustrated in Fig. 4.11 for each trained energy bin, in which one can appreciate that the contribution of each feature is of the same order of magnitude and, therefore, none of the input variable is redundant.

4.2 Charge Identification

Charge assignment is the last selection step before obtaining the measured energy spectrum. In helium analysis, charge identification is a crucial task

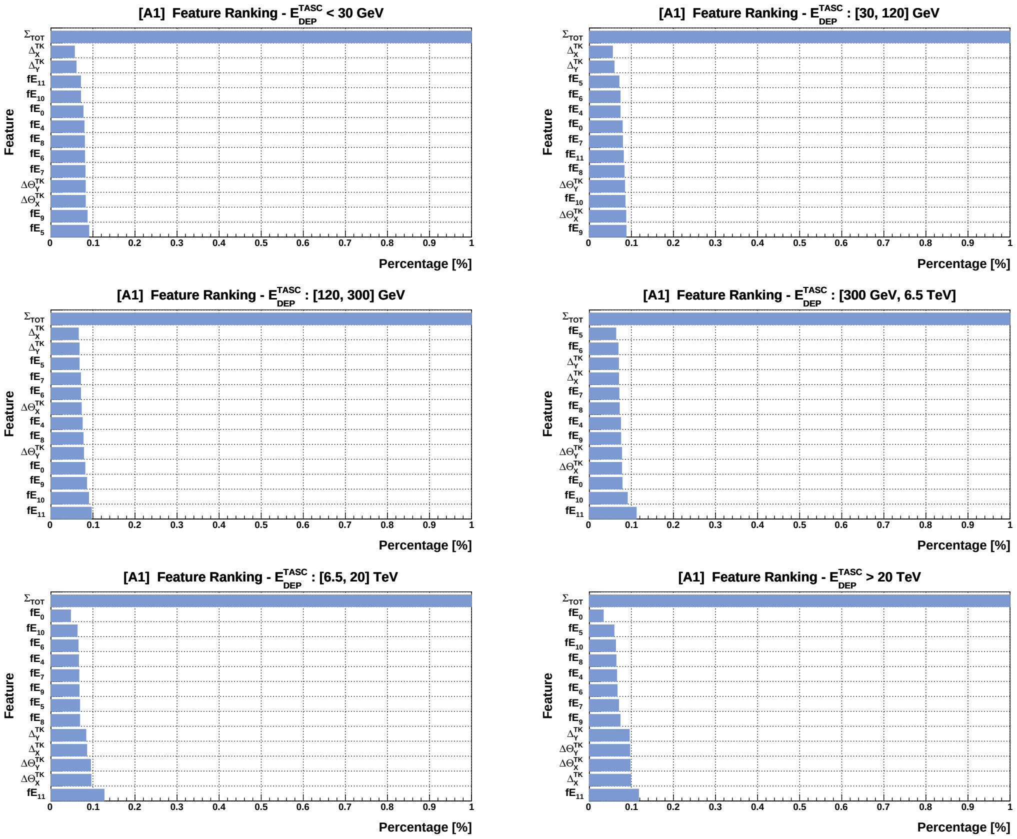

FIGURE 4.11: Feature ranking provided by the `TMVA` package for each energy interval in which the BDT training has been performed.

to ensure reliable proton rejection over the entire energy range. Since the helium and proton distributions get wider as the deposited energy increases, a simple rectangular cut leads to a non-uniform charge selection efficiency that decreases significantly in the high-energy region. Therefore, an energy-dependent charge selection strategy was implemented[9] as extensively described in the next subsection.

Energy-dependent charge selection

As a starting point, the deposited energy range is divided into 20 logarithmic bins, ranging from 10 GeV up to 1 PeV. Proton and helium charge distributions for IMC and CHD are then considered. Each peak is fitted[10] with the convolution of a Landau with a Gaussian distribution (*Langaus*) $f_i(Z)$, to take into account both the instrumental noise and the ionization energy losses of charged particles in scintillators. Peak centroid[11] $\mu_i(E)$, the FWHM $\phi_i(E)$ and

---

[9] This procedure is a variation of the one originally presented in Ref. [8] and modified in Ref. [101].

[10] Since the distribution does not have a closed analytical expression, the fit is performed in `ROOT` based on the *"langaus.C"* routine written by H.Pernegger and M.Friedl.

[11] The peak position is evaluated numerically extracting the maximum of the fitted function $f_i(Z)$.

the Left Half Width at Half Maximum (σ_L) and the Right Half Width at Half Maximum (σ_R), defined as $\sigma_R + \sigma_L = \phi$, are retrieved for each energy interval. An example of this procedure is shown in Fig. 4.12 for several energy bins of IMC-based charge derived from FD.

Thereafter, the extracted parameters $\mu_i(E), \sigma_L(E), \sigma_R(E)$ and $\phi_i(E)$ are fitted with logarithmic polynomials, *i.e.*

$$p_n(E) = \sum_{i=0}^{n} c_i \log^i(E).$$

such that are continuously defined for each deposited energy. A third order log-polynomial has been chosen for this analysis ($n = 3$). The results for helium, obtained by analysing 87 months of FD, are shown in Fig. 4.13.

Then, helium event selection is performed in two steps, using both CHD and IMC sub-detectors. Specifically, the IMC-based charge estimator permits a better proton-helium separation at higher energies because it is less prone to back-scattered particle background due to the higher detector segmentation. Therefore, a tighter cut is applied on the charge estimator from this detector, whereas the information from the CHD sub-system is basically used to further reduce the prominent proton background. For the CHD-based estimator, a fixed-threshold Z^{CHD}_{min} is set for the minimum charge value that the event can take, regardless of the energy deposited.

In the analysis of this work, the Z^{CHD}_{min} is set to 1.6 as good trade-off between proton rejection efficiency and helium signal efficiency. This can be appreciated by looking at Fig. 4.14, where the distributions are shown for several energy intervals.

The, helium nuclei are selected according to the following energy-dependent cut on the IMC-based charge estimator

$$\mu_{He}(E) - n_L\sigma_L(E) \;<\; Z \;<\; \mu_{He}(E) + n_R\sigma_R(E) \tag{4.1}$$

where $\mathrm{n_R}$ is fixed at 5 over the entire energy range, whereas $\mathrm{n_L}$ is set to 3 in the central energy region (from to 300 GeV to 1 TeV of deposited energy), and then[12] it is lowered up to 2.5 (above 2.8 TeV of deposited energy) to both ensure a nearly constant charge selection efficiency and to improve purity by rejecting protons from the energy related broadening of charge distributions.

The IMC-based charge distributions, after the preliminary charge selection on Z_{CHD}, is shown, for several energy intervals, in Fig. 4.15 together with the expected proton and helium contributions derived from EPICS simulations.

---

[12] More in detail, $\mathrm{n_L}$ is set to 2.75, from 1 TeV to 2.8, whereas is 3.25 from 100 GeV to 300 GeV and 3.5 from 10 GeV to 100 GeV of deposited energy. The latter ensures a better uniformity of the helium selection efficiency.

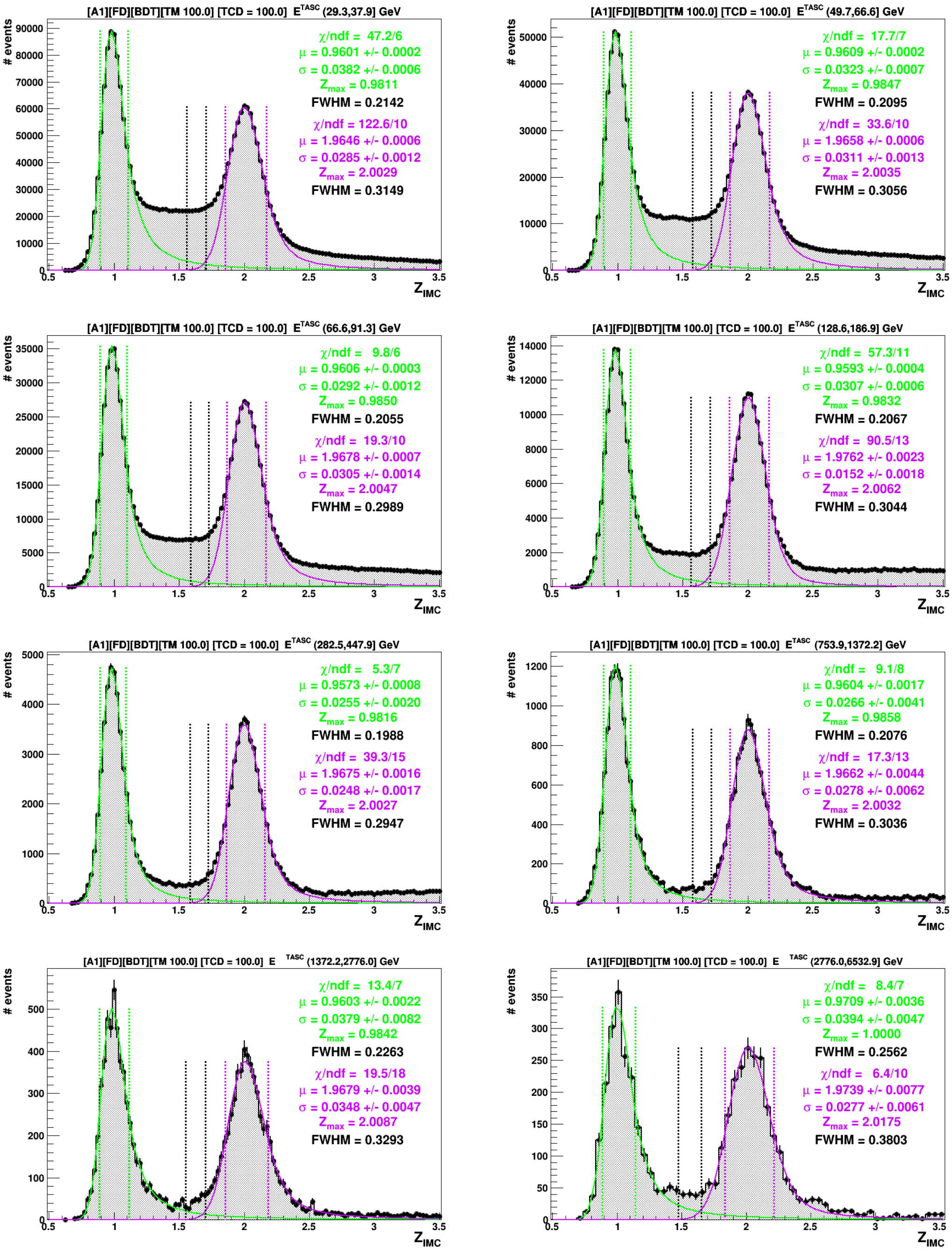

FIGURE 4.12: IMC charge distributions derived from 87 months of *in-flight* data in `A1` acceptance for several TASC energy bins. The proton and helium peaks are fitted with *Langaus* functions. The magenta dashed vertical lines represent the helium FWHMs derived from the fitted function, while the black dashed lines are the lower bounds of the charge selection at $2\sigma_L$ and $3\sigma_L$, respectively.

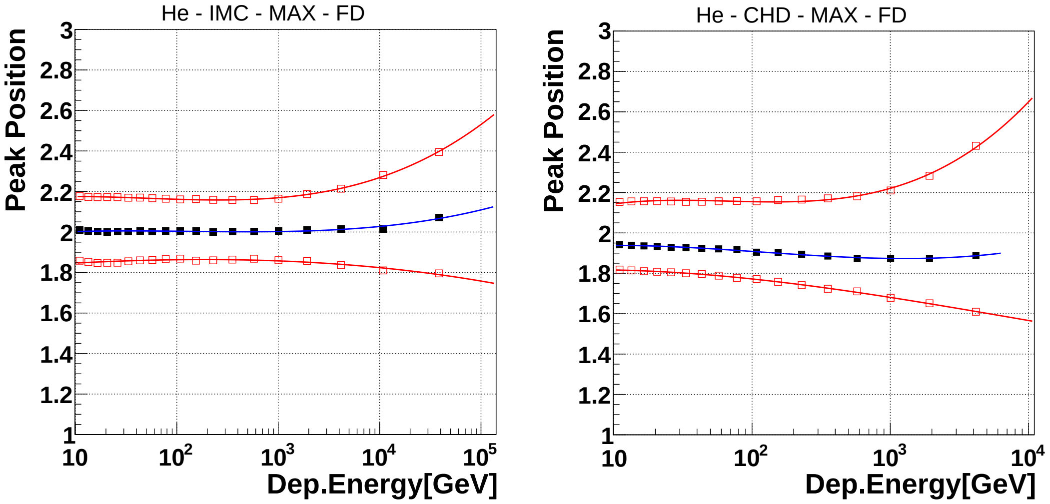

FIGURE 4.13: Peak positions $\mu_{He}(E)$, and LHWHM $\sigma_L(E)$, and RHWHM $\sigma_R(E)$ as function of TASC deposited energy for helium in FD. All are fitted with third-order log-polynomial. Right and left panels represent the results for CHD and IMC charge estimators, respectively.

Fine-tuning for MC peak-width bias correction

Since the widths and, to lesser extent, the peak positions of MC charge distributions are still not fully compatible[13] with those derived from FD, despite the calibration procedure already applied and discussed in paragraph 3.2.2, MC charges are corrected on event-by-event basis, both for CHD and IMC. Specifically, the same fitting procedure aforementioned is applied to get μ_i^{MC} and ϕ_i^{MC} from the related MC-sample. Then, the linear transformation

$$\hat{Z}_i^{MC}(E) = \alpha_i(E) \times Z_i^{MC}(E) + \beta_i(E)$$

in which $\alpha_i(E) = \frac{\phi_i^{FD}(E)}{\phi_i^{MC}(E)}$ and $\beta_i(E) = \mu_i^{FD}(E) - \alpha_i(E) \times \mu_i^{MC}(E)$, is applied to MC events. The correction functions for proton and helium are shown in Fig. 4.16 for IMC-based charge.

A consistency test is performed aiming to assess in a quantitative way the overall improvement after the applied correction. Thus, a χ^2-like test-statistic[14] is introduced taking into account FD and MC histograms in a given energy interval. This quantity is computed as follows

$$T = \sum_{i=1}^{N} \frac{\Delta_i^2}{\sigma_i^2} = \sum_{i=1}^{N} \frac{(u_i - v_i)^2}{u_i + v_i} \tag{4.2}$$

where: U and V being the FD and MC histograms with N bins; u_i and v_i being the i^{th} bin contents of the U and V histograms. The test is based on the evaluation of T before and after applying the fine-tuning charge correction

---

[13] Mainly due to sub-optimal MC modeling of back-scattering particles.

[14] This test-statistics is described in Ref. [111]

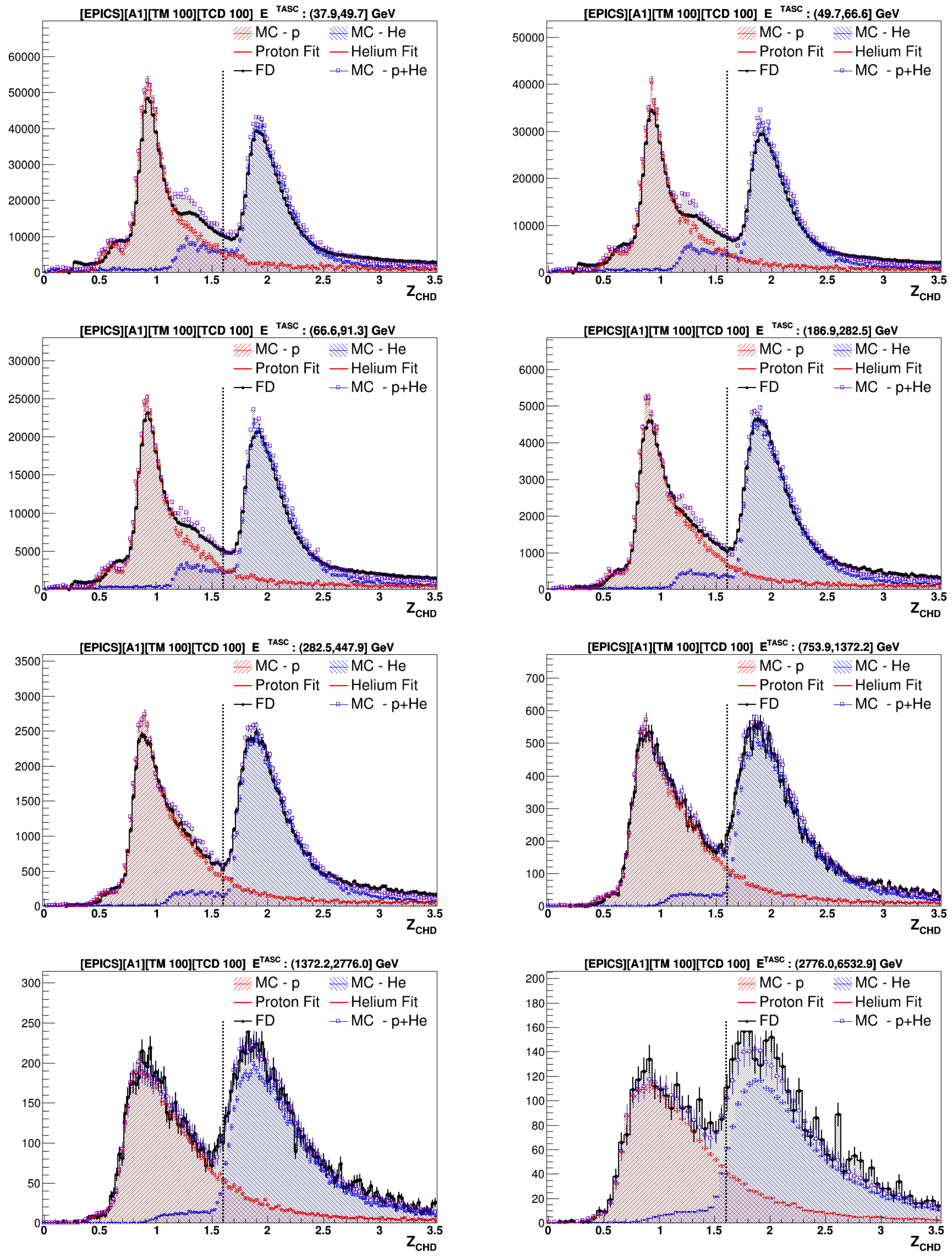

FIGURE 4.14: CHD charge distributions for several TASC energy intervals. The FD distributions are represented with black markers, in red and blue are shown the MC distributions for proton and helium MC samples, respectively. The total MC distributions are represented with violet open circle markers. The black dashed vertical lines represent the Z_{min}^{CHD} fixed at 1.6 value.

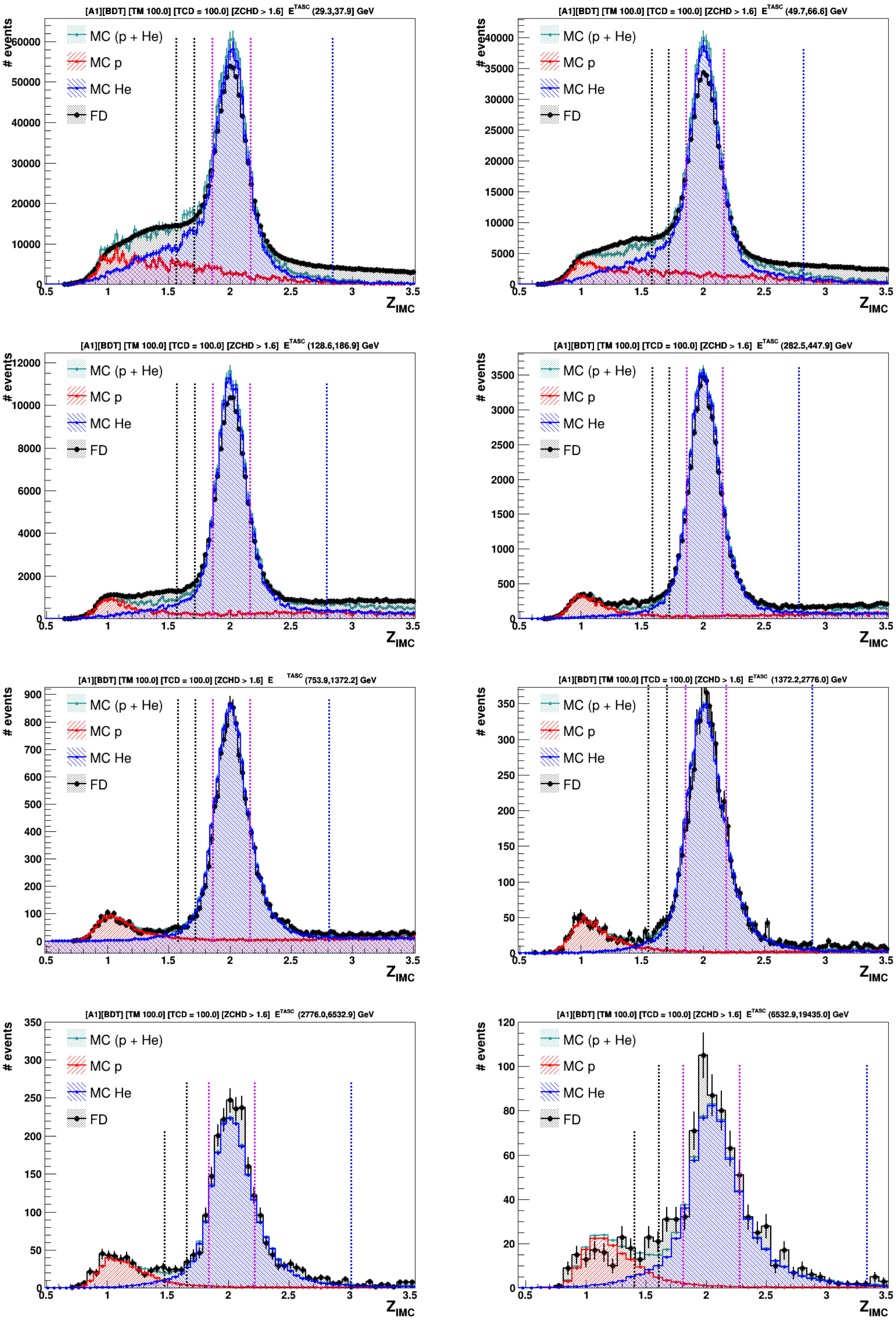

FIGURE 4.15: IMC charge distributions after CHD cut Z_{min}^{CHD}, for several TASC energy intervals. The FD distributions are represented with black markers, in red and blue are shown the MC distributions for proton and helium, respectively. The total MC distributions are represented with green filled circle markers. The magenta dashed vertical lines represent the helium FWHMs, while the black dashed lines are the lower bounds of the charge selection at $2\sigma_L$ and $3\sigma_L$, respectively. The blue dashed lines are the upper bounds of the charge selection at $5\sigma_R$.

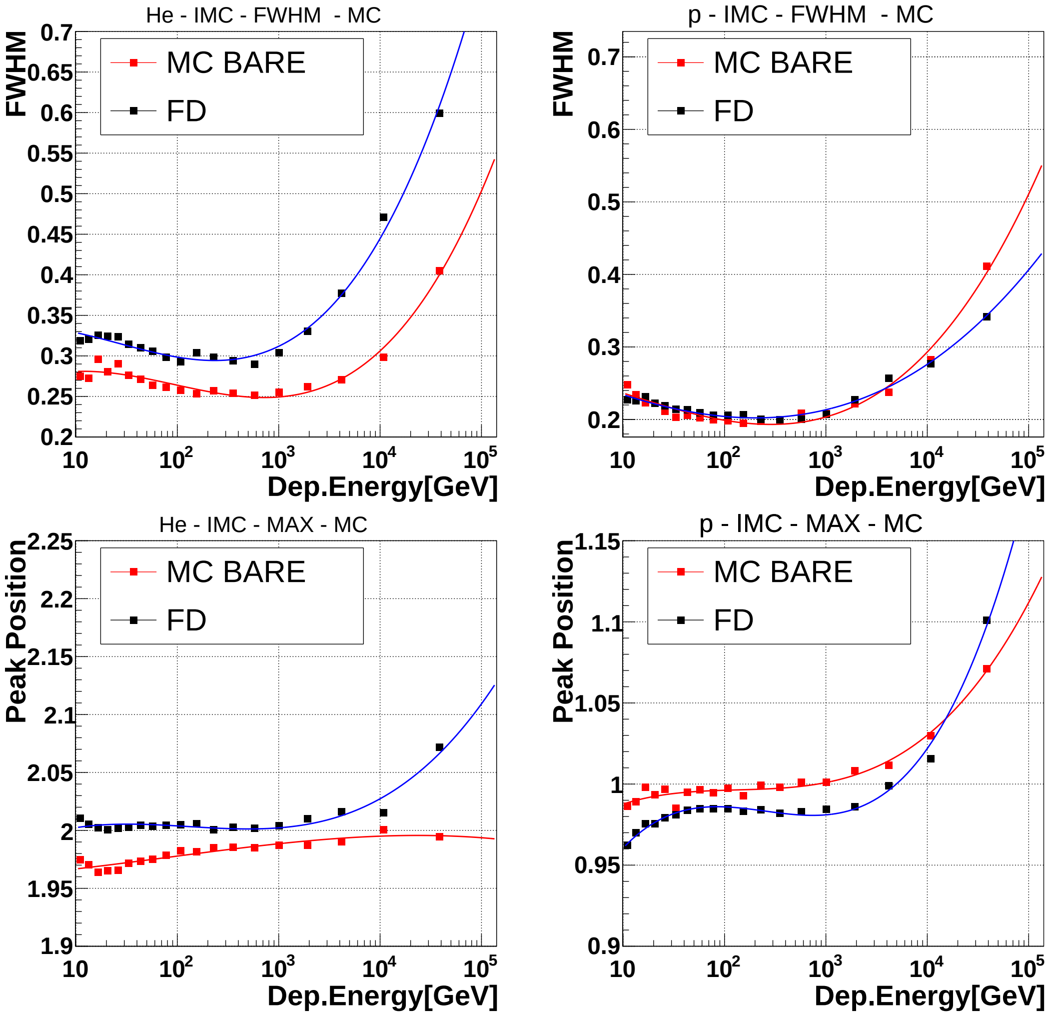

FIGURE 4.16: (Top half) FWHMs and (bottom half) peak positions, from maximum of *Langaus* fits, as function of TASC deposited energy for helium (left panel) and proton (right panel) for FD and *EPICS-based* MC. Both are fitted with $p_3(E)$.

and thereafter checking whether or not the ratio $r_{TS} = T_{after}/T_{before}$ is less than 1. If it is, the test is passed. An example is shown in Fig. 4.17, for IMC and CHD charge estimators in the energy interval 0.75-1.37 TeV.

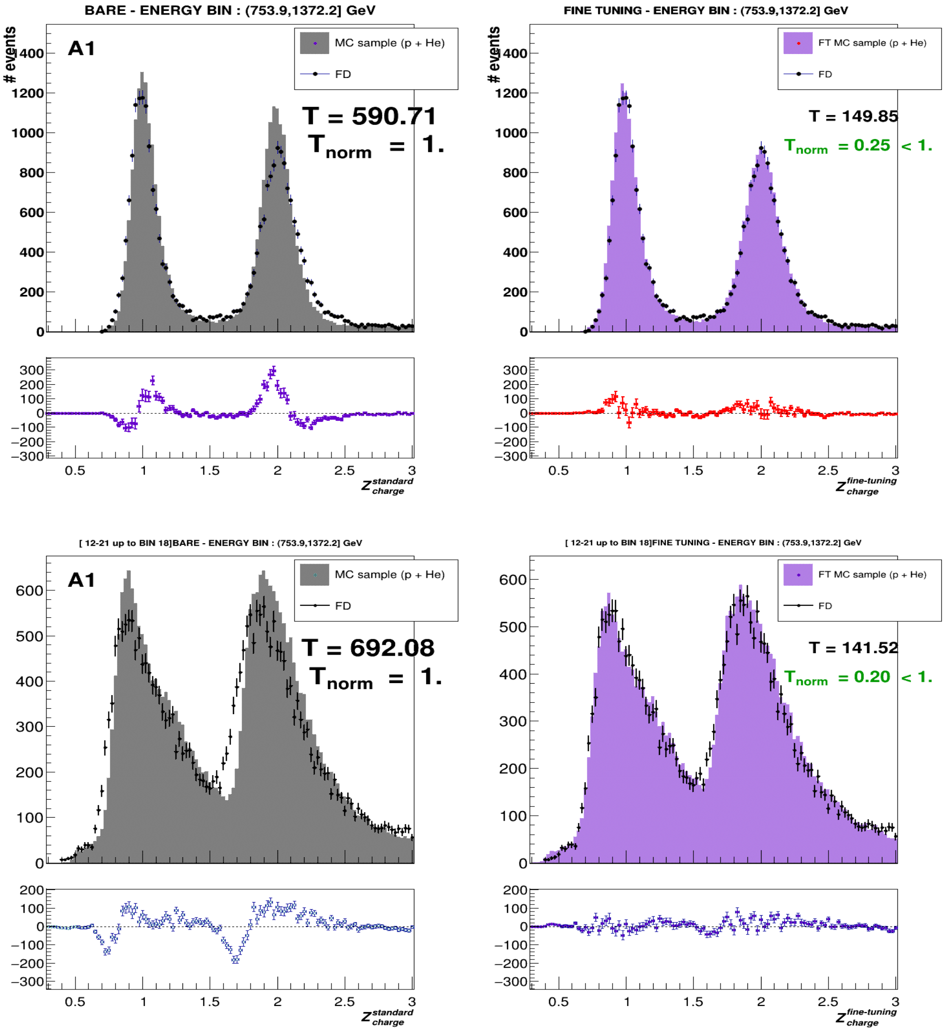

FIGURE 4.17: Comparison of the overall improvement of the FD and MC agreement after the fine-tuning charge correction for the energy interval 0.75-1.37 TeV for IMC and CHD charge estimators in `A1` acceptance. The χ^2-like test-statistic ratio r_{TS} is 0.25 and 0.2 for the IMC and CHD charges, respectively.

4.3 Background subtraction

Although the majority of the background can be discarded by the aforementioned charge selections, residual sources are still present and need to be subtracted before the application of the unfolding procedure to the *in-flight* data. These can be divided into two categories as follows:

- **Proton contamination** is composed of protons in `A1` acceptance that cannot be disentangled from the selected helium sample, due to the large tail of the proton charge distribution that goes beneath the helium peak.
- **Off-acceptance background** is made of helium and proton nuclei with the real acceptance being different from `A1` but which are reconstructed as `A1` helium candidates due to misidentification of the primary particle by the tracking algorithm and, thus also to an incorrect charge assignment.

On the other hand, after the pre-selection, electron contamination is completely negligible for helium analysis over the entire energy range.

The assessment of each background components has been performed in analogy to that described in Ref. [8]. MC simulations have been exploited to determine the relative ratio for each background species. In contrast, *in-flight* data where used to evaluate the absolute number of helium and proton events as function of the TASC deposited energy. In this way, the estimate is slightly dependent on the prior hypothesis about the spectral shape of the proton and helium CR fluxes, especially in the high-energy region, and is completely independent from the assumed normalization of MC samples.

Figure 4.18 shows the results decomposed for each component, where $\frac{\mathrm{dB}}{\mathrm{dE}}\Big|^{\mathrm{p}\to\mathrm{He}}_{\mathrm{A1}\to\mathrm{A1}}$, $\frac{dB}{dE}\Big|^{\mathrm{p}\to\mathrm{He}}_{\neq\mathrm{A1}\to\mathrm{A1}}$ and $\frac{dB}{dE}\Big|^{\mathrm{He}\to\mathrm{He}}_{\neq\mathrm{A1}\to\mathrm{A1}}$ are, accordingly, the proton background component from acceptance `A1`, the off-acceptance background contributions from proton and helium species. In detail, the proton and the off-acceptance contamination ratios are computed from MC simulations as follows:

- *Proton* contamination ratio

$$C^{\mathrm{A1}}_{\mathrm{proton}} = \left(\frac{\frac{\mathrm{dN}}{\mathrm{dE}}\Big|^{\mathrm{p}\to\mathrm{He}}_{\mathrm{A1}\to\mathrm{A1}}}{\frac{\mathrm{dN}}{\mathrm{dE}}\Big|^{\mathrm{p}\to\mathrm{p}}_{\mathrm{A1}\to\mathrm{A1}} + \frac{\mathrm{dN}}{\mathrm{dE}}\Big|^{\mathrm{He}\to\mathrm{p}}_{\mathrm{A1}\to\mathrm{A1}}} \right)_{\mathrm{MC}}$$

- *Off-acceptance* contamination ratios

$$\Omega^{\mathrm{MCp}}_{\mathrm{helium}} = \Omega^0_1 = \left(\frac{\frac{\mathrm{dN}}{\mathrm{dE}}\Big|^{\mathrm{p}\to\mathrm{He}}_{\neq\mathrm{A1}\to\mathrm{A1}}}{\frac{\mathrm{dN}}{\mathrm{dE}}\Big|^{\mathrm{p}\to\mathrm{p}}_{\mathrm{A1}\to\mathrm{A1}} + \frac{\mathrm{dN}}{\mathrm{dE}}\Big|^{\mathrm{p}\to\mathrm{p}}_{\neq\mathrm{A1}\to\mathrm{A1}} + \frac{\mathrm{dN}}{\mathrm{dE}}\Big|^{\mathrm{He}\to\mathrm{p}}_{\mathrm{A1}\to\mathrm{A1}} + \frac{\mathrm{dN}}{\mathrm{dE}}\Big|^{\mathrm{He}\to\mathrm{p}}_{\neq\mathrm{A1}\to\mathrm{A1}}} \right)_{\mathrm{MC}}$$

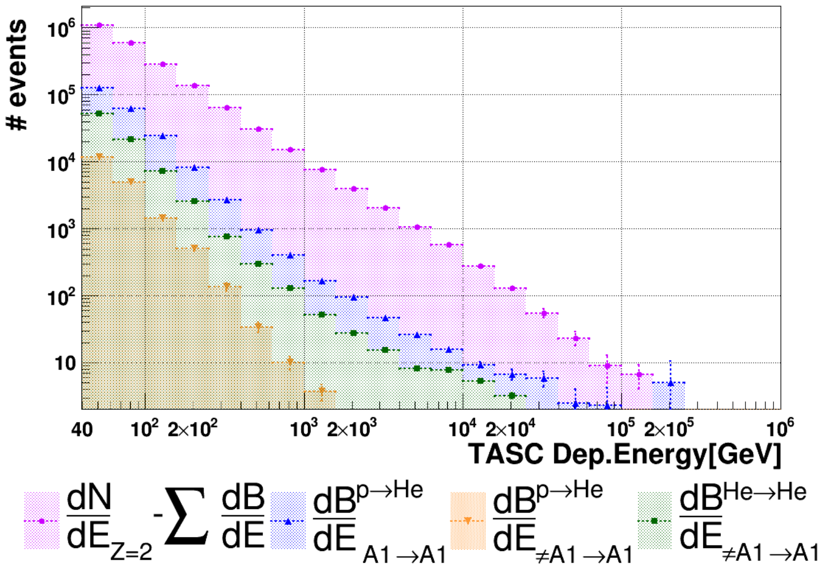

FIGURE 4.18: Deposited energy spectrum of helium candidate events after the background subtraction in `A1` acceptance, represented with magenta filled circle, obtained with 87 months of CALET data. The estimated background components from proton events in `A1` acceptance and from *off-acceptance* helium and proton events are shown with the markers: upper blue triangle, green square and orange downward triangle, respectively.

$$\Omega^{\mathrm{MCp}}_{\mathrm{proton}} = \Omega^0_0 = \left(\frac{\frac{\mathrm{dN}}{\mathrm{dE}}\Big|^{\mathrm{p}\to\mathrm{p}}_{\neq\mathrm{A1}\to\mathrm{A1}}}{\frac{\mathrm{dN}}{\mathrm{dE}}\Big|^{\mathrm{p}\to\mathrm{p}}_{\mathrm{A1}\to\mathrm{A1}} + \frac{\mathrm{dN}}{\mathrm{dE}}\Big|^{\mathrm{p}\to\mathrm{p}}_{\neq\mathrm{A1}\to\mathrm{A1}} + \frac{\mathrm{dN}}{\mathrm{dE}}\Big|^{\mathrm{He}\to\mathrm{p}}_{\mathrm{A1}\to\mathrm{A1}} + \frac{\mathrm{dN}}{\mathrm{dE}}\Big|^{\mathrm{He}\to\mathrm{p}}_{\neq\mathrm{A1}\to\mathrm{A1}}} \right)_{\mathrm{MC}}$$

$$\Omega^{\mathrm{MChe}}_{\mathrm{helium}} = \Omega^1_1 = \left(\frac{\frac{\mathrm{dN}}{\mathrm{dE}}\Big|^{\mathrm{He}\to\mathrm{He}}_{\neq\mathrm{A1}\to\mathrm{A1}}}{\frac{\mathrm{dN}}{\mathrm{dE}}\Big|^{\mathrm{p}\to\mathrm{He}}_{\mathrm{A1}\to\mathrm{A1}} + \frac{\mathrm{dN}}{\mathrm{dE}}\Big|^{\mathrm{p}\to\mathrm{He}}_{\neq\mathrm{A1}\to\mathrm{A1}} + \frac{\mathrm{dN}}{\mathrm{dE}}\Big|^{\mathrm{He}\to\mathrm{He}}_{\mathrm{A1}\to\mathrm{A1}} + \frac{\mathrm{dN}}{\mathrm{dE}}\Big|^{\mathrm{He}\to\mathrm{He}}_{\neq\mathrm{A1}\to\mathrm{A1}}} \right)_{\mathrm{MC}}$$

$$\Omega^{\mathrm{MChe}}_{\mathrm{proton}} = \Omega^1_0 = \left(\frac{\frac{\mathrm{dN}}{\mathrm{dE}}\Big|^{\mathrm{He}\to\mathrm{p}}_{\neq\mathrm{A1}\to\mathrm{A1}}}{\frac{\mathrm{dN}}{\mathrm{dE}}\Big|^{\mathrm{p}\to\mathrm{He}}_{\mathrm{A1}\to\mathrm{A1}} + \frac{\mathrm{dN}}{\mathrm{dE}}\Big|^{\mathrm{p}\to\mathrm{He}}_{\neq\mathrm{A1}\to\mathrm{A1}} + \frac{\mathrm{dN}}{\mathrm{dE}}\Big|^{\mathrm{He}\to\mathrm{He}}_{\mathrm{A1}\to\mathrm{A1}} + \frac{\mathrm{dN}}{\mathrm{dE}}\Big|^{\mathrm{He}\to\mathrm{He}}_{\neq\mathrm{A1}\to\mathrm{A1}}} \right)_{\mathrm{MC}}$$

Then, the *proton background* component is evaluated as

$$\frac{dB}{dE}\bigg|^{p\to He}_{A1\to A1} = C^{A1}_{proton} \times \left(\frac{dN}{dE}\bigg|^{Z=1}_{FD} - \Omega^0_0 \times \frac{dN}{dE}\bigg|^{Z=1}_{FD} - \Omega^1_0 \times \frac{dN}{dE}\bigg|^{Z=2}_{FD} \right)$$

where $\frac{\mathrm{dN}}{\mathrm{dE}}|_{\mathrm{FD}}$ are extracted from *in-flight* data based on the charge selection described in section 5.3 for helium candidates and a fixed charge window cut for proton[15].

The *off-acceptance background* components are computed as

$$\left.\frac{dB}{dE}\right|^{p\to He}_{\neq A1\to A1} = \Omega^0_1 \times \left.\frac{dN}{dE}\right|^{Z=1}_{FD}, \qquad \left.\frac{dB}{dE}\right|^{He\to He}_{\neq A1\to A1} = \Omega^1_1 \times \left.\frac{dN}{dE}\right|^{Z=2}_{FD}$$

and lastly, the fiducial spectrum to be provided as input to the unfolding routine is given by

$$\left.\frac{dN}{dE}\right|^{Z=2}_{BKSUB} = \left.\frac{dN}{dE}\right|^{Z=2}_{FD} - \sum \frac{dB}{dE} = \left.\frac{dN}{dE}\right|^{Z=2}_{FD} - \left.\frac{dB}{dE}\right|^{p\to He}_{A1\to A1} - \left.\frac{dB}{dE}\right|^{p\to He}_{\neq A1\to A1} - \left.\frac{dB}{dE}\right|^{He\to He}_{\neq A1\to A1}$$

4.4 Unfolding

4.4.1 Introduction

In the HEP context, the measured distribution of an observable is usually affected by the finite resolution and efficiency of the detector. Therefore, unfolding is being used to recover its true distribution by deconvolving it from the distortions caused by the instrument itself.

Following the treatment of Ref. [60], the measured distribution can be modelled as follows

$$f_{\text{meas}}(x) = \frac{1}{Z}\int dy\, S(x|y)\, \varepsilon(y) f_{\text{true}}(y) \tag{4.3}$$

in which Z is the normalization factor, $f_{\text{true}}(y)$ and $\varepsilon(y)$ are, respectively, the *true distribution* and the *efficiency* as function of the true value of the event (y), whereas $S(x|y)$ is the *resolution* function that accounts the conditional probability to measure the value x when the true value is y. Additionally, the *response function* is defined as $r(x|y) = S(x|y)\varepsilon(y)$.

However, in almost every real-world case, it is more convenient to *discretize* these functions by working with the related histograms. Hence, one can define

- $p_j = \int_{\Delta j} dy f_{\text{true}}(y)$ as the probability to find y in the bin Δj.
- μ_{tot} and $\mu_j = \mu_{\text{tot}} p_j$ as the expected number of true events in total and on bin[16] j, respectively.
- n_i and $n_{\text{tot}} = \sum_{i=1}^{N} n_i$ are the measured number of events for variable x in bin Δ_i and total number of detected events, respectively.
- $\nu_i = \mathbb{E}(n_i)$ is the expected number of measured entries in bin i.

The last term can be reformulated as

---

[15] $0.5 < Z_{\text{IMC}} < 1.7$ and $0.5 < Z_{\text{CHD}} < 1.7$

[16] $\vec{\mu} = \{\mu_1, \dots, \mu_N\}$ is usually referred to as the *true* histogram.

$$\begin{aligned} \nu_i &= \mu_{\text{tot}}\, Pr(x \in \Delta_i) \\ &= \mu_{\text{tot}} \int_{\Delta_i} dx \int dy\, r(x|y) f_{\text{true}}(y) \\ &= \sum_{j=1}^{N} \int_{\Delta_i} dx \int_{\Delta_j} dy\, \frac{r(x|y) f_{\text{true}}(y)}{\mu_j/\mu_{\text{tot}}} \mu_j \end{aligned}$$

Therefore, the *response matrix* R_{ij} is defined as

$$\nu_i = \sum_{j=1}^{N} R_{ij}\mu_j \longrightarrow \vec{\nu} = R\vec{\mu}$$

and it represents the conditional probability of observing an event with measured value x in bin Δ_i given that the true value y comes from bin Δ_j. It is worth noting that the mean efficiency ε_j for the bin j is derived by summing over the index i the response matrix, *i.e.* as $\sum_i R_{ij} = \varepsilon_j$.

At first glance, the inversion of the matrix R_{ij} seems to be the straightforward way to recover the true distribution $\vec{\mu}$. Nevertheless, this is an ill-posed problem because the measured histogram $\vec{n}$ is sampled from $\vec{\nu}$ but it is not $\vec{\nu}$ itself. In fact, the inversion of R-matrix leads to over-amplification of the just small statistical fluctuations[17] of the measured histogram $\vec{n}$ with respect to $\vec{\nu}$. Thus, the rationale behind any unfolding approach is to introduce a small bias to significantly reduce the variance. The best unfolding method for a given application is therefore the one that optimizes the bias-variance trade-off.

In this work, the measured value (x) is the energy deposited on TASC by the selected incoming particle $\text{E}_{\text{dep}}^{\text{TASC}}$, whereas the true value (y) is its primary energy E_{true} that is used to estimate the flux. To this aim, the `RooUnfold` package [22] integrated in the ROOT framework, was employed and the iterative bayesian [61, 62] and the SVD [90, 125] approaches have been tested in-depth as explained in the section 4.7.2. The measurements of the helium flux have thus been obtained via a two-iteration Bayesian unfolding, similar to the one used in the published CALET proton and helium analyses. In detail, the iterative bayesian unfolding algorithm starts from the probability $\Theta_{ij}^{(0)}$ calculated applying the Bayes' theorem

$$\Theta_{ij}^{(0)} = \Pr(y \in \Delta_j | x \in \Delta_i) = \frac{R_{ij} \Pr(y \in \Delta_j)}{\sum_j R_{ij} \Pr(y \in \Delta_j)}$$

The response matrix can be written as $R_{ij} = \Pr(x \in \Delta_i \,|\, y \in \Delta_j)$ where the probability $\Pr(y \in \Delta_j) = \mu_j^{(0)} / \sum_j \mu_j^{(0)}$ in which $\mu_j^{(0)}$ is the initial guess of

---

[17] Roughly speaking, the statistical fluctuations are treated as a residual fine structures of the true spectrum washed out by the folding with the response matrix at the reconstructed level. A toy example of such effect is reported in Refs. [59, 60] where the resulting estimators have no biases but extremely high variances.

truth spectrum in bin Δ_j. Thus, in the next iteration, the estimated number of true events in bin j is

$$\hat{\mu}_j^{(k+1)} = \frac{1}{\varepsilon_j}\sum_{i=1}^{N}\Theta_{ij}^{(k)} n_i$$

In contrast, the SVD approach belongs to the class of *regularized* unfolding algorithm, where instead of maximizing $\ln\mathcal{L}(\vec{\mu})$, the log-likelihood of matrix inversion[18], one defines a *smoothness* function[19] $S(\vec{\mu})$ and, thus it maximizes the function $\phi(\vec{\mu}) = \ln\mathcal{L}(\vec{\mu}) + \tau S(\vec{\mu})$ where the parameter τ controls the strength of the regularization.

4.4.2 Response matrix and unfolded spectrum

The response matrix obtained applying the aforementioned selections to the EPICS simulations, is shown in the left panel of Fig. 4.19. It is normalised by column[20] and the bin-to-bin migration is mainly between the two adjacent neighboring bins with respect to the next-to-reference deposited energy bin.

The preliminary unfolded energy spectrum is illustrated in the right panel of Fig. 4.19 along with the folded energy histogram achieved with the already described selections.

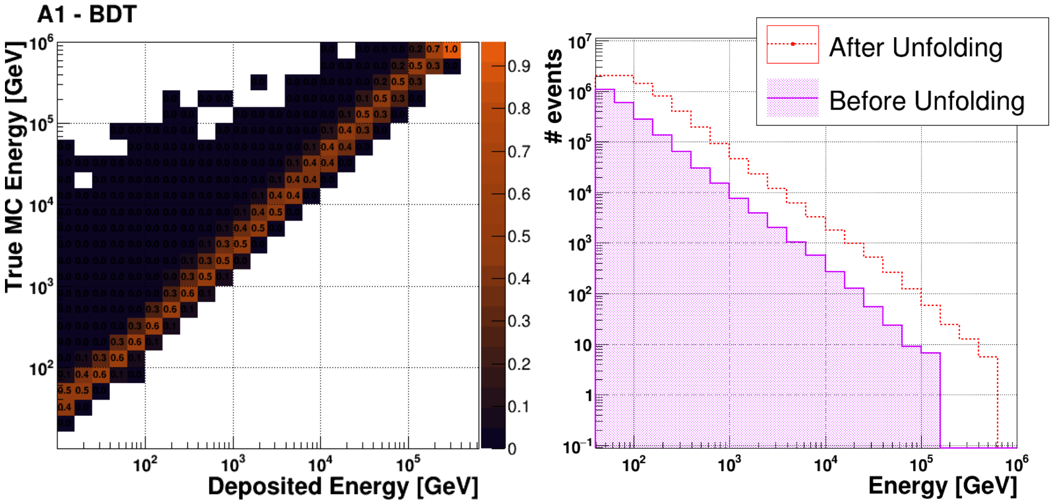

FIGURE 4.19: (Left) Response matrix, normalised by column and obtained with EPICS-based MC simulations. (Right) Preliminary energy spectra before and after the application of the bayesian unfolding with 2 iterations.

---

[18] For independent Poisson fluctuations,it is expressed as $\ln\mathcal{L}(\vec{\mu}) = \sum_{i=1}^{N}(n_i \ln\nu_i - \nu_i)$.

[19] In Tikhonov regularization, it assumes the form $S[f_{\text{true}}(y)] = -\int dy\left(\frac{d^k f_{\text{true}}(y)}{dy^k}\right)$ where k is set to 2. This formula can be discretized as function of $\vec{\mu}$, and it is used in SVD routine provided by `RooUnfold` .

[20] *i.e.* for each bin of deposited energy, the sum of the related bins of primary energy is equal to one

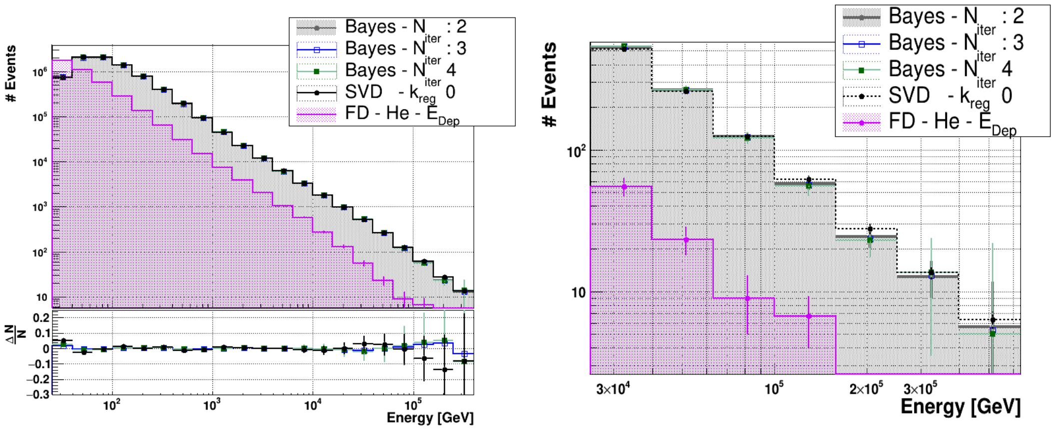

FIGURE 4.20: (Left) Preliminary energy spectra after the application of different unfolding procedures. In the bottom panel the relative error with respect to the reference unfolded spectrum achieved via bayesian unfolding with two iterations. (Right) Magnification on the high-energy region of the chart.

Unfolding FD spectrum with different approaches The FD deposited energy spectrum has been unfolded with the iterative Bayesian approach and with the SVD-based approach. In the former case, the number of iterations has been varied from 2 to 4. The preliminary unfolded energy spectra are shown in Fig. 4.20. The relative error with respect to the reference unfolded spectrum (bayesian unfolding with 2 iterations) are considered as systematics (see section 6.6) and they are within few percent over almost the entire energy range. In the high-energy region ($\gtrsim$ 100 TeV), the major source of uncertainty is from statistical fluctuations and the different spectra are compatible within the statistical errors as illustrated in the right panel of Fig. 4.20.

Assessment of statistical uncertainties

The `RooUnfold` unfolding routine provides an estimate of the statistical uncertainties. Nevertheless to assess its reliability, an independent evaluation is performed via the *bootstrap* method [70, 130]. The schematic is illustrated in the diagram 4.21. Each bin of the FD background-subtracted deposited energy spectrum is statistically fluctuated N_{trial} times according to a Gaussian distribution with mean equal to the number of events in the bin, and width equal to their RMS. Each *bootstrap* histograms are unfolded using the response matrix of the left panel of Fig. 4.19. Then, the *pull* distributions, normalized to the uncertainty provided by the unfolding routine, are constructed as described in paragraph 4.7.2 and, for each energy bin, the histograms are fitted with a Gaussian distribution. The results are shown in Fig. 4.22 where the energy bins ranging from 40 GeV to $\sim$ 400 TeV. In the bottom panel, the comprehensive view of the obtained fit parameters from the bin-by-bin fit of the pull distribution with a Gaussian function, shows a zero average bias and RMS compatible with the variance provided by the `RooUnfold` package.

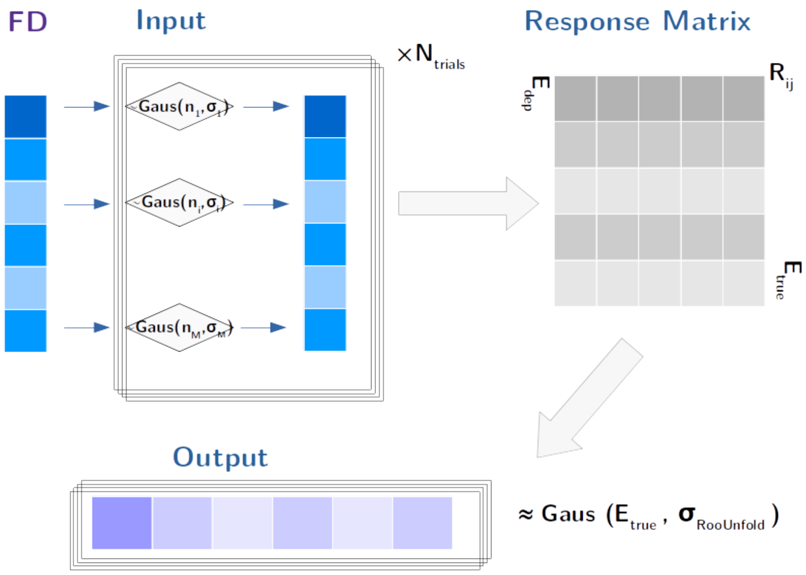

FIGURE 4.21: Schematic of the *bootstrap* technique used for assessing the statistical uncertainty related to the unfolding procedure.

4.5 Efficiency and Effective Acceptance

The estimation of CR helium flux requires two other quantities: the total efficiency of all the applied selections, as function of the primary energy, and the geometric factor of the detector.

The efficiency of a given selection in the energy interval ΔE, is defined as

$$\varepsilon_{\kappa}(\Delta E) = \frac{N_{\kappa}}{N_{\kappa-1}} \tag{4.4}$$

that is the ratio of the number of events passing the current cut κ to the number of events surviving the previous $\kappa - 1$ selections. A comprehensive view of the relative efficiencies for all the cuts utilized in this analysis is shown in the top panel of Fig. 4.23.

The geometric factor $S\Omega$ of the CALET for the `A1` acceptance is 510 cm^2 sr, evaluated via numerical integration of the *formulae* for symmetric telescope with rectangular cross-section reported in Ref. [124]. The bin-by-bin effective acceptance is illustrated in the bottom panel of Fig. 4.24 as function of the particle kinetic energy. The effective acceptance is defined as the product of the overall efficiency $\varepsilon_{\text{tot}}(\Delta E)$ multiplied by the geometric factor $(S\Omega)$.

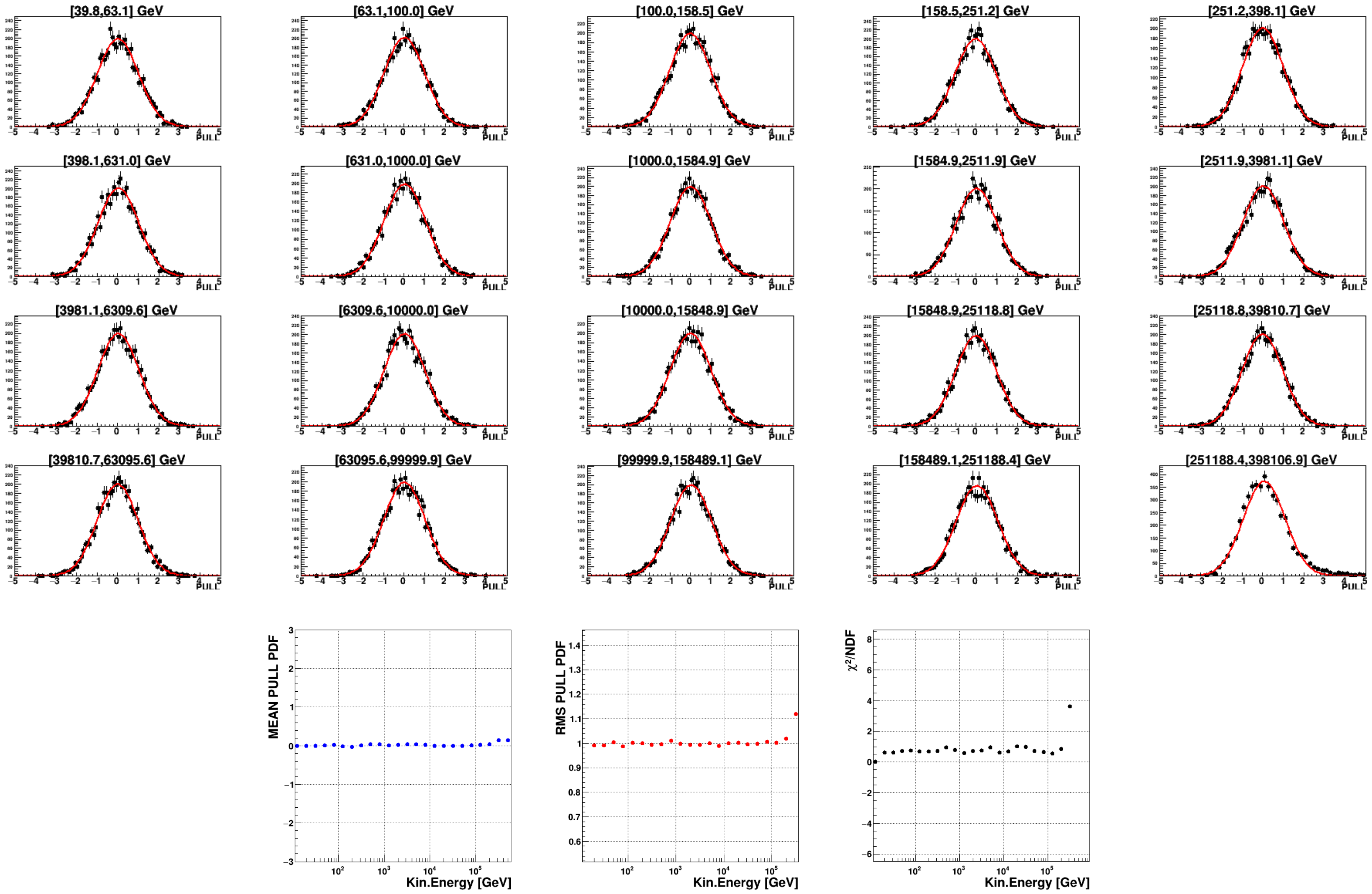

FIGURE 4.22: (Top) Pull distributions from *bootstrap* of FD unfolded spectrum obtained with $N_{\mathrm{trial}} = 5 \times 10^3$ trials. (Bottom) Comprehensive view of the bias, RMS and χ^2/NDF get from the Gaussian fit of pull distribution for each energy bin of the spectrum.

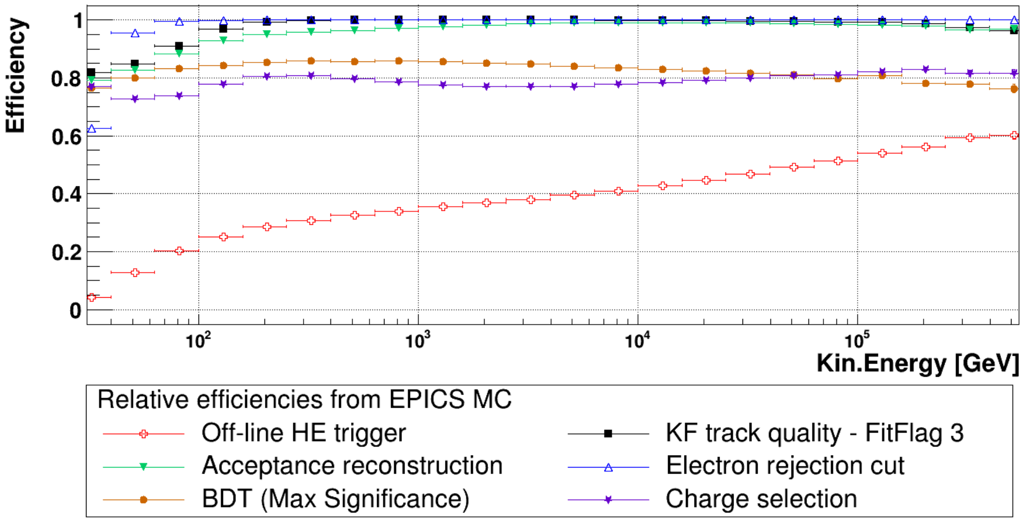

FIGURE 4.23: Relative efficiencies, as function of kinetic energy, from EPICS-based MC simulations in `A1` acceptance.

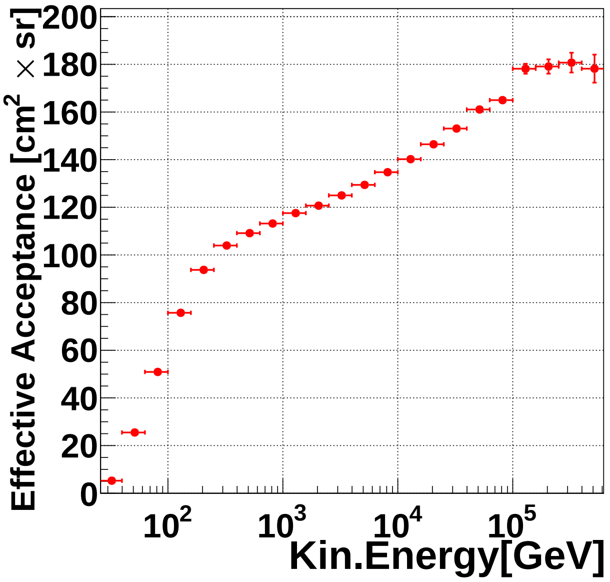

FIGURE 4.24: Effective acceptance, as function of kinetic energy.

4.6 Preliminary Flux Evaluation

The differential helium flux is experimentally derived according to the equation

$$\Phi_i^{\mathrm{He}} = \frac{U_i}{\Delta E_i \times (\varepsilon_i \times S\Omega) \times T} = \frac{U_i}{\Delta E_i \times A_i^{\mathrm{eff}} \times T} \tag{4.5}$$

where $\Phi_i^{\mathrm{He}}(E)$, ΔE_i, ε_i, A_i^{eff} and U_i represent, respectively, the measured flux, the energy interval, the overall efficiency, the effective acceptance and the number of events of the unfolded spectrum, in the i$^{\mathrm{th}}$ bin. The live-time and the geometric factor are symbolized by T and $S\Omega$.

The preliminary flux obtained using 87 months of CALET data, from October 13th, 2015 to December 31th, 2022, and the `A1` fiducial acceptance, is shown in Fig. 4.25, multiplied by $E^{2.6}$ and compared to the helium flux, published in the PRL journal [8] by the CALET collaboration in 2023. They are compatible, within the errors, with the PRL helium flux, over the entire energy range.

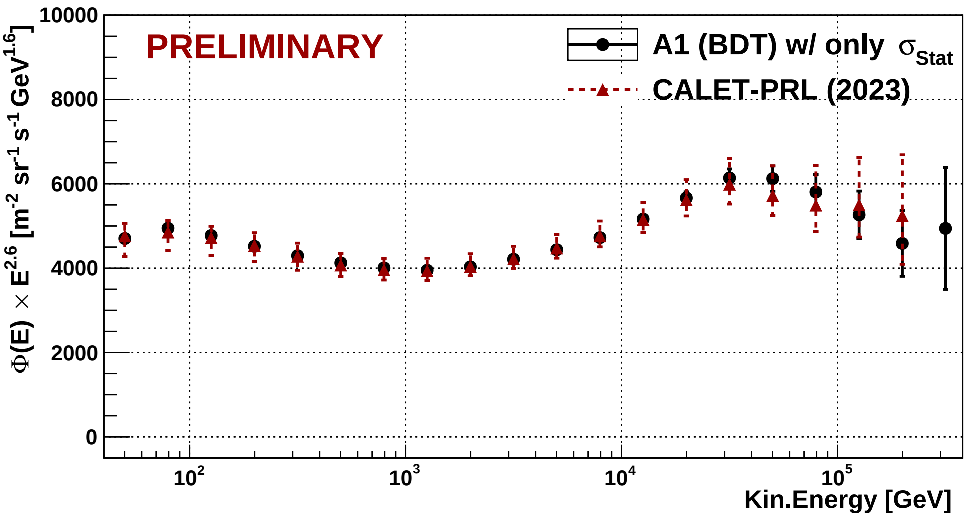

FIGURE 4.25: Helium flux multiplied by $E^{2.6}$, obtained using the selections described in this thesis. Vertical bars represent only statistical uncertainties derived by standard error propagation.

In addition, the comparison of the ratio of the sum of all background components to the total signal is represented in the left panel of Fig.4.26 as a function of kinetic energy. This indicates that the analysis of this work improves the background rejection at energies greater than about 1 TeV. The right panel of the same figure, shows the purity[21] quantity in this energy range. The better performance above about 3 TeV results in an improved statistical precision of the measured flux in this energy region.

---

[21] Defined as in Ref. [101], *i.e.* the number of helium events after the background subtraction divided by the total number of events reconstructed as helium.

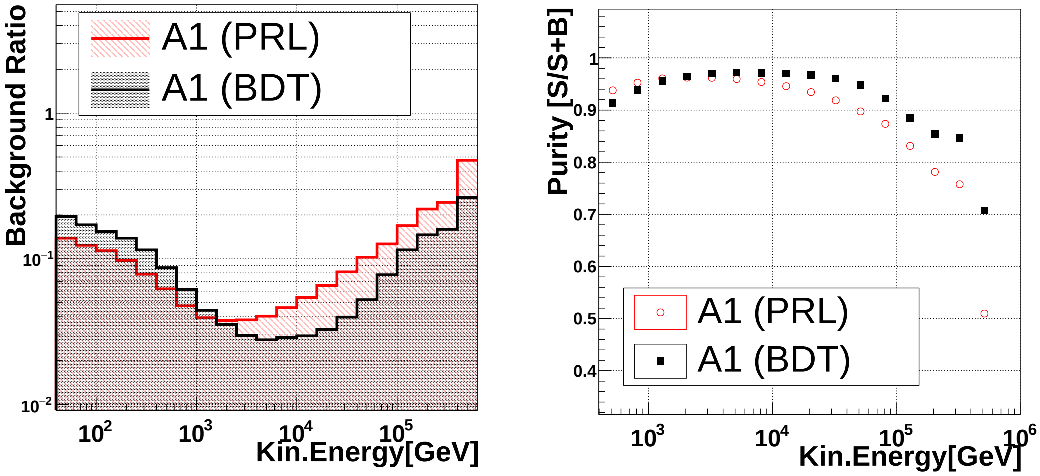

FIGURE 4.26: Comparison between PRL-like (red) analysis [8] and the BDT-based (black) analysis of this work in `A1` geometrical acceptance, as function of kinetic energy. (Left) Estimated total background ratios. (Right) Purity, defined as the number of helium events after the background subtraction divided by the total number of events reconstructed as helium $\frac{S}{S+B}$.

4.7 Additional validations

4.7.1 BDT Model

The robustness of the adopted BDT model (described in Section 4.1) has been tested by varying hyper-parameters as follows. Initially the number of trees was set equal to 500 and 1000, while fixing the maximum depth to 3. Subsequently, the maximum depth of the tree was scanned from 3 to 6, by letting the the number of trees equal to 1000, since it is actually the same for the values 500 and 850.

The overall results are shown in Fig. 4.27 where one can appreciate that the consistency is good over the entire energy range

4.7.2 Unfolding procedure

Unfolding is a complex procedure that needs to be extensively tested before it can be used to analyze data. In this work, the testing part has been performed on the simulated data based on EPICS MC generator. Specifically, it was divided in two main phases: the *technical* test and the *pull* test as explained in the next paragraphs.

Technical test

The technical test consists in providing MC deposited energy spectrum $\vec{n}^{\mathrm{MC}}_{\mathrm{dep}}$ as an input to the unfolding routine and in ensuring that the unfolded spectrum $\vec{n}^{\mathrm{MC}}_{\mathrm{true}}$ is compatible to the MC primary energy spectrum $\vec{\mu}^{\mathrm{MC}}_{\mathrm{true}}$. For this

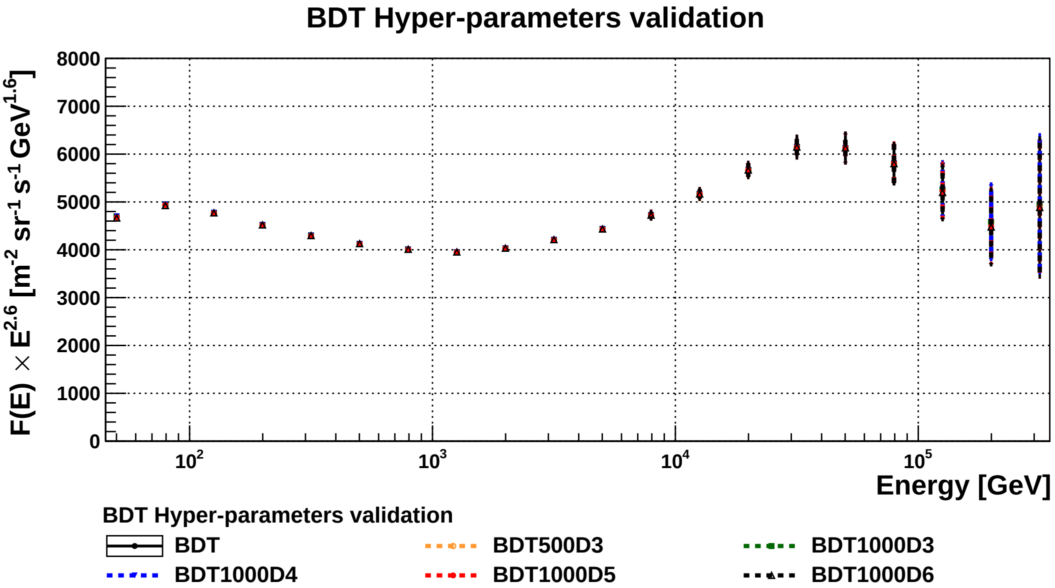

FIGURE 4.27: Preliminary helium fluxes in `A1` acceptance obtained by varying the BDT hyper-parameters: number of trees (n_{trees}) and the maximum depth t_{depth} of the tree. The reference configuration (black markers) has $t_{\text{depth}} = 3$ and $n_{\text{trees}} = 850$. The others are achieved both by scanning t_{depth} from 3 to 6 fixing $n_{\text{trees}} = 1000$, and by setting the n_{trees} equal to 500 and 1000 with $t_{\text{depth}} = 3$.

test, the MC sample is partitioned in two halfs. One sub-sample is considered to fill the deposited energy spectrum, whereas the other is used to build the response matrix. The unfolding methods that have been studied are: iterative Bayesian algorithm scanning the number of iterations from 2 to 4, and the SVD approach with an internally optimization of the regularization parameter[22].

The results are presented in Fig. 4.28 where the true spectrum is recovered within ∼ 2% in the energy range from ∼ 60 GeV to 250 TeV, for each unfolding approach. In the remaining energy bins, the outcomes are still compatible within the statistical errors.

Pull test A more sophisticated test based on *bootstrap* technique [70, 130], has been carried out to control in-depth the stability of the unfolding procedure over the entire energy range and its bias-variance trade-off. In the HEP field, such test is commonly referred to as *pull* test (*e.g.* see [42]) and the implementation of this work is schematically illustrated in the diagram of Fig. 4.29.

Each re-weighted MC helium event, passing all the selections described in the previous sections, is fluctuated according to a Poisson distribution with a mean of one. Hence, a statistically fluctuated replica of $\vec{n}_{\text{dep}}^{\text{MC}}$ is achieved. If such a procedure is repeated N_{toy} times, the set of *replicae* $\{ \vec{n}_{\text{dep}}^{\text{TOY,j}} \}_{j=1,..,\text{N}_{\text{toy}}}$

---

[22] $k_{reg} = 0$ option in `RooUnfold` package.

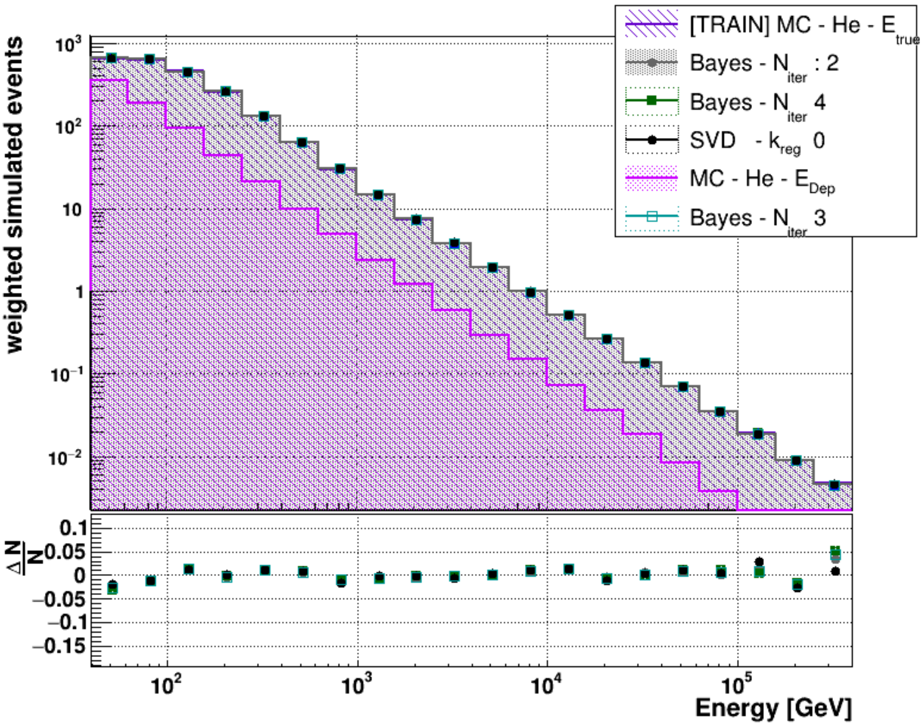

FIGURE 4.28: Results of the unfolding technical test using EPICS-based MC simulations. (Top) In magenta the histogram of MC deposited energy spectrum. The related unfolded spectra, achieved by using iterative Bayes algorithm (with the number of iterations from 2 to 4) and by using SVD approach, are shown with markers. The primary energy spectrum (true energy) is presented as violet filled histogram. (Bottom) Percentage difference between the unfolded spectra and the MC primary energy spectrum.

can thus be deconvolved, providing the standard matrix R_{ij}^{MC} to the unfolding routine. From the set of unfolded replica spectra $\{\ \vec{n}_{\mathrm{true}}^{\mathrm{TOY,j}}\ \}_{j=1,..,\mathrm{N_{toy}}}$, the histograms representing *pull* distributions are derived as follows

$$\vec{\pi} = \sum_{j=1}^{\mathrm{N_{toy}}} \frac{\vec{n}_{\mathrm{true}}^{\mathrm{TOY,j}} - \vec{n}_{\mathrm{UNFLD}}^{0}}{\sigma_{\mathrm{UNFLD}}^{0}}$$

where each entry i of the vector $\vec{\pi}$ corresponds to *pull* distribution for the primary energy interval ΔE_i and $\vec{n}_{\mathrm{UNFLD}}^{0}$, $\sigma_{\mathrm{UNFLD}}^{0}$ are the unfolded histogram $\vec{n}_{\mathrm{true}}^{\mathrm{MC}}$ and the related errors (computed analytically or provided by the unfolding routine) from the MC sample without fluctuations, respectively.

The stability of the unfolding procedure is ensured if each π_i histogram is Gaussian-shaped with mean and RMS approximately equal to 0 and 1, respectively. The average value centred at zero, means that the bias induced by unfolding is negligible, whereas the unitary width guarantees the reliability of the variance's estimation.

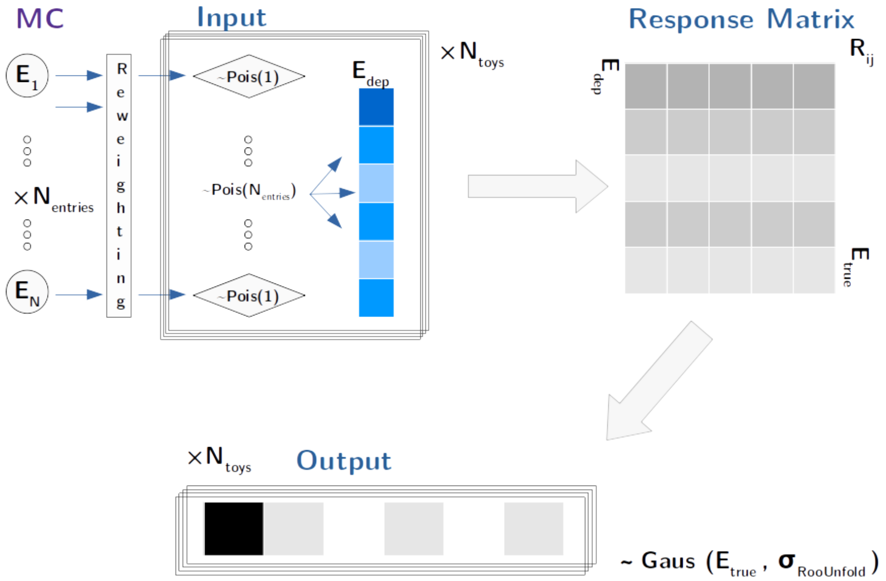

FIGURE 4.29: Schematic of the pull test for unfolding algorithm validation.

The *pull* distributions for the Bayesian unfolding with 2 iterations and for the SVD approach are shown in Figs. 4.30 and 4.31 where the energy range is from 15 GeV to 1 PeV, with 5 bins per decade. Results are stable over the entire range beside a little systematic bias that is present above 100 TeV for the SVD approach. Thus, the Bayesian unfolding with 2 iterations has been used in this analysis as the one published in Ref. [8].

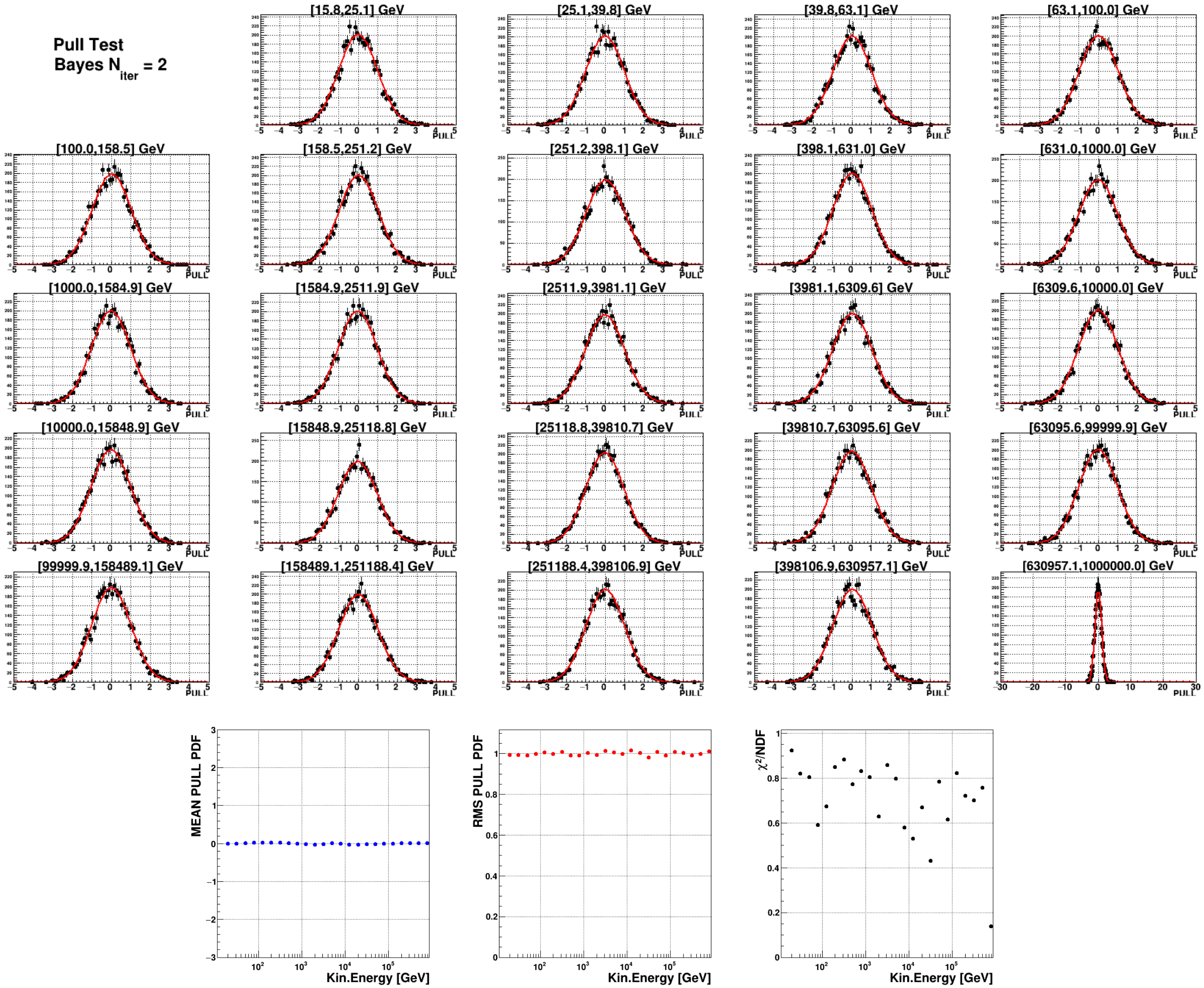

FIGURE 4.30: (Top) Pull distributions for a set of energy bin ranging from 15 GeV to 1 PeV, obtained with $N_{toy} = 5 \times 10^3$ simulations based on EPICS MC. The unfolding algorithm is the iterative Bayesian approach with $N_{iter} = 2$. (Bottom) Comprehensive view of the bias, RMS and χ^2/NDF get from the Gaussian fit of pull distribution for each energy bin of the spectrum.

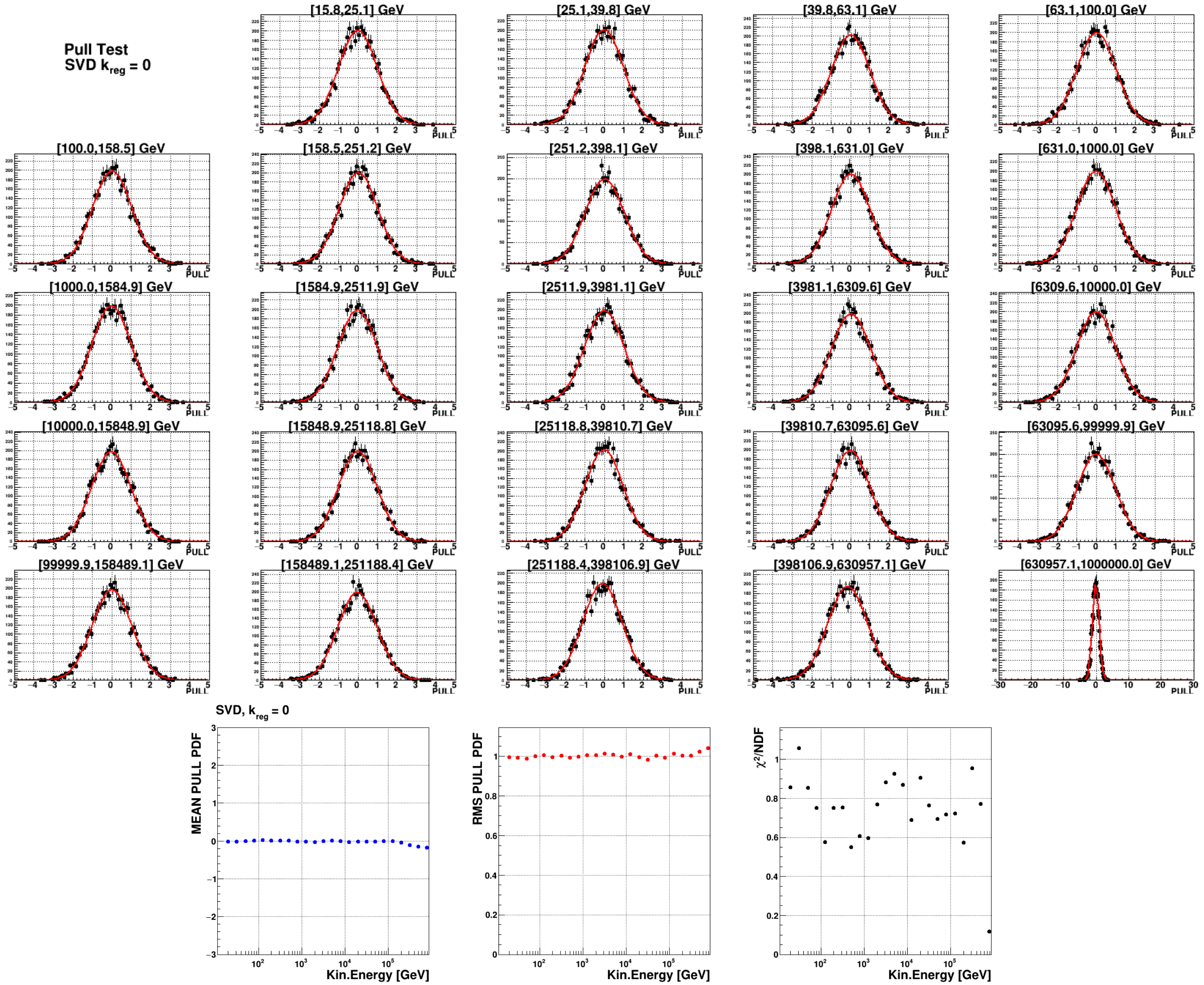

FIGURE 4.31: (Top) Pull distributions for a set of energy bin ranging from 15 GeV to 1 PeV, obtained with $N_{toy} = 5 \times 10^3$ simulations based on EPICS MC. The unfolding approach is based on SVD with the regularization parameter $k_{reg} = 0$ (optimized internally by the `RooUnfold` package). (Bottom) Comprehensive view of the bias, RMS and χ^2/NDF get from the Gaussian fit of pull distribution for each energy bin of the spectrum.

4.7.3 CHD contribution

As already pointed out, the charge identification for the helium analysis essentially rely on the IMC detector as energy increases, while the contribution from CHD sub-system gradually diminishes. Specifically, the degradation of CHD charge resolution results from the growing number of secondaries that are back-scattered[23] as the energy deposited increases.

The feasibility of measuring a flux using only the IMC sub-detector for charge tagging has been therefore investigated. The result obtained in acceptance `A1` is shown in Fig 4.32, where one can appreciate that the agreement is very good over the entire energy range. The slight deviation in the last bins is imputable to the very limited statistics.

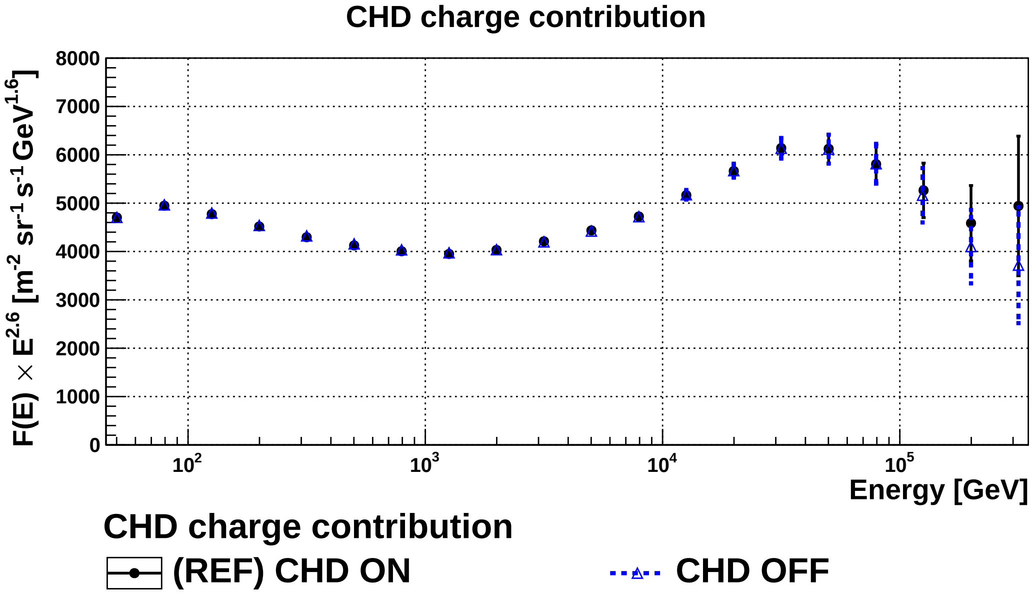

FIGURE 4.32: Contribution of the CHD sub-detector for performing charge identification in `A1` acceptance. In black the reference flux, while in blue the flux achieved using only the IMC sub-detector for helium charge identification with the same energy-dependent selection.

This has led to the study of more challenging geometrical configurations in which events enter laterally, *i.e.* essentially without crossing the CHD detector. Specifically, such events are required both to cross most of the IMC layers, but also to take a sufficiently long path through the calorimeter. The former is critical to reliably constructing the charge estimator, the latter to not deteriorate the energy resolution. Hence, enlarging the fiducial acceptance aims to improve the accuracy of the flux measurement, with special emphasis on the high energy region, where statistics is the main limiting factor. The next chapter is devoted to a detailed explanation of the extensions in acceptance that have been investigated.

---

[23] They are also referred to as *albedo* particles.

Chapter 5

Helium flux measurements in extended acceptances

The main source of uncertainty in the measurement of helium flux at high energies arises from the very limited statistics. Extending the geometrical acceptance beyond `A1`, it is a possible way to partially overcome this problem. This chapter describes a newly developed analysis based on a broader geometric acceptance than `A1`. For this measurement only the IMC is used for charge identification (see section 4.7.3), and BDT-based selections are applied to keep the background under control.

5.1 Analysis strategy

The main objective of this analysis is to include events that pass through the detector at a greater tilt angle with respect to the ones from `A1` acceptance. Namely, events that belong to the $\mathtt{K}_i$ geometric acceptance categories. This will improve the statistical accuracy of the helium flux measurement with CALET data. Specifically, when the the largest acceptance `K5` is considered, the expected statistical gain is about a factor of two. Table 5.1 details the geometric factors and the expected statistical gains for $\mathtt{K}_i$ acceptances.

TABLE 5.1: Geometric factors for $\mathtt{K}_i$ extended acceptances with the related statistical gain normalized to `A1` fiducial acceptance.

Acceptance Category	Geometric Factor [cm^2 sr]	Statistical Gain
`A1`	510	1
`K0` = `A1` + `D0`	590.6	1.16
`K1` = `K0` + `C1+D1`	688	1.35
`K2` = `K1` + `C2+D2`	750.7	1.47
`K3` = `K2` + `C3+D3`	819.6	1.6
`K4` = `K3` + `C4+D4`	898.1	1.76
`K5` = `K4` + `C5+D5`	985.3	1.93

The reliability of charge identification and the rejection of the additional *off-acceptance* background are the main challenges that arise when relaxing the geometrical requirements for helium event selection. In particular, an increase in proton contamination, especially at low energies, is foreseen for events crossing only the IMC sub-system when the same selections described in the previous chapter are used. In addition, a further increase in the *off-acceptance* contamination is expected due to the partial degradation of the tracking algorithm performance for very tilted events.

The strategy to obtain preliminary measurements of helium flux in the `K1` and `K3` extended acceptances is discussed in the following sections. These allow a statistical gain of up to 60 percent in the high-energy region. Further extensions to `K4` and `K5` acceptances are beyond the scope of this Thesis because they require additional studies due to the limited number of IMC layers that are crossed.

In summary, after a pre-selection, identical to the one described in Chapter 3, a dedicated BDT-based selection is applied. This selection is specific for *off-acceptance* background rejection and it is defined for the `A1+D0`, `C1+D1`, `C2+D2`, and `C3+D3` acceptances separately[1]. For each of these categories, the distributions of both the features and the classifiers are studied with the simulated and real data, in the same way as described for the `A1` analysis. Subsequently, energy-dependent charge selection is performed for each one of the acceptance categories listed above, using only the IMC charge estimator. Next, the extended acceptances `K1` and `K3` are considered, and both the energy response and background components are evaluated for these configurations. After background subtraction, the unfolding procedure is applied and its stability is tested using the *bootstrap* method. Then the efficiencies of the different selections are calculated and, the fluxes are evaluated with their statistical uncertainties.

5.2 BDT-based *off-acceptance* selections

After the pre-selection step and by additionally requiring the existence of IMC charge (*i.e.* greater than zero), the distributions of the same features used in `A1` analysis (see section 4.1) have been examined for the construction of BDT classifiers, with the aim of improving the performance of the *off-acceptance* background rejection. As anticipated in the introduction of the Chapter 4, this ML technique allows the definition of customized selections based on the topology of the reconstructed event.

5.2.1 Feature validation

The first step is to check the agreement of the topological variables for the real and simulated data. In Figs. 5.1 and 5.2 are depicted the distributions for the Θ^X_{TK} variable (similar results are achieved for the Θ^Y_{TK} variable). The data-MC agreement is good over the entire energy range and the signal-to-noise separation power is similar to that of `A1` for all extended acceptances

---

[1] Since for geometric acceptances $\mathtt{C}_i$, $\mathtt{D}_i$, and `D0` the statistics of the FD is limited, different categories where combined together. The configurations `A1+D0` and $\mathtt{C}_i$+$\mathtt{D}_i$ were chosen because the event topologies are similar and the IMC charge distributions are fairly compatible.

considered. Next, variables related to the deposited energy profile have been investigated. As an example, some of them are shown in the Figs. 5.3, 5.4, 5.5 and 5.6, representing the fractional energy deposit in the `X1` and `Y6` layers of the TASC detector. The agreement between the FD and MC data is good over the entire energy range, at least up to where the statistics is sufficient for comparison.

This validation is particularly important and provides a first check of the energy response of the detector for events occurring at a larger tilt angle. The signal-to-background separation power turns out to be similar for `A1+D0` and `C1+D1`, while slightly lower for `C2+D2` and `C3+D3`. After this validation procedure, the same 13 features used in the analysis of `A1` have been applied to define BDT-based selections in the extended acceptances.

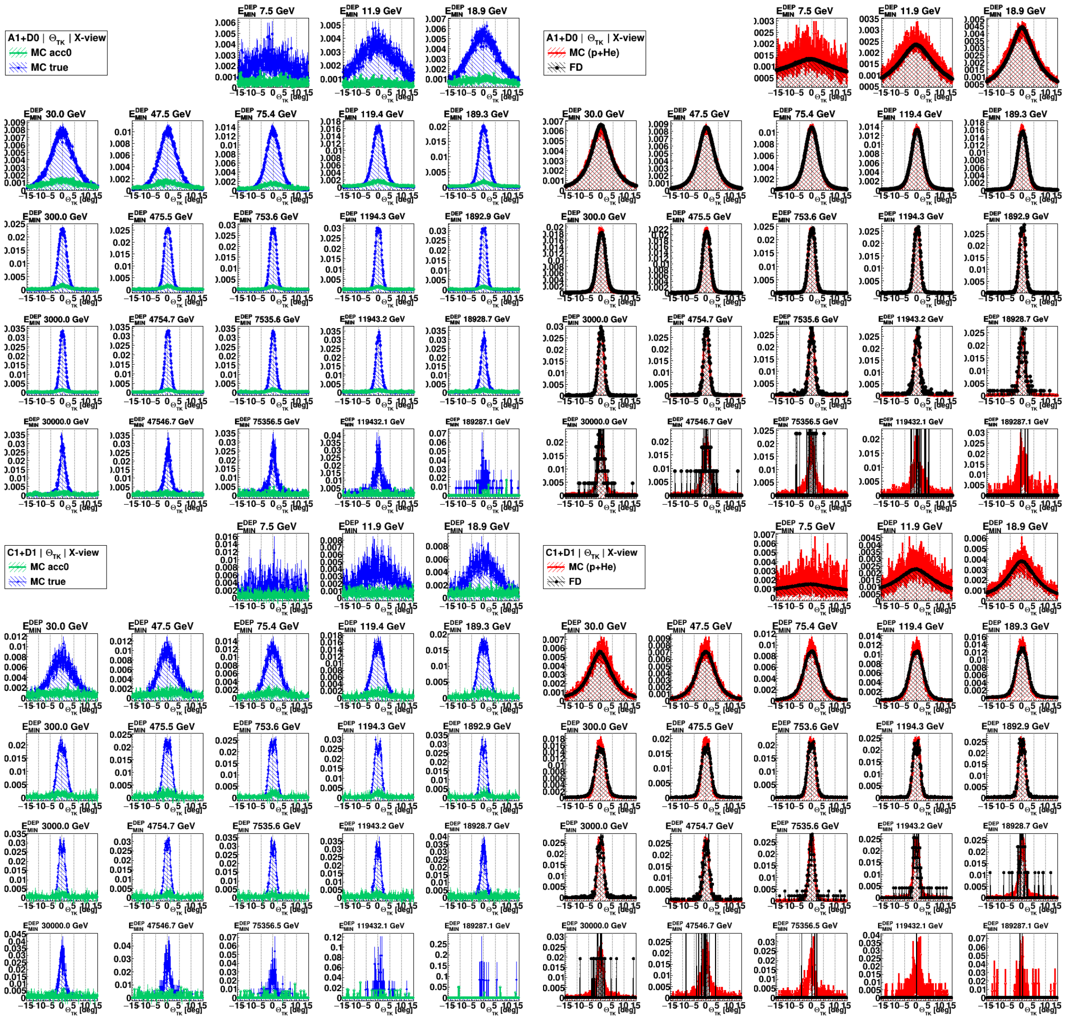

FIGURE 5.1: (Left) Signal-to-background separation and (right) comparison of FD and MC distributions for Θ^{X}_{TK} variable in `A1+D0` (top half) and `C1+D1` (bottom half) acceptances. The MC data are from EPICS simulations. The TASC deposited energy bins ranges from 7.5 GeV up to 300 TeV.

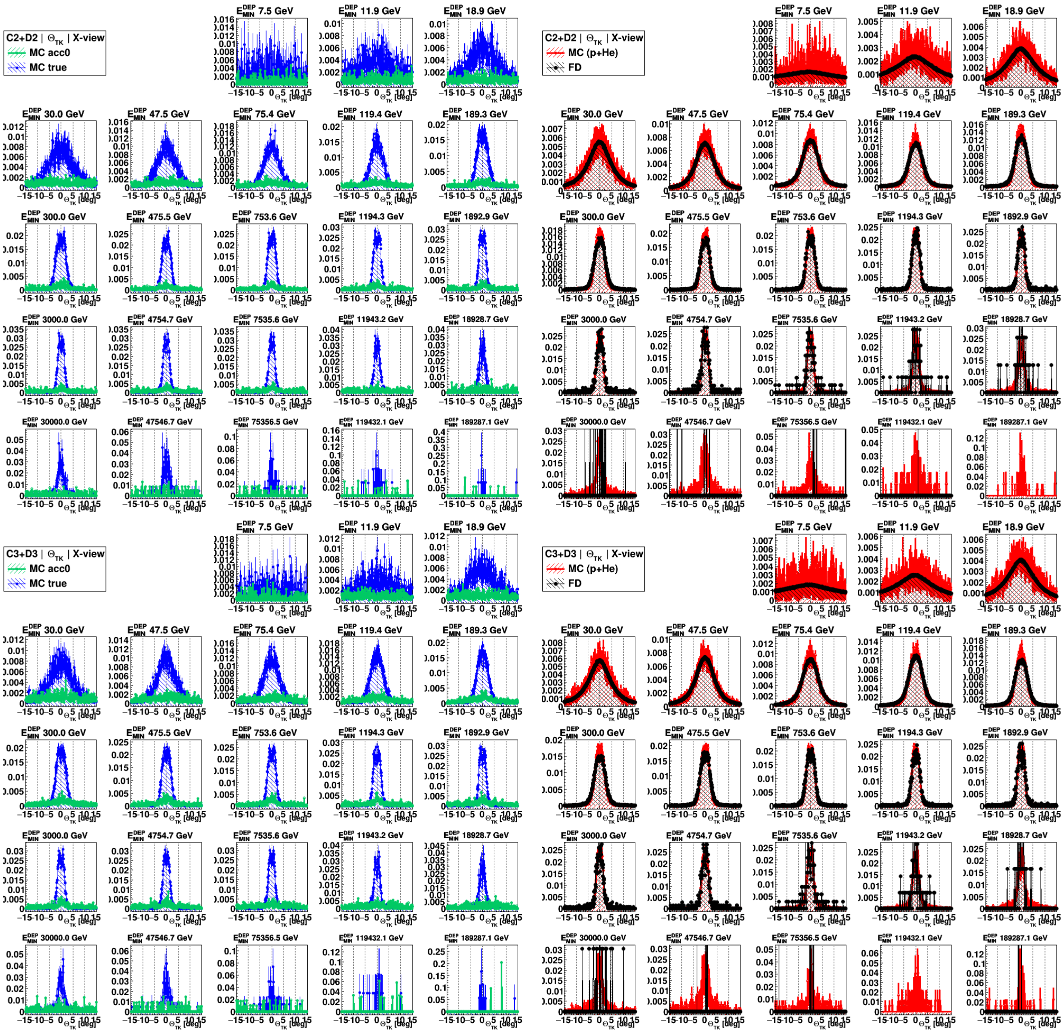

FIGURE 5.2: (Left) Signal-to-background separation and (right) comparison of FD and MC distributions for Θ^{X}_{TK} variable in C2+D2 (top half) and C3+D3 (bottom half) acceptances. The MC data are from EPICS simulations. The TASC deposited energy bins ranges from 7.5 GeV up to 300 TeV.

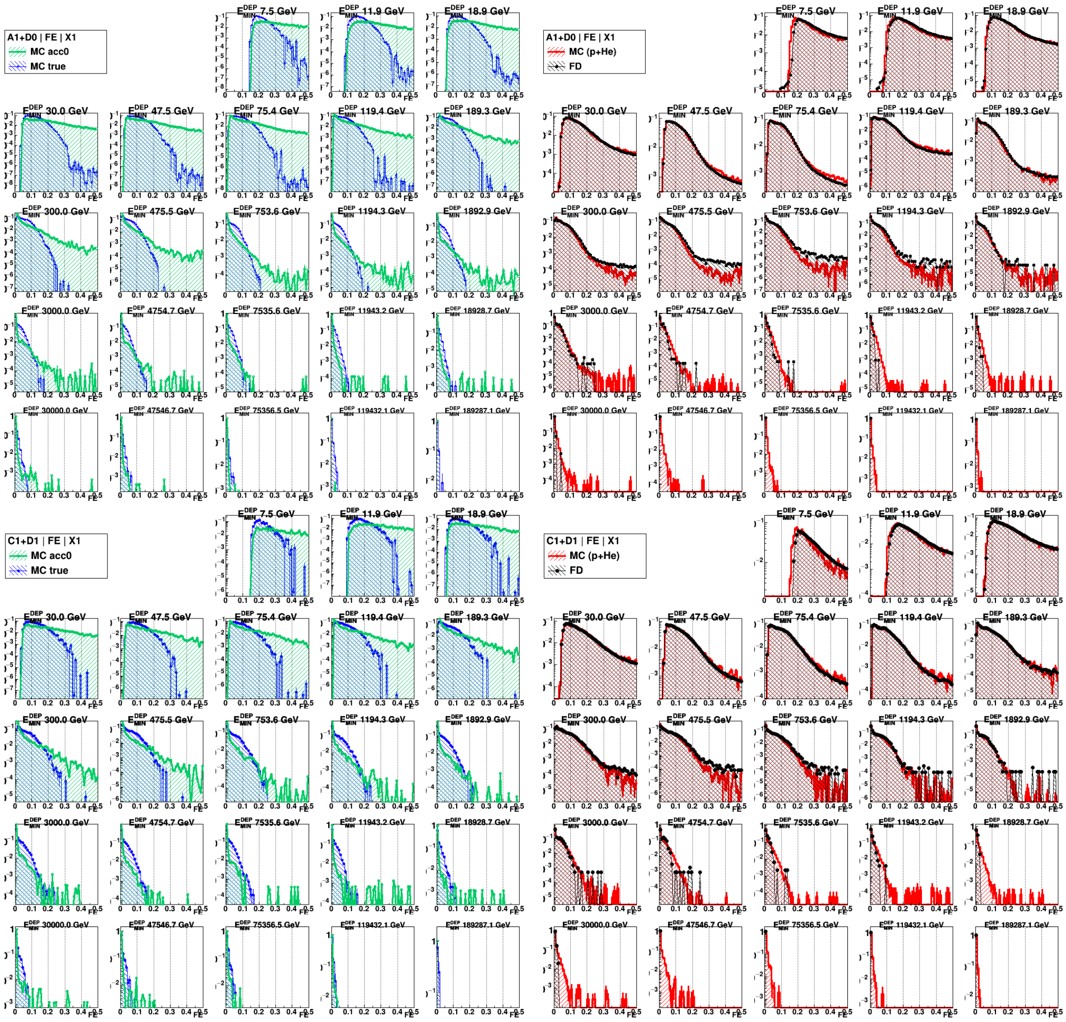

FIGURE 5.3: (Left) Signal-to-background separation and (right) comparison of FD and MC distributions for the fraction of energy deposited in the first layer (X1) in `A1+D0` (top half) and `C1+D1` (bottom half) acceptances. The MC data are from EPICS simulations. The TASC deposited energy bins ranges from 7.5 GeV up to 300 TeV.

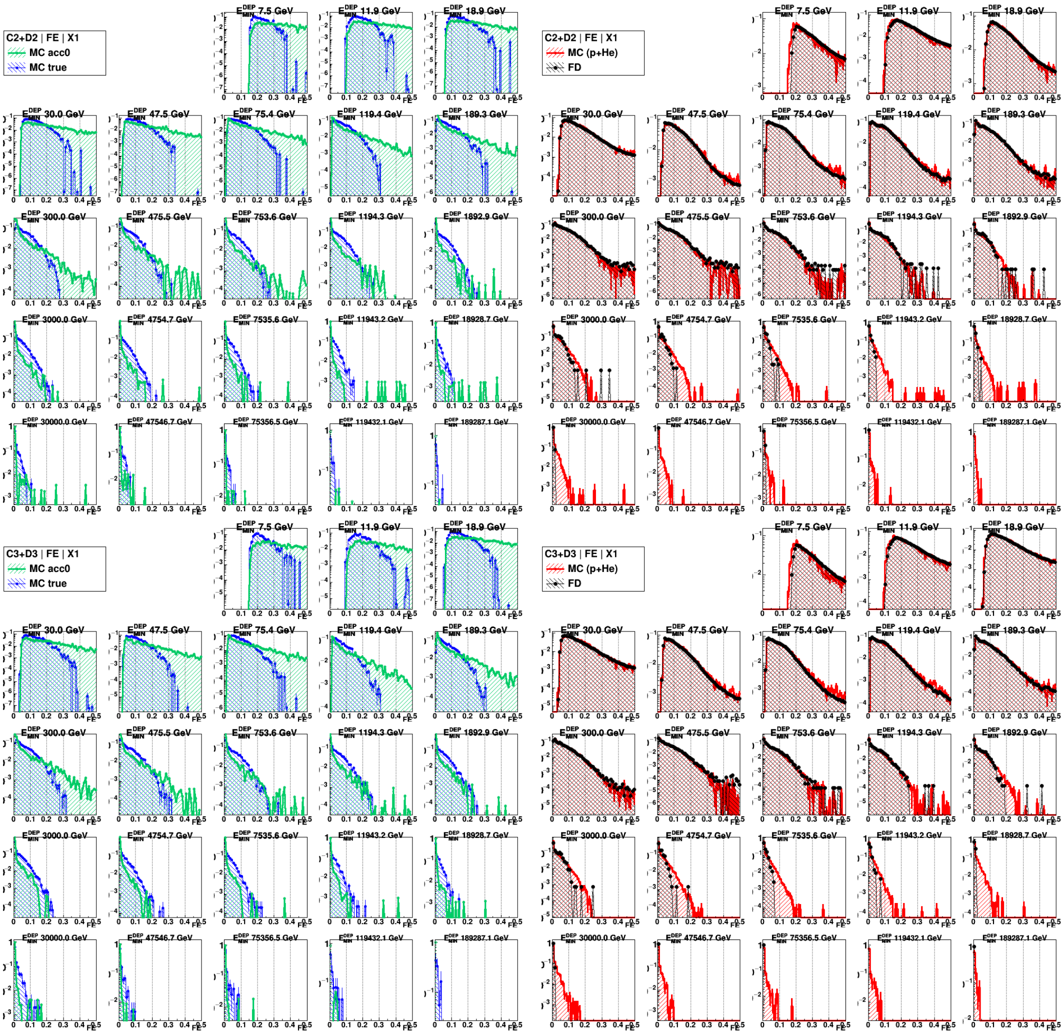

FIGURE 5.4: (Left) Signal-to-background separation and (right) comparison of FD and MC distributions for the fraction of energy deposited in the first layer (X1) in `C2+D2` (top half) and `C3+D3` (bottom half) acceptances. The MC data are from EPICS simulations. The TASC deposited energy bins ranges from 7.5 GeV up to 300 TeV.

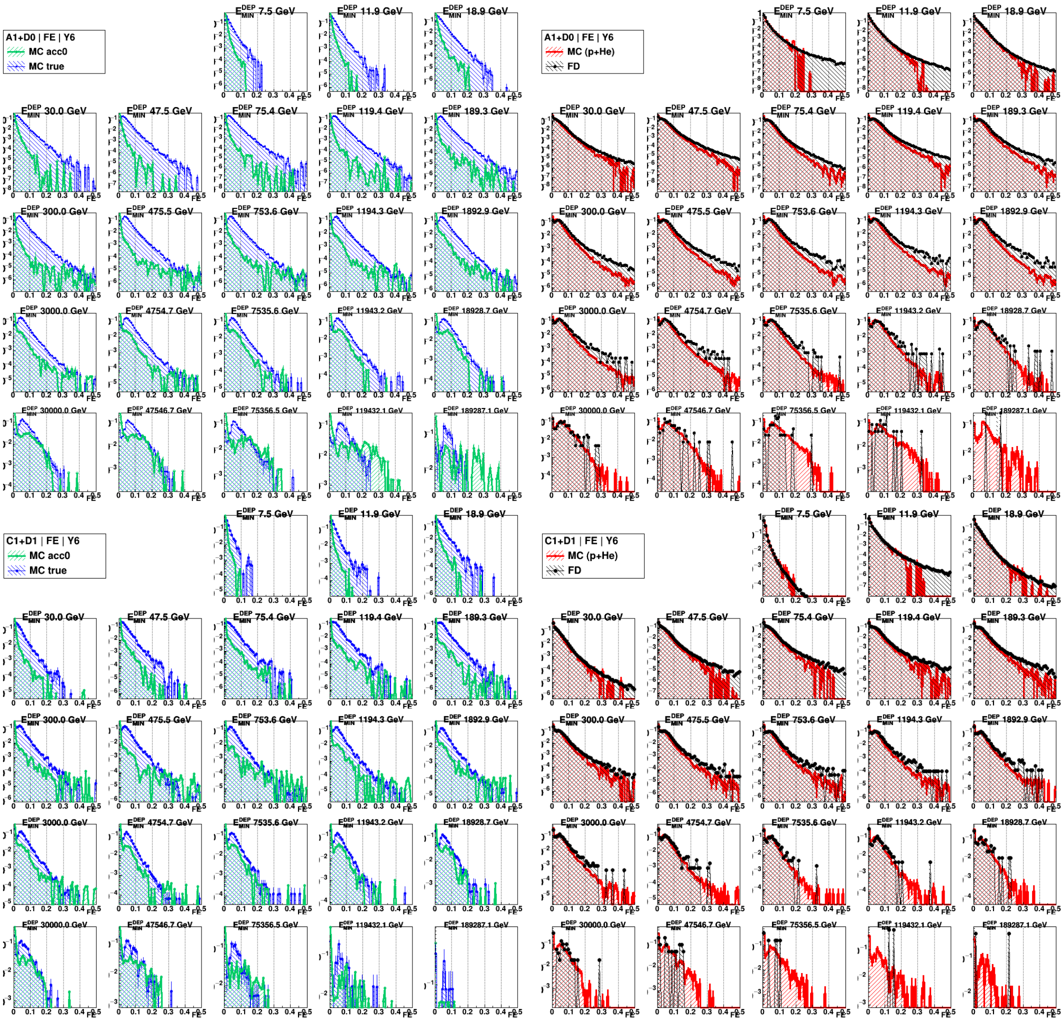

FIGURE 5.5: (Left) Signal-to-background separation and (right) comparison of FD and MC distributions for the fraction of energy deposited in the last layer (Y6) in `A1+D0` (top half) and `C1+D1` (bottom half) acceptances. The MC data are from EPICS simulations. The TASC deposited energy bins ranges from 7.5 GeV up to 300 TeV.

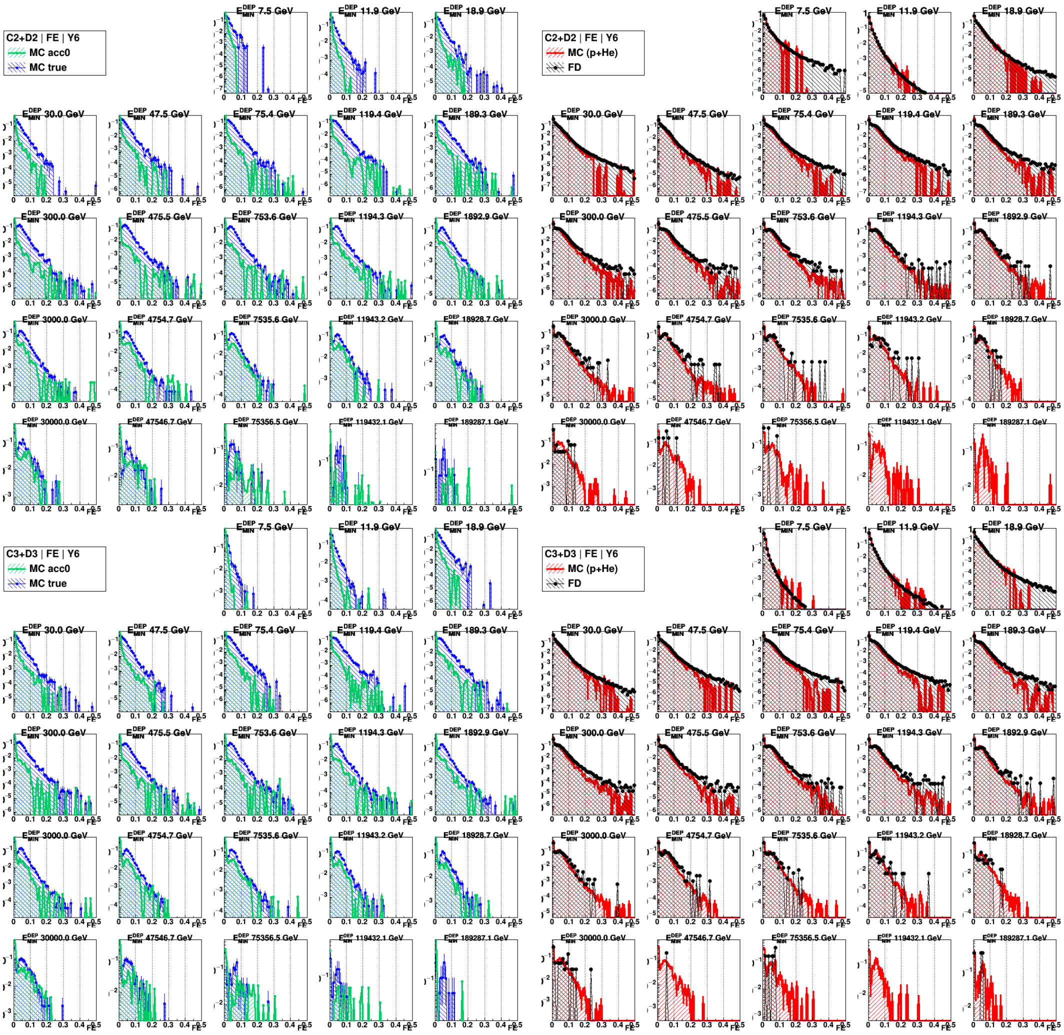

FIGURE 5.6: (Left) Signal-to-background separation and (right) comparison of FD and MC distributions for the fraction of energy deposited in the last layer (Y6) in `C2+D2` (top half) and `C3+D3` (bottom half) acceptances. The MC data are from EPICS simulations. The TASC deposited energy bins ranges from 7.5 GeV up to 300 TeV.

5.2.2 Classifier distributions

The BDT classifier distributions have been evaluated dividing the deposited energy range into the same six intervals reported in the subsection 4.1.3. The results of the over-training test for geometric acceptances `A1+D0`, `C1+D1`, `C2+D2` and `C3+D3` in the energy intervals 30-120 GeV and 6.5-20 TeV, are shown in the top and bottom panel of Fig. 5.7, respectively. The distributions exhibit good agreement for each acceptance category considered. Similar performance is achieved in the other energy intervals.

In Fig. 5.8, the BDT classifiers from FD have been compared with the response derived from simulations, in the same energy intervals. They show a fairly good agreement for all the acceptance considered. Similar results are also obtained for other energy bins. Finally, table 5.2 summarizes the BDT working points for the geometric acceptances `A1+D0`, `C1+D1`, `C2+D2` and `C3+D3`, that have been evaluated numerically by taking the maximum of the *significance* figure of merit.

BDT working point Deposited Energy Range	`A1+D0`	`C1+D1`	`C2+D2`	`C3+D3`
$10 - 30$ GeV	-0.004	-0.022	-0.013	-0.001
$30 - 120$ GeV	-0.023	-0.012	0.008	-0.012
$120 - 300$ GeV	-0.015	0.020	-0.012	0.015
$0.3 - 6.5$ TeV	-0.028	-0.012	-0.016	-0.029
$6.5 - 20$ TeV	-0.026	0.003	0.011	-0.008
> 20 TeV	-0.009	-0.008	-0.051	0.062

TABLE 5.2: BDT working points for the geometric acceptances `A1+D0`, `C1+D1`, `C2+D2` and `C3+D3`, evaluated by taking the maximum of the *significance* figure of merit.

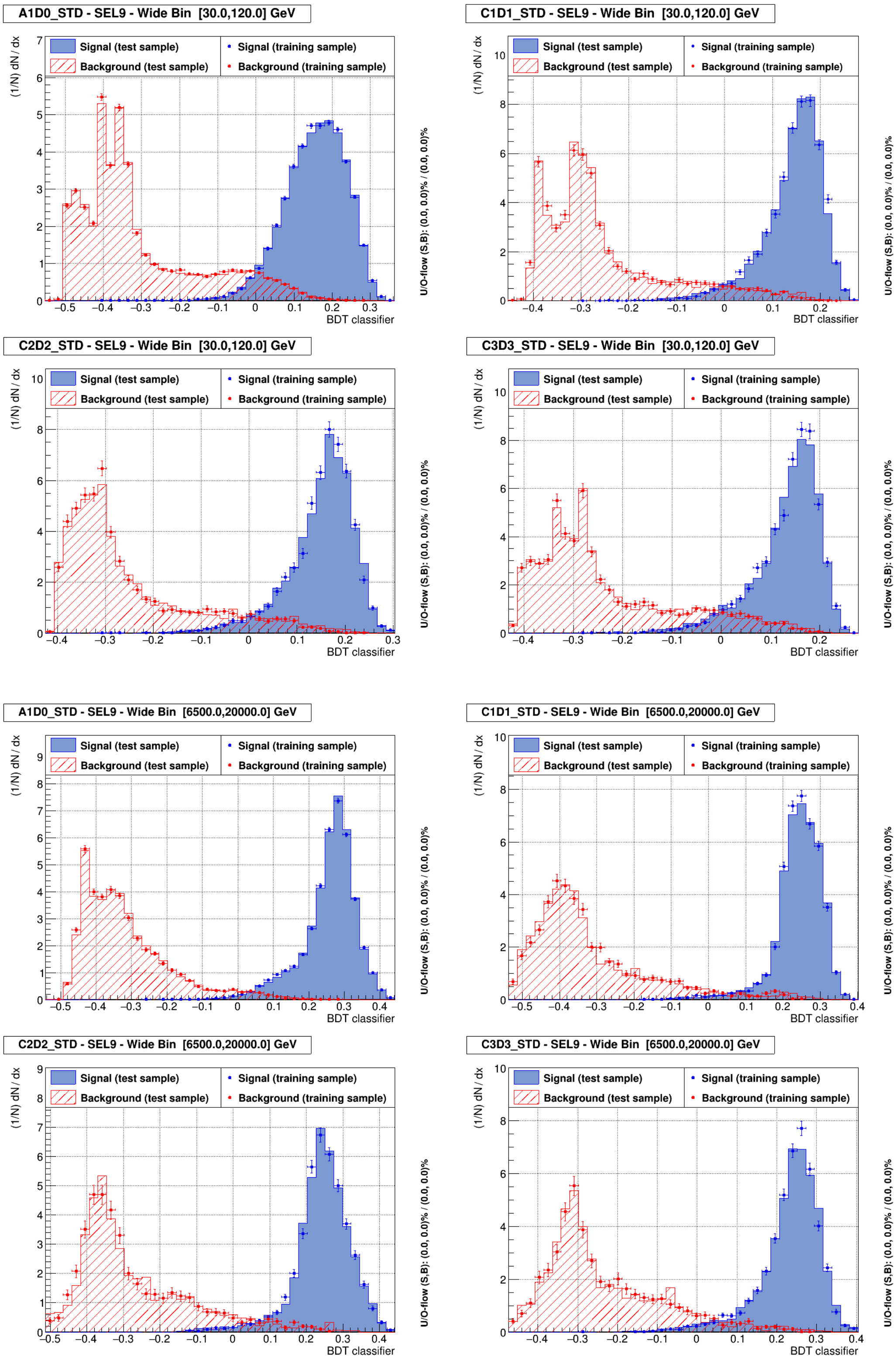

FIGURE 5.7: BDT model performance for the geometric acceptances A1+D0, C1+D1, C2+D2 and C3+D3 in the energy intervals 30-120 GeV (top half) and 6.5-20 TeV (bottom half). The BDT classifier distributions of the test samples are represented by histograms filled in blue (signal) and red (background) respectively. The same distributions from the training samples are superimposed with markers of the same colors.

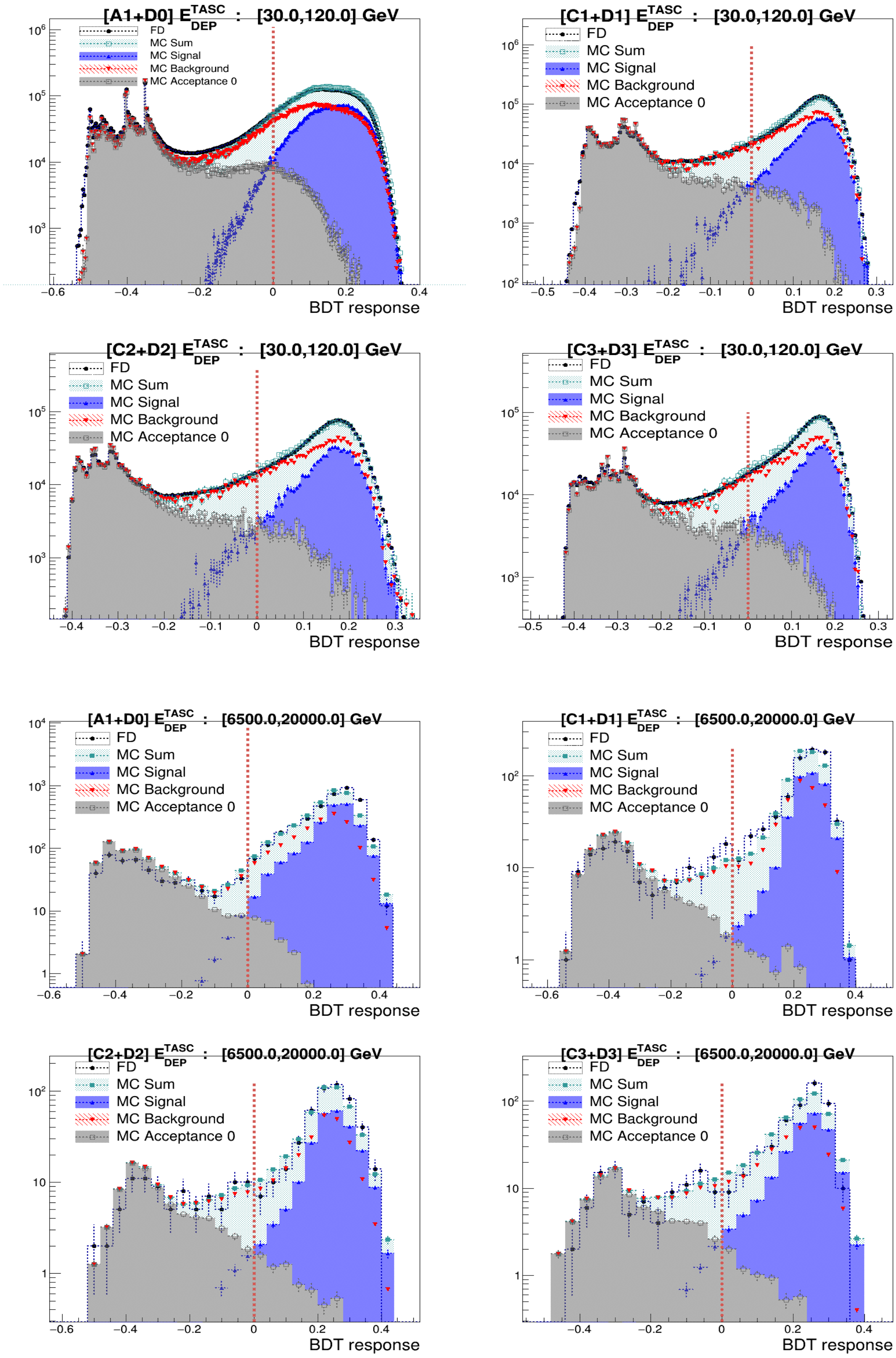

FIGURE 5.8: BDT distributions of *in-flight* and simulated data for geometric acceptances `A1+D0`, `C1+D1`, `C2+D2` and `C3+D3` in the energy intervals 30-120 GeV (top half) and 6.5-20 TeV (bottom half). The individual contributions due to signal (blue), background (red), and off-acceptance (grey open square) events of type `0` are shown. The red dashed line is placed at 0, which is approximately the selected threshold set to distinguish the signal from the background.

5.3 Charge Identification

Charge identification for the combined acceptances has been performed using a procedure similar to that described in the 4.2 section for the IMC-based estimator in `A1` acceptance. Specifically, the helium and proton peaks of the IMC charge, have been fitted with a *LanGaus* function from which both the peak positions and widths of the distributions were extracted, and consequently the σ_L and σ_R. Fig. 5.9 shows the charge distributions for the deposited energy range 1.4-2.8 TeV. It is worth noting that such distributions broaden as the slope of the tracks increases[2]. This is also demonstrated in Fig. 5.10, which shows the fits of σ_L for FD as a function of deposited energy for different combinations of acceptances. In particular, similar widths are observed for `A1+D0` and `C1+D1`. This is expected since they cross the same number of IMC layers. Conversely, the widths become progressively broader

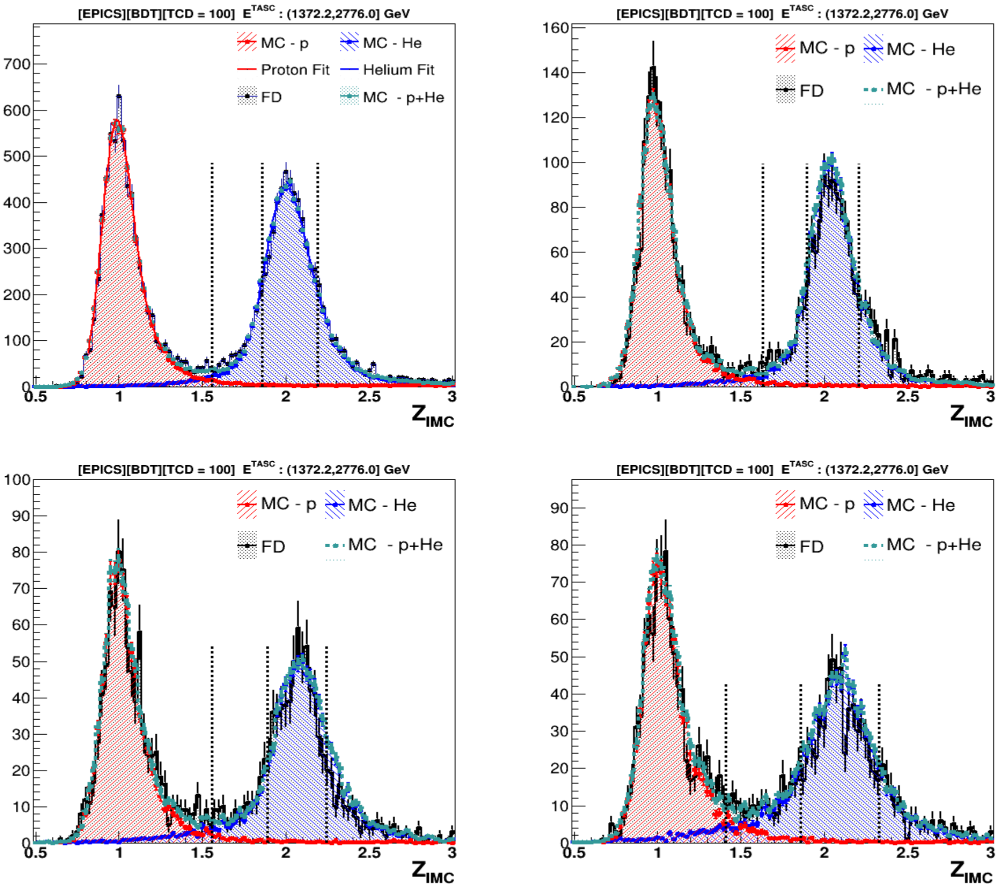

FIGURE 5.9: Charge distributions for geometric acceptances `A1+D0`, `C1+D1`, `C2+D2` and `C3+D3` in the energy interval 1.4 TeV $<$ E^{TASC}_{dep} $<$ 2.8 TeV. The distributions from MC proton and helium samples are superimposed to FD. The dashed vertical lines represent respectively, from left to right, the lower bound of the charge selection at $3\sigma_L$, the σ_L and σ_R from the *Langaus* fit.

---

[2] The average track tilt angle is related to the acceptance category.

for more inclined tracks, *i.e.* for `C`$_i$+`D`$_i$, with i greater than one. Therefore, for `C2+D2` and `C3+D3` it was decided to select helium events by fixing the number of left sigmas n_L to 2 in the equation 4.1 over the entire energy range. This approach guarantees an high, and almost flat charge selection efficiency on the whole energy range for the acceptances `K1` and `K3`, as can be seen from Fig. 5.11, while limiting the proton background. In addition, Fig. 5.10 shows that charge distributions gets broader for acceptance combinations `C4+D4` and `C5+D5`. This further motivates the need to conduct more in-depth investigations before incorporating these extended acceptances into the measurement of helium flux.

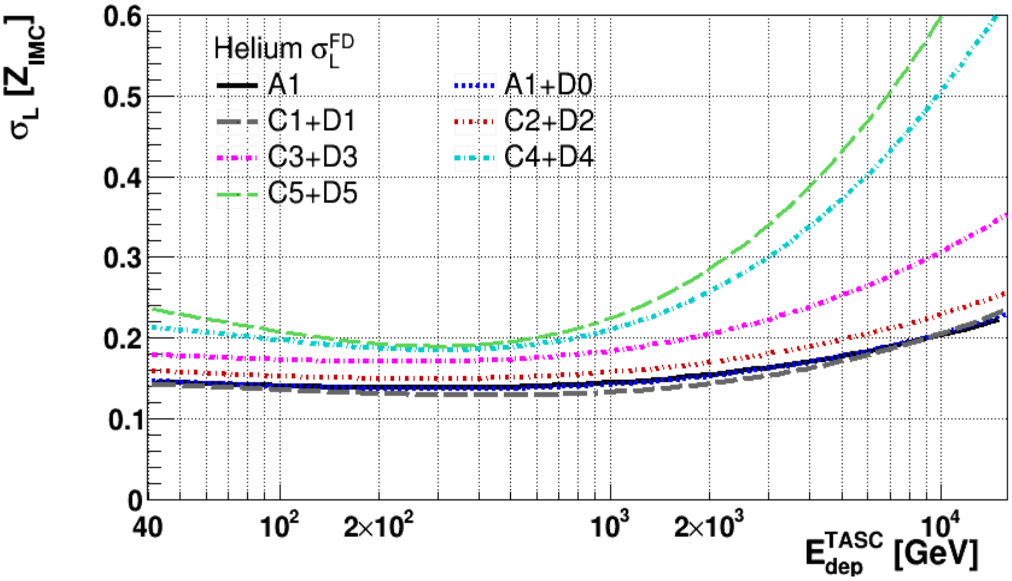

FIGURE 5.10: Fitted σ_L from FD distributions as function of TASC deposited energy for geometric acceptances `A1+D0`, `C1+D1`, `C2+D2` , `C3+D3` , `C4+D4` and `C5+D5`.

5.4 Efficiencies

The evaluation of efficiencies for `K1` and `K3` acceptances has been performed separately after all selection criteria for candidate helium events had been defined. The results are shown in Fig. 5.11 where it can be seen that the efficiencies of the charge selection are very good and almost constant, on the whole energy range. Only a slight increase can be found in the low energy region ($\lesssim$ 5%). In comparison with the results of `A1` analysis, shown in Fig. 4.23, a lower efficiency of acceptance reconstruction and KF tracking is noted in the region of higher energies. This is motivated by the increasing difficulty of reconstructing more inclined tracks, due to the reduced number of hits in the IMC, and a more biased shower axis reconstruction in the TASC.

The comparison of the effective acceptances for `A1`, `K1` and `K3` geometrical conditions, with the previously described analysis using only IMC detector for charge identification, is shown in the top panel of Fig. 5.12. On the other

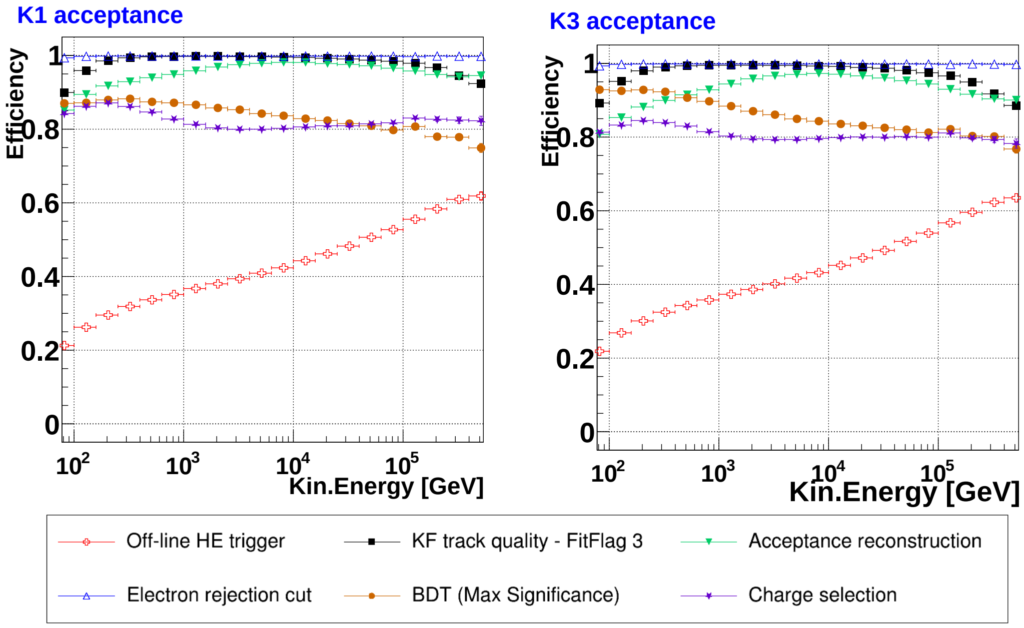

FIGURE 5.11: Relative efficiencies for extended acceptances `K1` and `K3`. The efficiency for each selection step is defined as the ratio of the number of events passing the current cut to the number of events surviving the previous selection.

hand, the statistical gain is computed as $\frac{dN}{dE}$ after the unfolding, normalized to the one obtained from `A1` acceptance. This is about 40% and 60% for `K1` and `K3` configurations, respectively, and roughly constant over the entire energy range, as shown in the bottom panel of Fig. 5.12. Only the highest energy bins show some discrepancies mainly due to statistical fluctuations.

5.5 Background subtraction and unfolding

Before proceeding with the estimation and subsequent subtraction of the background components for the extended acceptances `K1` and `K3`, response matrices were evaluated using the EPICS-based simulations, as shown in Fig. 5.13, and the stability of the unfolding procedure was verified using the “pull test"(already described extensively in the section 4.7.2).

The results, achieved via the Bayesian iterative unfolding (with two iterations), are shown in Fig. 5.14 for the `K1` and `K3` configurations, respectively. The pull distributions are obtained with $N_{toy} = 5 \times 10^3$ simulations for a set of energy bins ranging from 15 GeV to 1 PeV, and are well fitted by a Gaussian with zero mean and unitary width. Thus, the stability is verified over the entire energy range, *i.e.* up to $\sim$ 600 TeV energy, for both cases.

Afterwards, the deposited energy spectrum of the FD is considered. The background components are estimated and subtracted using the same procedure described in section 4.3. Both the spectra in deposited energy obtained after background subtraction and the corresponding components for the `K1`

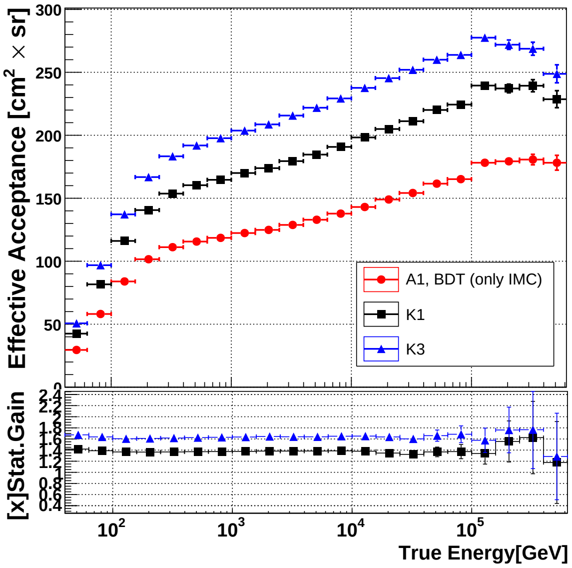

FIGURE 5.12: (Top) Effective acceptances for configurations `A1`, `K1` and `K3`, using only IMC for charge identification. (Bottom) The statistical gain for `K1` and `K3` extended acceptances, with respect to `A1` configuration.

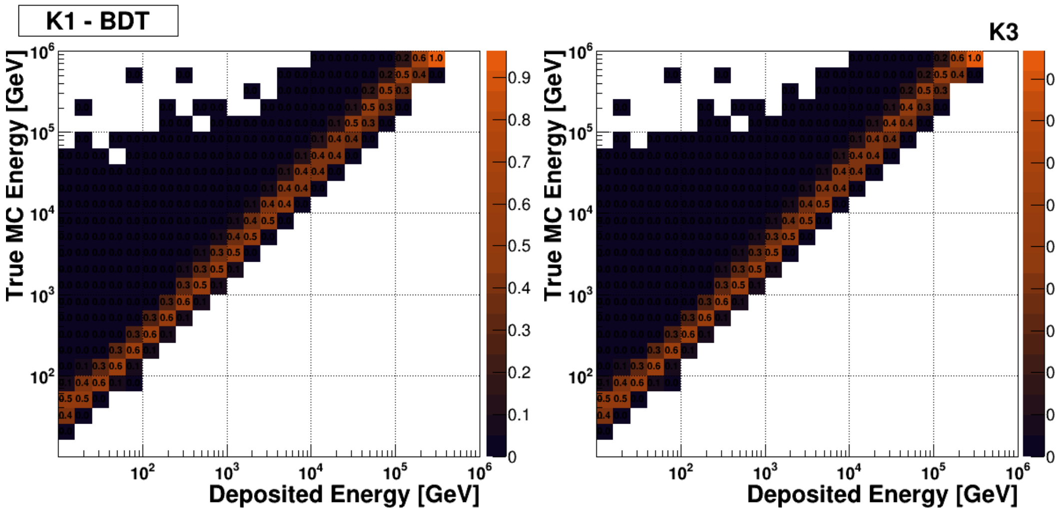

FIGURE 5.13: Response matrix, normalized by column and obtained with EPICS-based MC simulations for `K1` (left panel) and `K3` (right panel) extended acceptances.

and `K3` configurations, are shown in Fig. 5.15, where the background components from proton contamination, off-acceptance helium and protons are represented respectively by the blue, green and orange markers.

The unfolding procedure is then applied to infer the spectrum in terms of primary particle energy as shown in Fig. 5.16. The statistical uncertainties are evaluated using the *bootstrap* method described in subsection 4.4.2. The results are shown in Fig. 5.17 and they turn out to be stable up to about $\sim$ 600 TeV energy, where enough statistics is available, for both the extended

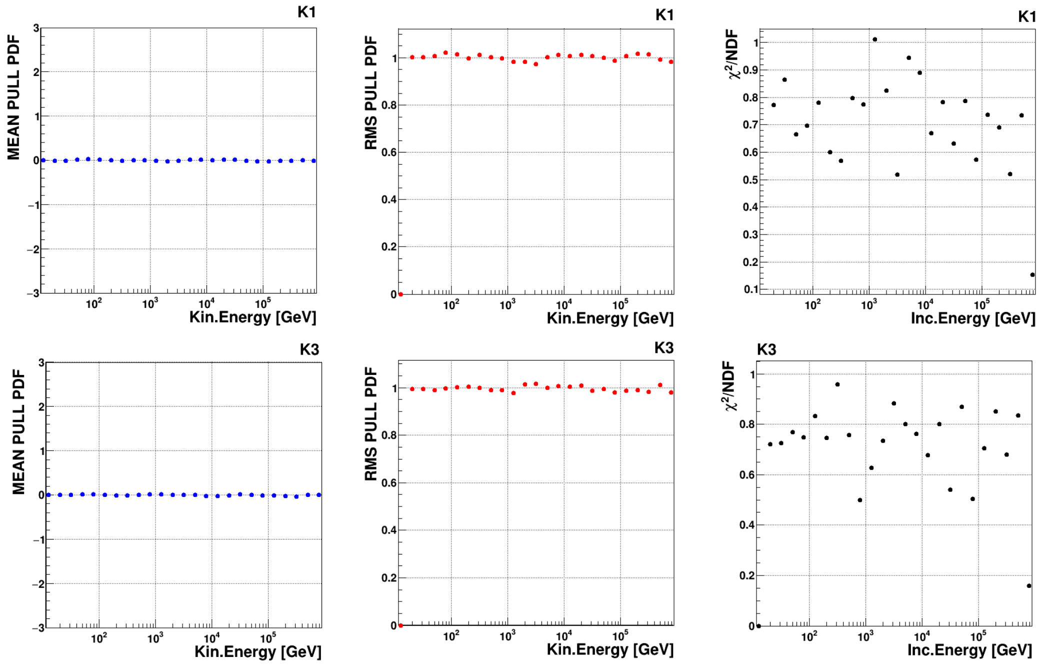

FIGURE 5.14: Comprehensive results of the *pull test* with EPICS simulated data, for `K1` (top) and `K3` (bottom) extended acceptances. Bias, RMS and χ^2/NDF are extracted from the Gaussian fit of pull distribution for each energy bin of the spectrum.

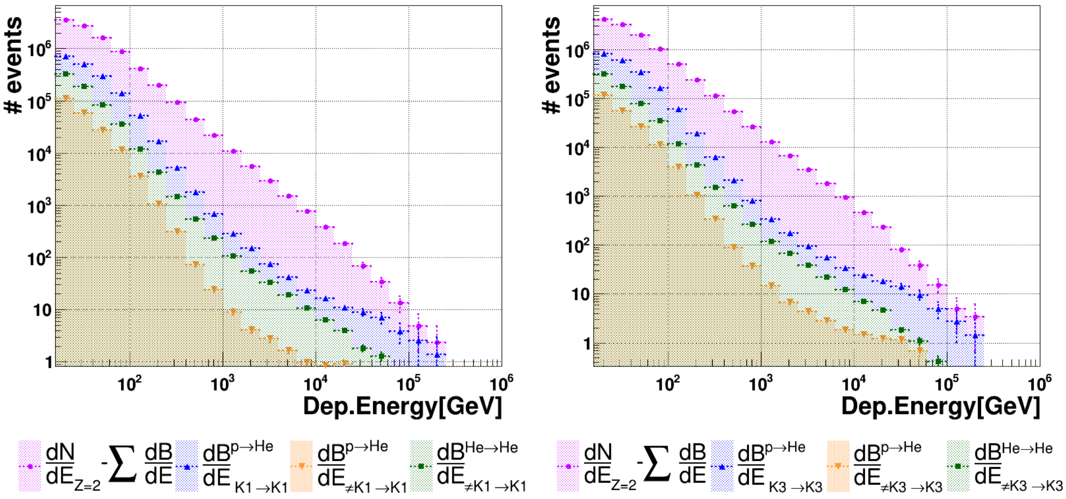

FIGURE 5.15: Deposited energy spectrum of helium candidate events in `K1` (left panel) and `K3` (right panel) acceptances, obtained with 87 months of CALET data, after the background subtraction.

acceptances.

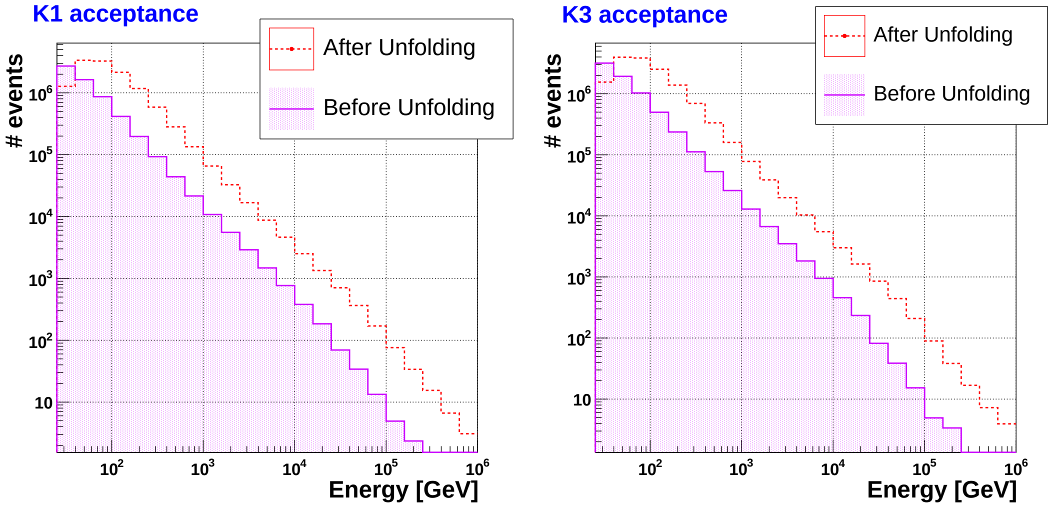

FIGURE 5.16: Preliminary energy spectra before and after the application of the iterative bayesian unfolding with 2 iterations. (Left panel) `K1` and (right panel) `K3` acceptances.

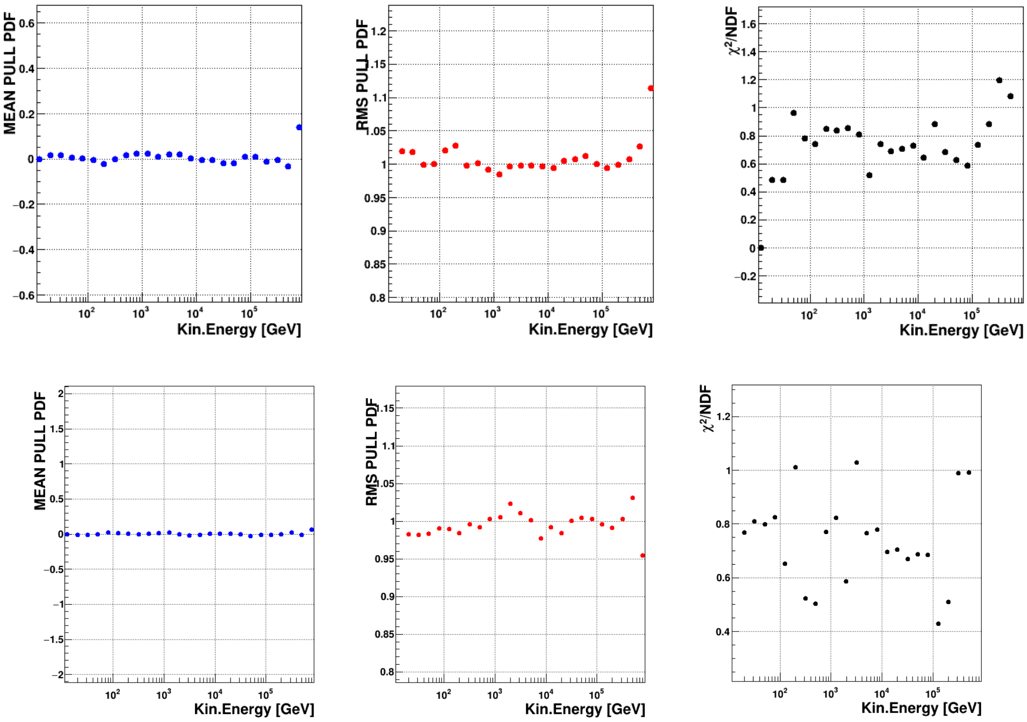

FIGURE 5.17: Comprehensive results from *bootstrap* of FD unfolded spectrum, obtained with $N_{\text{trial}} = 5 \times 10^3$ trials, for `K1` (top) and `K3` (bottom) Bias, RMS and χ^2/NDF are extracted from the Gaussian fit of pull distribution for each energy bin of the spectrum.

5.6 Preliminary fluxes

The preliminary helium fluxes for the extended acceptances `K1` and `K3` are presented in this section. They have been calculated according to the formula 4.5 and the statistical uncertainties are derived by standard error propagation, the reliability of which has been tested as explained in the last section of the previous paragraph. The results are shown in the top and bottom panels of Fig. 5.18 for `K1` and `K3` configurations, respectively. Only statistical uncertainties are reported and they are compatible, within the errors, with the helium flux published in the PRL journal [8] by the CALET collaboration in 2023, over the entire energy range.

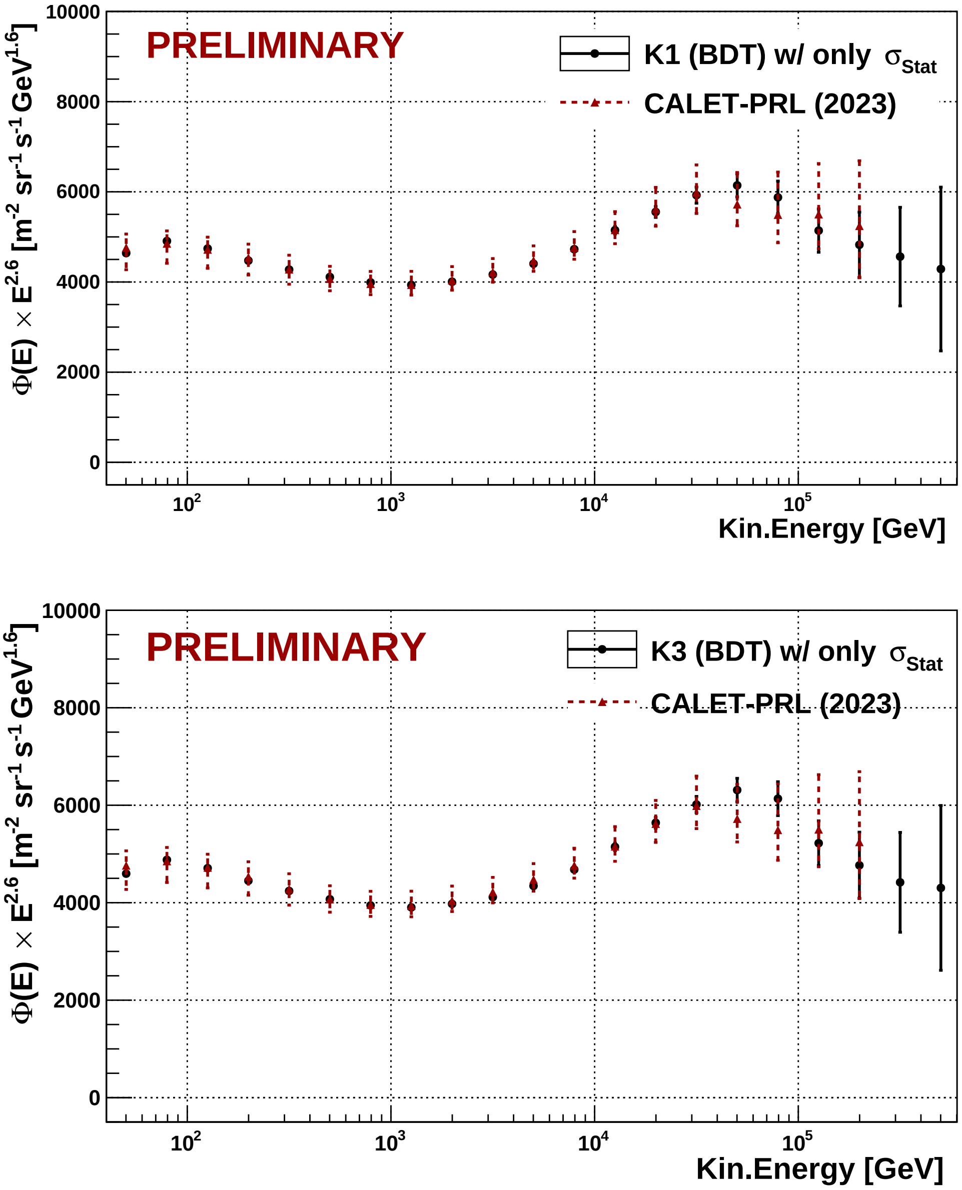

FIGURE 5.18: Helium flux multiplied by $E^{2.6}$ for `K1` (top) and `K3` (bottom) extended acceptances. Vertical bars represent only statistical uncertainties.

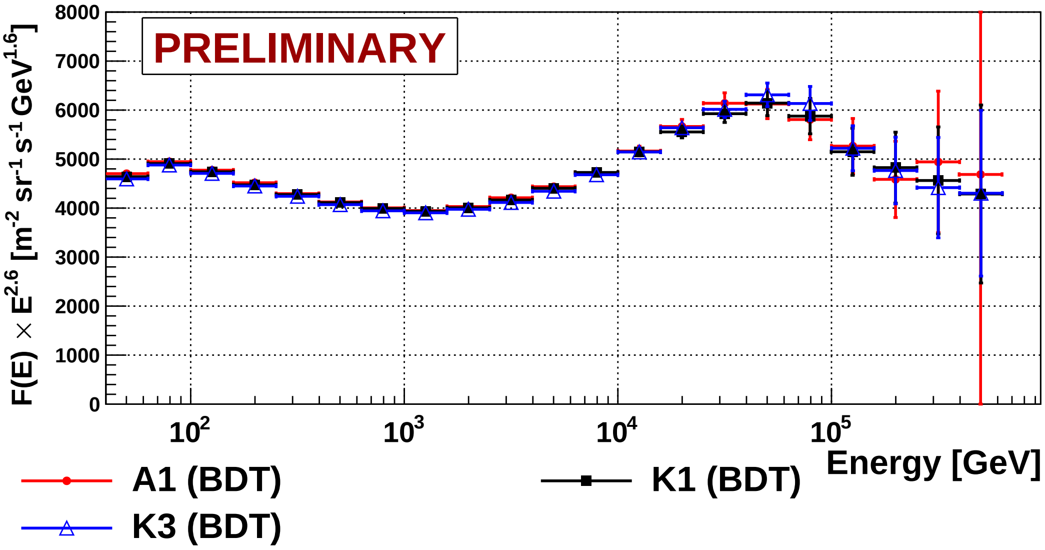

FIGURE 5.19: Comparison of the preliminary helium fluxes obtained with BDT-based analyses in `A1`, `K1` and `K3` acceptances.

A comparison of the preliminary helium fluxes obtained with BDT-based selections in `A1`, `K1` and `K3` acceptances, is shown in Fig. 5.19. The results are consistent in the whole energy range within the errors. The relative statistical error improves with the widening of the fiducial acceptance as shown in Fig. 5.20. Specifically, an improvement can be seen in the last high-energy bins, where the `K1` and `K3` acceptances allow the extension of the measurable energy range up to $\sim$ 600 TeV, albeit with rather large statistical errors.

Finally, figure 5.21 shows the helium flux in `K3` acceptance compared with the results from several other experiments[3], *viz.* CALET [8], DAMPE [29], AMS-02 [23], PAMELA [18] and NUCLEON-KLEM [83]. The result is compatible within the errors, with those of the AMS-02 and PAMELA magnetic spectrometers below $\sim$ 1 TeV of kinetic energy. It is also fairly consistent, within errors, with both the DAMPE and the NUCLEON-KLEM helium fluxes above this energy, up to hundreds of TeV.

---

[3] The data are extracted from two different Cosmic Rays Databases [66, 103].

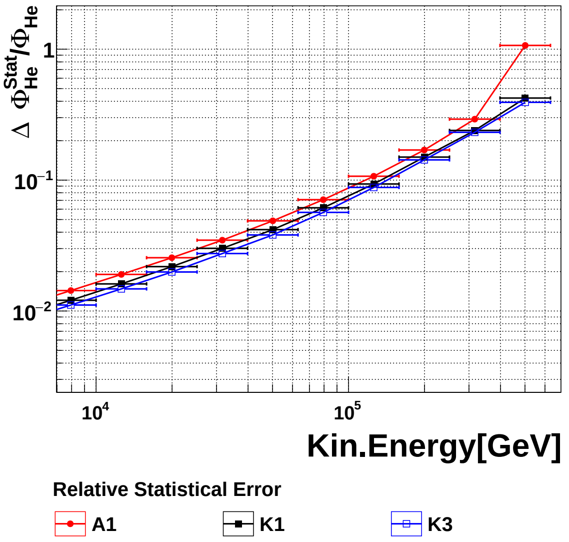

FIGURE 5.20: Relative statistical errors of the helium flux measurements in `A1`, `K1` and `K3` acceptances, obtained with BDT-based analyses. Only the energy region where the relative error is greater than 1% is shown.

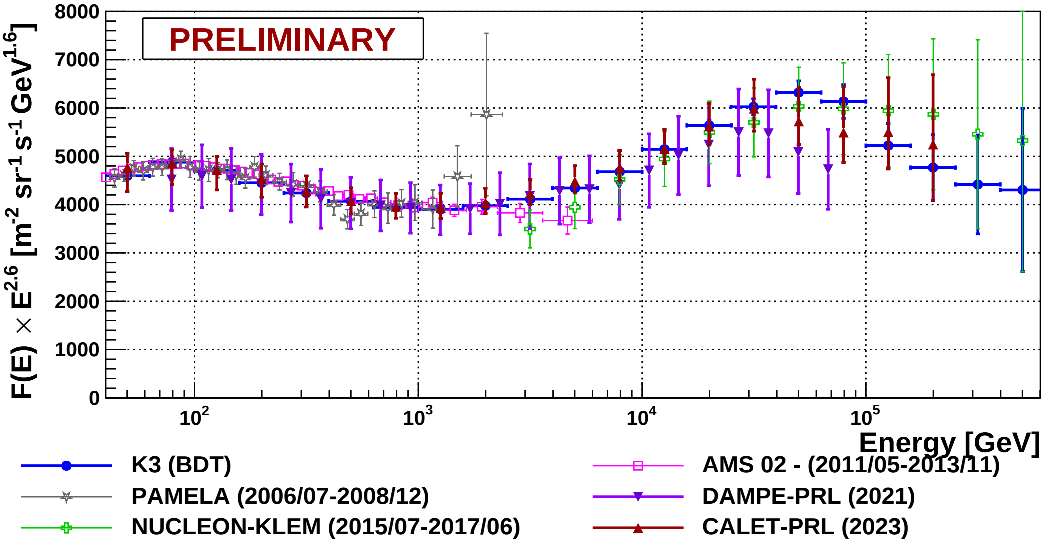

FIGURE 5.21: Preliminary helium flux (multiplied by $E^{2.6}$) in `K3` (filled blue dots) extended acceptance using 87 months of CALET data, where vertical bars represent only statistical uncertainties. The results from other experiments, *viz.* CALET-PRL [8], DAMPE [29], AMS-02 [23], PAMELA [18] and NUCLEON [83], are shown for comparison.

Chapter 6

Systematics Uncertainties

The estimate of an overall systematic error for the measurements of helium flux, is crucial to understand the reliability of the analyses described in Chapters 4 and 5. The systematic uncertainty is not negligible in this kind of measurements, and it has a significant impact on the total error. This is especially critical at low energies where it is the dominant component [8][50], but also at the highest attainable energies where it becomes of the same order-of-magnitude as the statistical error. In this chapter a detailed analysis of the systematic errors is provided both for the flux measurement in the fiducial acceptance `A1` and in the extended acceptances `K1` and `K3`. Finally, the flux measurements with their total uncertainties are then presented in comparison with other experiments.

6.1 Overview

In the assessment of total systematic error, two types of contributions can be distinguished: energy-dependent and energy-independent. The energy-dependent systematic arises from the adopted pre-selection and selection cuts, as well as from the correction and calibration applied to MC simulation. The different contributions that have been studied are summarized as follows:

- The thresholds set for the off-line high-energy trigger (HET) validation.
- The track quality criteria.
- The definition of the geometric requirements.
- The effect of the shower energy corrections.
- The assumed re-weighting factors in the MC simulated data.
- The BDT-based selections for background rejection.
- The charge selection.
- The unfolding algorithm.

All of theses contributions have been evaluated based on EPICS simulations. Their assessment with other MC generators, such as `GEANT` or `FLUKA` , will be the subject of future studies and they are thus not covered in this Thesis. In contrast, the energy-independent systematics are assumed to be fixed at 4.1% over the entire energy range as reported in Ref. [8]. In particular, this value represents the addition in quadrature of the following three components[1]: long-term stability(1.4%), live-time(3.4%) evaluation and radiation environment (1.8%).

6.2 Pre-selection

Off-line HET validation

The systematics related to the chosen value of the off-line high-energy trigger are evaluated by increasing the threshold of the first TASC layer (X1) up to 150 MIP. The relative differences between the flux achieved in this way and the reference one threshold set to 100 MIP, is taken as systematics error. The comprehensive results are shown in Fig. 6.1 for (top) `A1`, (middle) `K1` and (bottom) `K3` acceptances. The related systematics are less than about 4% over the entire energy range for `A1`, and it is slightly higher for `K1` and `K3`, below 100 GeV.

Track Quality Criteria

The systematics related to the tracking algorithm are assessed by relaxing the track quality criteria required. Specifically, the `FitFlags` are allowed to assume one among the following values 3, 6, 9, 12 that depend on how the track is reconstructed in X and Y views. A more detailed explanation can be found in Section 3.3.2 and summarized in Table 3.4. The comprehensive results are shown in Fig. 6.2 for (top) `A1`, (middle) `K1` and (bottom) `K3` acceptances. The uncertainties are within $\sim \pm 1\%$ except in the energy interval 400-630 TeV, where the slightly higher values are mainly due to statistical fluctuations.

Geometric requirements

The systematics related to the definition of the geometric requirements are evaluated by shrinking and widening the acceptance conditions with respect to the reference configuration. For fiducial acceptance `A1`, the geometric conditions are shrunk to `A` and widened to `A1+D0`. For extended acceptance `K1`, the geometric conditions are shrunk to `A1+D0` and widened to `K2`, while for the flux in `K3` acceptance the geometric condition is varied between `K2` and `K4`. The comprehensive results are shown in Fig. 6.3 for (top) `A1`, (middle) `K1` and (bottom) `K3` acceptances.

---

[1] The strategy adopted for their evaluation is reported in Ref. [14].

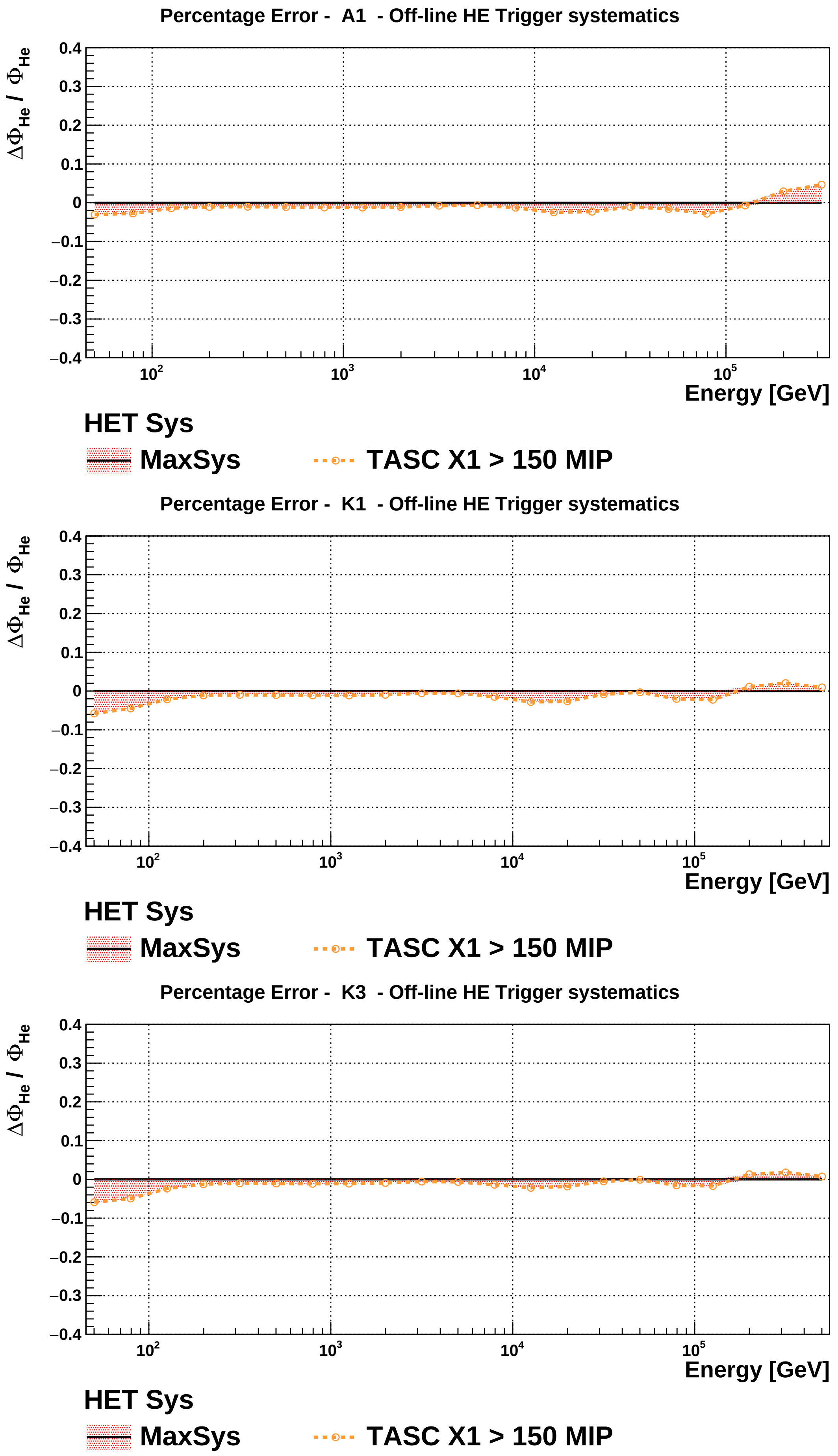

FIGURE 6.1: Systematics related to the off-line high-energy trigger (HET) for the preliminary helium flux in `A1` (top), `K1` (middle) and in `K3` (bottom) acceptances.

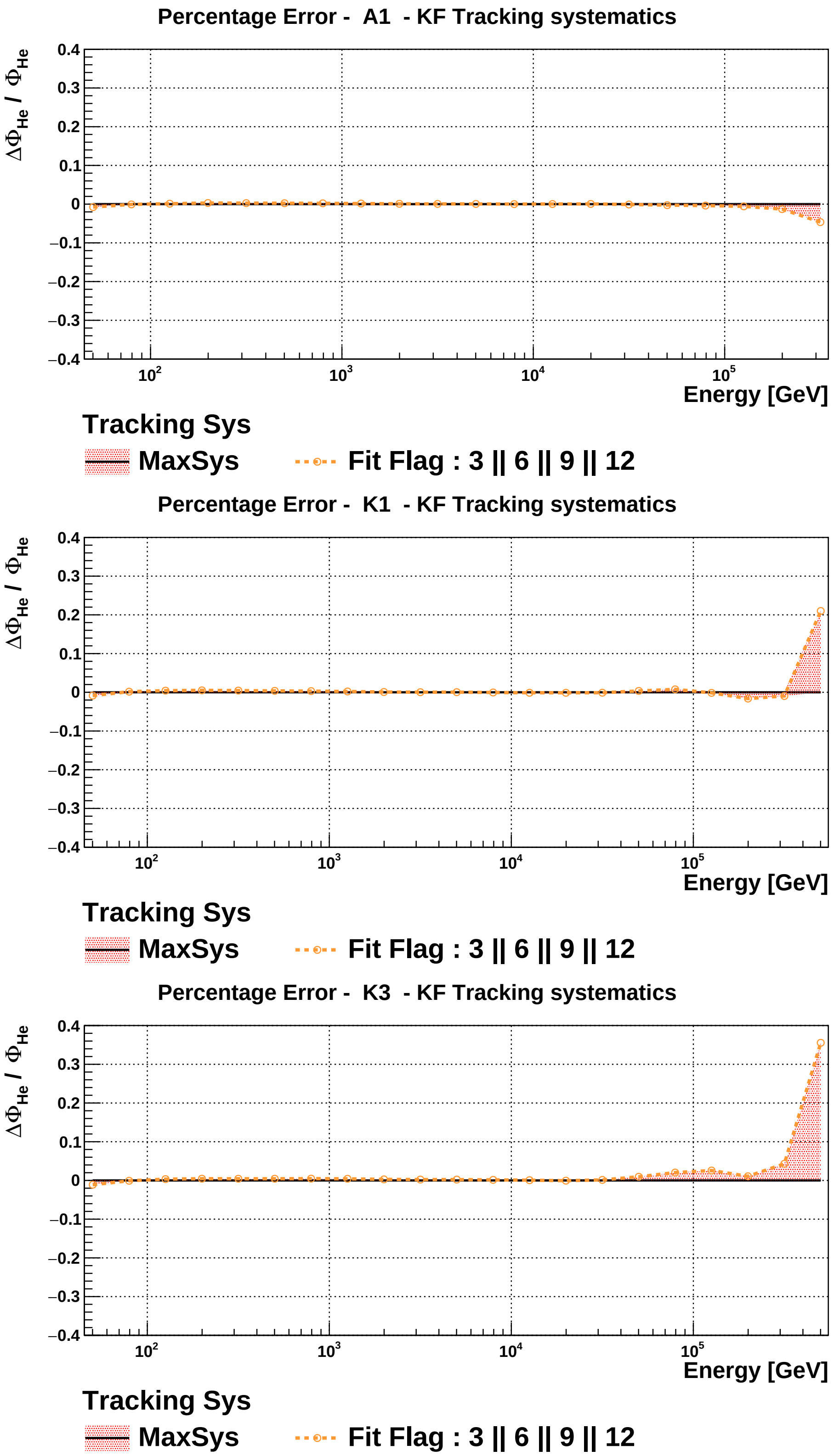

FIGURE 6.2: Systematics related to the tracking algorithm. The relative flux error is achieved by relaxing the track quality criteria with respect to the reference preliminary helium flux in `A1` (top), `K1` (middle) and in `K3` (bottom) acceptances.

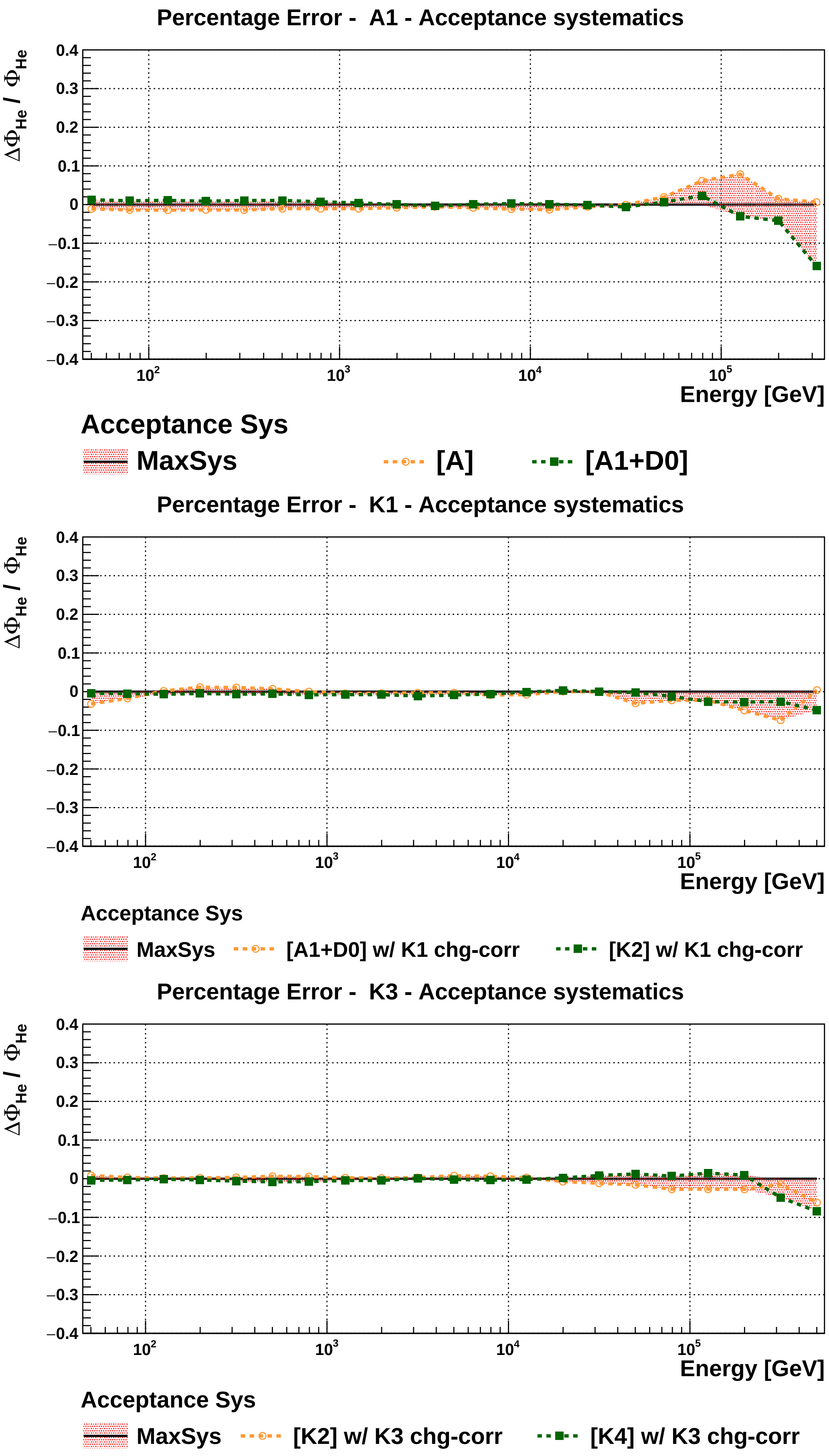

FIGURE 6.3: Systematics related to the required geometric conditions for the preliminary helium flux in `A1` (top), `K1` (middle) and in `K3` (bottom) acceptances.

6.3 MC modelling

6.3.1 Shower Energy Correction

One of the major contributions to the total systematic error is due to the energy scale correction described in paragraph 3.2.3. The systematics of this procedure has been evaluated by changing the proton and helium shower energy correction factors (obtained from test-beam results) using different energy-dependent functions, referred to as *models*. Specifically, the models considered are shown in Fig. 6.4 and summarized as follows.

- `Constant` derived by zero order polynomial fit of the correction factors.
- `Linear` obtained by first order polynomial fit of the correction factors.
- `Log-linear` derived by first order logarithmic polynomial fit of the correction factors.
- `Default` each pair of correction factors are interpolated with a first order logarithmic polynomial as in Refs. [8, 9, 19], and described in paragraph 3.2.3.

The comprehensive results are shown in Fig. 6.5 for (top) `A1`, (middle) `K1` and (bottom) `K3` acceptances. The uncertainties are within about ±5%.

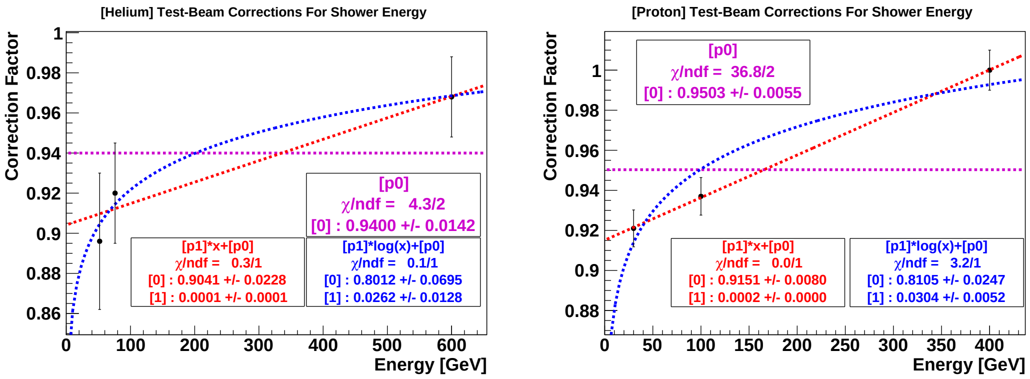

FIGURE 6.4: Test beam energy corrections for proton and helium MC samples with the related *models*.

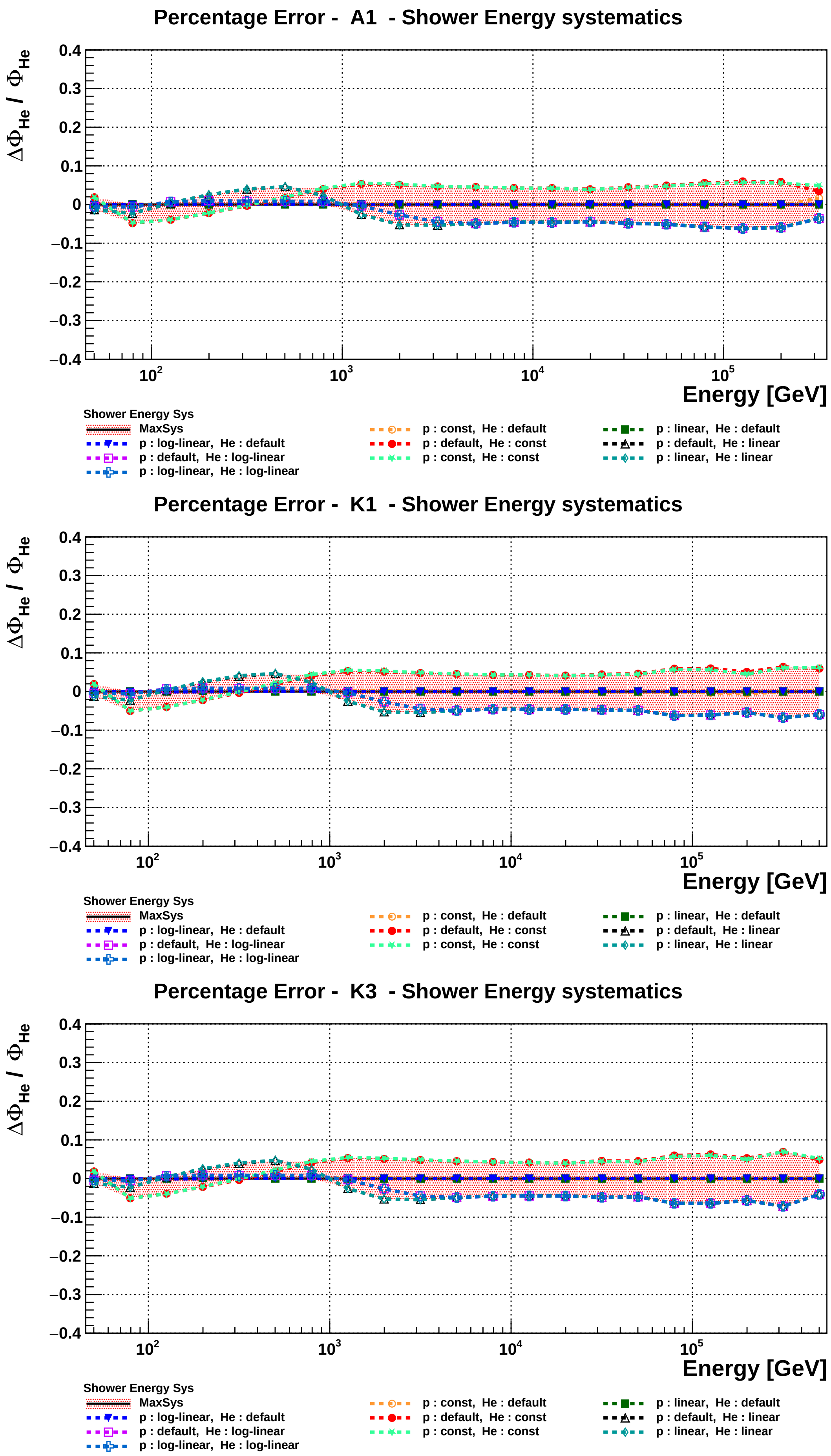

FIGURE 6.5: Systematics related to the shower energy corrections for the preliminary helium flux in `A1` (top), `K1` (middle) and in `K3` (bottom) acceptances.

6.3.2 Re-weighting of MC samples

The assumed spectral shape and abundance of the MC simulated proton and helium samples, can also affect the flux measurement, since simulated data are used to estimate the background components, the response matrix, and the selection efficiencies. Regarding the proton-to-helium abundance ratio, the contribution is negligible because the strategy used for the background subtraction, explained in section 4.3, provides the relative abundances directly from the FD. A proof can be appreciated in Fig. 6.6, where the systematics from this contribution have been assessed by artificially varying of ±50% the helium abundance factor[2].

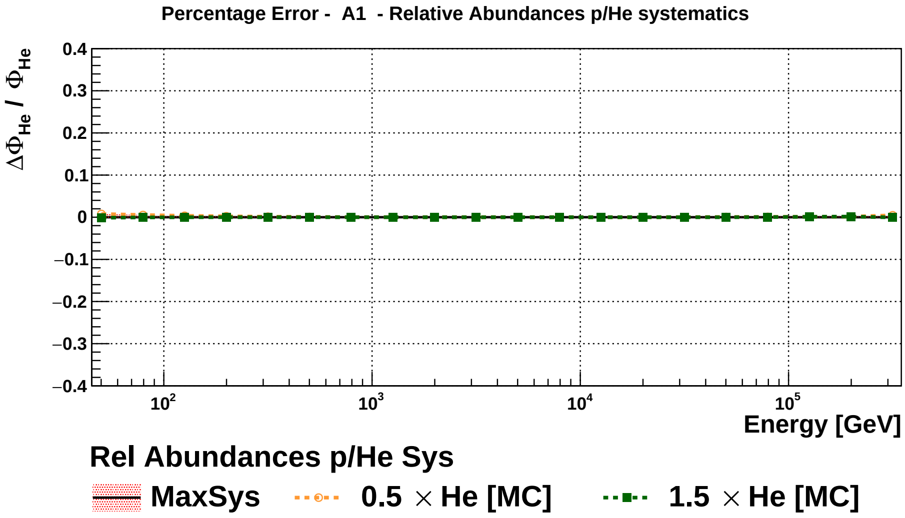

FIGURE 6.6: Monitoring the effects of the assumed abundance ratio of proton and helium MC samples in the flux evaluation for `A1` acceptance.

Conversely, the re-weighting functions for proton and helium MC samples could be a potentially large source of systematic uncertainty. In this case, the method developed to evaluate this contribution is based on varying the re-weighting functions. The alternative functions are power-law $E^{-\gamma}$ where the γ index is scanned from 2.5 to 2.8, with a step-size of 0.1, for proton and helium events in an independent manner. The comprehensive results are shown in Fig. 6.7 for (top) `A1`, (middle) `K1` and (bottom) `K3` acceptances, compared with the reference flux obtained with the standard re-weighting functions, described in paragraph 3.1. The uncertainties are below about 5% in the whole energy range, except for the last bins of `K1` and `K3` acceptances where relative values are driven by proton re-weighting function with γ index equal to 2.8, , and are probably due to the limited statistics of the MC samples for acceptance $\mathtt{C}_i$+$\mathtt{D}_i$. Nevertheless, these errors are still smaller than the related statistical uncertainties.

---

[2] Similar results are obtained for `K1` and `K3` acceptances.

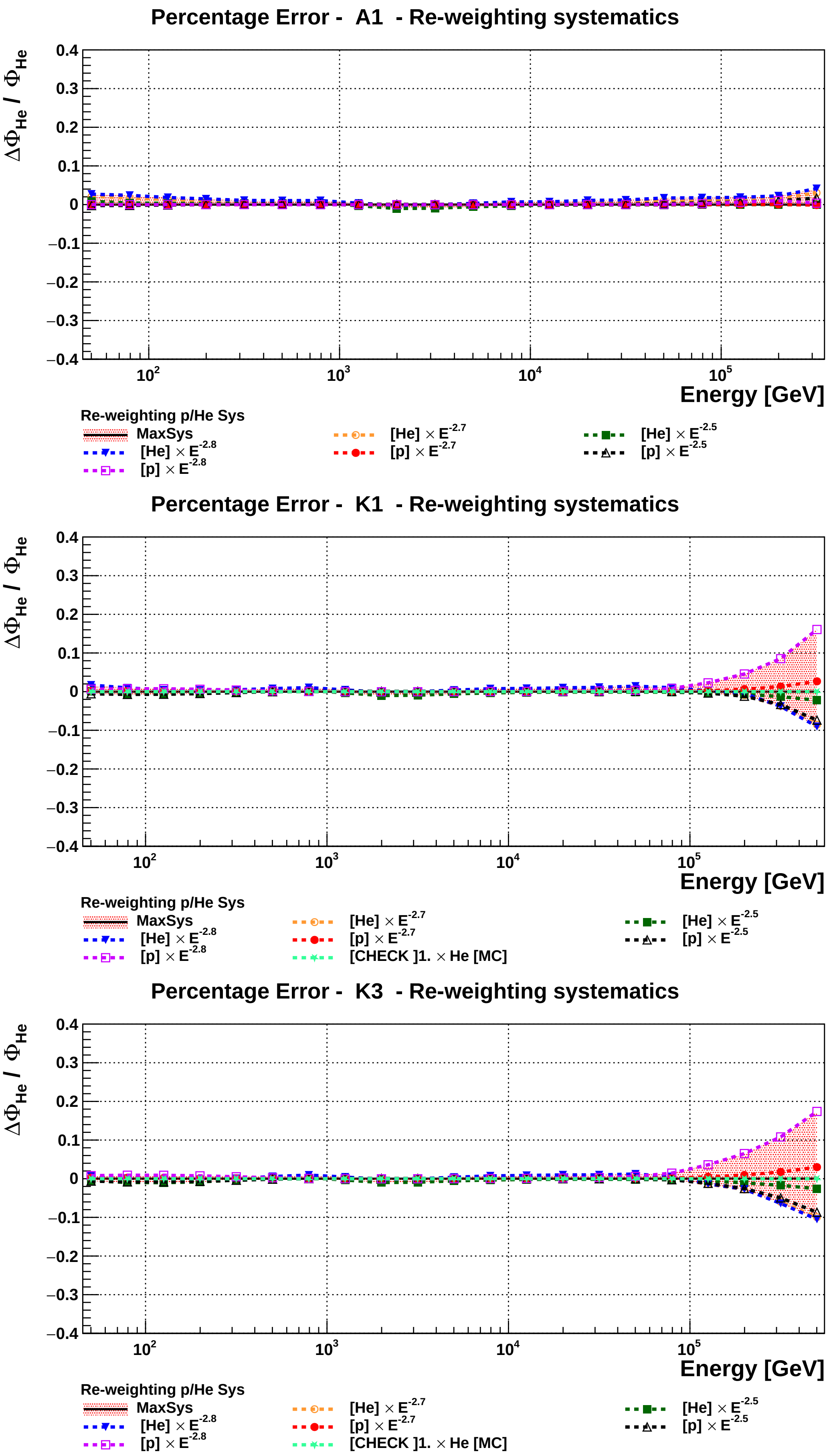

FIGURE 6.7: Systematics related to the re-weighting procedure for events that belong to proton and helium MC samples, for the analysis related to `A1` (top), `K1`(middle) and `K3`(bottom) acceptances.

6.4 BDT selection

Following the validation of the hyper-parameters for the BDT model and the reliability of the resulting classifiers, a source of systematic error is related to the definition of BDT working points. This contribution has been evaluated by varying all the BDT working points of ± 0.1 with respect to the their reference values, based on the optimization of significance estimator. The fluxes are then computed for each of the two configurations and the relative differences with respect to reference flux is considered as systematics error.

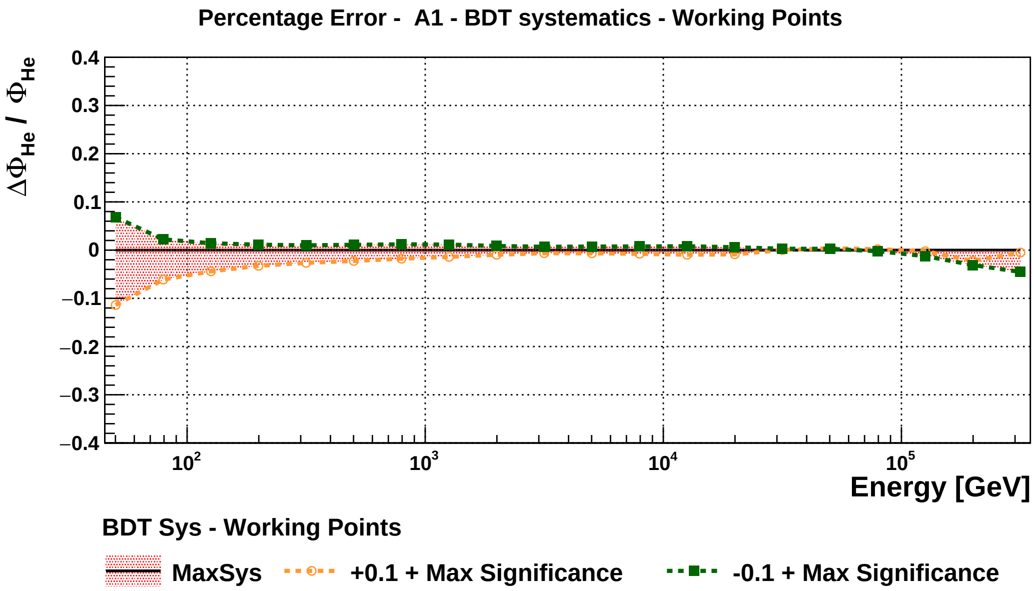

FIGURE 6.8: Systematics related to the BDT-based *off-acceptance* selections, for the preliminary helium flux in `A1` acceptance. The relative flux error is achieved by varying all the BDT working points of ± 0.1 with respect to the standard values.

The results are shown in Fig. 6.8 for `A1`, and in Fig. 6.9 for (top) `K1` and (bottom) `K3` acceptances. The uncertainties are within few percent above about 150 GeV, whereas larger fluctuations (of the order of $\pm 10\%$) can be seen below 100 GeV of kinetic energy. These are likely due to the degradation of the performance of track reconstruction algorithms, especially the one based on the method of moments which exploits only the information provided by the TASC detector.

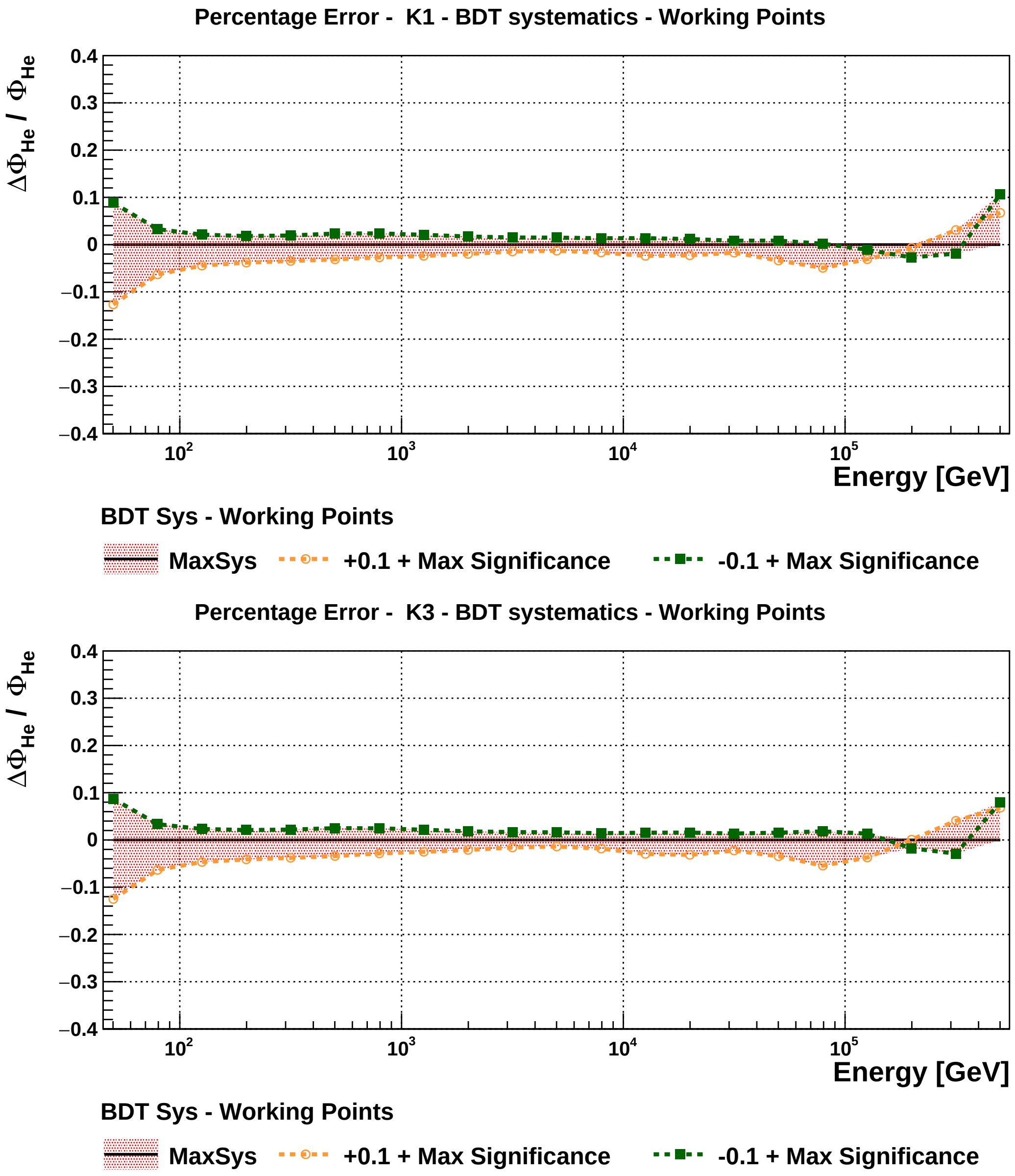

FIGURE 6.9: Systematics related to the BDT-based *off-acceptance* selections, for the preliminary helium fluxes in `K1` (top) and `K3` (bottom) acceptances.

6.5 Charge selection

Charge selection is a key cut for this analysis, and a potential source of large systematics. The error related to the charge identification is evaluated by varying the selection in three independent manners for `A1` acceptance. On the one hand, the lower limit of the CHD-based charge estimator is scanned from 1.5 to 1.8 with a step size of 0.1e. On the other hand, for the IMC-based estimator, the number of σ_L (n_L) is scanned from 2 to 4, while the number of σ_R (n_R) undergo a variation from 4 to 6. The results are shown in Fig. 6.10 and the uncertainties are within about ±5% over almost all the entire energy range.

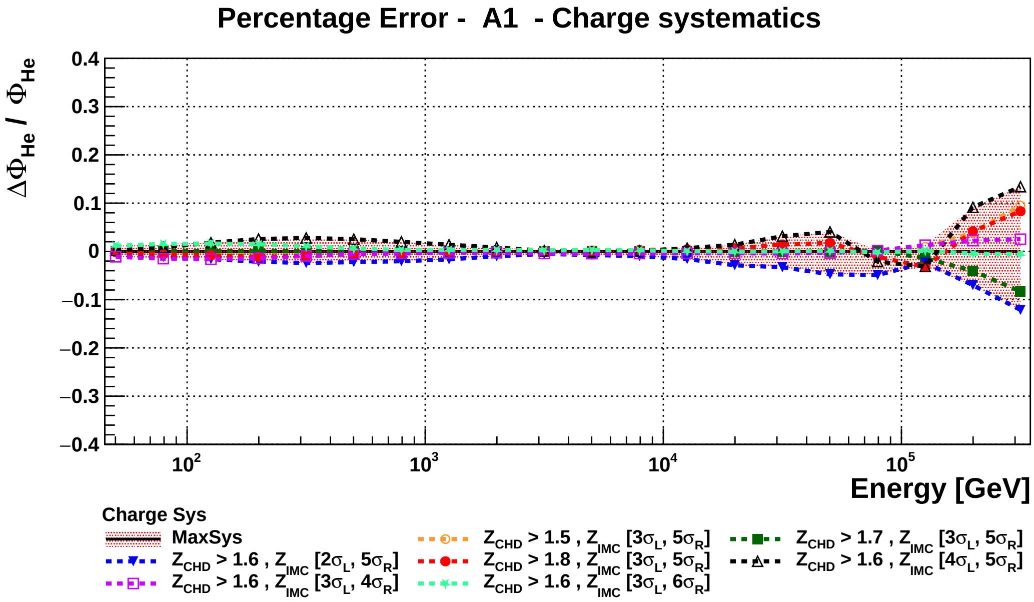

FIGURE 6.10: Systematics related to the charge selection for the helium flux in `A1` acceptances.

Regarding the analysis in `K1` and `K3` acceptances, the charge systematics are computed varying only the number of σ_L and σ_R for the IMC-based charge estimator, since the CHD detector is not used.

At higher energies the systematics increases progressively because of the limited statistics and the gradual broadening of the charge distributions for acceptances $\mathtt{C}_i$+$\mathtt{D}_i$ (as discussed in the section 5.3) which makes this selection more challenging. Nevertheless, it remains well below ±20%.

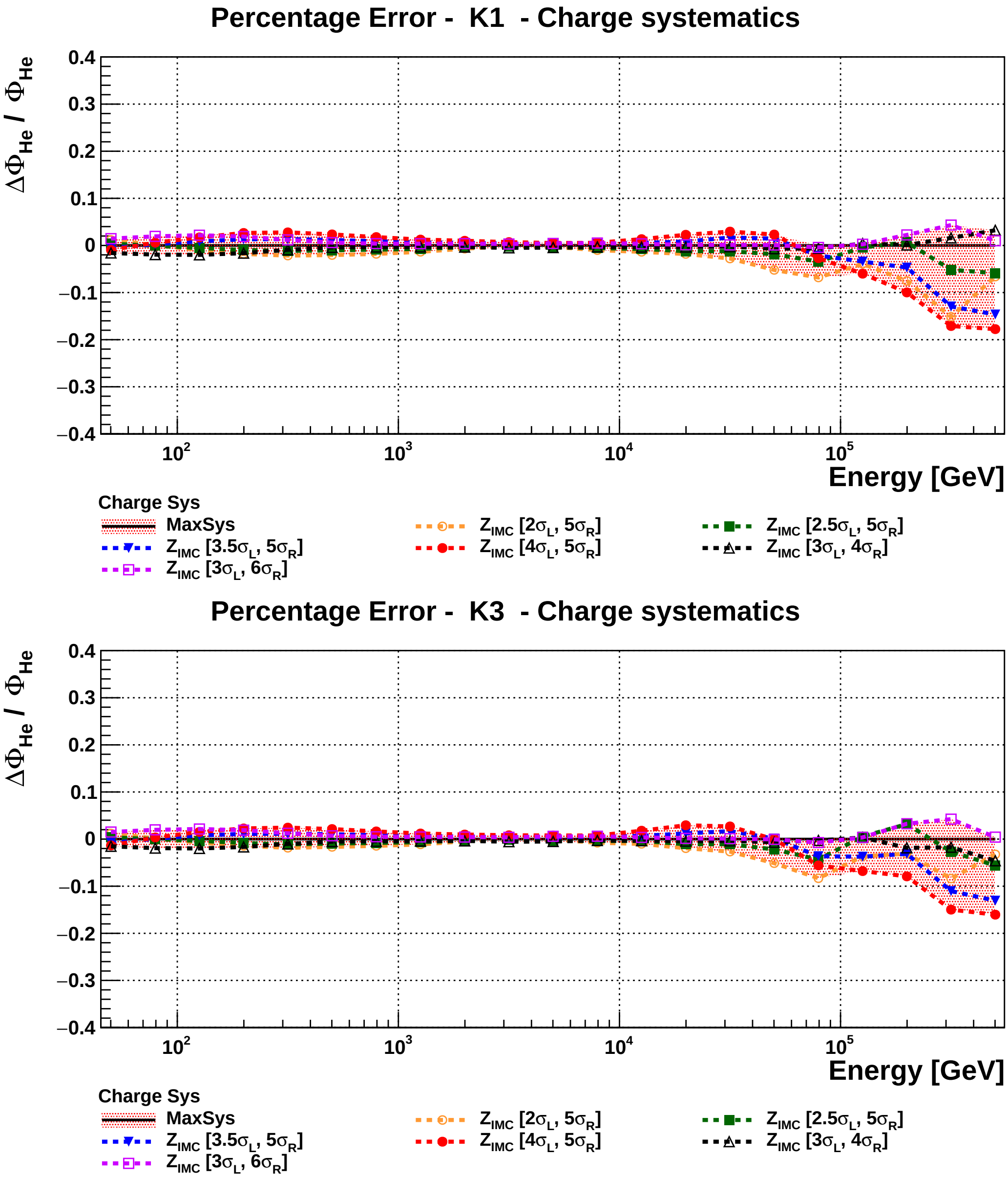

FIGURE 6.11: Systematics related to the charge selection for the helium flux in `K1` (top) and in `K3` (bottom) acceptances.

6.6 Unfolding

The strategy adopted to assess the systematics related to the unfolding procedure follows the treatment of subsection 4.4.2. The deposited energy spectrum $\vec{n}_{\text{dep}}^{\text{FD}}$ is unfolded with the SVD approach (where the regularization parameter has been internally optimized by the `RooUnfold` routine) and with the iterative Bayesian approach, where the number of iterations is increased to 3 and 4. The results are shown in Fig. 6.12 for `A1`acceptance. The uncertainties are within $\lesssim \pm 5\%$ over almost the entire energy range. The high uncertainties in the last bins are driven by statistical fluctuations due to the small number of events.

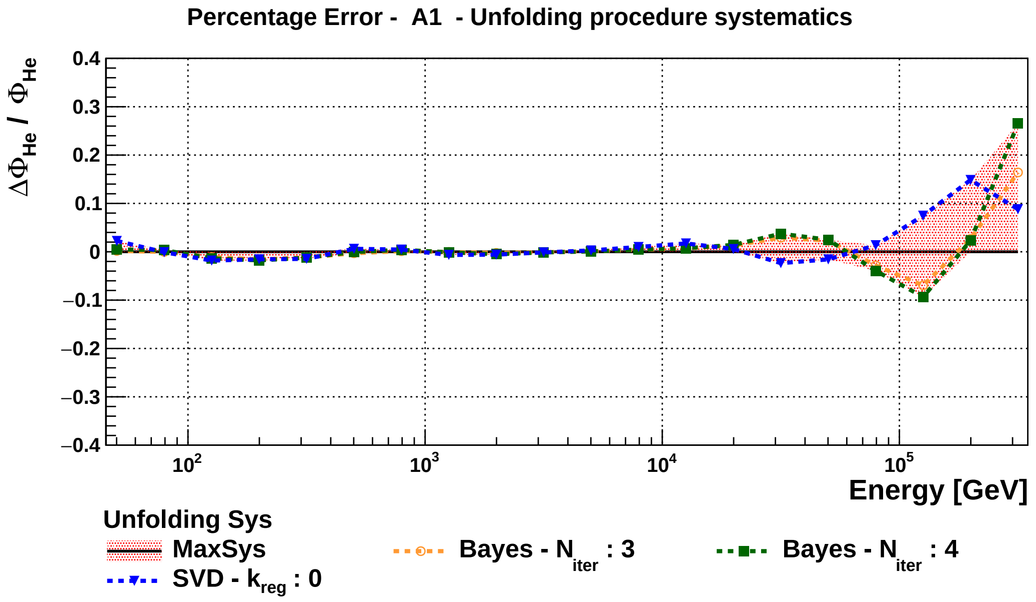

FIGURE 6.12: Systematics related to the unfolding procedure for reconstructing the primary energy spectrum of the selected helium nuclei in `A1` acceptance.

Regarding the analyses in `K1` and `K3` acceptances, it is worth pointing out that the uncertainties are lower in the highest energy bins, because of the larger number of events collected as a result of the extension of the fiducial acceptance.

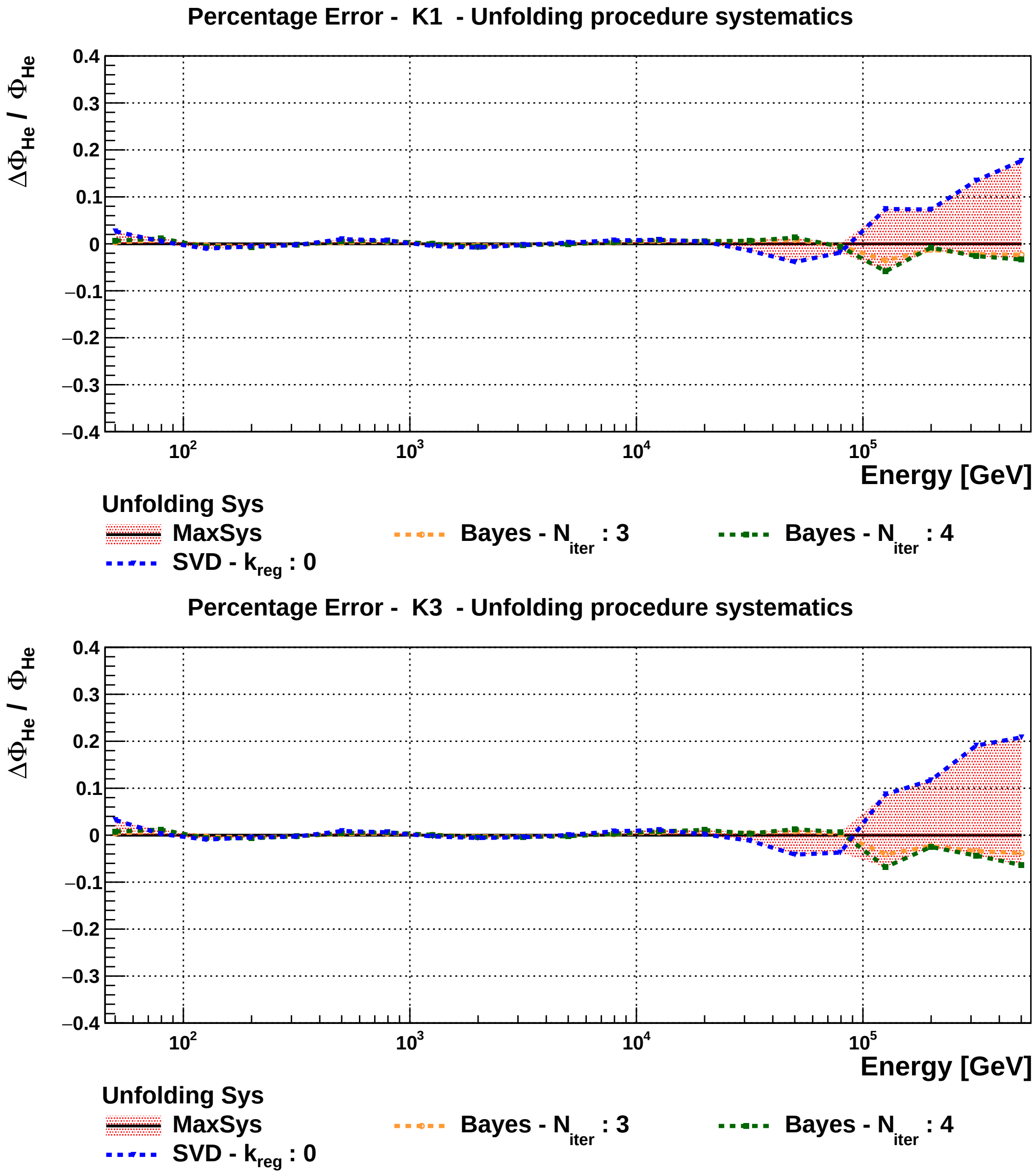

FIGURE 6.13: Systematics related to the unfolding procedure for preliminary helium flux in `K1` and `K3` acceptances.

6.7 Total Systematics and Fluxes

The total systematic uncertainties are calculated by adding in quadrature all the energy-dependent components described in the previous sections. The energy-independent contribution is also included in the sum. The result for all contributions as function of the primary energy, is shown in Fig. 6.14 for `A1`, and in Fig. 6.15 for `K1` and `K3` acceptances.

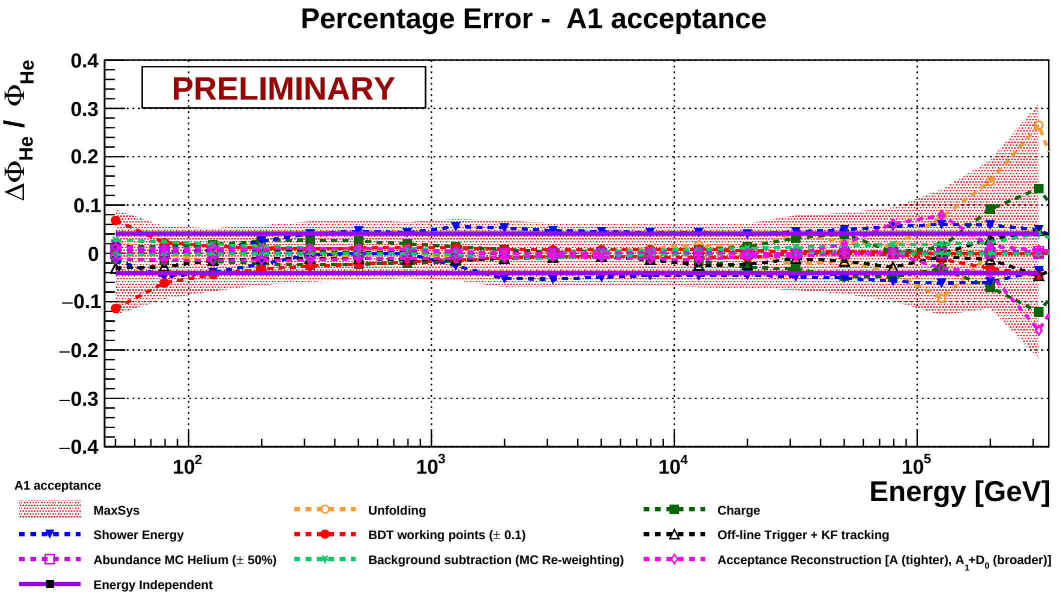

FIGURE 6.14: Breakdown of systematic uncertainty for `A1` acceptance. The colored filled areas represent the total uncertainty, whereas the individual contribution are encoded by different markers and lines as in legenda.

In each analysis, below 100 GeV, the main contribution comes from the definition of BDT working point. Between 100 GeV and 100 TeV, the total systematic error is within about ±10%, where the main source is the systematics associated with the shower energy correction in MC data. In the high-energy region ($\gtrsim$ 100 TeV) the systematics of the individual contribution are generally higher than in the other energy ranges. However, in most cases, they are also raised by the small number of events, and thus, a fit of the bin-by-bin estimate of uncertainty is likely to improve the overall accuracy. Nevertheless, since this work is still preliminary a more conservative approach has been preferred.

A comparison of the systematic errors is shown in Fig. 6.16 for the `A1`, `K1` and `K3` acceptances. In particular, it can be seen that below 100 TeV, these contributions are almost identical , while at higher energies the lowest systematic error is provided by the analysis in `K1` acceptances, followed by those in `K3` and `A1` acceptances. Nevertheless, it is worth noting that the largest errors in the last bins for the `A1` configuration, are determined by the very limited statistics available in the analysis of this Thesis work.

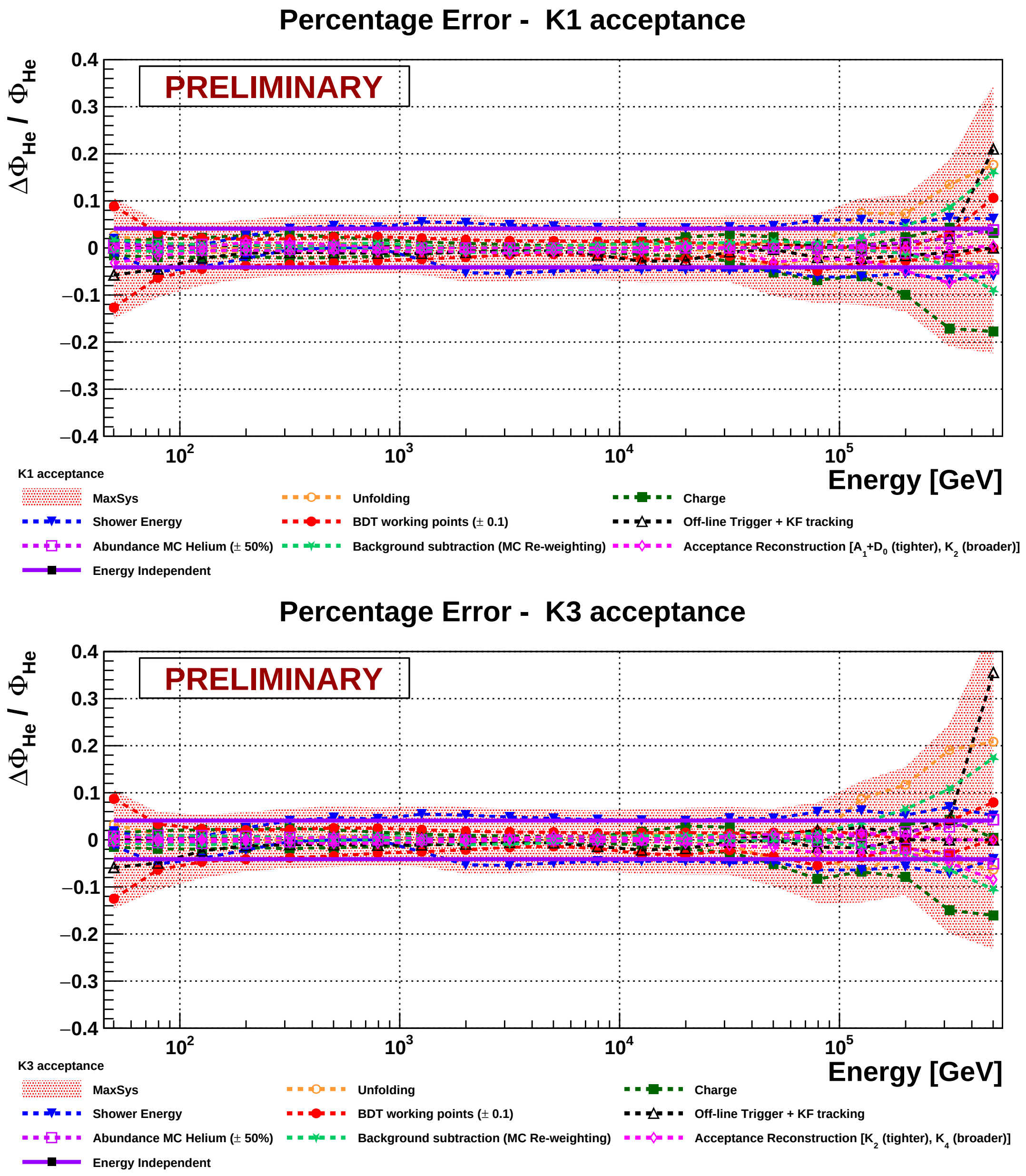

FIGURE 6.15: Breakdown of systematic uncertainty for `K1` (top) and `K3` (bottom) acceptances. The colored filled areas represent the total uncertainty, whereas the individual contribution are encoded by different markers and lines as in the legenda.

The total relative error, given by the addition in quadrature of the statistical and systematic uncertainties, remains slightly better for `K1` than for `K3` as shown in Fig. 6.17

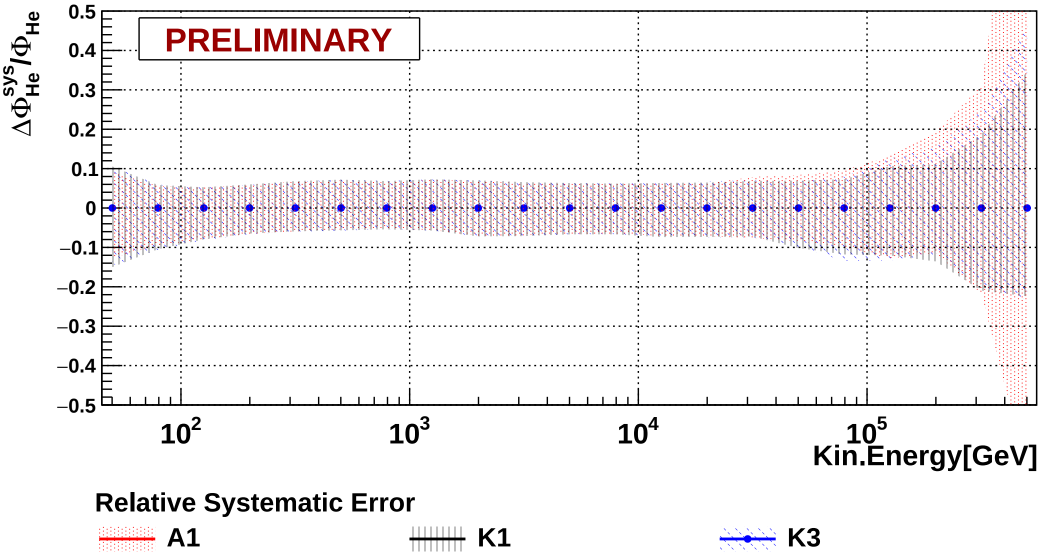

FIGURE 6.16: Relative systematic errors of the helium flux measurements in `A1`, `K1` and `K3` acceptances.

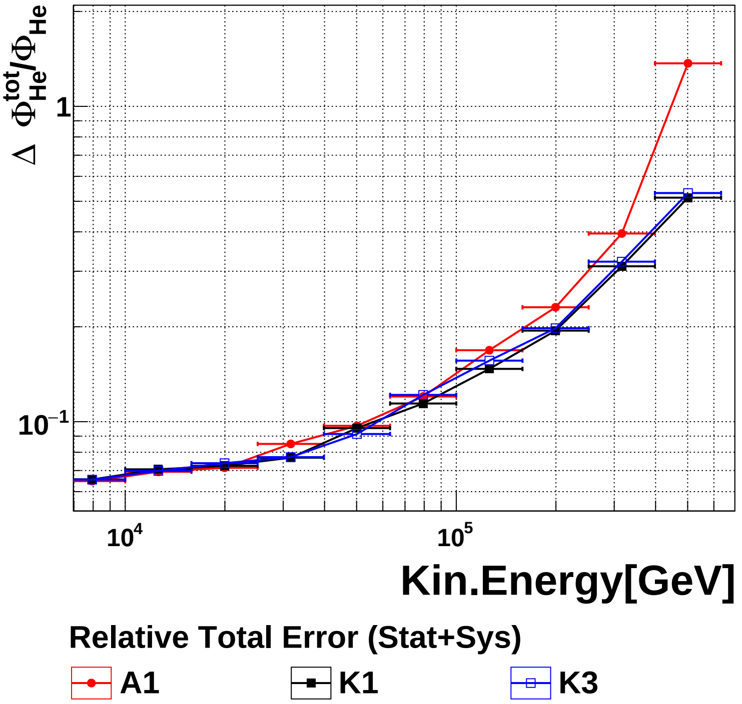

FIGURE 6.17: Relative total errors of the helium flux measurements in `A1`, `K1` and `K3` acceptances.

The preliminary fluxes, together with their statistical (vertical bars), systematics (red band) and total (blue band) errors and compared with the CALET-PRL [8] flux, are shown in Fig. 6.18 for `A1` , and in Fig. 6.19 `K1` and `K3` acceptances.

In conclusion, the `K1` acceptance is currently the best in terms of total error and, thus the candidate configuration to extend the helium flux measurement beyond 250 TeV. Nevertheless, the `K3` acceptance seems also promising for this extension, since it has better statistical accuracy and from this preliminary assessment it has only slightly worse systematic error.

Figure 6.20 shows again the preliminary helium flux in `K1` acceptance with the results obtained from other experiments, *viz.* DAMPE [29], AMS-02 [23], PAMELA [18] and NUCLEON [83]. This flux is compatible, within the errors, with the results of the other experiments over the entire energy range.

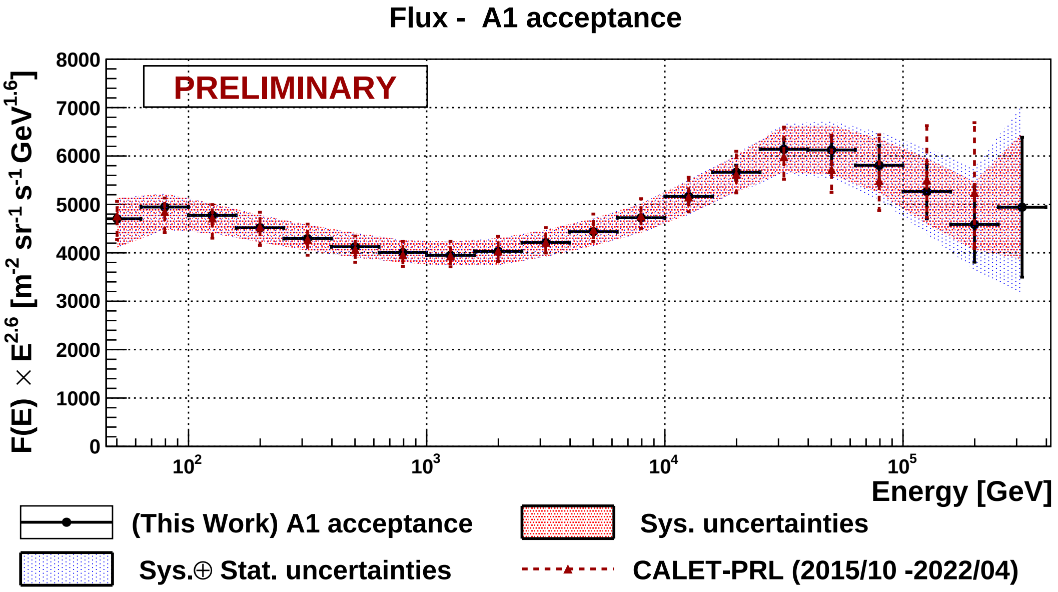
Flux - A1 acceptance

FIGURE 6.18: Preliminary helium fluxes in `A1` acceptance, together with the statistical (vertical bars), systematics (red band) and total (blue band) uncertainties. The flux from CALET-PRL [8] is shown for comparison.

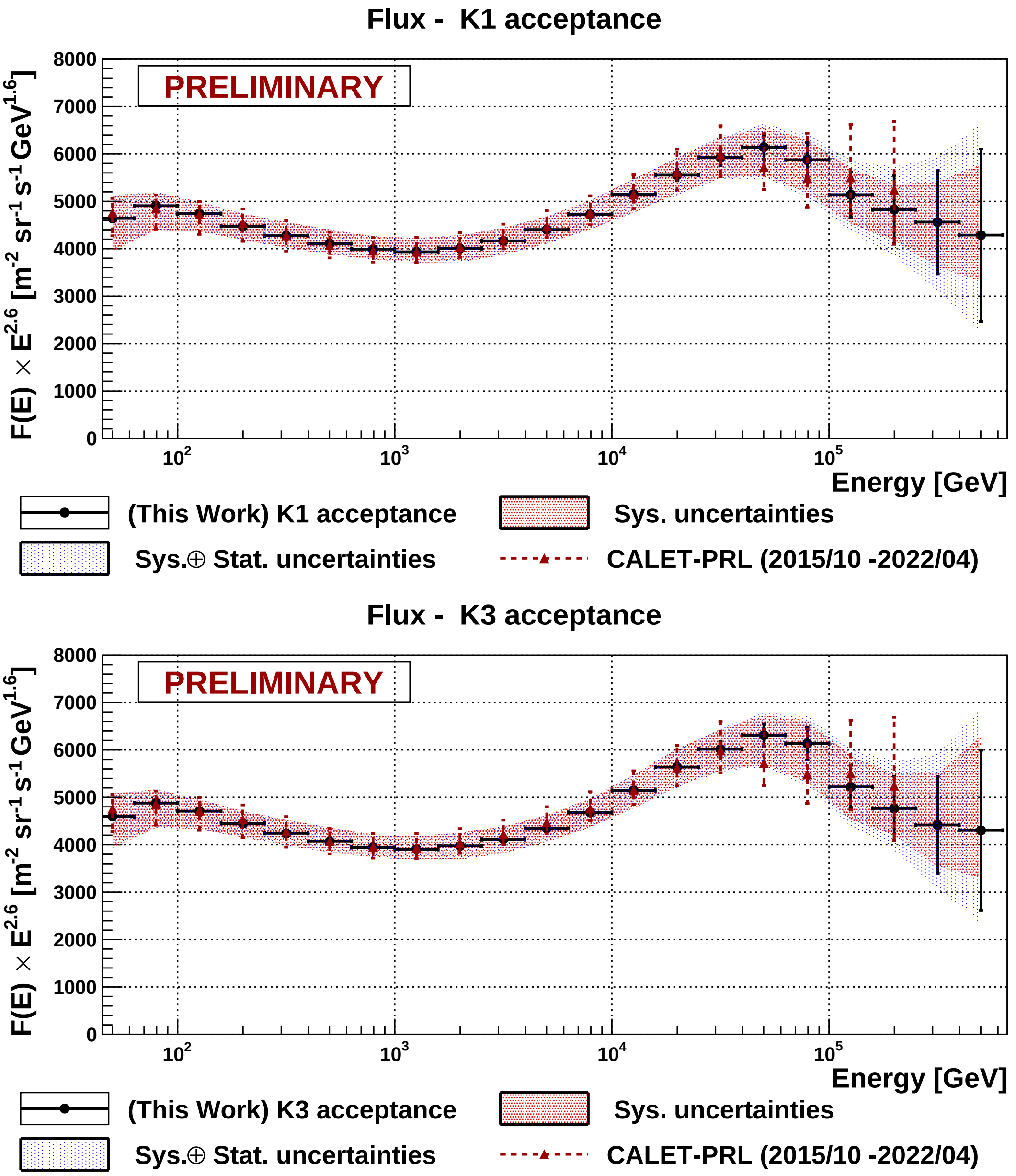

FIGURE 6.19: Preliminary helium fluxes together with the statistical (vertical bars), systematics (red band) and total (blue band) uncertainties for (top) K1 and (bottom) K3 acceptances. The flux from CALET-PRL [8] is also shown for comparison.

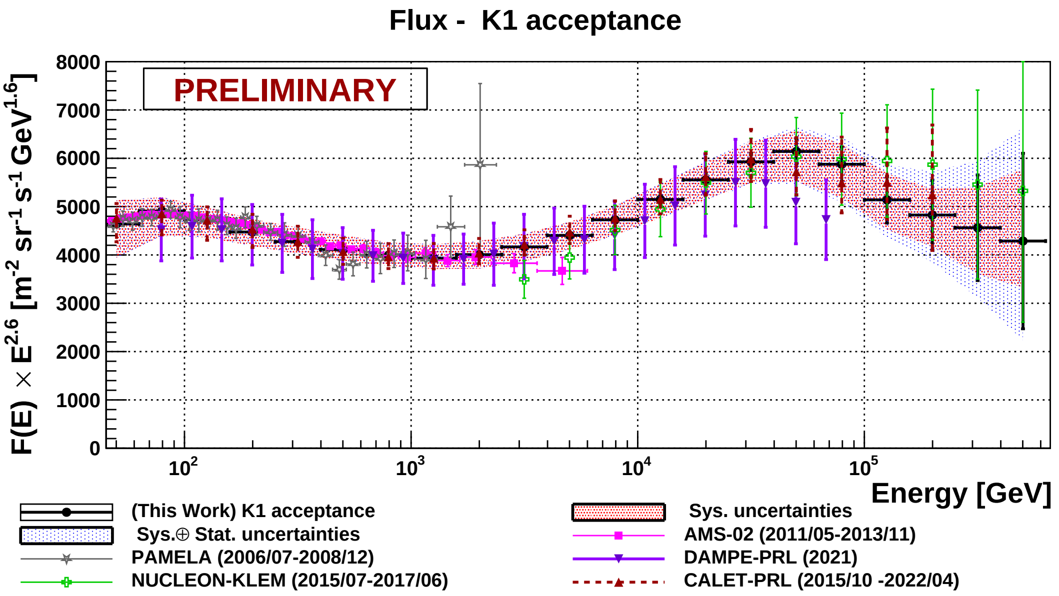

FIGURE 6.20: Preliminary helium flux in `K1` acceptance using 87 months of CALET data. The statistical (vertical bars), systematics (red band) and total (blue band) errors are represented. The results from other experiments, *viz.* CALET-PRL [8], DAMPE [29], AMS-02 [23], PAMELA [18] and NUCLEON [83], are shown for comparison.

Summary and Conclusions

In this Thesis, two separate analyses have been presented for the measurement of the helium flux. The first is carried out in fiducial acceptance `A1`, while the second is performed in two different enlarged acceptances `K1` and `K3`. These extensions aim to improve the statistical precision of the helium flux measurement at the highest energies achievable by the CALET instrument, while maintaining the systematics under control. Both are in agreement with the analysis published in 2023 by the CALET collaboration [8].

After a brief introduction to the Cosmic-Ray physics and the CALET instrument, in Chapter 3 the event reconstruction and the first step of the analysis are described.

In Chapter 4, the main new feature of this work is introduced, *i.e.* a multivariate analysis based on Boosted Decision Trees (BDT) to enhance the accuracy of the event selection by substantially reducing the background component from the off-acceptance events. The BDT selection has been implemented using 13 features as input. These can be grouped into two categories: the energy deposition profile and the variables related to the event topology. The former is constituted by the fractional energy deposits on various TASC layer, whereas the others are based on the difference between the track reconstructed with a combinatorial Kalman filter and with the method of moments. It is worth mentioning that this feature selection is the result of an extensive test campaign where variables have been characterized for their power to separate the signal from the background, and the data-MC consistency over the entire energy range. Subsequently, the BDT classifiers have been constructed for different energy intervals and several figures of merit have been studied in order to find the optimal definition of the BDT working points. The reliability of the BDT model has been validated by checking the distributions of BDT classifiers both for FD and MC data. Overall, the performances of the BDT selection are found to be fairly stable and consistent with the published analysis in the whole energy range, with an improvement in the high-energy region.

Taking advantage of this accurate event selection, a highly efficient charge identification is then performed as a function of the deposited energy. This provides nearly constant and very high (about 80%) selection efficiency over the entire energy range, while limiting the background component of protons up to the highest energies.

Another relevant step of the analysis is the unfolding procedure because it permits to infer the primary energy of the incident particle from the fraction of energy deposited in the calorimeter. For this reason, two different approaches have been studied: the iterative Bayesian algorithm and the SVD method. In both cases, the stability of the unfolding procedure and its bias-variance trade-off have been validated by the *pull test* described in the subsection 4.7.2 before unfolding the deposited energy spectrum derived from the *in-flight* data. Moreover, the statistical uncertainty of this procedure has been evaluated by using the *bootstrap* statistical method (see subsection 4.4.2), that provides an additional check of its stability.

Finally, the flux measurement in acceptance `A1`, is presented taking into account only the statistical error. It shows very good compatibility with the results published in PRL [8] by the CALET collaboration. In particular, the deviation of the helium flux from a single power law is confirmed and also an improvement of the signal purity at energies above $\sim$ 10 TeV is achieved. This results into a higher statistical accuracy of the measured flux in this important energy region.

Furthermore, it was observed that with increasing energy, the CHD contribution to charge selection becomes progressively weaker, as described in subsection 4.7.3. Therefore, the possibility of measuring the helium flux using only the IMC charge has been investigated. This has led to the main goal of this Thesis, which is to extend the fiducial geometrical acceptance of the helium flux measurement by including events with a larger incidence angle. These events are required to cross both the majority of the IMC layers and a sufficiently long path in the calorimeter to ensure a good energy reconstruction.

Chapter 5 is dedicated to the analysis in this enlarged acceptance. Two separate extensions, one more conservative (`K1`) than the other (`K3`) are considered. For both of them, BDT classifiers and energy-dependent charge selections have been custom developed as discussed in sections 5.2 and 5.3. As in `A1` acceptance, the behaviour of the various features has been characterized and the stability of the unfolding procedure has been validated to exclude any significant impact on the energy reconstruction (especially at high-energies) due to the inclusion of events with more tilted tracks (see section 5.5).

The preliminary fluxes in acceptance `K1` and `K3` are thus evaluated taking into account only the statistical uncertainties. The results are compatible, within the errors, with the CALET flux in `A1` acceptance as well as with the fluxes obtained by the AMS-02 [23] and PAMELA [18] magnetic spectrometers below $\sim$ 1 TeV and in fair agreement with the results published by DAMPE [29] and by NUCLEON [83] above, up to hundreds of TeV. It is also worth noting that the enlargement of the acceptance together with the new BDT-based selections permits the extension of the measurable energy range up to $\sim$ 600 TeV, albeit with a relatively large statistical error.

Finally, Chapter 6 is dedicated to the preliminary assessment of the systematic uncertainty for all the presented fluxes. This evaluation is particularly important for testing the reliability of the analyses developed in this Thesis. Specifically, the single components of the systematic uncertainty have been evaluated as a function of energy, using EPICS simulations. They turn out to be of the same order-of-magnitude as those presented in the Refs. [8, 50] and compatible with each other for the different acceptances considered.

However, the MC model-dependent contribution to systematics has not been addressed in this work, and therefore its evaluation will be a priority for future developments in the analysis.

In conclusion, this Thesis demonstrates that a ML approach for *off-acceptance* background rejection can improve the helium flux measurement, especially in the high-energy region. In addition, the extension of the geometrical acceptance has been shown to be feasible, with a statistical gain up to $\sim 60\%$ with respect to the current fiducial acceptance. This can provide a key contribution to future CALET measurements of helium flux towards the PeV energy scale, paving the way for the potential discovery of unknown spectral features.

List of Figures

List of Tables

Bibliography

[1] S. Abdollahi et al. “Cosmic-ray electron-positron spectrum from 7 GeV to 2 TeV with the Fermi Large Area Telescope”. In: *Phys. Rev. D* 95 (8 2017), p. 082007. DOI: `10.1103/PhysRevD.95.082007`. URL: `https://link.aps.org/doi/10.1103/PhysRevD.95.082007`.

[2] Anushka Udara Abeysekara et al. “HAWC measurements of the energy spectra of cosmic ray protons, helium and heavy nuclei in the TeV range”. In: *PoS* ICRC2021 (2021), p. 374. DOI: `10.22323/1.395.0374`. arXiv: `2108.03208 [astro-ph.HE]`.

[3] O. Adriani et al. “CALET Search for Electromagnetic Counterparts of Gravitational Waves during the LIGO/Virgo O3 Run”. In: *The Astrophysical Journal* 933.1 (2022), p. 85. DOI: `10.3847/1538-4357/ac6f53`. URL: `https://dx.doi.org/10.3847/1538-4357/ac6f53`.

[4] O. Adriani et al. “CALET Search for Electromagnetic Counterparts of Gravitational Waves during the LIGO/Virgo O3 Run”. In: *The Astrophysical Journal* 933.1 (2022), p. 85. DOI: `10.3847/1538-4357/ac6f53`. URL: `https://dx.doi.org/10.3847/1538-4357/ac6f53`.

[5] O. Adriani et al. “Charge-Sign Dependent Cosmic-Ray Modulation Observed with the Calorimetric Electron Telescope on the International Space Station”. In: *Phys. Rev. Lett.* 130 (21 2023), p. 211001. DOI: `10.1103/PhysRevLett.130.211001`. URL: `https://link.aps.org/doi/10.1103/PhysRevLett.130.211001`.

[6] O. Adriani et al. “Cosmic-Ray Boron Flux Measured from 8.4 GeV/n to 3.8 TeV/n with the Calorimetric Electron Telescope on the International Space Station”. In: *Phys. Rev. Lett.* 129.25 (2022), p. 251103. DOI: `10.1103/PhysRevLett.129.251103`. arXiv: `2212.07873 [astro-ph.HE]`.

[7] O. Adriani et al. “Direct Measurement of the Cosmic-Ray Carbon and Oxygen Spectra from 10 GeV/n to 2.2 TeV/n with the Calorimetric Electron Telescope on the International Space Station”. In: *Phys. Rev. Lett.* 125 (Dec. 2020), p. 251102. DOI: `10.1103/PhysRevLett.125.251102`. arXiv: `2012.10319 [astro-ph.HE]`.

[8] O. Adriani et al. “Direct Measurement of the Cosmic-Ray Helium Spectrum from 40 GeV to 250 TeV with the Calorimetric Electron Telescope on the International Space Station”. In: *Phys. Rev. Lett.* 130 (17 2023), p. 171002. DOI: `10.1103/PhysRevLett.130.171002`. URL: `https://link.aps.org/doi/10.1103/PhysRevLett.130.171002`.

[9] O. Adriani et al. "Direct Measurement of the Cosmic-Ray Proton Spectrum from 50 GeV to 10 TeV with the Calorimetric Electron Telescope on the International Space Station". In: *Phys. Rev. Lett.* 122 (18 2019), p. 181102. DOI: `10.1103/PhysRevLett.122.181102`. URL: `https://link.aps.org/doi/10.1103/PhysRevLett.122.181102`.

[10] O. Adriani et al. "Direct Measurement of the Nickel Spectrum in Cosmic Rays in the Energy Range from 8.8 GeV/n to 240 GeV/n with CALET on the International Space Station". In: *Phys. Rev. Lett.* 128.13 (2022), p. 131103. DOI: `10.1103/PhysRevLett.128.131103`. arXiv: `2204.00845 [astro-ph.HE]`.

[11] O. Adriani et al. "Direct Measurement of the Spectral Structure of Cosmic-Ray Electrons + Positrons in the TeV Region with CALET on the International Space Station". In: *Phys. Rev. Lett.* 131 (19 2023), p. 191001. DOI: `10.1103/PhysRevLett.131.191001`. URL: `https://link.aps.org/doi/10.1103/PhysRevLett.131.191001`.

[12] O. Adriani et al. "Direct measurements of cosmic - ray iron and nickel with CALET on the International Space Station". In: *Advances in Space Research* (2024). ISSN: 0273-1177. DOI: `https://doi.org/10.1016/j.asr.2024.03.052`. URL: `https://www.sciencedirect.com/science/article/pii/S0273117724002874`.

[13] O. Adriani et al. "Energy Spectrum of Cosmic-Ray Electron and Positron from 10 GeV to 3 TeV Observed with the Calorimetric Electron Telescope on the International Space Station". In: *Phys. Rev. Lett.* 119.18 (2017), p. 181101. DOI: `10.1103/PhysRevLett.119.181101`. arXiv: `1712.01711 [astro-ph.HE]`.

[14] O. Adriani et al. "Energy Spectrum of Cosmic-Ray Electron and Positron from 10 GeV to 3 TeV Observed with the Calorimetric Electron Telescope on the International Space Station". In: *Phys. Rev. Lett.* 119 (18 2017), p. 181101. DOI: `10.1103/PhysRevLett.119.181101`. URL: `https://link.aps.org/doi/10.1103/PhysRevLett.119.181101`.

[15] O. Adriani et al. "Extended Measurement of the Cosmic-Ray Electron and Positron Spectrum from 11 GeV to 4.8 TeV with the Calorimetric Electron Telescope on the International Space Station". In: *Phys. Rev. Lett.* 120.26 (2018), p. 261102. DOI: `10.1103/PhysRevLett.120.261102`. arXiv: `1806.09728 [astro-ph.HE]`.

[16] O. Adriani et al. "Measurement of boron and carbon fluxes in cosmic rays with the PAMELA experiment". In: *Astrophys. J.* 791.2 (2014), p. 93. DOI: `10.1088/0004-637X/791/2/93`. arXiv: `1407.1657 [astro-ph.HE]`.

[17] O. Adriani et al. "Measurement of the Iron Spectrum in Cosmic Rays from 10 GeV/n to 2.0 TeV/n with the Calorimetric Electron Telescope on the International Space Station". In: *Phys. Rev. Lett.* 126.24 (2021), p. 241101. DOI: `10.1103/PhysRevLett.126.241101`. arXiv: `2106.08036 [astro-ph.HE]`.

[18] O. Adriani et al. “Measurements of cosmic-ray proton and helium spectra with the PAMELA calorimeter”. In: *Advances in Space Research* 51.2 (2013). The Origins of Cosmic Rays: Resolving Hess’s Century-Old Puzzle, pp. 219–226. ISSN: 0273-1177. DOI: `https://doi.org/10.1016/j.asr.2012.09.029`. URL: `https://www.sciencedirect.com/science/article/pii/S0273117712006199`.

[19] O. Adriani et al. “Observation of Spectral Structures in the Flux of Cosmic-Ray Protons from 50 GeV to 60 TeV with the Calorimetric Electron Telescope on the International Space Station”. In: *Phys. Rev. Lett.* 129 (10 2022), p. 101102. DOI: `10.1103/PhysRevLett.129.101102`. URL: `https://link.aps.org/doi/10.1103/PhysRevLett.129.101102`.

[20] Oscar Adriani et al. “Boron flux in cosmic rays and its flux ratio to primary species measured with CALET on the International Space Station”. In: *PoS* ICRC2023 (2023), p. 058. DOI: `10.22323/1.444.0058`.

[21] Oscar Adriani et al. “Results from CALorimetric Electron Telescope (CALET) Observations of Gamma-rays on the International Space Station”. In: *PoS* ICRC2023 (2023), p. 708. DOI: `10.22323/1.444.0708`.

[22] Tim Adye. “Unfolding algorithms and tests using RooUnfold”. In: *PHYSTAT 2011*. Geneva: CERN, 2011, pp. 313–318. DOI: `10.5170/CERN-2011-006.313`. arXiv: `1105.1160 [physics.data-an]`.

[23] M. Aguilar et al. “Precision Measurement of the Helium Flux in Primary Cosmic Rays of Rigidities 1.9 GV to 3 TV with the Alpha Magnetic Spectrometer on the International Space Station”. In: *Phys. Rev. Lett.* 115 (21 2015), p. 211101. DOI: `10.1103/PhysRevLett.115.211101`. URL: `https://link.aps.org/doi/10.1103/PhysRevLett.115.211101`.

[24] M. Aguilar et al. “Precision Measurement of the Proton Flux in Primary Cosmic Rays from Rigidity 1 GV to 1.8 TV with the Alpha Magnetic Spectrometer on the International Space Station”. In: *Phys. Rev. Lett.* 114 (17 2015), p. 171103. DOI: `10.1103/PhysRevLett.114.171103`. URL: `https://link.aps.org/doi/10.1103/PhysRevLett.114.171103`.

[25] M. Aguilar et al. “The Alpha Magnetic Spectrometer (AMS) on the international space station: Part II — Results from the first seven years”. In: *Physics Reports* 894 (2021). The Alpha Magnetic Spectrometer (AMS) on the International Space Station: Part II - Results from the First Seven Years, pp. 1–116. ISSN: 0370-1573. DOI: `https://doi.org/10.1016/j.physrep.2020.09.003`. URL: `https://www.sciencedirect.com/science/article/pii/S0370157320303434`.

[26] F. Aharonian et al. “Energy Spectrum of Cosmic-Ray Electrons at TeV Energies”. In: *Phys. Rev. Lett.* 101 (26 2008), p. 261104. DOI: `10.1103/PhysRevLett.101.261104`. URL: `https://link.aps.org/doi/10.1103/PhysRevLett.101.261104`.

[27] Y. Akaike and Calet Collaboration. “Simulations for CALET Energy Calibration Confirmed Using CERN-SPS Beam Tests”. In: *34th International Cosmic Ray Conference (ICRC2015)*. Vol. 34. International Cosmic Ray Conference. July 2015, 613, p. 613. DOI: `10.22323/1.236.0613`.

[28] Yosui Akaike. “CALET Observational Performance Expected by CERN Beam Test”. In: *International Cosmic Ray Conference*. Vol. 33. International Cosmic Ray Conference. Jan. 2013, p. 2162.

[29] F. Alemanno et al. “Measurement of the Cosmic Ray Helium Energy Spectrum from 70 GeV to 80 TeV with the DAMPE Space Mission”. In: *Phys. Rev. Lett.* 126 (20 2021), p. 201102. DOI: `10.1103/PhysRevLett.126.201102`. URL: `https://link.aps.org/doi/10.1103/PhysRevLett.126.201102`.

[30] Luis Alvarez and Arthur H. Compton. “A Positively Charged Component of Cosmic Rays”. In: *Phys. Rev.* 43 (10 1933), pp. 835–836. DOI: `10.1103/PhysRev.43.835`. URL: `https://link.aps.org/doi/10.1103/PhysRev.43.835`.

[31] Carl D. Anderson. “The Positive Electron”. In: *Phys. Rev.* 43 (6 1933), pp. 491–494. DOI: `10.1103/PhysRev.43.491`. URL: `https://link.aps.org/doi/10.1103/PhysRev.43.491`.

[32] Y. Asaoka et al. “Energy calibration of CALET onboard the International Space Station”. In: *Astroparticle Physics* 91 (2017), pp. 1–10. ISSN: 0927-6505. DOI: `https://doi.org/10.1016/j.astropartphys.2017.03.002`. URL: `https://www.sciencedirect.com/science/article/pii/S0927650517300786`.

[33] Y. Asaoka et al. “On-orbit operations and offline data processing of CALET onboard the ISS”. In: *Astroparticle Physics* 100 (2018), pp. 29–37. ISSN: 0927-6505. DOI: `https://doi.org/10.1016/j.astropartphys.2018.02.010`. URL: `https://www.sciencedirect.com/science/article/pii/S0927650517303213`.

[34] Pierre Auger, Raymond Maze, and Thérèse Grivet-Mayer. “Grandes gerbes cosmiques atmosphériques contenant des corpuscules ultrapénétrants”. In: *Compt. Rend. Hebd. Seances Acad. Sci.* 206.23 (1938), pp. 1721–1723.

[35] W. I. Axford, E. Leer, and G. Skadron. “The Acceleration of Cosmic Rays by Shock Waves”. In: *International Cosmic Ray Conference*. Vol. 11. International Cosmic Ray Conference. Jan. 1977, p. 132.

[36] W. Baade and F. Zwicky. “Cosmic Rays from Super-novae”. In: *Proceedings of the National Academy of Science* 20.5 (May 1934), pp. 259–263. DOI: `10.1073/pnas.20.5.259`.

[37] M.G. Bagliesi et al. "Front-end electronics with large dynamic range for space-borne cosmic ray experiments". In: *Nuclear Physics B - Proceedings Supplements* 172 (2007). Proceedings of the 10th Topical Seminar on Innovative Particle and Radiation Detectors, pp. 156–158. ISSN: 0920-5632. DOI: `https://doi.org/10.1016/j.nuclphysbps.2007.08.147`. URL: `https://www.sciencedirect.com/science/article/pii/S0920563207005798`.

[38] A. R. Bell. "The acceleration of cosmic rays in shock fronts - I." In: *Monthly Notices of the Royal Astronomical Society, Vol. 182, 147-156 (1978)* 182 (Jan. 1978), pp. 147–156. DOI: `10.1093/mnras/182.2.147`.

[39] E.G. Berezhko. "Maximum energy of cosmic rays accelerated by supernova shocks". In: *Astroparticle Physics* 5.3 (1996), pp. 367–378. ISSN: 0927-6505. DOI: `https://doi.org/10.1016/0927-6505(96)00037-0`. URL: `https://www.sciencedirect.com/science/article/pii/0927650596000370`.

[40] V. S. Berezinskii et al. *Astrophysics of cosmic rays*. 1990.

[41] E. Berti et al. "The analysis strategy for the measurement of the electron flux with CALET on the International Space Station". In: *37th International Cosmic Ray Conference*. Mar. 2022, 65, p. 65. DOI: `10.22323/1.395.0065`.

[42] Katharina Bierwagen, Ulla Blumenschein, and Arnulf Quadt. "Bayesian Unfolding". In: *PHYSTAT 2011*. Geneva: CERN, 2011, pp. 260–263. DOI: `10.5170/CERN-2011-006.260`.

[43] Gabriele Bigongiari. "CALET perspectives for calorimetric measurements of high energy electrons based on beam test results". In: *PoS* ICRC2015 (2016), p. 592. DOI: `10.22323/1.236.0592`.

[44] Roger D Blandford and James P Ostriker. "Particle acceleration by astrophysical shocks". In: *Astrophysical Journal, Part 2-Letters to the Editor, vol. 221, Apr. 1, 1978, p. L29-L32.* 221 (1978), pp. L29–L32.

[45] Luisa Bonolis. "Walther Bothe and Bruno Rossi: The birth and development of coincidence methods in cosmic-ray physics". In: *American Journal of Physics* 79.11 (Nov. 2011), pp. 1133–1150. ISSN: 0002-9505. DOI: `10.1119/1.3619808`. eprint: `https://pubs.aip.org/aapt/ajp/article-pdf/79/11/1133/13103440/1133\_1\_online.pdf`. URL: `https://doi.org/10.1119/1.3619808`.

[46] L. Breiman et al. *Classification and Regression Trees*. Wadsworth, 1984.

[47] Leo Breiman. "Arcing the Edge". In: *Ann. Prob.* 26 (1998), pp. 1683–1702.

[48] Leo Breiman. "Prediction Games and Arcing Algorithms". In: *Neural Comput.* 11 (1999), pp. 1493–1517. DOI: `10.1162/089976699300016106`.

[49] Paolo Brogi. *Tracking and Identification of Proton and Helium in CALET and Perspectives for Flux Measurements*. PhD Thesis, 2015, p. 166.

[50] Paolo Brogi and Kazuyoshi Kobayashi. “Measurement of the energy spectrum of cosmic-ray helium with CALET on the International Space Station”. In: *PoS* ICRC2021 (2021), p. 101. DOI: `10.22323/1.395.0101`.

[51] Paolo Brogi et al. “CALET measurements with cosmic nuclei: expected performances of tracking and charge identification”. In: *PoS* ICRC2015 (2016), p. 595. DOI: `10.22323/1.236.0595`.

[52] Calet et al. “Optimization of the proton background rejection in the measurement of the electron flux at high energies with CALET on the International Space Station”. In: *PoS* ICRC2023 (2023), p. 090. DOI: `10.22323/1.444.0090`.

[53] N. Cannady et al. “Characteristics and Performance of the CALorimetric Electron Telescope (CALET) Calorimeter for Gamma-Ray Observations”. In: *The Astrophysical Journal Supplement Series* 238.1 (2018), p. 5. DOI: `10.3847/1538-4365/aad6a3`. URL: `https://dx.doi.org/10.3847/1538-4365/aad6a3`.

[54] Caterina Checchia. *Study of cosmic-ray light nuclei on the ISS: identification of the interaction point in the Calorimetric Electron Telescope (CALET)*. PhD Thesis, 2018, p. 166.

[55] J Clay. “Results of the dutch cosmic-ray expedition 1933: Briefly communicated”. In: *Physica* 1.1 (1934), pp. 363–382. ISSN: 0031-8914. DOI: `https://doi.org/10.1016/S0031-8914(34)90043-4`. URL: `https://www.sciencedirect.com/science/article/pii/S0031891434900434`.

[56] Yann Coadou. “Boosted decision trees”. In: (Mar. 2022). DOI: `10.1142/9789811234033_0002`. arXiv: `2206.09645 [physics.data-an]`.

[57] DAMPE Collaboration et al. “Measurement of the cosmic ray proton spectrum from 40 GeV to 100 TeV with the DAMPE satellite”. In: *Science Advances* 5.9 (2019), eaax3793. DOI: `10.1126/sciadv.aax3793`. eprint: `https://www.science.org/doi/pdf/10.1126/sciadv.aax3793`. URL: `https://www.science.org/doi/abs/10.1126/sciadv.aax3793`.

[58] Arthur H. Compton. “A Geographic Study of Cosmic Rays”. In: *Phys. Rev.* 43 (6 1933), pp. 387–403. DOI: `10.1103/PhysRev.43.387`. URL: `https://link.aps.org/doi/10.1103/PhysRev.43.387`.

[59] G. Cowan. “A survey of unfolding methods for particle physics”. In: *Conf. Proc. C* 0203181 (2002). Ed. by M. R. Whalley and L. Lyons, pp. 248–257.

[60] G. Cowan. *Statistical data analysis*. 1998. ISBN: 978-0-19-850156-5.

[61] G. D’Agostini. “A multidimensional unfolding method based on Bayes’ theorem”. In: *Nuclear Instruments and Methods in Physics Research Section A: Accelerators, Spectrometers, Detectors and Associated Equipment* 362.2 (1995), pp. 487–498. ISSN: 0168-9002. DOI: `https://doi.org/10.1016/0168-9002(95)00274-X`. URL: `https://www.sciencedirect.com/science/article/pii/016890029500274X`.

[62] G. D'Agostini. "Improved iterative Bayesian unfolding". In: *arXiv e-prints*, arXiv:1010.0632 (Oct. 2010), arXiv:1010.0632. DOI: `10.48550/arXiv.1010.0632`. arXiv: `1010.0632 [physics.data-an]`.

[63] DAMPE Collaboration et al. "Direct detection of a break in the tera-electronvolt cosmic-ray spectrum of electrons and positrons". In: *Nature* 552.7683 (Dec. 2017), pp. 63–66. DOI: `10.1038/nature24475`. arXiv: `1711.10981 [astro-ph.HE]`.

[64] A. De Angelis. *L'enigma dei raggi cosmici: Le più grandi energie dell'universo*. I blu. Springer Milan, 2011. ISBN: 9788847020474. URL: `https://books.google.it/books?id=XeUa5MH-96EC`.

[65] Alessandro De Angelis and Mario Pimenta. *Introduction to Particle and Astroparticle Physics: Multimessenger Astronomy and its Particle Physics Foundations*. Undergraduate Lecture Notes in Physics. Heidelberg: Springer Nature, 2018. ISBN: 978-3-319-78180-8, 978-3-319-78181-5.

[66] V. Di Felice et al. "Looking for cosmic ray data? The ASI Cosmic Ray Database". In: *35th International Cosmic Ray Conference (ICRC2017)*. Vol. 301. International Cosmic Ray Conference. July 2017, 1073, p. 1073. DOI: `10.22323/1.301.01073`.

[67] Rebecca Diesing. "The Maximum Energy of Shock-accelerated Cosmic Rays". In: *The Astrophysical Journal* 958.1 (2023), p. 3. DOI: `10.3847/1538-4357/ad00b1`. URL: `https://dx.doi.org/10.3847/1538-4357/ad00b1`.

[68] Fiorenza Donato. "Indirect searches for dark matter". In: *Physics of the Dark Universe* 4 (2014). DARK TAUP2013, pp. 41–43. ISSN: 2212-6864. DOI: `https://doi.org/10.1016/j.dark.2014.06.001`. URL: `https://www.sciencedirect.com/science/article/pii/S221268641400020X`.

[69] L. Oc. Drury. "REVIEW ARTICLE: An introduction to the theory of diffusive shock acceleration of energetic particles in tenuous plasmas". In: *Reports on Progress in Physics* 46.8 (Aug. 1983), pp. 973–1027. DOI: `10.1088/0034-4885/46/8/002`.

[70] Bradley Efron and Robert J. Tibshirani. *An Introduction to the Bootstrap*. Monographs on Statistics and Applied Probability 57. Boca Raton, Florida, USA: Chapman & Hall/CRC, 1993.

[71] Carmelo Evoli. *The Cosmic-Ray Energy Spectrum*. Dec. 2020. DOI: `10.5281/zenodo.4396125`. URL: `https://doi.org/10.5281/zenodo.4396125`.

[72] Carmelo Evoli et al. "Cosmic-ray propagation with DRAGON2: I. numerical solver and astrophysical ingredients". In: *JCAP* 2017.2, 015 (Feb. 2017), p. 015. DOI: `10.1088/1475-7516/2017/02/015`. arXiv: `1607.07886 [astro-ph.HE]`.

[73] Carmelo Evoli et al. “Cosmic-ray propagation with DRAGON2: II. Nuclear interactions with the interstellar gas”. In: *JCAP* 2018.7, 006 (July 2018), p. 006. DOI: `10.1088/1475-7516/2018/07/006`. arXiv: `1711.09616 [astro-ph.HE]`.

[74] Christian W. Fabjan and Fabiola Gianotti. “Calorimetry for particle physics”. In: *Rev. Mod. Phys.* 75 (4 2003), pp. 1243–1286. DOI: `10.1103/RevModPhys.75.1243`. URL: `https://link.aps.org/doi/10.1103/RevModPhys.75.1243`.

[75] E. Fermi. “Galactic Magnetic Fields and the Origin of Cosmic Radiation.” In: *"Astrophysical Journal"* 119 (Jan. 1954), p. 1. DOI: `10.1086/145789`.

[76] Enrico Fermi. “On the Origin of the Cosmic Radiation”. In: *Physical Review* 75 (1949), pp. 1169–1174.

[77] Yoav Freund and Robert E. Schapire. “Experiments with a New Boosting Algorithm”. In: *Proceedings of the Thirteenth International Conference on Machine Learning*. ICML’96. Bari, Italy, 1996, 148—156.

[78] R. Fruhwirth. “Application of Kalman filtering to track and vertex fitting”. In: *Nucl. Instrum. Meth. A* 262 (1987), pp. 444–450. DOI: `10.1016/0168-9002(87)90887-4`.

[79] Thomas K. Gaisser, Ralph Engel, and Elisa Resconi. *Cosmic Rays and Particle Physics*. 2nd ed. Cambridge University Press, 2016.

[80] C. Gini. *Variabilità e Mutabilità*. (reprinted in *Memorie di Metodologica Statistica*, eds. E. Pizetti and T. Salvemini, Libreria Eredi Virgilio Veschi, Rome, 1955). 1912.

[81] V. L. Ginzburg and S. I. Syrovatskii. *The Origin of Cosmic Rays*. 1964.

[82] J. J. Gomez, J. Velasco, and E. Maestro. “STUDY OF AN ALGORITHM FOR ELECTRON HADRON SEPARATION IN MODULAR HOMOGENEOUS CALORIMETERS”. In: *Nucl. Instrum. Meth. A* 262 (1987), pp. 284–290. DOI: `10.1016/0168-9002(87)90865-5`.

[83] V. Grebenyuk et al. “Energy spectra of abundant cosmic-ray nuclei in the NUCLEON experiment”. In: *Advances in Space Research* 64.12 (Dec. 2019), pp. 2546–2558. DOI: `10.1016/j.asr.2019.10.004`.

[84] Kenneth Greisen. “End to the Cosmic-Ray Spectrum?” In: *Phys. Rev. Lett.* 16 (17 1966), pp. 748–750. DOI: `10.1103/PhysRevLett.16.748`. URL: `https://link.aps.org/doi/10.1103/PhysRevLett.16.748`.

[85] T. Gregory Guzik. “The CALorimeter Electron Telescope (CALET) Ground Data Handling and Processing System”. In: *International Cosmic Ray Conference*. Vol. 33. International Cosmic Ray Conference. Jan. 2013, p. 1888.

[86] M. Hanasz, A. Strong, and P. Girichidis. “Simulations of cosmic ray propagation”. In: (June 2021). DOI: `10.1007/s41115-021-00011-1`. arXiv: `2106.08426 [astro-ph.HE]`.

[87] Trevor Hastie, Robert Tibshirani, and Jerome Friedman. *The Elements of Statistical Learning*. Springer Series in Statistics. New York, NY, USA: Springer New York Inc., 2001.

[88] Victor F. Hess. "Über Beobachtungen der durchdringenden Strahlung bei sieben Freiballonfahrten". In: *Phys. Z.* 13 (1912), pp. 1084–1091.

[89] A. M. Hillas. "The Origin of Ultra-High-Energy Cosmic Rays". In: *Annual review of astronomy and astrophysics* 22 (Jan. 1984), pp. 425–444. DOI: `10.1146/annurev.aa.22.090184.002233`.

[90] Andreas Hocker and Vakhtang Kartvelishvili. "SVD approach to data unfolding". In: *Nucl. Instrum. Meth. A* 372 (1996), pp. 469–481. DOI: `10.1016/0168-9002(95)01478-0`. arXiv: `hep-ph/9509307`.

[91] Andreas Hoecker et al. "TMVA — Toolkit for Multivariate Data Analysis". In: (2007). arXiv: `physics/0703039 [physics.data-an]`.

[92] Daijiro Ito et al. "High-dynamic range readout system using dual APD/PD for the CALET-TASC". English. In: *Proceedings of the 32nd International Cosmic Ray Conference, ICRC 2011*. Vol. 6. 32nd International Cosmic Ray Conference, ICRC 2011 ; Conference date: 11-08-2011 Through 18-08-2011. Institute of High Energy Physics, 2011, pp. 375–378. DOI: `10.7529/ICRC2011/V06/0824`.

[93] K. Kasahara. "Introduction to Cosmos and some Relevance to Ultra High Energy Cosmic Ray Air Showers". In: *International Cosmic Ray Conference*. Vol. 1. International Cosmic Ray Conference. Jan. 1995, p. 399.

[94] Yuta Kawakubo. "Gamma-ray burst observations with the CALET Gamma-ray Burst Monitor". In: *PoS* ICRC2019 (2021), p. 571. DOI: `10.22323/1.358.0571`.

[95] Kilian Weinberger. *Lecture Note 19 - Boosting - Course : Machine Learning for Intelligent Systems -fall 2018*. `http://www.cs.cornell.edu/courses/cs4780/2018fa/lectures/lecturenote19.html`.

[96] G. F. Krymskii. "A regular mechanism for the acceleration of charged particles on the front of a shock wave". In: *Akademiia Nauk SSSR Doklady* 234 (June 1977), pp. 1306–1308.

[97] John Linsley. "Evidence for a primary cosmic-ray particle with energy 10**20-eV". In: *Phys. Rev. Lett.* 10 (1963), pp. 146–148. DOI: `10.1103/PhysRevLett.10.146`.

[98] Katharina Lodders. "Solar System Abundances and Condensation Temperatures of the Elements". In: *"Astrophysical Journal"* 591.2 (July 2003), pp. 1220–1247. DOI: `10.1086/375492`.

[99] Malcolm S. Longair. *High Energy Astrophysics*. 2011.

[100] P. Maestro, Calet Collaboration, and N. Mori. "Particle tracking in the CALET experiment". In: *35th International Cosmic Ray Conference (ICRC2017)*. Vol. 301. International Cosmic Ray Conference. July 2017, 208, p. 208. DOI: `10.22323/1.301.0208`.

[101] Marco Mattiazzi et al. "Feasibility study on an analysis of CR helium flux with the CALET detector based on an extended acceptance". In: *PoS* ICRC2023 (2023), p. 082. DOI: `10.22323/1.444.0082`.

[102] David Maurin. "USINE: Semi-analytical models for Galactic cosmic-ray propagation". In: *Computer Physics Communications* 247, 106942 (Feb. 2020), p. 106942. DOI: `10.1016/j.cpc.2019.106942`. arXiv: `1807.02968 [astro-ph.IM]`.

[103] David Maurin et al. "Cosmic-Ray Database Update: Ultra-High Energy, Ultra-Heavy, and Antinuclei Cosmic-Ray Data (CRDB v4.0)". In: *Universe* 6.8 (2020). ISSN: 2218-1997. DOI: `10.3390/universe6080102`. URL: `https://www.mdpi.com/2218-1997/6/8/102`.

[104] Ryohei Miyata, Yoichi Asaoka, and S. Torii. "Full Dynamic Range Energy Calibration of CALET onboard the International Space Station". In: *PoS* ICRC2017 (2018), p. 207. DOI: `10.22323/1.301.0207`.

[105] Igor V Moskalenko. "Direct measurements of cosmic rays and their possible interpretations". In: *PoS* ICRC2023 (2023), p. 020. DOI: `10.22323/1.444.0020`.

[106] Holger Motz et al. "Dark Matter Limits from the CALET Electron+Positron Spectrum with Individual Astrophysical Source Background". In: *PoS* ICRC2023 (2023), p. 1385. DOI: `10.22323/1.444.1385`.

[107] Holger Motz et al. "Investigating the Vela SNR's Emission of Electron Cosmic Rays with CALET at the International Space Station". In: *PoS* ICRC2021 (2021), p. 100. DOI: `10.22323/1.395.0100`.

[108] Tae Niita et al. "Energy calibration of Calorimetric Electron Telescope (CALET) in space". In: *Adv. Space Res.* 55 (2015), pp. 2500–2508. DOI: `10.1016/j.asr.2015.03.006`.

[109] J. Nishimura, M. Fujii, and T. Taira. "Electron Spectrum of the High Energy Side". In: *International Cosmic Ray Conference*. Vol. 1. International Cosmic Ray Conference. Jan. 1979, p. 488.

[110] A. D. Panov et al. "Energy spectra of abundant nuclei of primary cosmic rays from the data of ATIC-2 experiment: Final results". In: *Bulletin of the Russian Academy of Sciences, Physics* 73.5 (June 2009), pp. 564–567. DOI: `10.3103/S1062873809050098`. arXiv: `1101.3246 [astro-ph.HE]`.

[111] Frank C. Porter. *Testing Consistency of Two Histograms*. 2008. DOI: `10.48550/ARXIV.0804.0380`. URL: `https://arxiv.org/abs/0804.0380`.

[112] Stefan Roesler, Ralph Engel, and Johannes Ranft. "The Monte Carlo event generator DPMJET-III". In: *International Conference on Advanced Monte Carlo for Radiation Physics, Particle Transport Simulation and Applications (MC 2000)*. Dec. 2000, pp. 1033–1038. DOI: `10.1007/978-3-642-18211-2_166`. arXiv: `hep-ph/0012252`.

[113] Arshia Ruina. "Measuring the Cosmic Ray Helium Flux with the DAMPE Experiment". PhD thesis. U. Geneva (main), 2023. DOI: `10.13097/archive-ouverte/unige:170702`.

[114] T. Sako et al. "COSMOS X as a general purpose air shower simulation tool". In: *37th International Cosmic Ray Conference*. Mar. 2022, 431, p. 431. DOI: 10.22323/1.395.0431.

[115] Robert E. Schapire and Yoav Freund. *Boosting: Foundations and Algorithms*. MIT Press, 2012.

[116] Reinhard Schlickeiser. *Cosmic Ray Astrophysics*. 2002.

[117] Yuki Shimizu. "The CALET CHD for determination of nuclear charge". In: *International Cosmic Ray Conference*. Vol. 6. International Cosmic Ray Conference. Jan. 2011, p. 391. DOI: 10.7529/ICRC2011/V06/0898.

[118] Maurizio Spurio. *Probes of Multimessenger Astrophysics: Charged cosmic rays, neutrinos, γ-rays and gravitational waves*. 2018. URL: https://api.semanticscholar.org/CorpusID:126131637.

[119] Francesco Stolzi. *Identification of Cosmic Nuclei with the CALET Electron Telescope on the International Space Station*. PhD Thesis, 2017, p. 166.

[120] Are Strandlie and Rudolf Frühwirth. "Track and vertex reconstruction: From classical to adaptive methods". In: *Rev. Mod. Phys.* 82 (2 2010), pp. 1419–1458. DOI: 10.1103/RevModPhys.82.1419. URL: https://link.aps.org/doi/10.1103/RevModPhys.82.1419.

[121] A. W. Strong et al. "The GALPROP Cosmic-Ray Propagation Code". In: *arXiv e-prints*, arXiv:0907.0559 (July 2009), arXiv:0907.0559. DOI: 10.48550/arXiv.0907.0559. arXiv: 0907.0559 [astro-ph.HE].

[122] Andrew W. Strong and Igor V. Moskalenko. "Propagation of Cosmic-Ray Nucleons in the Galaxy". In: *The Astrophysical Journal* 509.1 (1998), p. 212. DOI: 10.1086/306470. URL: https://dx.doi.org/10.1086/306470.

[123] Andrew W. Strong, Igor V. Moskalenko, and Vladimir S. Ptuskin. "Cosmic-Ray Propagation and Interactions in the Galaxy". In: *Annual Review of Nuclear and Particle Science* 57.1 (Nov. 2007), 285–327. ISSN: 1545-4134. DOI: 10.1146/annurev.nucl.57.090506.123011. URL: http://dx.doi.org/10.1146/annurev.nucl.57.090506.123011.

[124] J.D. Sullivan. "Geometric factor and directional response of single and multi-element particle telescopes". In: *Nuclear Instruments and Methods* 95.1 (1971), pp. 5–11. ISSN: 0029-554X. DOI: https://doi.org/10.1016/0029-554X(71)90033-4. URL: https://www.sciencedirect.com/science/article/pii/0029554X71900334.

[125] Kerstin Tackmann and Andreas Hoecker. *SVD-based unfolding: implementation and experience*. 2011. arXiv: 1112.2226 [physics.data-an].

[126] T. Tamura and Calet Collaboration. "Status of the operations of CALET for 7.5 years on the International Space Station". In: *PoS* ICRC2023 (2023), p. 094. DOI: 10.22323/1.444.0094.

[127] Tadahisa Tamura. "Heavy ion beam test at CERN-SPS with the CALET Structure Thermal Model". In: *PoS* ICRC2015 (2016), p. 589. DOI: 10.22323/1.236.0589.

[128] Tadahisa Tamura and Calet Collaboration. "Particle Beam Tests of the Calorimetric Electron Telescope, presented by Tadahisa TAMURA". In: *International Cosmic Ray Conference*. Vol. 33. International Cosmic Ray Conference. Jan. 2013, p. 643.

[129] G. Tarle, S. P. Ahlen, and B. G. Cartwright. "Cosmic ray isotope abundances from chromium to nickel." In: 230 (June 1979), pp. 607–620. DOI: 10.1086/157119.

[130] The ATLAS collaboration. "Evaluating statistical uncertainties and correlations using the bootstrap method". In: (2021). URL: {https://cds.cern.ch/record/2759945?ln=en}.

[131] S. Torii et al. "Development of front-end electronics with large dynamic range for space applications". In: *Nuclear Physics B - Proceedings Supplements* 150 (2006). Proceedings of the 9th Topical Seminar on Innovative Particle and Radiation Detectors, pp. 390–393. ISSN: 0920-5632. DOI: https://doi.org/10.1016/j.nuclphysbps.2004.08.047. URL: https://www.sciencedirect.com/science/article/pii/S0920563205008832.

[132] Shoii Torii. "Highlights from the CALET observations for 7.5 years on the International Space Station". In: *PoS* ICRC2023 (2023), p. 002. DOI: 10.22323/1.444.0002.

[133] R. Voltz et al. "Influence of the Nature of Ionizing Particles on the Specific Luminescence of Organic Scintillators". In: 45.9 (Nov. 1966), pp. 3306–3311. DOI: 10.1063/1.1728106.

[134] R. L. Workman and Others. "Review of Particle Physics". In: *PTEP* 2022 (2022), p. 083C01. DOI: 10.1093/ptep/ptac097.

[135] Hongyi Wu, Eun-Suk Seo, and Vladimir Ptuskin. "Study Of Cosmic Ray Spectral Hardening Using GALPROP". In: *PoS* ICRC2021 (2021), p. 155. DOI: 10.22323/1.395.0155.

[136] Kazutaka Yamaoka, Atsumasa Yoshida, and Yuki Nonaka. "The CALET Gamma-ray Burst Monitor (CGBM)". In: *32nd International Cosmic Ray Conference*. Vol. 9. 2011, p. 111. DOI: 10.7529/ICRC2011/V09/0839.

[137] T. Yamashita et al. "Performance of 64-Multi-Anode Photomultiplier and Scintillating Fiber for the CALET Detector". In: *International Cosmic Ray Conference*. Vol. 4. International Cosmic Ray Conference. July 2003, p. 2193.

[138] Y. S. Yoon et al. "COSMIC-RAY PROTON AND HELIUM SPECTRA FROM THE FIRST CREAM FLIGHT". In: *The Astrophysical Journal* 728.2 (2011), p. 122. DOI: 10.1088/0004-637X/728/2/122. URL: https://dx.doi.org/10.1088/0004-637X/728/2/122.

[139] Chuan Yue et al. "Implications on the origin of cosmic rays in light of 10 TV spectral softenings". In: *Frontiers of Physics* 15.2, 24601 (Dec. 2019), p. 24601. DOI: 10.1007/s11467-019-0946-8. arXiv: 1909.12857 [astro-ph.HE].

[140] G. T. Zatsepin and V. A. Kuzmin. “Upper limit of the spectrum of cosmic rays”. In: *JETP Lett.* 4 (1966), pp. 78–80.